On the dynamic response of additively manufactured 316L stainless steel and the development of an orthotropic Johnson-Cook viscoplastic strength model.



Mr. Liam C. Smith

St. Edmund Hall

University of Oxford

A thesis submitted for the degree of

Doctor of Philosophy

Hilary 2023

UK Ministry of Defence © Crown Owned Copyright 2023/AWE

"What a useful thing a pocket-map is!" I remarked.

"That's another thing we've learned from your Nation," said Mein Herr, *"map-making. But we've carried it much further than you. What do you consider the largest map that would be really useful?"*

"About six inches to the mile."

"Only six inches!" exclaimed Mein Herr. *"We very soon got to six yards to the mile. Then we tried a hundred yards to the mile. And then came the grandest idea of all! We actually made a map of the country, on the scale of a mile to the mile!"*

"Have you used it much?" I enquired.

"It has never been spread out, yet," said Mein Herr: *"the farmers objected: they said it would cover the whole country, and shut out the sunlight! So we now use the country itself, as its own map, and I assure you it does nearly as well."*

. . . from *Sylvie and Bruno Concluded*, by Lewis Carroll.

Abstract

Materials produced using additive manufacturing (**AM**) techniques are becoming evermore prevalent within industry, especially where complex designs render conventional manufacturing (**CM**) norms economically impractical. Understanding the mechanical response of these novel materials to loads encountered during their lifetimes will allow for improved material selection and performance optimisation through microstructural design. A more detailed knowledge of the nascence and evolution of failure will also allow for an increased awareness of safety margins facilitating further optimisation of component design, especially where the AM microstructure significantly deviates from traditional CM equivalents.

The mechanical response of AM materials to quasi-static loading and fatigue are already the subject of significant academic study, however currently there is a relative lack of research focused on the high strain rate mechanical behaviour (both constitutive response and failure mechanisms). This dearth of research is especially prevalent at strain rates exceeding $10^3\,\mathrm{s}^{-1}$ likely due to the increased experimental complexity. As such, how AM components behave under such extreme conditions is poorly understood.

This thesis focuses on the mechanical response at strain rates ranging from $10^2\,\mathrm{s}^{-1}$ to $10^8\,\mathrm{s}^{-1}$ of AM 316L stainless steel, a corrosion resistant austenitic steel alloy widely used throughout engineering. It establishes links between observed material characteristics in AM samples, notably the spatial distribution of porosity defects, and both their dynamic response and failure modes with comparison against widely available CM equivalents. Precision impact testing to interrogate dynamic behaviour was achieved through means of reverse Taylor impact and plate impact spallation testing. This testing was undertaken on two distinct batches of AM 316L stainless steel, one possessing porosity just above 1 % on average, and a second with a porosity two orders of magnitude less, both were compared to CM equivalents for context. Reverse Taylor impacts revealed not only the role of oriented, layered, porosity defects in the dispersion of localised stress fronts, but also their role in varying the directional constitutive strength at high strain rates when compared to both the behaviour of dense AM material and also the CM counterparts. Spallation testing on porous AM highlighted a radically atypical and potentially directional tensile failure response at high strain rates. In comparison dense AM samples showed a typical pull-back response and a directional variance in the high strain rate tensile strength across loading directions, with intralayer mechanical performance exceeding interlayer responses in agreement with similar testing available within literature.

Augmenting experimental work, an associative non-tabulated orthotropic constitutive strength model combining the widely used Johnson-Cook strength model with a numerical routine harnessing abstract deviatoric stress eigenspaces to improve computational efficiency was developed. This model seeks to address limitations of already implemented alternatives that either offer limited capabilities, or require complex parametrisation workflows that limit widespread adoption. Following conception,

the model was implemented as a custom user-material into the commercial finite element package LS-DYNA, where it successfully recreated observed experimental responses. This achievement showcased the improvement to predictive capabilities for independently orthotropic strain, strain rate and temperature sensitive material responses, reducing the need going forward for large scale high strain rate component level testing of as-built AM material, a known challenge facing industry. The developed constitutive model sees direct applicability to as-built powder-bed AM material and also to the wider field of dynamic material behaviour modelling.

Applying the developed constitutive model, digital twins of experiments were created and optimised to experimental behaviour from two distinct batches of AM material, each with differing defect distributions, using machine learning techniques. The optimised model parameters offer insight into the role of layered porosity in the dynamic behaviour in AM materials, revealing that porosity not only reduces specific strength closer to that seen in CM equivalents, but also exacerbates the microstructural orthotropy present within the dense as-built material. These results underline the need for consistent defect-free AM as a baseline capability, and show the potential to leverage defect distributions in deliberately altering the dynamic response and failure modes of AM components.

Publications

- **Liam C. Smith**, Simone Falco, David Wason, David J. Chapman, Daniel E. Eakins. "A modified Johnson-Cook strength model: orthotropy, viscoplasticity and "normality" within material eigenspaces". **In Preparation**.

- **Liam C. Smith**, David J. Chapman, John C. Jonsson, Emilio M. Escauriza, Richard J. Williams, Kwan Lok Wong, Paul A. Hooper, Daniel E. Eakins. "Quantifying the effects of porosity on directional dynamic responses in as-built additively manufactured 316L stainless steel". **In Preparation**.

- **Liam C. Smith**, David J. Chapman, Daniel E. Eakins. "Extended heterodyne velocimetry baseline corrections using sequential evolving phase offsets.". **In Preparation**.

- Lukasz Farbaniec, David J. Chapman, Jack R.W. Patten, **Liam C. Smith**, James D. Hogan, Alexander Rack, and Daniel E. Eakins. "In-situ visualisation of dynamic fracture and fragmentation of an L-type ordinary chondrite by combined synchrotron X-ray radiography and microtomography". In: *Icarus 359*. December 2020 (2021), p. 114346. ISSN: 10902643. DOI: 10.1016/j.icarus.2021.114346

- Emilio M. Escauriza, Joao P. Duarte, David J. Chapman, Lukasz Farbaniec, John C. Jonsson, **Liam C. Smith**, Michael E. Rutherford, Daniel E. Eakins, Margie P. Olbinado, and Alexander Rack. "Ultra-high-speed X-ray imaging of shock-induced cavity collapse in a solid medium". In: *AIP Conf. Proc. 2272*. November (2020). ISSN: 15517616. DOI: 10.1063/12.0000933

- J. C. Jonsson, L. Farbaniec, E. M. Escauriza, **Liam C. Smith**, D. J. Chapman, and D. E. Eakins. "Effect of texture on elastic precursor decay in magnesium alloy AZ31B". In: *AIP Conf. Proc.* 2272. November (2020). ISSN: 15517616. DOI: 10.1063/12.0000818

- Martin Jäcklein, Konstantin Kappe, Aron Pfaff, Marius Bierdel, Klaus Hoschke, Matthias Wickert, Werner Riedel, Jacob Forster, Daniel Eakins, E M Escauriza, **Liam C. Smith**, and Alexander Rack. "Dynamic compression of 3D printed metallic mesostructures with in-situ X-ray imaging". In: *Proc. ISIE 2019 10th Int. Symp. Impact Eng. Gmunden: Trauner Verlag*, 2019

- D. J. Miller, R. S. Crum, M. A. Homel, D. E. Eakins, D. J. Chapman, J. C.Z. Jonsson, M. E. Rutherford, E. M. Escauriza, **L. C. Smith**, E. B. Herbold, J. Lind, and M. C. Akin. "Hugoniot Measurements Utilizing In Situ Synchrotron X-ray Radiation". In: *J. Dyn. Behav. Mater.* 5.1 (2019), pp. 93–104. ISSN: 21997454. DOI: 10.1007/s40870-019-00187-x

Presentations

- "Reverse Taylor Testing of Conventionally and Additively Manufactured 316L Stainless Steel". Poster Presentation, At: *Shock Compression of Condensed Matter*, St. Louis, USA. July 2017.
- "Dynamic Behaviour of Additively Manufactured 316L Stainless Steel". Poster Presentation, At: *Defence and Security Doctoral Symposium*, Swindon, UK. November 2018.
- "The Role of Defects in the Dynamic Response of AM SLM 316L". Poster Presentation, At: *The Minerals, Metals & Materials Society*, San Diego, USA. February 2020.
- "An orthotropic Johnson-Cook strength model using eigenspace transforms for radial-return within material subspaces.". Poster Presentation, At: *CornerStone Prosperity Partnership and Doctoral Training Conference*, Belfast, UK. June 2022.

Proceedings

- **Liam C. Smith**, David J. Chapman, Paul A. Hooper, Glenn Whiteman, and Daniel E. Eakins. "On the dynamic response of additively manufactured 316L". In: *AIP Conf. Proc.* Vol. 1979. July 2018, p. 060007. ISBN: 9780735416932. DOI: 10.1063/1.5044804

Acknowledgements

Succinctly, research is the collaborative product of extraordinary teams of students, academics, technicians, administrators, *et al.* . There are however, those deserving of explicit thanks.

Dan, your patience, expertise, and advice have been invaluable. David, Simone, and Lukasz, thank you all for teaching and later questioning. John and Emilio, thank you for all the hours of assistance. Ending academic recognition, Glenn and Matthew, your help has been genuinely thesis-saving.

Beyond academia, the Teem, the Hall, OUCCC, and habbitual caffeination have kept me somewhat sane and then there are my family, without whom this thesis would not exist.

Contents

I Introduction, Aims & Context **1**

1 Additive Processes, the Formative Years **2**

1.1 Possibilities & Challenges . . . 3

1.2 Research Goals & Strategy . . . 6

2 AM Dynamic Testing & Modelling: State of the Art **9**

2.1 Experimental Endeavours . . . 9

2.2 Modelling . . . 13

3 Material Theory **19**

3.1 Underpinning Concepts . . . 19

3.2 Plasticity; von Mises & Hill . . . 24

3.3 Johnson-Cook Model . . . 32

3.4 Eigenspace Radial Return . . . 34

4 Dynamic Material Response **43**

4.1 Shock Loading . . . 43

4.2 The Lagrangian Diagram . . . 48

4.3 Spallation . . . 48

II Experimental Methods & Results **67**

5 Manufacturing & Characterisation **68**

5.1 Manufacture . . . 68

5.2 Microscopy . . . 71

5.3 Tomography . . . 74

6 Photon Doppler Velocimetry **80**

6.1 Superposition & The Doppler Effect . . . 80

6.2 Conventional (Homodyne) Implementation . . . 84

6.3 Frequency Shifted (Heterodyne) Implementation . . . 86

6.4 System Implementation . . . 87

6.5 Phase Evolution Baseline Removal . . . 90

6.6 PDVTool . . . 95

7 Taylor Test Experimental Data **97**

7.1 Overview . . . 97

7.2 Experimental Setup . . . 101

7.3 Imaging . . . 105

7.4 Rear Surface Velocity . . . 115

7.5 Conclusions . . . 122

8 Spallation Testing: Atypical Behaviour **124**
8.1 Overview . . . 124
8.2 Initial Campaign: Porous Response . . . 124
8.3 Second Campaign: Dense Response . . . 129
8.4 Conclusions . . . 137

III Modelling & Optimisations **145**

9 Orthotropic Material Model **146**
9.1 Johnson-Cook Parameters . . . 146
9.2 Pseudocode Algorithm . . . 149
9.3 Model Validation . . . 157
9.4 Conclusions . . . 182

10 Optimisations & Parametrisation **184**
10.1 Parameter Identification Routine . . . 184
10.2 Digital Twins . . . 186
10.3 Porous AM 316L . . . 188
10.4 Dense AM 316L . . . 189
10.5 Conclusions . . . 194

IV Conclusions & Future Work **204**

11 Conclusions **205**

12 Future Work **210**
12.1 Microscopy & EBSD . . . 210
12.2 Residual Stress . . . 211
12.3 Computational Refinements . . . 211
12.4 Thermal Sensitivity . . . 213
12.5 Stochastic Parametrisation . . . 213
12.6 Non-Associative Flow . . . 214
12.7 Full Anisotropy . . . 214
12.8 Mapping the Manufacturing Domain . . . 215

V Appendix **237**

13 Additional Experimental Data **238**
13.1 Light Gate Example . . . 238
13.2 Reverse Taylor Impact Data . . . 240

Part I

Introduction, Aims & Context

Within the opening part of this thesis some key questions will be considered. Firstly, why is this research important, what are the key areas of research covered, and where lie the current limits of understanding in these applicable areas? From this basis, the potential areas where new understanding may be sought, the specific routes of the project, and the outcomes of this study will be presented, with the aim of contextualising the work detailed thereafter for the reader.

Chapter 1

Additive Processes, the Formative Years

Additive manufacturing (**AM**) is an umbrella term describing a group of component fabrication techniques typified by the successive consolidation of an aggregate to a predefined volume of material. This process is controlled such that upon completion little to no subtractive or deformative manufacturing processes are then required to realise the intended design. Circumventing the the need for the removal or deformation of material represents a fundamental evolution to the manufacturing processes that have formed the foundations of engineering since the industrial revolution [1].

Preliminary forms of AM, introduced in the mid 1980's [2–7], were focused upon streamlining early stages of the design process, coining them the moniker rapid prototyping. Such processes offered a clear advantage against the traditional use of machinists for the trial of several different designs where there was no requirement for production grade components in visualising concepts. These early additive processes were primarily based around either the selective solidification of resin to a solid (known as stereolithography or digital light processing), or from the deposition of molten polymer filaments upon a solid (known as fused deposition modelling).

Ultimately, AM outgrew its initial confines, progressing from prototyping to production and solidifying its place as an effective, albeit niche, manufacturing technique within engineering, attributable in part to the unique capabilities of AM processes. The transition point is of course subjective, however a reasonable juncture may be identified as the establishment of metal based processes in the mid 1990s [7–11]. These processes fall into two broad categories, directed energy deposition and powder bed fusion processes using lasers or electron beams as heat sources.

This thesis focuses upon a laser based powder bed fusion AM technique, termed selective laser melting (**SLM**) by Abe *et al.* in 2001 [12], involving precisely controlled

partial exposure of horizontal layers of powder atop a solid to a powerful laser. The exposure rapidly and completely melts the powder bed in the immediate locality, in contrast to sintering techniques that fail to achieve complete fusion, with the post-exposure cooling and solidification joining the powder to the solid below. The primary capability of this technique above other AM processes, producing parts in commercial alloys with low fractional porosities, ideally suit it to the production of high quality, high performance parts. However, the nuances associated with this technique, and AM processes in a wider sense, are both significant and complex, limiting adoption. It is into these nuances that this thesis seeks to build understanding.

1.1 Possibilities & Challenges

As indicated above, additive techniques offer a range of new avenues for the manufacture of production level components; these avenues will facilitate the realisation of higher performance designs that were previously economically impractical or beyond the capabilities of currently existing conventional norms. Some examples of the benefits afforded by these new avenues include:

- the facilitation of novel geometries that were previously unfeasible; an ideal example is the possibility of creating internal cooling channels [13, 14] with conformal paths or even capillary structures that mimic those observed in nature,
- the capability to produce functionally graded materials [15] where alloy elemental composition is deliberately varied throughout the component to create heterogeneous material characteristics. An example of this is designing components with high specific strength cores and corrosion resistant surface layers [15, 16], or the seamless linking of components with distinct alloy compositions, negating the need for fasteners and their associated weight increase and compliance,
- the potential to deliberately vary the microstructure of a given alloy within a component through print parameter variation [17], in turn altering the resultant mechanical response [14] and failure threshold [18] so as to allow components to

posses strength where stressed, ductility where desired, and maybe even allowing for the foreplanning of failure modes.

In order for these capabilities to be successfully realised across industry, a number of key processes must be understood to link each successive stage of manufacture and the resultant component end performance. The links that must be established by academics working within the AM field fall into two main domains.

1. An understanding of the print process, linking each characteristic of the process to the resultant microstructures for each alloy used. Ideally an understanding of the relationships linking alloy composition [19, 20], powder characteristics [21–23], component geometries [24, 25], print parameters [26] and resultant microstructures [27] will eventually be realised. This understanding will allow the subsequent development of predictive capabilities that seek to produce a specific distribution of microstructures, leading to the creation of higher performance components than are currently available, where the microstructure is tuned to the specific demands of the component.

2. An understanding of variations in additively manufactured microstructures from their conventional equivalents and how these relate to component performance. Over the longer term an understanding of how gradations in microstructure affect performance [16, 28, 29] and how these gradations are best applied to real world component design would also be created. This understanding will allow the full capitalisation of variations in alloy elemental composition and print parameters that are mentioned above to optimise resultant component performance.

Without understanding these processes industry will lack the ability to capitalise on the unique advantages offered by AM, advantages that are applicable to many fields including medical, aerospace, automotive and defence [30–33].

Presently, where manufacturers push the boundaries of the additive manufacturing process, they risk introducing components to situations where unpredictable performance could cost lives, a risk that is especially pertinent in situations involving

dynamic loading [34]. Dynamic loading presents a criticality to the understanding of mechanical response and failure for safety concerns, as failure will occur over a short $< 1\,\mathrm{s}$ time scale where human response to warnings are likely impossible. Currently this risk is mitigated through the use of destructive component level validation [35] and large safety margins [36]. The required testing is both expensive and time consuming, limiting the adoption of AM components to only those applications which demand the highest performance regardless of cost, despite the benefits that may be realised through harnessing such manufacturing processes across a much wider range of applications. The secondary need for large safety margins is found throughout engineering, however the inherent variability [24] and relative lack of knowledge pertaining to additive microstructures necessitates that the safety margins remain significant, with any future safe reduction of these margins directly beneficial to the potential performance of AM components.

Further complicating the adoption of AM components in their as-built state are the limitations to predictive capabilities presently available within commercial finite-element packages. Firstly, the highly non-linear and multivariate nature of dynamic component responses ensures that without clear understanding and robust numerical modelling, simple extrapolation of component level responses can result in significant disparities between predicted and actual component behaviour. Against this backdrop, material strength models must therefore robustly account for several competing environmental, microstructural, and loading factors if they are to successfully guide future efforts into improving component response. Presently however, there is a gap in currently implemented material codes, whereby rate-dependent, history aware, and thermally sensitive constitutive strength models designed to model dynamic impact are almost exclusively isotropic [34]. Those few models that offer such dependencies tied to a directional response depend themselves on either tabulated inputs [37] or the use of such a large suite of parameters that they require extensive experimental campaigns to evaluate optimal material parameters. At some point this becomes an exercise in over-parametrisation [38], with exquisite models requiring countless tests

and significant computational resources, thus hindering the ease with which they may be implemented in all but the most specific of applications.

This situation highlights the potential for a directional constitutive strength model, where strain hardening, rate effects and thermal dependencies are provided in an accessible form, aiding adoption of AM components within industry. Ideally the dependencies used would follow familiar forms, facilitating the adaptation of preexisting conventional material responses to their additive counterparts.

1.2 Research Goals & Strategy

This body of work focuses on the second major domain of research listed in section 1.1, with the research goals consisting of:

1. drawing links between the atypical additive microstructure of as-built AM 316L steel, an austenitic corrosion resistant stainless steel, and its dynamic strength and failure modes,

2. improving the foundations for effective adoption of as-built AM components into industrial applications where dynamic loading is of concern by developing predictive capabilities well suited to the application.

Of note here is the decision to focus on as-built additive components, this choice was taken due to the opportunities offered by heterogeneous microstructures, with post printing heat treatments often homogenising and therefore mitigating such benefits. The strategy employed to achieve these goals involved several steps, with these and the underpinning prerequisites forming the bulk of this thesis in parts II and III. Including the opening and closing arguments, the structure of this thesis is as follows.

Part I offers an underpinning to the thesis, introducing both the broad context and motivations behind the work. From here the present state of research within the field is presented with key pieces of theory also covered that are required to support work detailed in latter parts.

Part II covers experimental work undertaken in the thesis. Tackling the first research goal this initially develops an understanding of the microstructural characteristics of tested additive material with comparison to conventionally manufactured equivalents. This understanding focuses primarily on porosity distributions, initially via readily available optical microscopy and later by micro-computed tomography (µCT) scans [39], as this is often a dominant factor in altering dynamic performance [40]. From here measurement of CM and AM response under complex loading conditions via reverse Taylor impact is described. Testing was completed on as-built AM material both along and normal to the build direction and across varying defect structures, with corresponding tests on CM equivalents providing a baseline. Following this, CM and AM spallation response is investigated, using established literature techniques [41–44] to draw conclusions on directionality in the spallation response of AM 316L, and the implications of porosity on dynamic tensile strength. The combination of complex constitutive testing via reverse Taylor impact and high rate spallation testing seek to tackle parts of the first research goal, notably the challenges of dynamic strength and failure respectively. These results, discussed alongside the characterised porosity distributions, reveal links between the microstructure and response.

Part III seeks to tackle the second research goal by investigating the modelling of AM materials, seeking to successfully recreate the observed dynamic behaviour. This process includes the development of a suitable model from theory detailed within part I into an implemented material routine, with systematic validation simulations presented given the models several dependencies. Following on from the definition of the model, an inverse modelling routine is presented, using experimental observations of AM response to populate a suitable material constitutive model. This will serve to demonstrate the developed predictive capability for the dynamic response of as-built 316L. Comparison between optimised outputs of this predictive capability will also provide links between as-built additive

microstructures and their constitutive response.

Part IV consolidates conclusions reached within this body of work, with a summative view taken aiming to link together the conclusions reached. Augmenting this, a discussion of future avenues of research including the merits and challenges of each avenue, provides an onward outlook into the next steps for accelerating the uptake of AM within engineering scenarios involving dynamic loading.

Part V offers further information omitted from the main body of work to retain concision. This supplementary information brings the thesis to a close.

Chapter 2

AM Dynamic Testing & Modelling: State of the Art

The field of additive manufacturing (**AM**) has seen significant research over the last two decades, with the comprehensiveness of work immediately apparent upon studying review papers by Gu *et al.* [33] and the encyclopaedic work of DebRoy *et al.* [45]. To this end there exists a diverse repository of literature from which to appreciate the complexity of underpinning dependencies within additive routes of manufacture, how these then affect the resultant behaviour, and the development of relevant predictive capabilities. Within this chapter a summary of the current literature is presented, with areas directly applicable to this body of work covered at length.

2.1 Experimental Endeavours

2.1.1 Manufacturing Conditions

Whilst outside the specific area of research studied, progression over the last 15 years has improved the quality of material produced using powder bed processes. The conclusions reached help to underpin studies on mechanical response, whilst building upon earlier, more conceptual, research published by Kruth [2], Badrinarayan and Barlow [3], Agarwala *et al.* [8], and others thereafter [9, 12, 46–48].

Succinctly, this work reduced defect prevalence in established AM alloys through variation of print parameters and powder feedstock [22, 49–52], it also explored novel alloys offering greater resilience to the extreme thermal paths of additive processes [19, 53–57] or controlled gradations of mechanical response [16, 28, 29]. Of note in this work is the coining of a characteristic oft-referred to as *printability* [19, 20], quantifying resilience to AM process conditions. Following from these, recent studies [58, 59] have

presented predictive capabilities for as-built microstructure and quasi-static response.

Concurrently to broader studies, the effects of variations in powder feedstock, including size distribution and powder defect prevalence have been thoroughly investigated [21, 23, 60–62]. Furthermore, how print parameters influence the as-built microstructure of consistent powder feedstock have been studied repeatedly, in titanium [63, 64], steel [65], aluminium [55, 66, 67], and nickel based superalloys [51, 68].

Studies linking print parameters to microstructure have even looked beyond those comprising energy density, a low resolution value for quantifying the build conditions. Interesting examples include beam profile variations [69], build volume layout [70], scanning strategy [71], and the remelting of the powder bed at every layer [72].

Whilst the aforementioned studies seek to minimise defect prevalence, others focus on the underlying formation mechanisms of specific defects. This research has observed keyhole mode voiding and melt pool instability *in situ* using synchrotron X-ray imaging [73] or micro computerised tomography (**μCT**) [39], as well as melt pool ejecta dynamics using high speed imaging [74] and concurrent X-ray imaging and diffraction [75], building valuable low level knowledge of laser-powder interactions.

Considering the printing of 316L stainless steel, many articles cover laser based powder bed processes [76–86] and alternate additive methods [18, 87, 88]. Of particular interest is Cherry *et al.* [26] and Zhong *et al.* [89], due to the use of Renishaw AM 250 SLM printers in the manufacture of samples, as used within this research, contextualising the manufacture route of observed material responses.

Summarising the above studies, 316L displays a high degree of printability, with the manufacture of defect-free material possible. The presence of oriented thermal gradients during manufacture is commonplace, with steep spatio-temporal gradients leading to a highly refined sub-grain cellular microstructure [89] with large columnar grains that grow epitaxially [70]. The hierarchical nature of microstructural characteristics provides multiple sources for the typically enhanced mechanical performance [86]. Porosity, when present, is primarily found at the edges of melt tracks, with this preferentially seeding interlayer porosity above intralayer voiding [90].

2.1.2 Mechanical Testing of AM Metals

Of greater applicability to this thesis are studies focused on the mechanical response of additively manufactured alloys, with these still including discussion of print parameters to link performance and manufacturing route. Contrasting research into phenomena occurring within additive manufacturing processes, there already exist established frameworks within which to evaluate material mechanical performance, with comprehensive texts [36, 91, 92] for reference. Retaining concision, mechanical testing of materials in general is omitted here, with brief histories of applied techniques given preceding relevant experimental data later within this work.

Looking at alloys other than 316L stainless steel, several studies have investigated the quasi-static response of AM materials beginning with Abe *et al.* [63] in 2003 on titanium and Kruth *et al.* [93] in 2004 on iron based powders. Later work has covered titanium [94–96], aluminium [97, 98], steels [18, 94, 96, 99, 100], and nickel based super alloys [101]. More interestingly for this thesis, many have also considered the effects of heat treatments [99], directionality in both elastic [102] and plastic [94–98, 103] regimes as well as the impacts of porosity [98, 104].

In the dynamic regime comparatively little work exists on material response. Most testing employs split Hopkinson bar in compressive [32, 105, 106] or tensile modes [25, 107] with porosity [40, 104, 108] and orientation [25, 107, 109] effects also quantified. Above $10^3\,\mathrm{s}^{-1}$ plate impact spallation testing has probed orientation [110, 111] and porosity [112] effects on dynamic tensile strength, with laser shock loading [113] echoing conclusions from plate impacts of elevated specific strength, with porosity degrading performance, especially normal to build directions.

Reviewing laser powder bed AM 316L, studies have found directionality in the elastic response [114], yield stress [23, 76, 115] and hardening [114] under quasi-static loading. Elevated specific strength with minimal loss of ductility [116] and improved fatigue performance [117] are possible given near full density components. Elevated performance occurs only if optimal manufacture routes are used, with deviation re-

ducing yield strength and ductility [23, 118]. Directionality is identified as transverse isotropy [119], this follows as thermal gradients fall parallel to the build direction with epitaxial grain growth preferentially orienting microstructural features [70, 120, 121]. In laser based processes this elevated performance falls normal to the build direction [84, 114, 119, 121], interestingly contradicting electron beam powder bed methods [88].

Studies investigating the dynamic response of additive 316L are by comparison, significantly rarer. The majority of dynamic material responses are seen under split Hopkinson pressure bar compressive loading [122–124] where elevated performance is seen compared to conventionally manufactured equivalents. Aside from split Hopkinson pressure bar testing, Gray *et al.* [125] showed elevated as-built spallation strength compared to conventional baselines under plate impact, with a reduction of the disparity in performance following recrystallisation in additive samples.

Moving beyond additively manufactured bulk material, lattice geometries that were previously impractical to manufacture have now been investigated under quasi-static loading [31, 126–128], and by Jäcklein *et al.* [129] at higher rates of deformation.

Concluding the overview of mechanical testing on additively manufactured materials, in particular that of 316L stainless steel, significant work has undoubtedly been completed. Quasi-static performance is well studied in comparison to conventionally manufactured (**CM**) equivalents, the effects of porosity on performance and the presence of anisotropies have been investigated across a number of different alloys. It is in the dynamic regime where greater opportunity for research is found, a conclusion echoed by Carlson in 2021 stating:

> '*Although prior studies on 316L AM exists, they are only focused on process optimisation and quasi-static mechanical testing. Current research on high strain rate testing of AM materials is limited since it does not account for the influence of build orientation.*' [123]

when introducing a study of dynamic compressive response in SLM 316L under split Hopkinson pressure bar loading.

Taking this further, the dynamic constitutive response of AM 316L is still poorly understood, with as-built material response to complex dynamic loading across a range

of strain rates not yet studied. A second gap exists in the effects of porosity on dynamic response in 316L stainless steel; limited work has been conducted so far with strain rates above $10^3\,s^{-1}$ lacking detailed study. These gaps present the opportunity to improve understanding of dynamic response at strain rates above $10^3\,s^{-1}$, where experimental challenges hinder effective measurements. The potential to probe complex loading states that will better challenge predictive capabilities, and seek to excite new mechanical responses, is ideal for working to build understanding of the limitations of dynamic performance in AM components in the long term.

2.1.3 Reviewing AM

Summarising additive research, review papers including those mentioned in the opening of this chapter [33, 45], and others have highlighted the range of applications, potential benefits, and limitations. These papers are vital to accelerating adoption and have included Kruth *et al.* [130], Wong and Hernandez [6], Udupa *et al.* [15], Herzog *et al.* [131], Mower *et al.* [132], and Oliveira *et al.* [133]. Whilst not requiring the authors undertake experimentation or modelling, the effective summarisation of such a diverse field of research is of immense value.

2.2 Modelling

There is a wealth of literature pertaining to the constitutive response of CM metals, however few studies have sought to optimise constitutive models for AM responses. Of those that do, Asala *et al.* [134, 135] have successfully modelled direct impact Hopkinson bar responses in AM nickel based super alloys, using either isotropic Arrhenius-type [136] or isotropic modified Johnson-Cook [137] models that showed improved performance over solely Arrhenius-type models. Preceding this, Zhao *et al.* [138] compared traditional and aforementioned modified Johnson-Cook strength models in modelling FeCr alloys under split Hopkinson pressure bar loading conditions across a range of temperatures, again this assumed isotropic responses but verified improved agreement with the modified Johnson-Cook and its increased number of dependencies. Consid-

ering 316L stainless steel, Ahmadi *et al.* [139] conducted small scale crystal plasticity modelling of quasi-static behaviour. Scaling up, and including higher strain rates, Bevan *et al.* [122] showed similarity to CM norms in the dynamic response of AM 316L at strain rates of $10^3\,s^{-1}$, modelling experimental data with isotropic Johnson-Cook strength models, an approach echoed by Brown *et al.* [105] on AM Ti-6Al-4V.

Unfortunately, none of these studies consider anisotropy, let alone attempt to model it, despite there being a wealth of experimental data showing this to exist in as-built AM materials [18, 66, 95, 110, 125, 140].

Summarising the above research, there have been attempts to develop predictive capabilities for as-built AM materials, however so far these have yet to look deeply into anisotropy or the effects of defects on the constitutive behaviour. Furthermore there exists a complete lack of constitutive prediction at strain rates of above $10^3\,s^{-1}$ and also under complex loading states that would increase the complexity of reproducing observed behaviours. It is clear that a gap exists, specifically regarding the capability to describe and then predict the behaviour of AM materials subjected to dynamic and complex loading along and perpendicular to the build direction. This capability would be ideally realised in a way that allows comparisons between CM and AM responses to better frame the results within the context of current CM literature.

2.2.1 Constitutive Behaviour & Yield Criteria

Of critical importance to achieving predictive capabilities of bulk ductile AM material mechanical response under a range of conditions are the yield criterion and plastic potential. This pairing serves to define a materials constitutive strength, effectively regulating the conversion of excess elastic strain energy into plastic work.

Within constitutive models, existing in FEA packages, suitable for modelling metals, only a subset allow the rate of energy absorption to depend on material conditions, such as prior plastic deformation, the rate of deformation, or the material temperature. This subset is further reduced if necessitating directionally dependant responses, to the point where it is summarised for the LS-DYNA FEA suite in table 2.1.

Material Name & (Number) or [Citation]	Anisotopic Yield	Strain Sensitive	Rate Sensitive	Thermally Sensitive	Anisotopic Evolution	Tabulated Parameters	Shell Only
Johnson-Cook (15)		•	•	•			
Orthotropic Johnson-Cook (264)	•	•	•	•	•	•	
Zerilli Armstrong (65)		•	•	•			
Barlat YLD96 (33_96)	•	•	•				•
Barlat YLD2000 (133)	•	•	•	•			•
Three Parameter Barlat (36)	•	•	•		•	•	•
Hill 3RC (122)	•	•					•
Hill 3R3D (122_3D)	•	•		•	•	•	
Hill 3R Tabulated (122_TAB)	•	•				•	•
Hill90 (243)	•	•	•	•		•	•
Bammann–Chiesa–Johnson (51)	•		•	•			
EMMI (151)	•	•	•	•	•		
Cousins, 2016 [141]	•	•	•	•			

Table 2.1: Implemented models of interest in the LS-DYNA FEA suite and their capabilities and limitations. Materials were only included if applicable to the modelling of bulk metal, with the **most applicable constitutive models** worthy of discussion distinguished using colours. An extra constututive model developed by Cousins in 2016 is also included, due to its applicability to the research and prior implementation into LS-DYNA. Where available in commercial distributions of the FEA suite, material numbers are provided to link to documentation, with citation provided in place of a material number if not commonly available. Where tabulated parameters are noted, this is as required to achieve the most capable form of the model. Unfortunately, negating tabulated inputs often removes strain rate or thermal sensitivities, so in these case the model is classified with all available sensitivities activated.

Considering the models presented in table 2.1, a subset of models of interest are discussed below with their limitations. These models are distinguished using bold font and colour as described in the table caption.

The first model of interest is material 264, titled within LS-DYNA manuals as the Tabulated Johnson-Cook Ortho Plasticity, herein referred to as the Tabulated Orthotropic Johnson-Cook model. This constitutive model, developed by Haight [34, 37] in 2016 to model the widely known titanium alloy Ti-6Al-4V, is capable in principle of recreating the three key material state sensitivities of interest, exhibiting tension compression asymmetry, and producing directionally dependant plastic responses atop an isotropic elastic response. It achieves this through the definition of tabulated responses, which are then sampled to create a plastic potential using calculations of deformation rate and loading state (including an orthotropic version of the Lode parameter [142]).

The model is undoubtedly impressive, with the ability to define an evolving plastic orthotropy under impact conditions. However the limitation to isotropic elasticity when paired with such a complex plastic response undoubtedly limits its applications. Furthermore, the complexity offered also limits its accessibility with a large number of tests required to inform responses. Following this extensive testing a highly complex numerical algorithm is used, consisting of well over 100 steps [34] when summarised. Furthermore, many of these steps are in fact iterative loops requiring upwards of 25 iterations to achieve convergence according to Haight himself. This complexity is paired with a need for large volume of tabulated data adhering to specific and consistent loading and material condition combinations, a requirement that is at best experimentally challenging and arguably at worst entirely unfeasible in dynamic loading scenarios. Furthermore, the requirement for specific load curves hampers the ability to underpin the model on complex loading paths that often form some of the most challenging conditions for constitutive models. This combination of limitations unfortunately reduce the potential applications of the model to all but a few of the most niche cases.

The second model of interest is the Hill 3R3D (material 122_3D) which again offers significant capabilities that only omit rate-sensitivity from the list of desired

dependencies. Unfortunately this insensitivity to deformation rates is of critical importance when seeking to develop a predictive capability for dynamic loading scenarios. This, paired again with the need for tabulated inputs and the associated limitations discussed above, once again diminish the suitability of the model for use in this work.

The third model, the evolving microstructure of mechanical inelasticity (**EMMI**) model [143], closely relates to the also noted Bammann-Chiesa-Johnson (**BCJ**) model [144]. This model offers perhaps the most capable currently implemented routine for handling complex multivariate directional plasticity. However, one issue of this model is the complexity, also seen in the less complex BCJ model described in LS-DYNA documentation as *"a fairly complex model that has many input parameters"* [145]. Whilst providing the required dependencies, without the need for tabulated input parameters that limit the potential for the modelling of dynamic behaviour, this model requires a total of up to 80 material parameters within its implementation. It is the author's opinion that defining so many parameters limits accessibility of the model to only the most exceptional of applications, well beyond the capabilities of the majority of engineering use-cases, and the goals of this work in both improving the quality of and reducing the barriers to effective predictive capabilities.

The final candidate within the preferred subset of constitutive models, that developed by B. Cousins at the University of Oxford in 2016 [141], is not implemented into standard distributions of the LS-DYNA package. However, this model is of interest as it, similarly to the EMMI model, draws inspiration from the BCJ model whilst applying enhancements that seek to add the modelling of both anisotropy and asymmetry into its arsenal. Within the Cousins model, associative anisotropic yielding is included through the widely used quadratic Hill model [146], with asymmetry provided through expansion to the commonly used von Mises criterion in the form of the Drucker-Prager criterion. Ultimately this model provides several aspects that would be desirable, however the lack of potential to allow for an evolving degree of material anisotropy, particularly anisotropy dependant on the rate of deformation is of concern. Furthermore, in application of the quadratic Hill yield criterion to provide associative

yielding, the model states,

> '*the radial return (**n**) is assumed in alignment with the direction of the effective stress.*' (p. 154) [141]

where here, the direction of radial return is used in reference to the incremental deviatoric plastic strain, a quantity that does not align with the effective stress when applying a Hill based yield criterion. Cousins appears to tackle this by scaling the effective stress by the Hill anisotropy tensor, an object that serves to represent the orthotropy in the yield surface. This approach raises questions as to the validity of assuming alignment between the deviatoric stress and direction of plastic flow, as the deviatoric stress state itself is distorted, using the Hill tensor, from its isotropic alignment. Such is this issue, that when paired with the inability to evolve the anisotropy and the preexisting complexity within the model, it was decided that incorporation of evolving anisotropy, and transition to a true associative flow basis would be prohibitively complex, especially when seeking to retain accessibility to a wide range of users. This limitation is noted by Cousins himself when discussing methods to implement an anisotropic yield criterion in his doctoral thesis, saying that:

> '*developments within this research shall surround the associated flow rule due to the simplicities of the quadratic Hill solution and given the complexities of the existing model*' [141]

where the existing model is a development of the already 'fairly complex' [145] BCJ model.

Ultimately, the surveyed literature further evidences a gap in the predictive capability available within the presently implemented non-isotropic constitutive models. This gap (omitting full anisotropic plasticity) may be defined succinctly as the need for a true implementation of an orthotropic Johnson-Cook or Zerilli-Armstrong strength model. More specifically, this may be interpreted as the lack of any widely implemented material models that allow an accessible predictive capability sensitive to strain, strain rate, and temperature that provide an orthotropic response, without the need for tabulated inputs.

Chapter 3

Material Theory

3.1 Underpinning Concepts

The material model developed within this body of work relies on several underpinning mathematical concepts, in following section a foundation for many of these mathematical steps is provided. These concepts are detailed to allow the reader a more complete description of the model as defined in chapter 9.

3.1.1 Elastic Behaviour

The initial stages of deformation in a material are assumed to be elastic with any incurred deformation from applied loads entirely recoverable given the removal of the applied load. The ratio between applied stress and incurred strain during this period is assumed to be proportional, with a linear mapping describing the relationship as such,

$$\boldsymbol{\sigma} = \mathbf{C}\boldsymbol{\epsilon}, \tag{3.1}$$

where $\boldsymbol{\sigma}$ and $\boldsymbol{\epsilon}$ are 2nd order (3×3) tensors describing the true stress and strain at a given location in the material continuum respectively. The tensor $\mathbf{C}$ is identified as the stiffness tensor, a 4th order $(3 \times 3 \times 3 \times 3)$ linear mapping between stress and strain. Owing to symmetry in $\boldsymbol{\sigma}$, the Cauchy stress tensor, it is possible to reduce the required number of terms needed to represent a given state. Using the widely adopted Voigt notation $\boldsymbol{\sigma}$ and $\boldsymbol{\epsilon}$ may be described by (6×1) element column vectors with $\mathbf{C}$ reduced to a 2nd order (6×6) tensor. The above mapping is given explicitly in Voigt

notation as,

$$\begin{bmatrix} \sigma_{11} \\ \sigma_{22} \\ \sigma_{33} \\ \sigma_{23} \\ \sigma_{31} \\ \sigma_{12} \end{bmatrix} = \begin{bmatrix} c_{11} & c_{12} & c_{13} & c_{14} & c_{15} & c_{16} \\ c_{21} & c_{22} & c_{23} & c_{24} & c_{25} & c_{26} \\ c_{31} & c_{32} & c_{33} & c_{34} & c_{35} & c_{36} \\ c_{41} & c_{42} & c_{43} & c_{44} & c_{45} & c_{46} \\ c_{51} & c_{52} & c_{53} & c_{54} & c_{55} & c_{56} \\ c_{61} & c_{62} & c_{63} & c_{64} & c_{65} & c_{66} \end{bmatrix} \begin{bmatrix} \epsilon_{11} \\ \epsilon_{22} \\ \epsilon_{33} \\ \epsilon_{23} \\ \epsilon_{31} \\ \epsilon_{12} \end{bmatrix}.$$

In the case a material displays a degree of symmetry, it is possible to further reduce the number of variables required to map strain and stress further by considering various reflections along coordinate axes. In Voigt notation the transformation tensor is given to be [147, 148]:

$$\mathbf{R} = \begin{bmatrix} r_{11}^2 & r_{12}^2 & r_{13}^2 & 2r_{12}r_{13} & 2r_{13}r_{11} & 2r_{11}r_{12} \\ r_{21}^2 & r_{22}^2 & r_{23}^2 & 2r_{22}r_{23} & 2r_{23}r_{21} & 2r_{21}r_{22} \\ r_{31}^2 & r_{32}^2 & r_{33}^2 & 2r_{32}r_{33} & 2r_{31}r_{33} & 2r_{31}r_{32} \\ r_{21}r_{31} & r_{22}r_{32} & r_{23}r_{33} & r_{23}r_{32} + r_{33}r_{22} & r_{21}r_{33} + r_{31}r_{23} & r_{22}r_{31} + r_{32}r_{21} \\ r_{31}r_{11} & r_{32}r_{12} & r_{33}r_{13} & r_{33}r_{12} + r_{13}r_{32} & r_{13}r_{31} + r_{11}r_{33} & r_{32}r_{11} + r_{12}r_{31} \\ r_{11}r_{21} & r_{12}r_{22} & r_{13}r_{23} & r_{13}r_{22} + r_{23}r_{12} & r_{11}r_{23} + r_{21}r_{13} & r_{12}r_{21} + r_{11}r_{22} \end{bmatrix}.$$

Taking this transformation it is then of interest to apply a reflection of the basis in the 33 direction, where the Cauchy form of $\mathbf{R}$ is:

$$(\mathbf{R})_{\text{Cauchy}} = \begin{bmatrix} r_{11} & r_{12} & r_{31} \\ r_{12} & r_{22} & r_{23} \\ r_{31} & r_{23} & r_{33} \end{bmatrix} = \begin{bmatrix} 1 & 0 & 0 \\ 0 & 1 & 0 \\ 0 & 0 & -1 \end{bmatrix},$$

and in knowing that the elastic stiffness matrix $\mathbf{C}$ for an orthotropic material is invariant given the reflection along an axis of orthotropy, to then equate the matrix before $(\mathbf{C})$ and after $\left(\mathbf{C}'\right)$ the transformation by $\mathbf{R}_{33}$. This results in the following

expression:

$$\mathbf{C} = \mathbf{C}' = (\mathbf{R}_{33})^{\mathsf{T}}\,\mathbf{C}\mathbf{R}_{33},$$

with this evaluating, following a conversion of $\mathbf{R}_{33}$ to its Voigt form, to give the following equality:

$$\begin{bmatrix} c_{11} & c_{12} & c_{13} & c_{14} & c_{15} & c_{16} \\ c_{21} & c_{22} & c_{23} & c_{24} & c_{25} & c_{26} \\ c_{31} & c_{32} & c_{33} & c_{34} & c_{35} & c_{36} \\ c_{41} & c_{42} & c_{43} & c_{44} & c_{45} & c_{46} \\ c_{51} & c_{52} & c_{53} & c_{54} & c_{55} & c_{56} \\ c_{61} & c_{62} & c_{63} & c_{64} & c_{65} & c_{66} \end{bmatrix} = \begin{bmatrix} c_{11} & c_{12} & c_{13} & -c_{14} & -c_{15} & c_{16} \\ c_{21} & c_{22} & c_{23} & -c_{24} & -c_{25} & c_{26} \\ c_{31} & c_{32} & c_{33} & -c_{34} & -c_{35} & c_{36} \\ -c_{41} & -c_{42} & -c_{43} & c_{44} & c_{45} & -c_{46} \\ -c_{51} & -c_{52} & -c_{53} & c_{54} & c_{55} & -c_{56} \\ c_{61} & c_{62} & c_{63} & -c_{64} & -c_{65} & c_{66} \end{bmatrix}.$$

In this equality it is shown that given the symmetry of $\mathbf{C}$, certain elements must be equal to their negative $\left(c_{ij} = -c_{ij}\right)$, a condition that is only valid if they are equal to zero. Repeating this for either the 11 or 22 directions, as is valid in the cases of either orthotropic or isotropic materials, a reduction in non-zero terms within $\mathbf{C}$ from 36 to 9 is possible, giving the following elastic relation:

$$\begin{bmatrix} \sigma_{11} \\ \sigma_{22} \\ \sigma_{33} \\ \sigma_{23} \\ \sigma_{31} \\ \sigma_{12} \end{bmatrix} = \begin{bmatrix} c_{11} & c_{12} & c_{31} & 0 & 0 & 0 \\ c_{12} & c_{22} & c_{23} & 0 & 0 & 0 \\ c_{31} & c_{23} & c_{33} & 0 & 0 & 0 \\ 0 & 0 & 0 & c_{44} & 0 & 0 \\ 0 & 0 & 0 & 0 & c_{55} & 0 \\ 0 & 0 & 0 & 0 & 0 & c_{66} \end{bmatrix} \begin{bmatrix} \epsilon_{11} \\ \epsilon_{22} \\ \epsilon_{33} \\ \epsilon_{23} \\ \epsilon_{31} \\ \epsilon_{12} \end{bmatrix}. \tag{3.2}$$

Further simplification of this relation is also possible if isotropy is assumed, as then $\mathbf{C}$ is also invariant under any rotation with this leading to:

$$c_{11} = c_{22} = c_{33} = 2\mu + \lambda,$$

$$c_{23} = c_{31} = c_{12} = \lambda,$$

$$c_{44} = c_{55} = c_{66} = \mu.$$

Reducing the total number of independent variables to just two. In these reduced expressions, λ and μ are identified as the first and second Lamé parameters respectively, which can be related to the more commonplace pairing of the bulk, K, and shear, G, moduli as such:

$$\lambda = K - \frac{2G}{3},$$

$$\mu = G.$$

It should be noted that $\mathbf{C}$ as defined in equation 3.2 is both symmetric and block-diagonal, properties that will be exploited to improve computational efficiency when implementing the model that is developed within this body of research.

3.1.2 Deviatoric & Volumetric Tensor Projections

Both stress and strain tensors, as seen in equation 3.1, can be divided into two components, with one describing purely volumetric change (no alteration of shape) and the other purely deviatoric change (purely resulting in alteration of shape). The separation into deviatoric and volumetric components is achieved by applying appropriate projections to the initial (3×3) tensors, with volumetric and deviatoric projections applied to an arbitrary 2nd order tensor, $\mathbf{x}$, given respectively as follows:

$$\text{vol}(\mathbf{x}) = \frac{1}{3} \sum_{i} x_{ii}, \tag{3.3}$$

$$\text{dev}(\mathbf{x}) = \mathbf{x} - \text{vol}(\mathbf{x}). \tag{3.4}$$

The above functions, in particular the deviatoric projection, may be recast to Voigt notation similarly to the Hill tensor, $\mathbf{A}$, and stiffness tensor, $\mathbf{C}$. The Voigt equivalent to the deviatoric projection as seen in equation 3.4 is identified as $\mathbf{P}_{\text{dev}}$ and defined by:

$$\mathbf{P}_{\text{dev}} = \frac{1}{3}\begin{bmatrix} 2 & -1 & -1 & 0 & 0 & 0 \\ -1 & 2 & -1 & 0 & 0 & 0 \\ -1 & -1 & 2 & 0 & 0 & 0 \\ 0 & 0 & 0 & 3 & 0 & 0 \\ 0 & 0 & 0 & 0 & 3 & 0 \\ 0 & 0 & 0 & 0 & 0 & 3 \end{bmatrix}. \tag{3.5}$$

Using the definition of this projection the deviatoric stress $\mathbf{s}$ may be related to the total stress $\boldsymbol{\sigma}$ in matrix form such that:

$$\mathbf{s} = \mathbf{P}_{\text{dev}}\boldsymbol{\sigma} \tag{3.6}$$

with the squared magnitude of the deviatoric stress $|\mathbf{s}|^2$ a quantity of key significance to a von Mises interpretation of the onset of yield, a foundation of which is discussed later in section 3.2.

3.1.3 Eigendecomposition

Whilst the application of this technique is not immediately apparent, the eigendecomposition of an arbitrary square $(n \times n)$ matrix $\mathbf{x}$, is a valuable tool in the construction of a computationally efficient and accurate orthotropic material model, facilitating a reduction in the dimensionality of the system being modelled. If the arbitrary square matrix, $\mathbf{x}$, is interpreted as representing a linear n-dimensional mapping, then calculating its eigendecomposition reveals key information about this mapping. Evaluating the eigendecomposition involves solving the well known eigenvalue equation;

$$\mathbf{xv} = \mathbf{v}\lambda, \tag{3.7}$$

with $\mathbf{v}$ a $(n \times 1)$ column vector and λ a scalar. For a non-singular n-dimensional square matrix there exist n eigenvalues (λ) and corresponding eigenvectors $(\mathbf{v})$. These may be combined into a diagonal square matrix of eigenvalues $(\mathbf{\Gamma})$ with a corresponding square matrix $(\mathbf{Q})$ of catenated column vectors, where each column vector is located to align with the associated eigenvector as such:

$$\mathbf{Q} = \begin{bmatrix} & & & & & \\ \vdots & \vdots & \vdots & \vdots & \vdots & \vdots \\ \mathbf{v}_1 & \mathbf{v}_2 & \mathbf{v}_3 & \mathbf{v}_4 & \mathbf{v}_5 & \mathbf{v}_6 \\ \vdots & \vdots & \vdots & \vdots & \vdots & \vdots \\ & & & & & \end{bmatrix}, \quad \mathbf{\Gamma} = \begin{bmatrix} \lambda_1 & 0 & 0 & 0 & 0 & 0 \\ 0 & \lambda_2 & 0 & 0 & 0 & 0 \\ 0 & 0 & \lambda_3 & 0 & 0 & 0 \\ 0 & 0 & 0 & \lambda_4 & 0 & 0 \\ 0 & 0 & 0 & 0 & \lambda_5 & 0 \\ 0 & 0 & 0 & 0 & 0 & \lambda_6 \end{bmatrix}.$$

This linear combination leads to the following alternative eigenvalue equation:

$$\mathbf{xQ} = \mathbf{Q\Gamma}, \tag{3.8}$$

what can be multiplied through by $\mathbf{Q}^{-1} = \mathbf{Q}^{\mathsf{T}}$ to give an expression for the original matrix, $\mathbf{x}$, as such:

$$\mathbf{xQ}\left(\mathbf{Q}\right)^{-1} = \mathbf{x} = \mathbf{Q\Gamma Q}^{\mathsf{T}}, \tag{3.9}$$

a process known as eigendecomposition or alternatively as diagonalisation. The evaluation of both $\mathbf{Q}$ and $\mathbf{\Gamma}$ can be graphically interpreted as finding the principal axes of the mapping defined by $\mathbf{x}$, and the scaling along each of those axes respectively.

3.2 Plasticity; von Mises & Hill

As stated in section 3.1.1, the initial response of a solid material to an applied load is a linearly proportional and purely elastic deformation, per Hooke's law. However, were the applied load to continue increasing it is reasonable to assume that after some time the material would undergo an irreversible change, involving distortional and potentially dilational deformation.

The plastic domain is defined from the end of the purely elastic domain, with the onset of a plastic response and irreversible material changes mathematically approximated using a yield criterion. This may usually be interpreted as a closed manifold in a six-dimensional linear space where the basis is defined using the six independent stress directions in the Cauchy stress tensor. A potentially infinite number of representations for a given space exist as the directions chosen are not exclusive, with the usual coordinate transform process allowing the yield surface to be recast to any basis.

Yield criteria define the aforementioned manifold using the stress state of a material, comparing it to an abstract threshold, beyond which plastic deformation serves to dissipate the excess strain energy that may not be supported elastically, this usually will take a form similar to:

$$f\left(\boldsymbol{\sigma}\right) \leq \sigma^{\mathrm{Y}}.$$

The evolution of the abstract threshold and the resulting dissipative rate, and form of deformation are described by the material's constitutive relations; specifically its flow rule and plastic potential, with the plastic potential specifically describing the evolution of the abstract threshold referenced within the yield criterion to define the yield surface.

3.2.1 von Mises

The von Mises yield criterion [149, 150], first published in 1913, is one of the most widely used yield criteria in modern engineering, with it defining a threshold for the onset of plastic deformation to be equal to a material-specific amount of shear stress. Its mathematical representation has the form:

$$f_{\text{von Mises}} = \frac{3}{2}\sum_{\mathrm{i}}\sum_{\mathrm{j}} \mathrm{s}_{\mathrm{ij}}\mathrm{s}_{\mathrm{ij}} = \frac{1}{2}\left(\left(\sigma_{22}-\sigma_{33}\right)^2 + \left(\sigma_{33}-\sigma_{11}\right)^2 + \left(\sigma_{11}-\sigma_{22}\right)^2\right) + 3\left({\sigma_{23}}^2 + {\sigma_{31}}^2 + {\sigma_{12}}^2\right) \leq \left(\sigma^{\mathrm{Y}}\right)^2, \quad (3.10)$$

where σ_{ij} represents the component of the Cauchy stress tensor in the specified direction and $\sum_i \sum_j s_{ij} s_{ij}$ represents a summation across all components, squared, of the deviatoric stress tensor. This expression may be visualised as a hypersphere of radius σ^Y in a six dimensional deviatoric stress space, with the hyperspherical shape of the manifold echoing the isotropic yield onset (at a deviatoric stress magnitude equal to the yield stress) that the model seeks to represent. While this yield surface effectively represents the behaviour of many conventional materials, it is by definition unable to represent a directionally dependent yield surface in conventional deviatoric stress space.

3.2.2 Hill

The Hill quadratic orthotropic yield criterion [146, 151, 152], modifies the von Mises criterion by introducing a scaling coefficient to each of the six axes. These scaling factors allow the criterion to define a hyperellipsoid in the same six dimensional deviatoric stress space, with the six additional coefficients usually assigned to F, G, H, L, M and N. Whilst the isotropy of von Mises ensures a non-unique axes choice, only axes aligned to the materials assumed axes of orthotropy are valid with the following form:

$$f_{\text{Hill}} = F\left(\sigma_{22} - \sigma_{33}\right)^2 + G\left(\sigma_{33} - \sigma_{11}\right)^2 + H\left(\sigma_{11} - \sigma_{22}\right)^2 + L\sigma_{23}^2 + M{\sigma_{31}}^2 + N{\sigma_{12}}^2 \leq \sigma^Y, \quad (3.11)$$

Here the on-axis scaling mirrors the ratios of orthotropy within the material, with directions characterised by higher flow stresses identified by smaller scaling coefficients, which may be thought of as defining an increased radius to the hyperellipsoidal manifold. A two-dimensional representation of this is shown in figure 3.1.

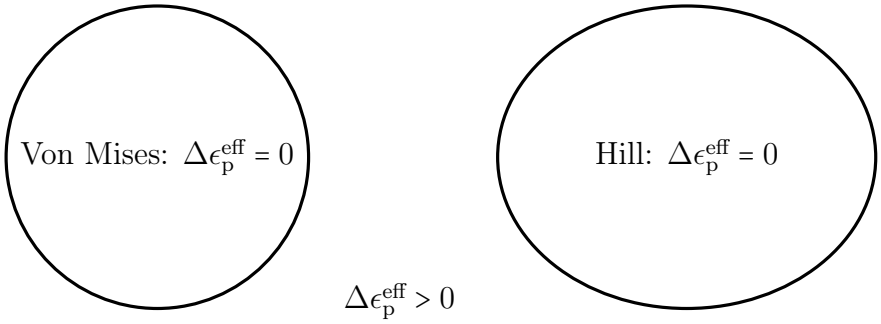

Figure 3.1: Two dimensional representation of von Mises and Hill yield criteria in deviatoric stress space. The major axis of the Hill ellipse corresponds to an axis with increased yield strength.

3.2.3 Matrix Representation of Hill yield criterion

The Hill quadratic yield criterion [146] as defined in equation 3.11 may also be condensed and expressed in the form

$$f_{\text{Hill}} = \mathbf{s}^{\mathsf{T}}\mathbf{A}\mathbf{s} \leq \sigma^{\text{Y}}, \tag{3.12}$$

where $\mathbf{s}$ is the deviatoric stress as defined in equation 3.4, and $\mathbf{A}$ is a 4th order tensor describing the anisotropy of the material. This fourth order tensor can be reduced (analogously to equation 3.2) to a 2nd order tensor using Voigt notation to allow seamless use with $\mathbf{C}$ and $\mathbf{P}_{\text{dev}}$ for example. In order to extract the components of $\mathbf{A}$ the deviatoric projection matrix is substituted into equation 3.12 and rearranged to give:

$$(\mathbf{P}_{\text{dev}}\boldsymbol{\sigma})^{\mathsf{T}}\mathbf{A}(\mathbf{P}_{\text{dev}}\boldsymbol{\sigma}) = \boldsymbol{\sigma}^{\mathsf{T}}(\mathbf{P}_{\text{dev}})^{\mathsf{T}}\mathbf{A}\mathbf{P}_{\text{dev}}\boldsymbol{\sigma}, \tag{3.13}$$

with this reducing to

$$\boldsymbol{\sigma}^{\mathsf{T}}(\mathbf{P}_{\text{dev}})^{\mathsf{T}}\mathbf{A}\mathbf{P}_{\text{dev}}\boldsymbol{\sigma} = \boldsymbol{\sigma}^{\mathsf{T}}\mathbf{A}\boldsymbol{\sigma}, \tag{3.14}$$

as $\mathbf{A}$ is deviatoric such that ${\mathbf{P}_{\text{dev}}}^{\mathsf{T}}\mathbf{A}\mathbf{P}_{\text{dev}} = \mathbf{A}$. Evaluating $\boldsymbol{\sigma}^{\mathsf{T}}\mathbf{A}\boldsymbol{\sigma}$ yields a dot product given below in terms of $\boldsymbol{\sigma}$ and $\mathbf{A}$ comparable to the standard Hill yield criterion as

given in equation 3.11.

$$\begin{bmatrix} a_{11} \\ a_{22} \\ a_{33} \\ 2a_{23} \\ 2a_{31} \\ 2a_{12} \\ a_{44} \\ a_{55} \\ a_{66} \end{bmatrix} \cdot \begin{bmatrix} (\sigma_{11})^2 \\ (\sigma_{22})^2 \\ (\sigma_{33})^2 \\ \sigma_{22}\sigma_{33} \\ \sigma_{33}\sigma_{11} \\ \sigma_{11}\sigma_{22} \\ (\sigma_{23})^2 \\ (\sigma_{31})^2 \\ (\sigma_{12})^2 \end{bmatrix} = 1. \tag{3.15}$$

By relating the components of equation 3.15 to the equivalent coefficients in equation 3.11, the elements of $\mathbf{A}$ are found such that:

$$\mathbf{A} = \begin{bmatrix} G+H & -H & -G & 0 & 0 & 0 \\ -H & F+H & -F & 0 & 0 & 0 \\ -G & -F & F+G & 0 & 0 & 0 \\ 0 & 0 & 0 & 2L & 0 & 0 \\ 0 & 0 & 0 & 0 & 2M & 0 \\ 0 & 0 & 0 & 0 & 0 & 2N \end{bmatrix}, \tag{3.16}$$

completing the definition of the Hill model using a matrix representation.

3.2.4 Hill Coefficients

To calculate the Hill coefficients introduced in equation 3.11, it is possible to imagine a series of uniaxial tests where the expected yield along principal material axes allows the evaluation of the Hill coefficients [153]. Firstly, considering the σ_{11} direction

under uni-axial stress at yield;

$$\boldsymbol{\sigma} = \begin{bmatrix} \sigma_{11}^{\mathrm{Y}} & 0 & 0 \\ 0 & 0 & 0 \\ 0 & 0 & 0 \end{bmatrix}. \tag{3.17}$$

Substituting this into the matrix form of Hill (equation 3.12 to) give (along with equivalent expressions following from symmetry):

$$\left(\sigma_{11}^{\mathrm{Y}}\right)^2 = (G+H)^{-1}, \tag{3.18}$$

$$\left(\sigma_{22}^{\mathrm{Y}}\right)^2 = (F+H)^{-1}, \tag{3.19}$$

$$\left(\sigma_{33}^{\mathrm{Y}}\right)^2 = (F+G)^{-1}. \tag{3.20}$$

These expressions rearrange and reduce to define $\{F, G, H\}$ such that:

$$F = \frac{1}{2}\left(\left(\sigma_{22}^{\mathrm{Y}}\right)^{-2} + \left(\sigma_{33}^{\mathrm{Y}}\right)^{-2} - \left(\sigma_{11}^{\mathrm{Y}}\right)^{-2}\right), \tag{3.21}$$

$$G = \frac{1}{2}\left(\left(\sigma_{33}^{\mathrm{Y}}\right)^{-2} + \left(\sigma_{11}^{\mathrm{Y}}\right)^{-2} - \left(\sigma_{22}^{\mathrm{Y}}\right)^{-2}\right), \tag{3.22}$$

$$H = \frac{1}{2}\left(\left(\sigma_{11}^{\mathrm{Y}}\right)^{-2} + \left(\sigma_{22}^{\mathrm{Y}}\right)^{-2} - \left(\sigma_{33}^{\mathrm{Y}}\right)^{-2}\right). \tag{3.23}$$

Considering shear directions, a primed axis may be constructed as shown in figure 3.2. Here, a uni-axial tensile test at the onset of yield angled at 45° anticlockwise from the 22 direction in the 22-33 plane is imagined. The primed axes rotated about the 11 direction by 45° is collinear to the axial direction of the test such that the stress is applied directly along the $\prime$ direction. This is then transformed back to the non-primed frame to give:

$$\boldsymbol{\sigma} = \left(\mathbf{Q}_{-\frac{\pi}{4}}\right)\boldsymbol{\sigma}'\left(\mathbf{Q}_{-\frac{\pi}{4}}\right)^{\mathsf{T}}, \tag{3.24}$$

where $\mathbf{Q}_\theta$ is a rotation matrix about the 11 direction in the anticlockwise direction by an amount θ in radians. From here the stress state in the non-primed frame can be explicitly calculated, with this scaled by the yield stress in the primed frame to give

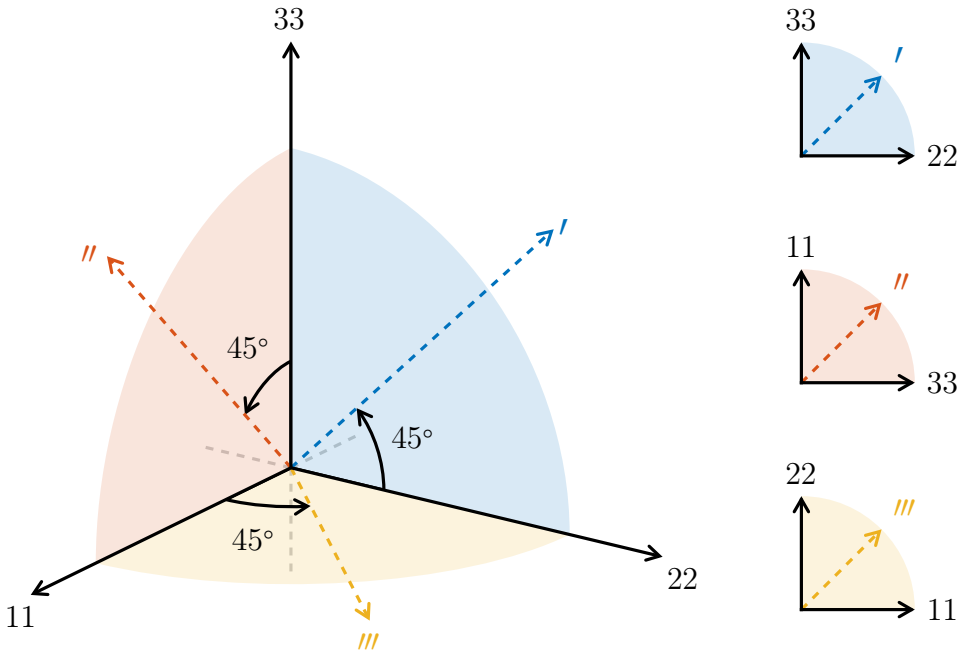

Figure 3.2: Graphical representation of $\prime$, $\prime\prime$, $\prime\prime\prime$ directions with respect to the standard cartesian coordinate axes. On the left an isometric view is shown with each of the three on-axis views included on the right for completeness.

the following expression:

$$\frac{\boldsymbol{\sigma}}{(\sigma^{\mathrm{Y}})'} = \begin{bmatrix} 1 & 0 & 0 \\ 0 & \cos\left(\frac{-\pi}{4}\right) & \sin\left(\frac{-\pi}{4}\right) \\ 0 & \sin\left(\frac{\pi}{4}\right) & \cos\left(\frac{-\pi}{4}\right) \end{bmatrix} \begin{bmatrix} 0 & 0 & 0 \\ 0 & 1 & 0 \\ 0 & 0 & 0 \end{bmatrix} \begin{bmatrix} 1 & 0 & 0 \\ 0 & \cos\left(\frac{\pi}{4}\right) & \sin\left(\frac{\pi}{4}\right) \\ 0 & \sin\left(\frac{-\pi}{4}\right) & \cos\left(\frac{\pi}{4}\right) \end{bmatrix}, \tag{3.25}$$

which evaluates to give:

$$\boldsymbol{\sigma} = \left(\sigma^{\mathrm{Y}}\right)' \begin{bmatrix} 0 & 0 & 0 \\ 0 & 0.5 & 0.5 \\ 0 & 0.5 & 0.5 \end{bmatrix}.$$

This can be substituted into equation 3.12, whilst also swapping to Voigt notation, such that:

$$\mathbf{s}^{\mathsf{T}}\mathbf{A}\mathbf{s} = \left(\frac{\left(\sigma^{\mathrm{Y}}\right)'}{6}\right)^2 \begin{bmatrix} -2 \\ 1 \\ 1 \\ 3 \\ 0 \\ 0 \end{bmatrix}^{\mathsf{T}} \begin{bmatrix} G+H & -H & -G & 0 & 0 & 0 \\ -H & F+H & -F & 0 & 0 & 0 \\ -G & -F & F+G & 0 & 0 & 0 \\ 0 & 0 & 0 & 2L & 0 & 0 \\ 0 & 0 & 0 & 0 & 2M & 0 \\ 0 & 0 & 0 & 0 & 0 & 2N \end{bmatrix} \begin{bmatrix} -2 \\ 1 \\ 1 \\ 3 \\ 0 \\ 0 \end{bmatrix},$$

where given the stress state is defined to be at the onset of yield:

$$\mathbf{s}^{\mathsf{T}}\mathbf{A}\mathbf{s} = 1 = 9\left(G+H+2L\right)\left(\frac{\left(\sigma^{\mathrm{Y}}\right)'}{6}\right)^2.$$

Substituting in equation 3.18 for $(G+H)$ in terms of σ_{11}^{Y} results in the following:

$$\left(\frac{\left(\sigma^{\mathrm{Y}}\right)'}{2}\right)^2\left(\frac{1}{{\sigma_{11}^{\mathrm{Y}}}^2}+2L\right)=2,$$

that rearranges to give (and following for other cases by symmetry):

$$L = \left(\frac{2}{\left(\sigma^{\mathrm{Y}}\right)'}\right)^2 - \frac{1}{2}\left(\sigma_{11}^{\mathrm{Y}}\right)^{-2},$$
$$M = \left(\frac{2}{\left(\sigma^{\mathrm{Y}}\right)''}\right)^2 - \frac{1}{2}\left(\sigma_{22}^{\mathrm{Y}}\right)^{-2},$$
$$N = \left(\frac{2}{\left(\sigma^{\mathrm{Y}}\right)'''}\right)^2 - \frac{1}{2}\left(\sigma_{33}^{\mathrm{Y}}\right)^{-2}.$$

Here $\left(\sigma^{\mathrm{Y}}\right)''$ and $\left(\sigma^{\mathrm{Y}}\right)'''$ are defined for the Z-X and X-Y planes respectively. Following from this there now exists a set of Hill coefficients expressed as a function of the effective flow stress along 6 different directions.

3.3 Johnson-Cook Model

In order to define the evolution of energy dissipation during plasticity a constitutive model must be used to define a plastic potential given the loading, material and environmental state. The Johnson-Cook model [154, 155] is an isotropic, strain dependent, strain rate dependent, and temperature dependent constitutive model that fulfils this need. The model is defined from a set of coefficients $\mathbf{x} = \left\{ \mathrm{x_i} \mid \mathrm{i} = 1, 2, 3, 4, 5 \right\}$ using the following form:

$$\sigma^{\mathrm{Y}} = \left(\mathrm{x}_1 + \mathrm{x}_2 \left(\epsilon_{\mathrm{p}}^{\mathrm{eff}} \right)^{\mathrm{x}_3} \right) \left(1 + \mathrm{x}_4 \ln \left(\epsilon^* \right) \right) \left(1 - \left(\mathrm{T}^* \right)^{\mathrm{x}_5} \right). \tag{3.26}$$

Where ϵ^* is a normalised effective strain rate and T^* is a homologous temperature; each defined as such:

$$\epsilon^* = \begin{cases} \frac{\dot{\epsilon}_{\mathrm{p}}^{\mathrm{eff}}}{\dot{\epsilon}_{\mathrm{p0}}^{\mathrm{eff}}} & \dot{\epsilon}_{\mathrm{p}}^{\mathrm{eff}} > \dot{\epsilon}_{\mathrm{p0}}^{\mathrm{eff}}, \\ 1.0 & \dot{\epsilon}_{\mathrm{p}}^{\mathrm{eff}} \leq \dot{\epsilon}_{\mathrm{p0}}^{\mathrm{eff}}, \end{cases} \tag{3.27}$$

$$\mathrm{T}^* = \frac{\mathrm{T} - \mathrm{T_r}}{\mathrm{T_m} - \mathrm{T_r}}. \tag{3.28}$$

In equation 3.27, $\dot{\epsilon}_{\mathrm{p0}}^{\mathrm{eff}}$ is defined to be an arbitrary reference plastic strain rate, in this body of work a value of $1\,\mathrm{s}^{-1}$ is used, with this a commonly chosen value for this constitutive model. $\mathrm{T_m}$ and $\mathrm{T_r}$, as seen in equation 3.28 are the material melting temperature and a reference temperature (here defined as 293 K) respectively, with T specified to be the temperature of the material that is undergoing plastic deformation.

Each of the three expressions comprising the expression for σ^{Y} within equation 3.26 allows the variation of the flow stress to a specific environmental or material factor. The first term $\left(\mathrm{x}_1 + \mathrm{x}_2 \left(\epsilon_{\mathrm{p}}^{\mathrm{eff}} \right)^{\mathrm{x}_3} \right)$ allows for an increase in the flow stress in response to an increasing amount of incurred effective plastic strain. The effective plastic strain is a monotonically non-decreasing intrinsic scalar material property that serves to quantify the amount of deformation existing at that point in the material at a given point in

time.

The second term, $\left(1 + \mathrm{x}_4 \ln\left(\epsilon^*\right)\right)$ allows the variation of flow stress under different rates of deformation, a phenomenon termed strain rate hardening or viscoplasticity. This variation in yield stress stems from different modes of deformation at the crystallographic level; with lower rates of deformation involving the generation and migration of dislocations, and higher rates involving the generation of greater dislocation densities that undergo less migration. The generation of these crystal dislocations dissipates greater amounts of energy than moving them, so modes of deformation that incur greater amounts of dislocation generation for a given amount of deformation will dissipate a larger amount of excess strain energy. A mathematical description of this effect is given in Orowan's equation [156, 157]:

$$\dot{\gamma}_{\mathrm{p}} = b\rho_{\perp}\frac{\mathrm{d}\bar{x}_{\perp}}{\mathrm{d}t} + b\frac{\mathrm{d}\rho_{\perp}}{\mathrm{d}t}. \tag{3.29}$$

Here $\dot{\gamma}_{\mathrm{p}}$ defines the rate of shear strain, b is the Burgers vector which quantifies the volume of shear strain per dislocation, $\rho_{\perp}$ is the density of dislocations within the material and $\frac{\mathrm{d}\bar{x}_{\perp}}{\mathrm{d}t}$ is the average velocity of a dislocation. The first term describes deformation as a result of movement of dislocations with the second term showing the alternate, more dissipative, mode of deformation stemming from the generation of dislocations.

The final term $\left(1 - \left(\mathrm{T}^*\right)^{\mathrm{x}_5}\right)$ allows for a reduction in the flow stress under heightened material temperatures, a situation that can arise from adiabatic heating during dynamic deformation. This reduction in flow stress stems from a decreased matrix binding potential at the crystallographic level. Decreasing the depth of the potential well within which an atom is confined decreases the amount of energy needed to escape the confines, and therefore introduce a dislocation which will result in deformation.

3.4 Eigenspace Radial Return

This technique, detailed by Versino and Bennett in 2018 [158], is a variation on the radial return algorithm [159] that is widely used within many finite element codes to increment the evolution of material stress under plastic strain. This particular variation expands the potential applications of the traditionally isotropic technique by mapping the orthotropic quadratic Hill yield criterion to the computationally efficient but isotropic von Mises yield criterion within a material subspace using a basis of scaled eigenvectors. The details of this method, when formulated with an anisotropic elastic response, are given below.

3.4.1 Flow Rule

The flow rule is a mathematical construct that links the evolution of material properties with the plastic potential, this is key for evaluating the amount of deformation needed to dissipate any excess elastic strain energy. The derivation of such a flow rule for an isotropic hardening material is given below. Starting from the second law of thermodynamics; the thermodynamic dissipation [152, 160, 161] given isotropic hardening defined by an internal material variable α may be expressed as

$$\mathbb{D}_{\text{loc}} = -\frac{\partial \Psi_{\text{p}}}{\partial \boldsymbol{\epsilon}_{\text{p}}} \frac{\mathrm{d}\boldsymbol{\epsilon}_{\text{p}}}{\mathrm{dt}} + \frac{\partial \Psi_{\text{p}}}{\partial \alpha} \frac{\mathrm{d}\alpha}{\mathrm{dt}} = \mathbf{s}\dot{\boldsymbol{\epsilon}}_{\text{p}} - \beta\dot{\alpha} \geq 0,$$

where Ψ_{p} is the plastic component of the Helmholtz free energy per unit volume and β is the force energy conjugate (affinity) to the internal hardening parameter. This hardening serves to increase the capacity for elastic energy storage within the material thereby decreasing the rate of dissipative energy loss during plastic deformation. From this principle of maximal plastic deformation, and knowing that the yield criterion (a function of $\{\mathbf{s}_{\text{n}}, \alpha\}$) must remain satisfied to create a bounded minimisation. Specifically, minimising energy retention and thereby maximising dissipation, with the

constraint of the yield condition using a lagrange multiplier technique such that:

$$\mathscr{L} = -\dot{\boldsymbol{\epsilon}}_{\mathrm{p}}\mathbf{s} + \dot{\alpha}\beta + \lambda_f f\left(\mathbf{s}, \beta\right).$$

Calculating the minima of this lagrangian by considering the differentials with respect to both $\mathbf{s}_{\mathrm{n}}$ and β it is possible to show that:

$$\dot{\boldsymbol{\epsilon}}_{\mathrm{p}} = \dot{\gamma}\,\frac{\partial f}{\partial \mathbf{s}}\,, \tag{3.30}$$

$$\dot{\alpha} = -\dot{\gamma}\,\frac{\partial f}{\partial \beta}\,. \tag{3.31}$$

Giving two relations; the first is merely a statement of the associated flow rule with the second relating the rate of change of the internal hardening variable to the plastic multiplier and the force conjugate to the hardening parameter, identified as the effective yield stress, σ^{Y}, given the material state. Equation 3.31 is key in linking the plastic multiplier, $\Delta\gamma$ (identified as the lagrange multiplier λ_f), to the rate of change of the internal hardening variable, $\dot{\alpha}$, identified as the effective plastic strain rate, $\dot{\epsilon}_{\mathrm{p}}^{\mathrm{eff}}$.

Substituting in $\dot{\epsilon}_{\mathrm{p}}^{\mathrm{eff}}$ and $\Delta\gamma$ into these relations and also defining the constraining yield function using the matrix representation of the Hill yield criterion, equation 3.12, it is possible to show that:

$$\dot{\boldsymbol{\epsilon}}_{\mathrm{p}} = \dot{\gamma}\,\frac{\partial f_{\mathrm{Hill}}}{\partial \mathbf{s}} = \dot{\gamma}\,\frac{\partial}{\partial \mathbf{s}}\left(\mathbf{s}^{\mathsf{T}}\mathbf{A}\mathbf{s}\right) = \dot{\gamma}\mathbf{A}\mathbf{s}, \tag{3.32}$$

$$\dot{\epsilon}_{\mathrm{p}}^{\mathrm{eff}} = \dot{\alpha} = -\dot{\gamma}\,\frac{\partial f_{\mathrm{Hill}}}{\partial \beta} = -\dot{\gamma}\,\frac{\partial f_{\mathrm{Hill}}}{\partial (\sigma^{\mathrm{Y}})}\,. \tag{3.33}$$

3.4.2 Strain Decomposition

When implementing a material model into a finite element code, the resulting algorithm will receive every time step: the total increment of true strain incurred during the time step ($\Delta\boldsymbol{\epsilon}$), the current effective plastic strain $\epsilon_{\mathrm{p}}^{\mathrm{eff}}$, and the temperature T, as well as any information passed forward from the previous time steps. The algorithm must calculate and then return the stress state at the end of the time step

along with the new parameters that describe the material state

Starting from the total incurred true strain increment, the elastic and plastic parts of this tensor may be defined as $\Delta\boldsymbol{\epsilon}_{\mathrm{e}}$ and $\Delta\boldsymbol{\epsilon}_{\mathrm{p}}$ respectively. The incurred plastic strain may then be related to the plastic multiplier $\Delta\gamma$ given the flow rule (equation 3.32) such that,

$$\Delta\boldsymbol{\epsilon} = \Delta\boldsymbol{\epsilon}_{\mathrm{e}} + \Delta\boldsymbol{\epsilon}_{\mathrm{p}} = \Delta\boldsymbol{\epsilon}_{\mathrm{e}} + \Delta\gamma\frac{\partial f_{\mathrm{Hill}}}{\partial \mathbf{s}} = \Delta\boldsymbol{\epsilon}_{\mathrm{e}} + \Delta\gamma\mathbf{A}\mathbf{s}_{\mathrm{n+1}}.$$

Here the deviatoric stress is taken at the end of the time step, as it is corresponding to the total incurred plastic strain during the time step. The deviatoric stress at the end of the time step may then be equated to the resultant elastic strain such that:

$$\Delta\boldsymbol{\epsilon} = \Delta\boldsymbol{\epsilon}_{\mathrm{e}} + \Delta\gamma\mathbf{A}\left(\boldsymbol{\sigma}_{\mathrm{n}} + \mathbf{C}\Delta\boldsymbol{\epsilon}_{\mathrm{e}}\right).$$

From this it is possible to multiply both sides by the elastic stiffness matrix, $\mathbf{C}$, giving:

$$\Delta\boldsymbol{\sigma}_{\mathrm{tr}} = \mathbf{C}\Delta\boldsymbol{\epsilon} = \mathbf{C}\Delta\boldsymbol{\epsilon}_{\mathrm{e}} + \Delta\gamma\mathbf{C}\mathbf{A}\left(\boldsymbol{\sigma}_{\mathrm{n}} + \mathbf{C}\Delta\boldsymbol{\epsilon}_{\mathrm{e}}\right). \tag{3.34}$$

This expression relates the initial stress state, $\boldsymbol{\sigma}_{\mathrm{n}}$, the plastic multiplier, $\Delta\gamma$, and the purely elastic trial stress increment, $\Delta\boldsymbol{\sigma}_{\mathrm{tr}}$, to the resulting increment of elastic strain, and henceforth the stress state at the end of the time step. However, to solve this equation in an iterative manor would require the repeated inversion of (6×6) matrices, a computationally expensive operation for a material strength algorithm. Thankfully, the problem may be simplified through the calculation of an appropriate material eigenspace, which serves to transform the aforementioned (6×6) matrices into diagonalised equivalents for which inversion is trivial.

3.4.3 Elastic Eigendecomposition

We can then calculate the eigendecomposition of $\mathbf{C}$ into $\mathbf{Q}_{\mathbf{C}}$ and $\boldsymbol{\Gamma}_{\mathbf{C}}$ such that $\mathbf{C} = \mathbf{Q}_{\mathbf{C}}\boldsymbol{\Gamma}_{\mathbf{C}}\left(\mathbf{Q}_{\mathbf{C}}\right)^{\mathsf{T}}$ where $\mathbf{Q}_{\mathbf{C}}$ and $\boldsymbol{\Gamma}_{\mathbf{C}}$ are as defined in section 3.1.3. This allows

equation 3.34 to be rewritten as:

$$\boldsymbol{\sigma}_{\mathrm{tr}} - \Delta\gamma\mathbf{C}\mathbf{A}\boldsymbol{\sigma}_{\mathrm{n}} = \mathbf{Q}_{\mathbf{C}}\left(\boldsymbol{\Gamma}_{\mathbf{C}} + \Delta\gamma\boldsymbol{\Gamma}_{\mathbf{C}}\mathbf{Q}_{\mathbf{C}}\mathbf{A}\left(\mathbf{Q}_{\mathbf{C}}\right)^{\mathsf{T}}\boldsymbol{\Gamma}_{\mathbf{C}}\right)\left(\mathbf{Q}_{\mathbf{C}}\right)^{\mathsf{T}}\Delta\boldsymbol{\epsilon}_{\mathrm{e}}. \tag{3.35}$$

We can then define two new variables $\mathbf{Q}'_{\mathbf{C}}$ and $\mathbf{B}$ as follows:

$$\mathbf{Q}'_{\mathbf{C}} \coloneqq \mathbf{Q}_{\mathbf{C}}\sqrt{\boldsymbol{\Gamma}_{\mathbf{C}}}, \tag{3.36}$$

$$\mathbf{B} \coloneqq \left(\mathbf{Q}'_{\mathbf{C}}\right)^{\mathsf{T}}\mathbf{A}\mathbf{Q}'_{\mathbf{C}}, \tag{3.37}$$

with these essentially representing a transformation of basis. Specifically, $\mathbf{B}$ provides a representation of the anisotropy in the material within an intermediary subspace with elastic isotropy but still with an orthotropic yield function, $\mathbf{Q}'_{\mathbf{C}}$ is the transform for this subspace with it formed from a new basis $\mathbf{Q}_{\mathbf{C}}$ and a scaling along the new basis $\boldsymbol{\Gamma}_{\mathbf{C}}$. Substituting these into the equation above gives:

$$\Delta\boldsymbol{\sigma}_{\mathrm{tr}} - \Delta\gamma\mathbf{C}\mathbf{A}\boldsymbol{\sigma}_{\mathrm{n}} = \mathbf{Q}'_{\mathbf{C}}\left(\mathbf{I} + \Delta\gamma\mathbf{B}\right)\left(\mathbf{Q}'_{\mathbf{C}}\right)^{\mathsf{T}}\Delta\boldsymbol{\epsilon}_{\mathrm{e}}. \tag{3.38}$$

3.4.4 Plastic Eigendecomposition

Having transformed into an elastically isotropic subspace with $\mathbf{Q}'_{\mathbf{C}}$, the next required step is to circumvent the remaining orthotropy in the material, found in the (now transformed) plastic response, that is characterised by $\mathbf{B}$. Given $\mathbf{B}$ is symmetric a second eigendecomposition can be computed such that

$$\mathbf{B} \coloneqq \mathbf{Q}_{\mathbf{B}}\boldsymbol{\Gamma}_{\mathbf{B}}\left(\mathbf{Q}_{\mathbf{B}}\right)^{\mathsf{T}}, \tag{3.39}$$

with this substituted into equation 3.38 and rearranged to give a an expression that contains a sequential series of basis transforms applied as such:

$$\Delta\boldsymbol{\epsilon}_{\mathrm{e}} = \left(\mathbf{Q}'_{\mathbf{C}}\right)^{\mathsf{T}}\mathbf{Q}_{\mathbf{B}}\left(\mathbf{I} + \Delta\gamma\boldsymbol{\Gamma}_{\mathbf{B}}\right)^{-1}\left(\mathbf{Q}_{\mathbf{B}}\right)^{\mathsf{T}}\left(\mathbf{Q}'_{\mathbf{C}}\right)^{-1}\left(\Delta\boldsymbol{\sigma}_{\mathrm{tr}} - \Delta\gamma\mathbf{C}\mathbf{A}\boldsymbol{\sigma}_{\mathrm{n}}\right).$$

This equation can be thought of as inverting equation 3.34, however where before the expression included both $\mathbf{C}$ and $\mathbf{A}$ asymmetric matrices tied to $\Delta\boldsymbol{\epsilon}_{\mathrm{e}}$, these have now been replaced by a series of transforms that facilitate a more efficient inversion and separation from $\Delta\boldsymbol{\epsilon}_{\mathrm{e}}$ to quantify the effects of a finite plastic multiplier. Following from this, $\Delta\boldsymbol{\epsilon}_{\mathrm{e}}$ can be multiplied by $\mathbf{C}\left(=\mathbf{Q}_{\mathbf{C}}\boldsymbol{\Gamma}_{\mathbf{C}}\left(\mathbf{Q}_{\mathbf{C}}\right)^{\mathsf{T}}=\mathbf{Q}'_{\mathbf{C}}\left(\mathbf{Q}'_{\mathbf{C}}\right)^{\mathsf{T}}\right)$ to give $\Delta\boldsymbol{\sigma}_{\mathrm{n}}$ such that:

$$\Delta\boldsymbol{\sigma}_{\mathrm{n}}=\mathbf{Q}'_{\mathbf{C}}\mathbf{Q}_{\mathbf{B}}\left(\mathbf{I}+\Delta\gamma\boldsymbol{\Gamma}_{\mathbf{B}}\right)^{-1}\left(\mathbf{Q}_{\mathbf{B}}\right)^{\mathsf{T}}\left(\mathbf{Q}'_{\mathbf{C}}\right)^{-1}\Delta\boldsymbol{\sigma}_{\mathrm{tr}}-\\ \mathbf{Q}'_{\mathbf{C}}\mathbf{Q}_{\mathbf{B}}\left(\mathbf{I}+\Delta\gamma\boldsymbol{\Gamma}_{\mathbf{B}}\right)^{-1}\left(\mathbf{Q}_{\mathbf{B}}\right)^{\mathsf{T}}\left(\mathbf{Q}'_{\mathbf{C}}\right)^{\mathsf{T}}\mathbf{A}\Delta\gamma\boldsymbol{\sigma}_{\mathrm{n}}.$$

Now with the substitution $\left(\mathbf{Q}'_{\mathbf{C}}\right)^{\mathsf{T}}\mathbf{A}=\mathbf{B}\left(\mathbf{Q}'_{\mathbf{C}}\right)^{-1}$ it can be shown that:

$$\Delta\boldsymbol{\sigma}_{\mathrm{n}}=\mathbf{Q}'_{\mathbf{C}}\mathbf{Q}_{\mathbf{B}}\left(\mathbf{I}+\Delta\gamma\boldsymbol{\Gamma}_{\mathbf{B}}\right)^{-1}\left(\mathbf{Q}_{\mathbf{B}}\right)^{\mathsf{T}}\left(\mathbf{Q}'_{\mathbf{C}}\right)^{-1}\Delta\boldsymbol{\sigma}_{\mathrm{tr}}-\\ \mathbf{Q}'_{\mathbf{C}}\mathbf{Q}_{\mathbf{B}}\left(\mathbf{I}+\Delta\gamma\boldsymbol{\Gamma}_{\mathbf{B}}\right)^{-1}\boldsymbol{\Gamma}_{\mathbf{B}}\left(\mathbf{Q}_{\mathbf{B}}\right)^{\mathsf{T}}\left(\mathbf{Q}'_{\mathbf{C}}\right)^{-1}\Delta\gamma\boldsymbol{\sigma}_{\mathrm{n}}. \quad (3.40)$$

Here the result is an expression similar in form to that seen in equation 3.34, however here the eigendecomposition of both $\mathbf{A}$ and $\mathbf{C}$ allow for a reduction in the computational cost of inversion, which would apply to the now diagonal term $(\mathbf{I}+\Delta\gamma\boldsymbol{\Gamma}_{\mathbf{B}})$. This is achieved through application of the coordinate transforms evaluated for both elastic, given by $\mathbf{Q}'_{\mathbf{C}}$, and plastic, given by $\mathbf{Q}_{\mathbf{B}}$, anisotropies to create an isotropic material subspace, radial return within which is detailed below.

3.4.5 Eigenspace Transform

Starting from equation 3.40, the coordinate transform $\boldsymbol{\Lambda}$, and transformed stress state $\tilde{\boldsymbol{\sigma}}$ are defined such that:

$$\boldsymbol{\Lambda}\coloneqq\mathbf{Q}'_{\mathbf{C}}\mathbf{Q}_{\mathbf{B}}, \quad (3.41)$$

$$\tilde{\boldsymbol{\sigma}}\coloneqq\boldsymbol{\Lambda}^{-1}\boldsymbol{\sigma}, \quad (3.42)$$

where the definition of $\mathbf{Q}'_{\mathbf{C}}$ is given in equation 3.36, and the definition of QB is as given in equation 3.39. The definition of both $\mathbf{\Lambda}$ and $\tilde{\boldsymbol{\sigma}}$ serve to simplify equation 3.40 as once substituted into the equation, it may be rearranged and simplified such that:

$$\Delta\tilde{\boldsymbol{\sigma}}_{\mathrm{n}} = \left(\mathbf{I} + \Delta\gamma\mathbf{\Gamma}_{\mathbf{B}}\right)^{-1}\Delta\tilde{\boldsymbol{\sigma}}_{\mathrm{tr}} - \left(\mathbf{I} + \Delta\gamma\mathbf{\Gamma}_{\mathbf{B}}\right)^{-1}\mathbf{\Gamma}_{\mathbf{B}}\tilde{\boldsymbol{\sigma}}_{\mathrm{n}}\Delta\gamma,$$

which rearranges further to give,

$$\left(\mathbf{I} + \Delta\gamma\mathbf{\Gamma}_{\mathbf{B}}\right)\Delta\tilde{\boldsymbol{\sigma}}_{\mathrm{n}} = \Delta\tilde{\boldsymbol{\sigma}}_{\mathrm{tr}} - \mathbf{\Gamma}_{\mathbf{B}}\tilde{\boldsymbol{\sigma}}_{\mathrm{n}}\Delta\gamma + \left(\tilde{\boldsymbol{\sigma}}_{\mathrm{n}} - \tilde{\boldsymbol{\sigma}}_{\mathrm{n}}\right).$$

Adding on $0 = \tilde{\boldsymbol{\sigma}}_{\mathrm{n}} - \tilde{\boldsymbol{\sigma}}_{\mathrm{n}}$ to the right hand side, then factorising by $\left(\mathbf{I} + \Delta\gamma\mathbf{\Gamma}_{\mathbf{B}}\right)$ and rearranging results in:

$$\left(\mathbf{I} + \Delta\gamma\mathbf{\Gamma}_{\mathbf{B}}\right)\left(\tilde{\boldsymbol{\sigma}}_{\mathrm{n}} + \Delta\tilde{\boldsymbol{\sigma}}_{\mathrm{n}}\right) = \tilde{\boldsymbol{\sigma}}_{\mathrm{n}} + \Delta\tilde{\boldsymbol{\sigma}}_{\mathrm{tr}}.$$

From here, defining $\tilde{\boldsymbol{\sigma}}_{\mathrm{n+1}} = \tilde{\boldsymbol{\sigma}}_{\mathrm{n}} + \Delta\tilde{\boldsymbol{\sigma}}_{\mathrm{n}}$, and $\tilde{\boldsymbol{\sigma}}_{\mathrm{tr}} = \tilde{\boldsymbol{\sigma}}_{\mathrm{n}} + \Delta\tilde{\boldsymbol{\sigma}}_{\mathrm{tr}}$ results in the simplified expression,

$$\tilde{\boldsymbol{\sigma}}_{\mathrm{n+1}} = \left(\mathbf{I} + \Delta\gamma\mathbf{\Gamma}_{\mathbf{B}}\right)^{-1}\tilde{\boldsymbol{\sigma}}_{\mathrm{tr}},$$

linking the transformed resultant stress to the transformed trial stress state and the plastic multiplier. Now using the inverse of equation 3.42 to map the stresses back from the eigenspace, the expression can be given as such:

$$\boldsymbol{\sigma}_{\mathrm{n+1}} = \mathbf{\Lambda}\left(\mathbf{I} + \Delta\gamma\mathbf{\Gamma}_{\mathbf{B}}\right)^{-1}\mathbf{\Lambda}^{-1}\boldsymbol{\sigma}_{\mathrm{tr}}. \tag{3.43}$$

This relation maps the initial trial stress, assuming no plastic deformation, to the resultant post yielding stress, $\boldsymbol{\sigma}_{\mathrm{n+1}}$, linking these using the plastic multiplier, $\Delta\gamma$, and a scaling matrix, $\mathbf{\Gamma}_{\mathbf{B}}$. The transformation defined by $\mathbf{\Lambda}$ represents a mapping between the deviatoric stress space where plasticity is orthotropic and an eigenspace where the deviatoric stress vector is collinear with the normal of the now hyperspherical (and therefore isotropic) transformed yield surface. This surface normal is itself collinear to

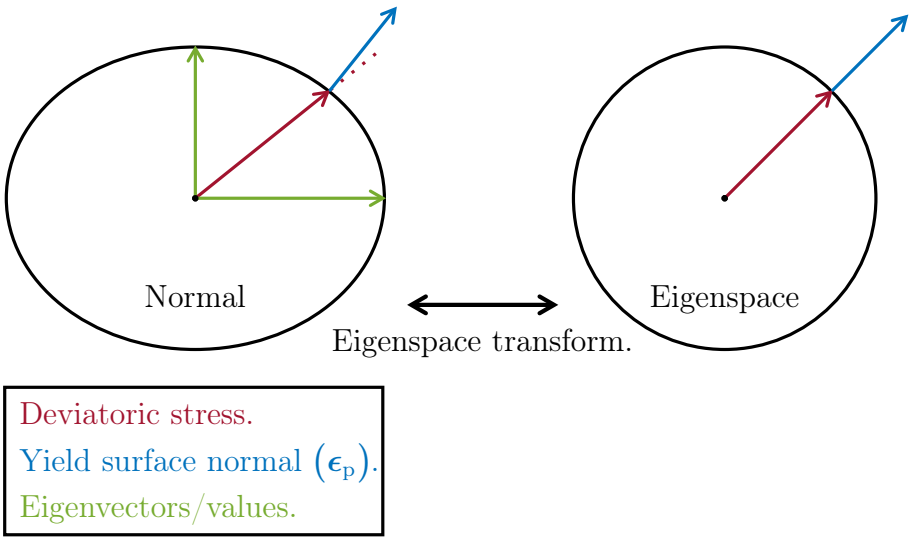

Figure 3.3: Two-dimensional representation of the eigenspace transform with respect to the alignment of deviatoric stress and plastic strain vectors.

the plastic strain vector in strain space, as seen in figure 3.3, in agreement with the normality condition.

This alignment reduces the iterative stress return calculation to a single dimension, with only the magnitude of both effective plastic strain and deviatoric stress vector of importance. This drastically reduces the computational complexity of evaluating the neccessary increment in effective plastic strain compared to other anisotropic plasticity algorithms whilst still maintaining the normality condition.

3.4.6 Radial Return

Given yielding occurs, a non-zero plastic multiplier will exist with the value of this ensuring the yield function remains satisfied such that $f_{\text{Hill}} \leq \sigma^{\text{Y}}$. Given the yield function has the form:

$$f_{\text{Hill}} \coloneqq \frac{1}{2}\left(\mathbf{s}_{\text{n}}\right)^{\mathsf{T}} \mathbf{A}\mathbf{s}_{\text{n}} = \frac{1}{2}\boldsymbol{\sigma}^{\mathsf{T}}\mathbf{A}\boldsymbol{\sigma} \leq \sigma^{\text{Y}},$$

the value of this function at t_{n+1} given plastic deformation can be determined, using equation 3.43, from evaluating:

$$f_{\text{Hill}} = \frac{1}{2}\left(\boldsymbol{\sigma}_{n+1}\right)^{\mathsf{T}}\mathbf{A}\boldsymbol{\sigma}_{n+1} = \frac{1}{2}\Big(\boldsymbol{\Lambda}\left(\mathbf{I}+\Delta\gamma\boldsymbol{\Gamma}_{\mathbf{B}}\right)^{-1}\boldsymbol{\Lambda}^{-1}\boldsymbol{\sigma}_{\text{tr}}\Big)^{\mathsf{T}}\mathbf{A}\Big(\boldsymbol{\Lambda}\left(\mathbf{I}+\Delta\gamma\boldsymbol{\Gamma}_{\mathbf{B}}\right)^{-1}\boldsymbol{\Lambda}^{-1}\boldsymbol{\sigma}_{\text{tr}}\Big) \leq \sigma^{\text{Y}}.$$

Where equation 3.43 explicitly has been used to relate the remaining stress at t_{n+1} (given by $\boldsymbol{\sigma}_{n+1}$) to the trial stress at the start of the time step ($\boldsymbol{\sigma}_{\text{tr}}$), assuming zero plastic deformation, for a given plastic multiplier. This expression may be further simplified using the transformed stress $\tilde{\boldsymbol{\sigma}}_{n}$ as defined in equation 3.42 to give:

$$f_{\text{Hill}} = \frac{1}{2}\left(\tilde{\boldsymbol{\sigma}}_{\text{tr}}\right)^{\mathsf{T}}\left(\mathbf{I}+\Delta\gamma\boldsymbol{\Gamma}_{\mathbf{B}}\right)^{-1}\boldsymbol{\Lambda}^{\mathsf{T}}\mathbf{A}\boldsymbol{\Lambda}\left(\mathbf{I}+\Delta\gamma\boldsymbol{\Gamma}_{\mathbf{B}}\right)^{-1}\tilde{\boldsymbol{\sigma}}_{\text{tr}}.$$

It can be shown that $\boldsymbol{\Lambda}^{\mathsf{T}}\mathbf{A}\boldsymbol{\Lambda} = \boldsymbol{\Gamma}_{\mathbf{B}}$, given that $\boldsymbol{\Lambda}$ represents a transform between an orthotropic space defined by $\mathbf{A}$ and an isotropic eigenspace where this orthotropy is reduced to a set of on-axis scaling terms forming the diagonal of $\boldsymbol{\Gamma}_{\mathbf{B}}$. Using this substitution, it is possible to simplify the yield function, such that:

$$f_{\text{Hill}} = \frac{1}{2}\left(\tilde{\boldsymbol{\sigma}}_{\text{tr}}\right)^{\mathsf{T}}\left(\mathbf{I}+\Delta\gamma\boldsymbol{\Gamma}_{\mathbf{B}}\right)^{-1}\boldsymbol{\Gamma}_{\mathbf{B}}\left(\mathbf{I}+\Delta\gamma\boldsymbol{\Gamma}_{\mathbf{B}}\right)^{-1}\tilde{\boldsymbol{\sigma}}_{\text{tr}}.$$

Finally, defining a diagonal matrix, $\boldsymbol{\kappa}$, dependent on the constant terms of the diagonal matrix $\boldsymbol{\Gamma}_{\mathbf{B}}$ and the scalar variable $\Delta\gamma$ such that:

$$\boldsymbol{\kappa} \coloneqq \left(\mathbf{I}+\Delta\gamma\boldsymbol{\Gamma}_{\mathbf{B}}\right)^{-1}\boldsymbol{\Gamma}_{\mathbf{B}}\left(\mathbf{I}+\Delta\gamma\boldsymbol{\Gamma}_{\mathbf{B}}\right)^{-1}, \tag{3.44}$$

it is possible to form an expression as follows:

$$f_{\text{Hill}} \coloneqq \frac{1}{2}\left(\mathbf{s}_{n}\right)^{\mathsf{T}}\mathbf{A}\mathbf{s}_{n} = \frac{1}{2}\left(\tilde{\boldsymbol{\sigma}}_{\text{tr}}\right)^{\mathsf{T}}\boldsymbol{\kappa}\tilde{\boldsymbol{\sigma}}_{\text{tr}}. \tag{3.45}$$

In equation 3.45 the matrix $\boldsymbol{\kappa}$ is, by definition, diagonal with the ith term of this diagonal explicitly given to be:

$$\kappa_{ii} = \frac{(\Gamma_B)_{ii}}{\left(1 + \Delta\gamma\,(\Gamma_B)_{ii}\right)^2},$$

where for completeness $(\Gamma_B)_{ii}$ is the value of the ith diagonal term in $\mathbf{\Gamma_B}$. From this expression it is possible to check if there is yielding at the end of a time step, given a non-zero plastic multiplier, from within the stress eigenspace. This allows the use of a standard iterative radial return convergence routine to evaluate a suitable value of $\Delta\gamma$ and hence a suitable increment in effective plastic strain and resultant post yield stress. From here what remains to create the material subroutine is to implement a suitable strength model, providing an anisotropic plastic potential to pair to the anisotropic yield function, the specifics of which are detailed in chapter 9.

Chapter 4

Dynamic Material Response

Up until now, the material theory introduced has covered the mechanical response to applied loads, with summary of linear elasticity and the concept of plasticity. Furthermore, concerning the computational descriptions of plasticity, a numerical algorithm adapting the quadratic Hill yield criterion to facilitate associative radial return has been introduced in detail. Within this section an overview of the thermodynamic response of materials to dynamic loading beyond the yield stress will be covered. The aim of this is to effectively underpin the spallation analysis introduced at the end of the chapter and used later within this work.

4.1 Shock Loading

Information flow regarding external loading conditions within a solid usually occurs at the characteristic sound speed of that material, with bulk, shear, and longitudinal variants each governed by different combinations of underlying material properties. In solids these sound speeds are commonly found to positively correlate with pressure, such that given a ramped compressive stress front of sufficiently large amplitude, when compared to the elastic limit of the material, the peak of the wavefront may travel faster than its foot. This variance in wave speed leads to a reduction in the width of the wavefront as seen in the left of figure 4.1. Extrapolated, this can lead to a near discontinuity in pressure propagating through uncompressed material, known as a shock wave, in a process known as *shocking up*.

Of note is that whilst compressive waves beyond the elastic limit will tend to discontinuous shock fronts, equivalents causing rarefaction will spread out to form what is known as a *release fan*, serving to abate the compressive stress in the initial shock front. Once formed, and prior to the arrival of the aforementioned release waves,

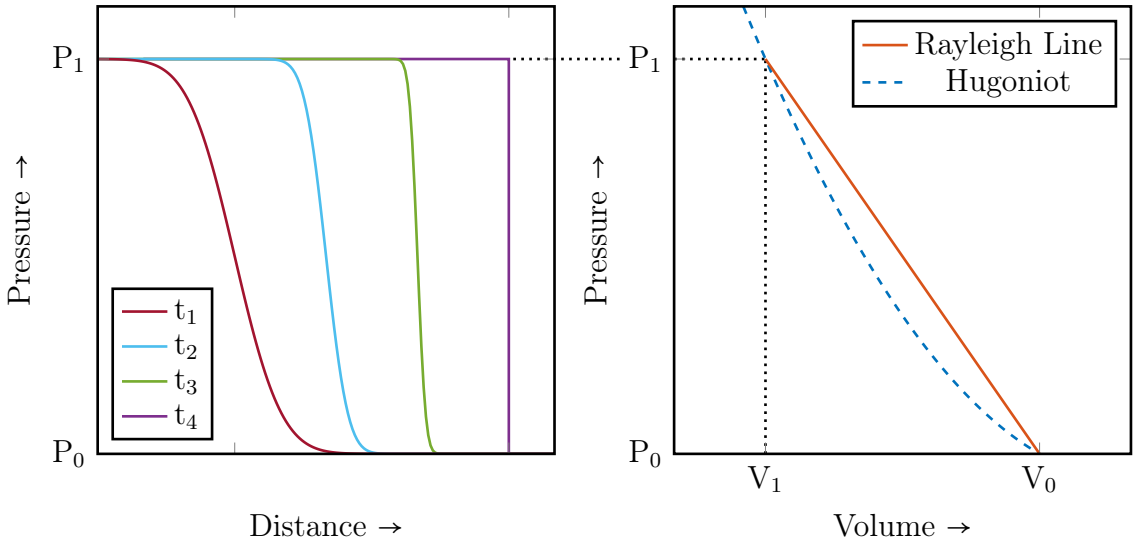

Figure 4.1: A one dimensional representation of the *shocking up* of a compressive pressure wave. To the left, the profile of a wavefront is shown moving left to right with a gradual transition between the early stage ramp and late state shock states. To the right a representation of the thermodynamic transition at the shock front in pressure-volume phase space is given. Dotted black lines are given to link between figures, and explicitly identify initial and shocked thermodynamic states.

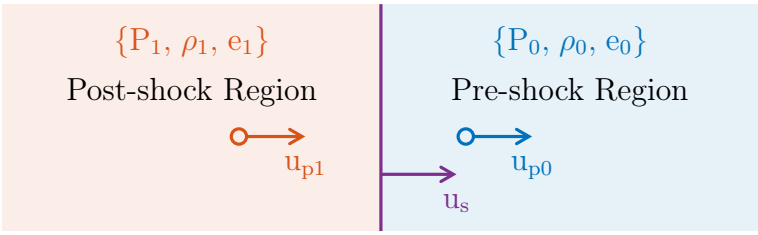

Figure 4.2: Intrinsic variables for pressure, P, density, ρ, specific internal energy, e, and particle velocity, u_p, before and after the passing of a one dimensional shock front moving left to right at a velocity of u_s.

a shock front exists in a steady state, subjecting the material to a discontinuous jump in thermodynamic state, altering the material pressure (P), density (ρ), particle velocity (u), and internal specific energy (e).

Considering the thermodynamic jump across the shock front, it is possible to relate the change in the aforementioned state variables given that the flux of mass, momentum, and energy across the wavefront are conserved. The resulting expressions, collectively known as the Rankine-Hugoniot jump conditions after the seminal works of William Rankine [162] and Pierre-Henri Hugoniot [163], underpin shock wave

analyses and are defined such that,

$$\rho_0 \left(u_s - u_{p0}\right) = \rho_1 \left(u_s - u_{p1}\right), \qquad \text{(Mass)} \qquad (4.1)$$

$$\rho_0 u_{p0} \left(u_{p0} - u_s\right) + P_0 = \rho_1 u_{p1} \left(u_{p1} - u_s\right) + P_1, \qquad \text{(Momentum)} \qquad (4.2)$$

$$e_0 + \frac{1}{2}\left(u_{p0} - u_s\right)^2 + \frac{P_0}{\rho_0} = e_1 + \frac{1}{2}\left(u_{p1} - u_s\right)^2 + \frac{P_1}{\rho_1}. \qquad \text{(Energy)} \qquad (4.3)$$

Here, as seen in figure 4.2, in these equations the subscripting of either 0 or 1 to a state variable identify it as either preceding or proceeding the shock front respectively, with the additional subscripting of either p or s denoting properties as belonging to either particles or shocks respectively.

Ignoring material strength, the thermodynamic transition occurring at the shock front can be mapped in pressure-volume phase space as a straight line joining two points. Both ends of this line are found to sit on the material's Hugoniot, which itself does not represent a valid thermodynamic path for a material undergoing shock compression, but is rather a locus of all states achievable under shock compression, with the straight thermodynamic path identified as the *Rayleigh line*. For the case of a single shock propagating through a material with no strength, an example of this transition in pressure-volume phase space, with the associated pressure wave shown alongside, is provided in figure 4.1. Of note here is the gradient of the Rayleigh line, here identified as m_{RL}, itself related to the velocity of the shock front using equations 4.1 and 4.2 such that,

$$m_{RL} = \frac{\Delta P}{\Delta v} = \frac{P_1 - P_0}{v_1 - v_0} = -\left(\rho_0 \left(u_s - u_{p0}\right)\right)^2, \qquad (4.4)$$

where v is given as the specific volume, the inverse of density, and where other quantities and subscripts remain as defined above. Within this expression the term u_{p0} is often taken to equal zero, with this either assuming an initially static state, or with the velocity taken in the reference frame of the pre-shocked material where the same assumption of $u_{p0} = 0$ would again be valid.

Such a thermodynamic transition does not exist in isolation, instead requiring application of a large external force to the material. Within the field of shock physics this is usually accomplished through means of plate impact, where the planar collision of two high aspect ratio cylindrical plates may drive compressive shock waves into each body with one-dimensional conditions (as assumed in equations 4.1–4.3) existing within the central region of each plate, until the arrival of rarefacting release waves propagating from the edges of each plate toward the centreline.

Material transition under shock impact is calculable in stages with knowledge of both impact and the shock front velocities within the respective material, as well as the initial material properties and the assumption that motion and pressure are conserved across the impact interface. Whilst the characteristics of the pre-shock material are evaluated by conventional methods, measurement of impact and shock velocities in present day experiments commonly employ velocimetry techniques such as photon Doppler velocimetry, discussed in detail in chapter 6.

Prediction of arbitrary thermodynamic shock histories is facilitated by careful mapping of several material Hugoniot curves. Whilst explicit worked examples of this process are omitted from this thesis, several reference texts provide excellent coverage [35, 41, 42, 164]. Instead the process, that builds upon knowledge of several material Hugoniot curves, with assumptions for the conservation of pressure and velocity across interfaces, is summarised as follows.

- Firstly, appropriate Hugoniot curves for each material are found from prior experimental measurements.

- Secondly, these curves are plotted in pressure-particle velocity phase space, with appropriate offsets accounting for initial particle velocities due to impact conditions. Additionally, the Hugoniot of a material is reflected laterally should generated shock waves propagate backwards, within the chosen frame of reference, following impact.

- Finally, the resulting intersection of the material Hugoniots is found. This in-

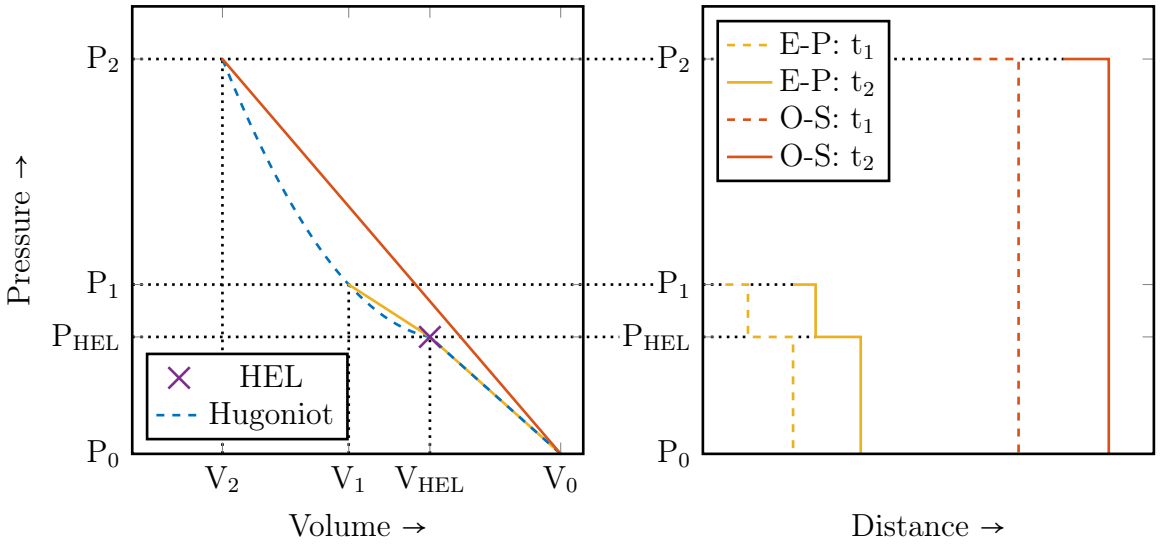

Figure 4.3: Two possible thermodynamic transitions for a material with strength: one undergoing a transition to a lower pressure resulting in a two wave structure and one to a higher pressure resulting in a single wave transition.

tersection represents a valid solution, conserving pressure and particle velocity across the interface, to post-impact material states following transit of each shock front.

Upon arrival of compressive shock fronts at unbounded surfaces, release waves of equal and opposite magnitude are generated to ensure no pressure is found at the free surface. Allowing what is known as the linear free surface approximation [164], these waves serve to approximately double the shocked particle velocity introduced by the compressive front, with the surface then moving at this doubled speed.

In reality such simple Hugoniot curves such as that seen in figure 4.1 are not found in solids. Instead finite material strength mandates a differing response at characteristic stresses below the Hugoniot elastic limit (**HEL**) of the material. Most materials are then well characterised by a piecewise Hugoniot structure, atop a linear elastic region, where multiple non-linear regions may be delimited by phase transitions within the material. Ignoring phase changes, the inclusion of strength may lead to a Hugoniot similar to that shown in figure 4.3.

This more realistic Hugoniot structure can lead to plastic and elastic waves forming simultaneously, when a straight line joining the initial and final Hugoniot states crosses

the Hugoniot itself. In the example two-wave case seen in figure 4.3, identified by E-P, elastic and plastic waves are seen with the plastic wave following the initial elastic pulse, further increasing the pressure upon its transit. This two wave structure is not found in the alternate case, identified by O-S, as the Rayleigh line bypasses the HEL to produce a single *overdriven shock*.

4.2 The Lagrangian Diagram

When tracking the propagation of pressure waves within a material subjected to shock loading, the use of Lagrangian diagrams provide clear understanding of the progression of both compressive and tensile wave fronts. Summarising the format of a Lagrangian diagram, a one dimensional profile is shown along the horizontal axis, with the temporal duration of the loading event represented in the vertical axis. Figure 4.4 shows the Lagrangian diagram of a spallation experiment, where a carefully constructed planar plate impact of a flyer upon a target generates a dynamic tensile load within the target bulk, leading to failure and the internal rupture of the target.

4.3 Spallation

As summarised above, plate impact spallation testing seeks to subject a material to a rapidly developing tensile stress state that is in an ideal case one dimensional. The behaviour of waves within the sample is represented with use of a Lagrangian diagram as seen in figure 4.4, with each individual expected stage given below. Assumed in this case is a target twice the thickness of the impacting flyer, where both flyer and target are made of the same material, and where one dimensional conditions persist beyond the formation of the spallation plane.

t_0 : The flyer strikes the target, in the purely plastic case visualised in figure 4.4 a pair of compressive plastic wavefronts propagate outwards from the impact interface. Should material strength effects produce a two-wave response, these plastic wavefronts will be preceded by compressive *elastic precursors*. Both wavefronts induce uniaxial compressive strain, with potential elastic wavefronts propagating

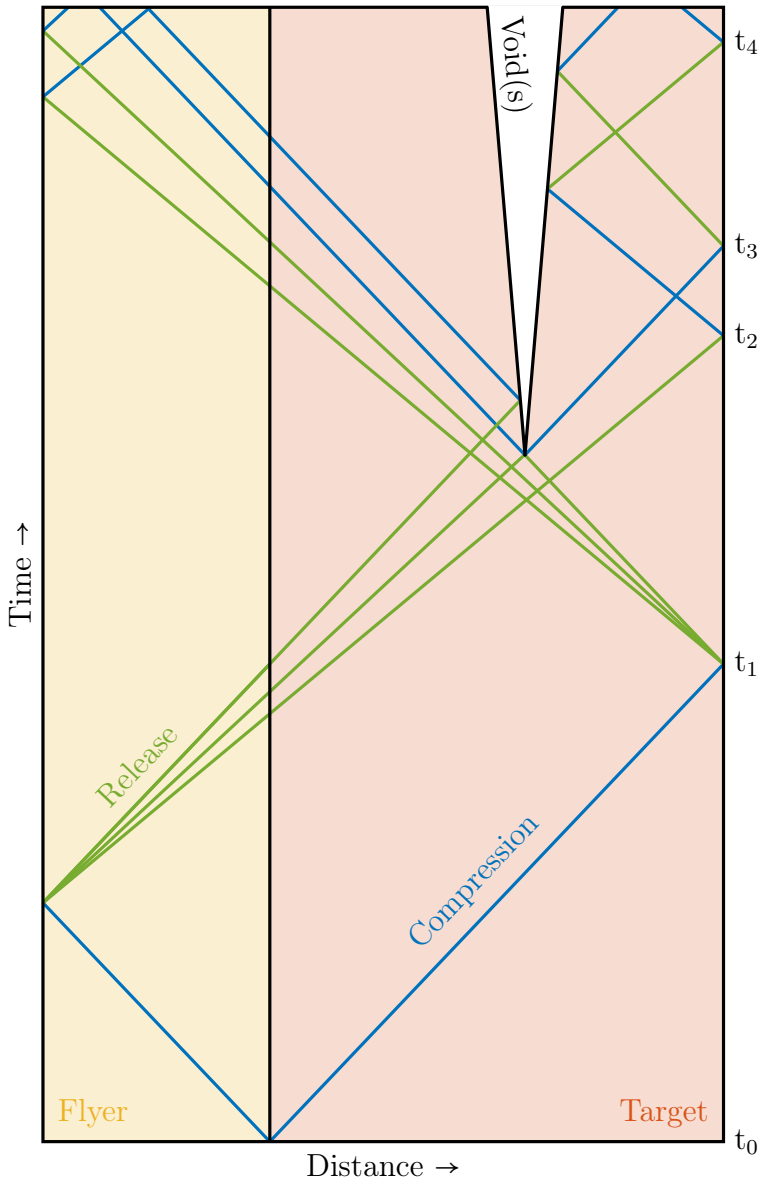

Figure 4.4: A simplified Lagrangian diagram of a plate impact spallation experiment where a flyer is impacted with a high degree of planarity upon a target twice its thickness and equal in material properties. The material here is shown with purely plastic behaviour, ignoring the propagation of elastic wavefronts during the impact. The location of wavefronts within the profile are defined by their location on the horizontal axis, with the vertical axis representing progression in time and therefore evolution in wavefront location implicitly. Compressive and release waves are differentiated using colour, with detailed description of the spallation process displayed here provided in section 4.3 including comments describing the convolving effects of material strength.

at the longitudinal sound speed and the plastic wavefronts moving at a speed dependent on the changes in pressure and density across each wavefront.

t_1 : With arrival of the plastic wavefront at the rear surface of the target, the rear surface velocity drastically increases. Given a purely plastic response the surface will previously have been at rest, however should an elastic precursor exist the surface will already have seen acceleration at an earlier time $\mathbf{t_{HEL}}$. Upon reflection, the plastic wavefront generates a release fan, as the leading edge of the release travels faster than its trailing edge. This occurs as the leading edge is travelling back through material at a pressure greater than the trailing edge. Following this there is a gap before other waves arrive at the rear of the target, with this creating a characteristic plateau on a plot of rear surface motion, as seen in figure 4.5 from 0.4 µs to 0.7 µs after impact.

t_2 : The first sign of the plastic release fan, generated at the flyers rear surface, is seen. Previously plastic release fans from both surfaces have interacted inside the target, generating a region of dynamic tensile uniaxial strain. The release characteristic now observed at the rear of the target has passed through the tensile interaction region prior to material failure. Upon arrival at the rear surface this wave reduces the velocity, with the continual arrival of further release characteristics furthering surface deceleration.

t_3 : Assuming that failure does occur, first sign of this is then observed at the rear surface of the sample. Between t_2 and the present time, the surface velocity has been gradually decreasing due to the continual arrival of release fan characteristics generated at the rear of the target. Should failure occur (assumed to be instant in this idealised case) a compressive wavefront is generated at the free internal failure surface. This wavefront offsets the previously existing tensile state, ensuring that no stress remains at the free surface. Once the free surface exists, no further plastic release characteristics seeded at the rear of the flyer may reach the rear surface of the target. The interruption to further transiting of forwards

propagating release characteristics, and arrival of a compressive pulse, result in the acceleration of the rear surface that until then had been decelerating. It is this arrival, that generates the *pull-back* signal associated with spallation in free surface velocity traces. An oft-omitted nuance to this event is the effect of material strength upon the observed pull-back. Should strength be considered, the compressive elastic pulse will propagate faster than the plastic characteristics generated at the flyer rear surface. Due to the increased velocity of the compressive elastic pulse, a small portion of the tensile plastic characteristics, those transiting the tensile interaction region immediately prior to failure, are abated before they may reduce the velocity at the rear surface. This interaction has motivated a series of corrections to the evaluated spallation strength, discussed later in this section.

t_4 : From here onwards, waves are taken as reverberating within the material either side of the spallation plane. This ongoing reverberation leads to a ringing effect in the observed rear surface motion, with oscillations gradually attenuated due to the dispersion of the wavefronts and lateral release effects.

When measuring the velocity of the target rear surface during each step of the spallation processes a common waveform is produced, an example of which is seen in figure 4.5 with annotations provided to link the velocity history to both the Lagrangian diagram and the stepwise description. The evaluation of this waveform is a subject of much theoretical debate, with several different expressions available within the literature.

Evaluation of the spall strength stems from equation 4.2, with the plastic wave stress equal to the jump in momentum exerted on the material at the wavefront. For material undergoing isochoric plasticity, this is calculable as,

$$\sigma = \rho_0 \, c_B \, \Delta u_p, \tag{4.5}$$

where Δu_p represents the change in particle velocity as the wavefront passes. When

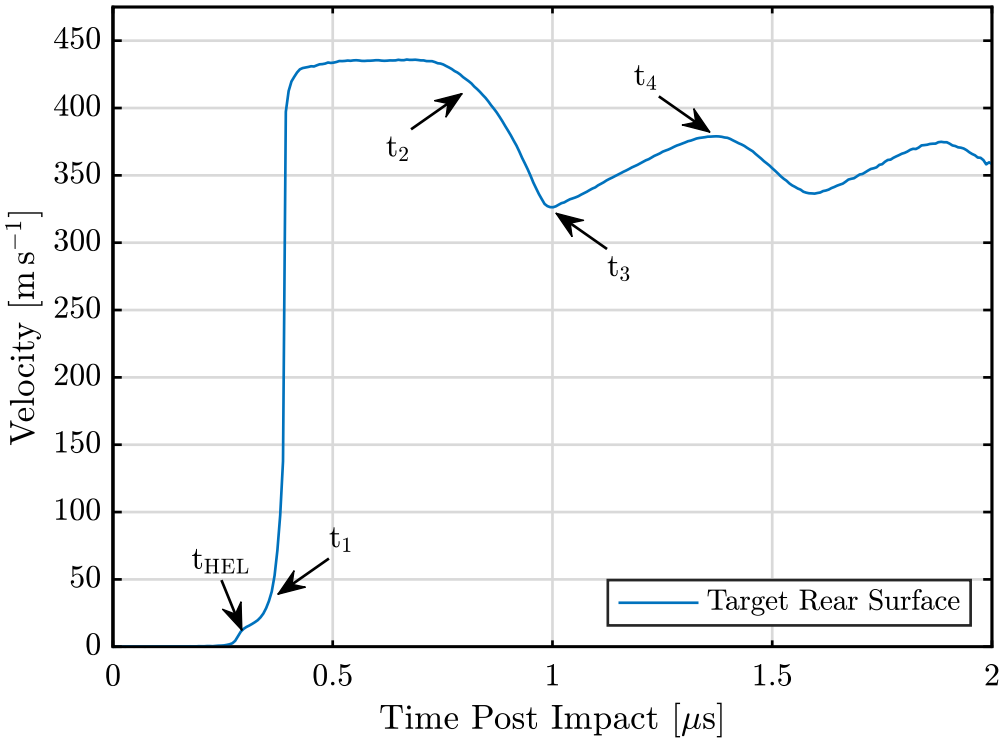

Figure 4.5: Example velocity history of the rear of a spallation target during impact.

this wave reaches the rear free surface of the target, assuming the pressure of the wave exceeds the Hugoniot elastic limit of the material (albeit not to the point of inducing phase changes), the change in surface velocity is approximately doubled following the necessary generation of the tensile counterpart with this leading to the widely used expression given as [165],

$$\sigma = \frac{1}{2}\rho_0 \, c_B \, \Delta u_{FS}. \tag{4.6}$$

Armed with this expression as a starting point, the evaluation of spall strength may use the change in velocity occurring within the post-plateau deceleration ($t_2 \rightarrow t_3$) as a value for Δu_{FS}, with the initial density used given the assumed isochoric plasticity, and a bulk sound speed taken either from literature or experimental measurement.

Further investigation of the potential relationship between spallation strength and rear surface motion reveals a spread of analyses. Within these, each variant seeks to quantify the aforementioned and oft-omitted nuance concerning the abating of plastic release characteristics by the advancing compressive elastic spallation pulse.

Coverage, such as that by Kanel [44] provides detailed description of wave propa-

gation within the system, ultimately suggesting use of a correction term applied to the change in velocity. This correction predicts the magnitude of abated plastic characteristics given the disparity between longitudinal and bulk sound speeds, the distance between the failure plane and the target rear surface, and the rate at which release characteristics were reducing the measured target rear surface velocity [41, 43, 166]. The resulting expression for spallation strength is given as,

$$\sigma_{\mathrm{Spall}} = \frac{1}{2}\rho_0\, c_B \left(\Delta u_{FS} + \left(\frac{H_S}{c_B} - \frac{H_S}{c_L} \right) \frac{\left| \left(\frac{d(u_{FS})}{dt} \right)_{\downarrow} \left(\frac{d(u_{FS})}{dt} \right)_{\uparrow} \right|}{\left| \left(\frac{d(u_{FS})}{dt} \right)_{\downarrow} \right| + \left(\frac{d(u_{FS})}{dt} \right)_{\uparrow}} \right), \tag{4.7}$$

where, in addition to the quantities outlined in equation 4.6, H_S is the thickness of the region behind the spallation plane (in examples to complete spallation this detached body is referred to as the scab), c_L is the longitudinal sound speed, and where $\left\{ \left(\frac{d(u_{FS})}{dt} \right)_{\downarrow}, \left(\frac{d(u_{FS})}{dt} \right)_{\uparrow} \right\}$ represent the rate of deceleration of the rear surface velocity prior to arrival of the compressive spallation pulse and the rate of acceleration proceeding the arrival of the compressive pulse respectively. This deceleration may be calculated as the gradient of the rear surface velocity just prior to pull-back ($t_2 \rightarrow t_3$), with the resulting correction found to alter the evaluated spallation strength by not more than 5 % to 7 % [44]. It is this analysis that is used when analysing spallation pull-back signals later in this thesis, mimicking other uses in literature [110, 112, 125], with an awareness that several interpretations of the process are possible.

References

[1] Y Koren. *Computer Control of Manufacturing Systems*. Mechanical engineering series. McGraw-Hill, 1983. ISBN: 9780070353411.

[2] Jean-Pierre Kruth. "Material Incress Manufacturing by Rapid Prototyping Techniques". In: *CIRP Ann.* 40.2 (1991), pp. 603–614. ISSN: 00078506. DOI: 10.1016/S0007-8506(07)61136-6.

[3] B. Badrinarayan and Joel W Barlow. "Metal parts from selective laser sintering of metal-polymer powders". In: *Int. Solid Free. Fabr. Symp.* 1. University of Texas at Austin, 1992, pp. 141–146. DOI: 10.15781/T2988346K.

[4] Terry Wohlers. "Future potential of rapid prototyping and manufacturing around the world". English. In: *Rapid Prototyp. J.* 1.1 (Mar. 1995), pp. 4–10. ISSN: 1355-2546. DOI: 10.1108/13552549510146630.

[5] Charles Hull et al. "Rapid prototyping: current technology and future potential". English. In: *Rapid Prototyp. J.* 1.1 (Mar. 1995), pp. 11–19. ISSN: 1355-2546. DOI: 10.1108/13552549510732026.

[6] Kaufui V. Wong and Aldo Hernandez. "A Review of Additive Manufacturing". In: *ISRN Mech. Eng.* 2012 (Aug. 2012), pp. 1–10. ISSN: 2090-5130. DOI: 10.5402/2012/208760.

[7] John O. Milewski. *Additive Manufacturing of Metals*. Vol. 258. Springer Series in Materials Science. Cham: Springer International Publishing, 2017, pp. 75–84. ISBN: 978-3-319-58204-7. DOI: 10.1007/978-3-319-58205-4.

[8] Mukesh Agarwala et al. "Direct selective laser sintering of metals". English. In: *Rapid Prototyp. J.* 1.1 (1995), pp. 26–36. ISSN: 13552546. DOI: https://doi.org/10.1108/13552549510078113.

[9] J G Conley and H L Marcus. "Rapid Prototyping and Solid Free Form Fabrication". In: *J. Manuf. Sci. Eng.* 119.4B (Nov. 1997), pp. 811–816. ISSN: 1087-1357. DOI: 10.1115/1.2836828.

[10] William E. Frazier. "Metal Additive Manufacturing: A Review". In: *J. Mater. Eng. Perform.* 23.6 (June 2014), pp. 1917–1928. ISSN: 1059-9495. DOI: 10.1007/s11665-014-0958-z.

[11] Amanda S. Wu et al. "An Experimental Investigation into Additive Manufacturing-Induced Residual Stresses in 316L Stainless Steel". In: *Metall. Mater. Trans. A* 45.13 (Dec. 2014), pp. 6260–6270. ISSN: 1073-5623. DOI: 10.1007/s11661-014-2549-x.

[12] F. Abe et al. "The manufacturing of hard tools from metallic powders by selective laser melting". In: *J. Mater. Process. Technol.* 111.1-3 (Apr. 2001), pp. 210–213. ISSN: 09240136. DOI: 10.1016/S0924-0136(01)00522-2.

[13] Hadley Brooks and Kevin Brigden. "Design of conformal cooling layers with self-supporting lattices for additively manufactured tooling". In: *Addit. Manuf.* 11 (July 2016), pp. 16–22. ISSN: 22148604. DOI: 10.1016/j.addma.2016.03.004.

[14] Adriaan B. Spierings, Thomas L. Starr, and Konrad Wegener. "Fatigue performance of additive manufactured metallic parts". In: *Rapid Prototyp. J.* 19.2 (2013), pp. 88–94. ISSN: 13552546. DOI: 10.1108/13552541311302932.

[15] Gururaja Udupa, S. Shrikantha Rao, and K.V. Gangadharan. "Functionally Graded Composite Materials: An Overview". In: *Procedia Mater. Sci.* 5 (2014), pp. 1291–1299. ISSN: 22118128. DOI: 10.1016/j.mspro.2014.07.442.

[16] Chao Wei et al. "Additive Manufacturing of Horizontal and 3D Functionally Graded 316L/Cu10Sn Components via Multiple Material Selective Laser Melting". In: *J. Manuf. Sci. Eng.* 141.8 (Aug. 2019), pp. 1–8. ISSN: 1087-1357. DOI: 10.1115/1.4043983.

[17] H.L. Wei, J. Mazumder, and T. DebRoy. "Evolution of solidification texture during additive manufacturing". In: *Sci. Rep.* 5.1 (Dec. 2015), p. 16446. ISSN: 2045-2322. DOI: 10.1038/srep16446.

[18] Zhuqing Wang, Todd A. Palmer, and Allison M. Beese. "Effect of processing parameters on microstructure and tensile properties of austenitic stainless steel 304L made by directed energy deposition additive manufacturing". In: *Acta Mater.* 110 (May 2016), pp. 226–235. ISSN: 13596454. DOI: 10.1016/j.actamat.2016.03.019.

[19] T. Mukherjee et al. "Printability of alloys for additive manufacturing". In: *Sci. Rep.* 6.1 (Apr. 2016), p. 19717. ISSN: 2045-2322. DOI: 10.1038/srep19717.

[20] T. Mukherjee et al. "Dimensionless numbers in additive manufacturing". In: *J. Appl. Phys.* 121.6 (Feb. 2017), p. 064904. ISSN: 0021-8979. DOI: 10.1063/1.4976006.

[21] Adriaan B. Spierings and G. Levy. "Comparison of density of stainless steel 316L parts produced with selective laser melting using different powder grades". In: *2009 Int. Solid Free. Fabr. Symp.* University of Texas at Austin, 2009, pp. 342–353. DOI: 10.26153/tsw/15113.

[22] Mohsen Badrossamay et al. "Improving Productivity Rate in SLM of Commercial Steel Powders". In: *Tech. Pap. - Soc. Manuf. Eng.* TP09PUB17 (2009), pp. 1–13.

[23] Adriaan B. Spierings, N. Herres, and G. Levy. "Influence of the particle size distribution on surface quality and mechanical properties in AM steel parts". In: *Rapid Prototyp. J.* 17.3 (Apr. 2011). Ed. by Dave Bourell, pp. 195–202. ISSN: 1355-2546. DOI: 10.1108/13552541111124770.

[24] A.A. Antonysamy, J. Meyer, and P.B. Prangnell. "Effect of build geometry on the β-grain structure and texture in additive manufacture of Ti6Al4V by selective electron beam melting". In: *Mater. Charact.* 84 (Oct. 2013), pp. 153–168. ISSN: 10445803. DOI: 10.1016/j.matchar.2013.07.012.

[25] B. Song et al. "Compressive and Tensile Stress–Strain Responses of Additively Manufactured (AM) 304L Stainless Steel at High Strain Rates". In: *J. Dyn. Behav. Mater.* 3.3 (Sept. 2017), pp. 412–425. ISSN: 2199-7446. DOI: 10.1007/s40870-017-0122-6.

[26] J. A. Cherry et al. "Investigation into the effect of process parameters on microstructural and physical properties of 316L stainless steel parts by selective laser melting". In: *Int. J. Adv. Manuf. Technol.* 76.5-8 (Feb. 2015), pp. 869–879. ISSN: 0268-3768. DOI: 10.1007/s00170-014-6297-2.

[27] K.G. Prashanth and J. Eckert. "Formation of metastable cellular microstructures in selective laser melted alloys". In: *J. Alloys Compd.* 707.October (June 2017), pp. 27–34. ISSN: 09258388. DOI: 10.1016/j.jallcom.2016.12.209.

[28] Pierre Muller, Pascal Mognol, and Jean-Yves Hascoet. "Modeling and control of a direct laser powder deposition process for Functionally Graded Materials (FGM) parts manufacturing". In: *J. Mater. Process. Technol.* 213.5 (May 2013), pp. 685–692. ISSN: 09240136. DOI: 10.1016/j.jmatprotec.2012.11.020.

[29] Qiang Wang et al. "Microstructure evolution and EBSD analysis of a graded steel fabricated by laser additive manufacturing". In: *Vacuum* 141 (July 2017), pp. 68–81. ISSN: 0042207X. DOI: 10.1016/j.vacuum.2017.03.021.

[30] E. Berry et al. "Preliminary experience with medical applications of rapid prototyping by selective laser sintering". In: *Med. Eng. Phys.* 19.1 (Jan. 1997), pp. 90–96. ISSN: 13504533. DOI: 10.1016/S1350-4533(96)00039-2.

[31] Junchao Li, Yanyan Zang, and Wei Wang. "Elastic modulus and stress analysis of porous titanium parts fabricated by selective laser melting". In: *J. Harbin Inst. Technol.* 23.2 (Apr. 2016), pp. 46–50. DOI: 10.11916/j.issn.1005-9113.2016.02.007.

[32] H. Nahme, E. Lach, and R. Rohr. "Dynamic materials behavior of a porous pressureless sintered steel and a HIPped steel". In: *J. Phys. IV* 134 (Aug. 2006), pp. 1047–1051. ISSN: 1155-4339. DOI: 10.1051/jp4:2006134160.

[33] Dongdong Gu et al. "Material-structure-performance integrated laser-metal additive manufacturing". In: *Science (80-.).* 372.6545 (2021). ISSN: 10959203. DOI: 10.1126/science.abg1487.

[34] Sean H Haight. "An anisotropic and asymmetric material model for simulation of metals under dynamic loading". PhD thesis. George Mason University, 2016.

[35] J Asay et al. *High-Pressure Shock Compression of Solids II: Dynamic Fracture and Fragmentation.* Ed. by Lee Davison, Dennis E. Grady, and Mohsen Shahinpoor. New York, NY: Springer New York, 1996. ISBN: 978-1-4612-7501-5. DOI: 10.1007/978-1-4612-2320-7.

[36] ASM Handbook Committee. *Mechanical Testing and Evaluation.* English. Vol. 8. 1. [Metals Park, Ohio]: ASM International, 2000. ISBN: 978-0-87170-389-7. URL: https://www.asminternational.org.

[37] Sean H Haight et al. *Development of a titanium alloy Ti-6Al-4V material model used in LS-DYNA.* Tech. rep. May. U.S. Department of Transportation, 2016, p. 353. URL: https://www.tc.faa.gov/its/worldpac/techrpt/tc15-23.pdf.

[38] Jürgen Mayer, Khaled Khairy, and Jonathon Howard. "Drawing an elephant with four complex parameters". In: *Am. J. Phys.* 78.6 (June 2010), pp. 648–649. ISSN: 0002-9505. DOI: 10.1119/1.3254017.

[39] Wayne E. King et al. "Observation of keyhole-mode laser melting in laser powder-bed fusion additive manufacturing". In: *J. Mater. Process. Technol.* 214.12 (Dec. 2014), pp. 2915–2925. ISSN: 09240136. DOI: 10.1016/j.jmatprotec.2014.06.005.

[40] Yihang Cui et al. "Effect of Porosity on Dynamic Response of Additive Manufacturing Ti-6Al-4V Alloys". In: *Micromachines* 13.3 (Mar. 2022), p. 408. ISSN: 2072-666X. DOI: 10.3390/mi13030408.

[41] Tarabay Antoun et al. *Spall Fracture.* Shock Wave and High Pressure Phenomena. New York: Springer-Verlag, 2003. ISBN: 0-387-95500-3. DOI: 10.1007/b97226.

[42] Cyril L. Williams. *Structure-Property Relationships under Extreme Dynamic Environments*. Ed. by SEM Kristin Zimmerman. Vol. 2. Synthesis / SEM Lectures on Experimental Mechanics 1. Cham: Springer International Publishing, Jan. 2019, pp. 1–155. ISBN: 978-3-031-79724-5. DOI: 10.1007/978-3-031-79725-5.

[43] V D Gluzman and G. I. Kanel. "Measurement of the tensile stresses behind a spalling plane". In: *J. Appl. Mech. Tech. Phys.* 24.4 (1984), pp. 582–585. ISSN: 0021-8944. DOI: 10.1007/BF00907912.

[44] G. I. Kanel. "Distortion of the Wave Profiles in an Elastoplastic Body upon Spalling". In: *J. Appl. Mech. Tech. Phys.* 42.2 (2001), pp. 358–362. ISSN: 1573-8620. DOI: 10.1023/A:1018804709273.

[45] T. DebRoy et al. "Additive manufacturing of metallic components – Process, structure and properties". In: *Prog. Mater. Sci.* 92 (Mar. 2018), pp. 112–224. ISSN: 00796425. DOI: 10.1016/j.pmatsci.2017.10.001.

[46] H H Zhu, J Y H Fuh, and L Lu. "Formation of Fe—Cu metal parts using direct laser sintering". In: *Proc. Inst. Mech. Eng. Part C J. Mech. Eng. Sci.* 217.1 (Jan. 2003), pp. 139–147. ISSN: 0954-4062. DOI: 10.1243/095440603762554686.

[47] T H C Childs, C Hauser, and Mohsen Badrossamay. "Selective laser sintering (melting) of stainless and tool steel powders: Experiments and modelling". In: *Proc. Inst. Mech. Eng. Part B J. Eng. Manuf.* 219.4 (Apr. 2005), pp. 339–357. ISSN: 0954-4054. DOI: 10.1243/095440505X8109.

[48] Kozo Osakada and Masanori Shiomi. "Flexible manufacturing of metallic products by selective laser melting of powder". In: *Int. J. Mach. Tools Manuf.* 46.11 (Sept. 2006), pp. 1188–1193. ISSN: 08906955. DOI: 10.1016/j.ijmachtools.2006.01.024.

[49] Mohsen Badrossamay and T.H.C. Childs. "Layer Formation Studies in Selective Laser Melting of Steel Powders". In: *Int. Solid Free. Fabr. Symp.* 2006, pp. 13–15. DOI: http://dx.doi.org/10.26153/tsw/7136.

[50] Mohsen Badrossamay and T.H.C. Childs. "Further studies in selective laser melting of stainless and tool steel powders". In: *Int. J. Mach. Tools Manuf.* 47.5 (Apr. 2007), pp. 779–784. ISSN: 08906955. DOI: 10.1016/j.ijmachtools.2006.09.013.

[51] Kamran Aamir Mumtaz, Poonjolai Erasenthiran, and Neil Hopkinson. "High density selective laser melting of Waspaloy®". In: *J. Mater. Process. Technol.* 195.1-3 (Jan. 2008), pp. 77–87. ISSN: 09240136. DOI: 10.1016/j.jmatprotec.2007.04.117.

[52] Petri Laakso et al. "Optimization and Simulation of SLM Process for High Density H13 Tool Steel Parts". In: *Phys. Procedia* 83 (2016), pp. 26–35. ISSN: 18753892. DOI: 10.1016/j.phpro.2016.08.004.

[53] John E. Smugeresky, David D. Gill, and Clinton J. Atwood. *New low cost material development technique for advancing rapid prototyping manufacturing technology*. Tech. rep. Albuquerque, NM, and Livermore, CA (United States): Sandia National Laboratories (SNL), Nov. 2007. DOI: 10.2172/926378.

[54] V. Manvatkar, A. De, and T. DebRoy. "Spatial variation of melt pool geometry, peak temperature and solidification parameters during laser assisted additive manufacturing process". In: *Mater. Sci. Technol.* 31.8 (June 2015), pp. 924–930. ISSN: 0267-0836. DOI: 10.1179/1743284714Y.0000000701.

[55] Yali Li and Dongdong Gu. "Parametric analysis of thermal behavior during selective laser melting additive manufacturing of aluminum alloy powder". In: *Mater. Des.* 63 (Nov. 2014), pp. 856–867. ISSN: 02613069. DOI: 10.1016/j.matdes.2014.07.006.

[56] C. H. Fu and Y.B. Guo. "Three-Dimensional Temperature Gradient Mechanism in Selective Laser Melting of Ti-6Al-4V". In: *J. Manuf. Sci. Eng.* 136.6 (Dec. 2014), pp. 1–7. ISSN: 1087-1357. DOI: 10.1115/1.4028539.

[57] Moataz M. Attallah et al. "Additive manufacturing of Ni-based superalloys: The outstanding issues". In: *MRS Bull.* 41.10 (Oct. 2016), pp. 758–764. ISSN: 0883-7694. DOI: 10.1557/mrs.2016.211.

[58] Xiaoyu Xie et al. "Mechanistic data-driven prediction of as-built mechanical properties in metal additive manufacturing". In: *npj Comput. Mater.* 7.1 (Dec. 2021), p. 86. ISSN: 2057-3960. DOI: 10.1038/s41524-021-00555-z.

[59] Dongju Chen et al. "Process optimization of selective laser melting 316L stainless steel by a data-driven nonlinear system". In: *Weld. World* 66.3 (Mar. 2022), pp. 409–422. ISSN: 0043-2288. DOI: 10.1007/s40194-021-01205-0.

[60] M. Averyanova, Ph Bertrand, and B. Verquin. "Studying the influence of initial powder characteristics on the properties of final parts manufactured by the selective laser melting technology". In: *Virtual Phys. Prototyp.* 6.4 (Dec. 2011), pp. 215–223. ISSN: 1745-2759. DOI: 10.1080/17452759.2011.594645.

[61] B. Verlee, T. Dormal, and J. Lecomte-Beckers. "Density and porosity control of sintered 316L stainless steel parts produced by additive manufacturing". In: *Powder Metall.* 55.4 (Sept. 2012), pp. 260–267. ISSN: 0032-5899. DOI: 10.1179/0032589912Z.00000000082.

[62] Benjamin M. Morrow et al. "Impact of Defects in Powder Feedstock Materials on Microstructure of 304L and 316L Stainless Steel Produced by Additive Manufacturing". In: *Metall. Mater. Trans. A* 49.8 (Aug. 2018), pp. 3637–3650. ISSN: 1073-5623. DOI: 10.1007/s11661-018-4661-9.

[63] F. Abe et al. "Influence of forming conditions on the titanium model in rapid prototyping with the selective laser melting process". In: *Proc. Inst. Mech. Eng. Part C J. Mech. Eng. Sci.* 217.1 (Jan. 2003), pp. 119–126. ISSN: 0954-4062. DOI: 10.1243/095440603762554668.

[64] Lore Thijs et al. "A study of the microstructural evolution during selective laser melting of Ti-6Al-4V". In: *Acta Mater.* 58.9 (2010), pp. 3303–3312. ISSN: 13596454. DOI: 10.1016/j.actamat.2010.02.004.

[65] G. Casalino et al. "Experimental investigation and statistical optimisation of the selective laser melting process of a maraging steel". In: *Opt. Laser Technol.* 65 (Jan. 2015), pp. 151–158. ISSN: 00303992. DOI: 10.1016/j.optlastec.2014.07.021.

[66] Lore Thijs et al. "Fine-structured aluminium products with controllable texture by selective laser melting of pre-alloyed AlSi10Mg powder". In: *Acta Mater.* 61.5 (Mar. 2013), pp. 1809–1819. ISSN: 13596454. DOI: 10.1016/j.actamat.2012.11.052.

[67] Xihe Liu et al. "Microstructure of selective laser melted AlSi10Mg alloy". In: *Mater. Des.* 168 (Apr. 2019), p. 107677. ISSN: 02641275. DOI: 10.1016/j.matdes.2019.107677.

[68] Kamran Mumtaz and Neil Hopkinson. "Top surface and side roughness of Inconel 625 parts processed using selective laser melting". In: *Rapid Prototyp.*

J. 15.2 (Mar. 2009), pp. 96–103. ISSN: 1355-2546. DOI: 10.1108/13552540910943397.

[69] Michael Cloots, Peter J. Uggowitzer, and Konrad Wegener. "Investigations on the microstructure and crack formation of IN738LC samples processed by selective laser melting using Gaussian and doughnut profiles". In: *Mater. Des.* 89 (Jan. 2016), pp. 770–784. ISSN: 02641275. DOI: 10.1016/j.matdes.2015.10.027.

[70] Alexander Leicht, Uta Klement, and Eduard Hryha. "Effect of build geometry on the microstructural development of 316L parts produced by additive manufacturing". In: *Mater. Charact.* 143.January (Sept. 2018), pp. 137–143. ISSN: 10445803. DOI: 10.1016/j.matchar.2018.04.040.

[71] Dan Stoia, Emanoil Linul, and Liviu Marsavina. "Influence of Manufacturing Parameters on Mechanical Properties of Porous Materials by Selective Laser Sintering". In: *Materials (Basel).* 12.6 (Mar. 2019), p. 871. ISSN: 1996-1944. DOI: 10.3390/ma12060871.

[72] Evren Yasa and Jean-Pierre Kruth. "Microstructural investigation of Selective Laser Melting 316L stainless steel parts exposed to laser re-melting". In: *Procedia Eng.* 19 (2011), pp. 389–395. ISSN: 18777058. DOI: 10.1016/j.proeng.2011.11.130.

[73] Chu Lun Alex Leung et al. "In situ X-ray imaging of defect and molten pool dynamics in laser additive manufacturing". In: *Nat. Commun.* 9.1 (Dec. 2018), p. 1355. ISSN: 2041-1723. DOI: 10.1038/s41467-018-03734-7.

[74] Sonny Ly et al. "Metal vapor micro-jet controls material redistribution in laser powder bed fusion additive manufacturing". In: *Sci. Rep.* 7.1 (Dec. 2017), p. 4085. ISSN: 2045-2322. DOI: 10.1038/s41598-017-04237-z.

[75] Cang Zhao et al. "Real-time monitoring of laser powder bed fusion process using high-speed X-ray imaging and diffraction". In: *Sci. Rep.* 7.1 (Dec. 2017), p. 3602. ISSN: 2045-2322. DOI: 10.1038/s41598-017-03761-2.

[76] H. Meier and Ch Haberland. "Experimental studies on selective laser melting of metallic parts". In: *Materwiss. Werksttech.* 39.9 (Sept. 2008), pp. 665–670. ISSN: 09335137. DOI: 10.1002/mawe.200800327.

[77] Jean-Pierre Kruth et al. "Part and material properties in selective laser melting of metals". In: *16th Int. Symp. Electromachining, ISEM 2010*. 2010, pp. 3–14. URL: https://lirias.kuleuven.be/retrieve/106724.

[78] Di Wang et al. "Fiber laser selective melting of 316L stainless steel powder". In: *High Power Laser Part. Beams* 22.8 (2010), pp. 1881–1886. ISSN: 1001-4322. DOI: 10.3788/HPLPB20102208.1881.

[79] Itziar Tolosa et al. "Study of mechanical properties of AISI 316 stainless steel processed by "selective laser melting", following different manufacturing strategies". In: *Int. J. Adv. Manuf. Technol.* 51.5-8 (Nov. 2010), pp. 639–647. ISSN: 0268-3768. DOI: 10.1007/s00170-010-2631-5.

[80] Baicheng Zhang, Lucas Dembinski, and Christian Coddet. "The study of the laser parameters and environment variables effect on mechanical properties of high compact parts elaborated by selective laser melting 316L powder". In: *Mater. Sci. Eng. A* 584 (Nov. 2013), pp. 21–31. ISSN: 09215093. DOI: 10.1016/j.msea.2013.06.055.

[81] Chandrika Kamath et al. "Density of additively-manufactured, 316L SS parts using laser powder-bed fusion at powers up to 400 W". In: *Int. J. Adv. Manuf.*

Technol. 74.1-4 (Sept. 2014), pp. 65–78. ISSN: 0268-3768. DOI: 10.1007/s00170-014-5954-9.

[82] K. Saeidi et al. "Hardened austenite steel with columnar sub-grain structure formed by laser melting". In: *Mater. Sci. Eng. A* 625 (Feb. 2015), pp. 221–229. ISSN: 09215093. DOI: 10.1016/j.msea.2014.12.018.

[83] Zhongji Sun et al. "Selective laser melting of stainless steel 316L with low porosity and high build rates". In: *Mater. Des.* 104 (Aug. 2016), pp. 197–204. ISSN: 02641275. DOI: 10.1016/j.matdes.2016.05.035.

[84] Arne Röttger et al. "Comparison of microstructure and mechanical properties of 316 L austenitic steel processed by selective laser melting with hot-isostatic pressed and cast material". In: *Mater. Sci. Eng. A* 678.October (Dec. 2016), pp. 365–376. ISSN: 09215093. DOI: 10.1016/j.msea.2016.10.012.

[85] Jason R. Trelewicz et al. "Microstructure and Corrosion Resistance of Laser Additively Manufactured 316L Stainless Steel". In: *JOM* 68.3 (Mar. 2016), pp. 850–859. ISSN: 1047-4838. DOI: 10.1007/s11837-016-1822-4.

[86] Y. Morris Wang et al. "Additively manufactured hierarchical stainless steels with high strength and ductility". In: *Nat. Mater.* 17.1 (Jan. 2018), pp. 63–71. ISSN: 1476-1122. DOI: 10.1038/nmat5021.

[87] Kai Zhang et al. "Characterization of stainless steel parts by Laser Metal Deposition Shaping". In: *Mater. Des.* 55 (Mar. 2014), pp. 104–119. ISSN: 02613069. DOI: 10.1016/j.matdes.2013.09.006.

[88] Chengcheng Wang et al. "Process parameter optimization and mechanical properties for additively manufactured stainless steel 316L parts by selective electron beam melting". In: *Mater. Des.* 147 (June 2018), pp. 157–166. ISSN: 02641275. DOI: 10.1016/j.matdes.2018.03.035.

[89] Yuan Zhong et al. "Intragranular cellular segregation network structure strengthening 316L stainless steel prepared by selective laser melting". In: *J. Nucl. Mater.* 470 (Mar. 2016), pp. 170–178. ISSN: 00223115. DOI: 10.1016/j.jnucmat.2015.12.034.

[90] Haniyeh Fayazfar et al. "A critical review of powder-based additive manufacturing of ferrous alloys: Process parameters, microstructure and mechanical properties". In: *Mater. Des.* 144 (Apr. 2018), pp. 98–128. ISSN: 02641275. DOI: 10.1016/j.matdes.2018.02.018.

[91] Elton N. Kaufmann. *Characterization of Materials: Volume 1*. Ed. by Elton N. Kaufmann. Hoboken, NJ, USA: John Wiley & Sons, Inc., Oct. 2003. ISBN: 0471266965. DOI: 10.1002/0471266965.

[92] William D. Callister and David G. Rethwisch. *Materials science and engineering : an introduction*. English. Ed. by Joseph P. Hayton and Kenneth Santor. 7th ed. New York: John Wiley & Sons, 2007. ISBN: 978-0-471-73696-7. URL: https://www.wiley.com/en-us/etextbooks-and-courseware/engineering/materials-science.

[93] Jean-Pierre Kruth et al. "Selective laser melting of iron-based powder". In: *J. Mater. Process. Technol.* 149.1-3 (June 2004), pp. 616–622. ISSN: 09240136. DOI: 10.1016/j.jmatprotec.2003.11.051.

[94] H. Khalid Rafi, Thomas L. Starr, and Brent E. Stucker. "A comparison of the tensile, fatigue, and fracture behavior of Ti–6Al–4V and 15-5 PH stainless steel parts made by selective laser melting". In: *Int. J. Adv. Manuf. Technol.*

69.5-8 (Nov. 2013), pp. 1299–1309. ISSN: 0268-3768. DOI: 10.1007/s00170-013-5106-7.

[95] Jingjing Yang et al. "Effect of crystallographic orientation on mechanical anisotropy of selective laser melted Ti-6Al-4V alloy". In: *Mater. Charact.* 127 (2017), pp. 137–145. ISSN: 10445803. DOI: 10.1016/j.matchar.2017.01.014.

[96] Hanchen Yu et al. "Comparison on mechanical anisotropies of selective laser melted Ti-6Al-4V alloy and 304 stainless steel". In: *Mater. Sci. Eng. A* 695.April (2017), pp. 92–100. ISSN: 09215093. DOI: 10.1016/j.msea.2017.04.031.

[97] Erhard Brandl et al. "Additive manufactured AlSi10Mg samples using Selective Laser Melting (SLM): Microstructure, high cycle fatigue, and fracture behavior". In: *Mater. Des.* 34 (Feb. 2012), pp. 159–169. ISSN: 02613069. DOI: 10.1016/j.matdes.2011.07.067.

[98] U. Tradowsky et al. "Selective laser melting of AlSi10Mg: Influence of post-processing on the microstructural and tensile properties development". In: *Mater. Des.* 105 (Sept. 2016), pp. 212–222. ISSN: 02641275. DOI: 10.1016/j.matdes.2016.05.066.

[99] Karolien Kempen et al. "Microstructure and mechanical properties of Selective Laser Melted 18Ni-300 steel". In: *Phys. Procedia* 12.PART 1 (2011), pp. 255–263. ISSN: 18753892. DOI: 10.1016/j.phpro.2011.03.033.

[100] Adriaan B. Spierings, Konrad Wegener, and G. Levy. "Designing material properties locally with additive manufacturing technology SLM". In: *23rd Annu. Int. Solid Free. Fabr. Symp. - An Addit. Manuf. Conf. SFF 2012*. Jan. 2012, pp. 447–455. DOI: 10.26153/tsw/15364.

[101] K.N. Amato et al. "Microstructures and mechanical behavior of Inconel 718 fabricated by selective laser melting". In: *Acta Mater.* 60.5 (Mar. 2012), pp. 2229–2239. ISSN: 13596454. DOI: 10.1016/j.actamat.2011.12.032.

[102] Ofer Tevet et al. "Measurement of the Anisotropic Dynamic Elastic Constants of Additive Manufactured and Wrought Ti6Al4V Alloys". In: *Materials (Basel).* 15.2 (Jan. 2022), p. 638. ISSN: 1996-1944. DOI: 10.3390/ma15020638.

[103] Lore Thijs et al. "Strong morphological and crystallographic texture and resulting yield strength anisotropy in selective laser melted tantalum". In: *Acta Mater.* 61.12 (July 2013), pp. 4657–4668. ISSN: 13596454. DOI: 10.1016/j.actamat.2013.04.036.

[104] Behzad Bahrami Babamiri et al. "Quantification of porosity and microstructure and their effect on quasi-static and dynamic behavior of additively manufactured Inconel 718". In: *Addit. Manuf.* 34.February (2020). ISSN: 22148604. DOI: 10.1016/j.addma.2020.101380.

[105] A. D. Brown et al. "Dynamic mechanical response of additive manufactured Ti-6Al-4V". In: *AIP Conf. Proc.* Vol. 1979. July. 2018, p. 070008. ISBN: 9780735416932. DOI: 10.1063/1.5044817.

[106] P. Ponnusamy et al. "High strain rate behaviour at high temperature of AlSi12 parts produced by selective laser melting". In: *IOP Conf. Ser. Mater. Sci. Eng.* 377.1 (June 2018), p. 012167. ISSN: 1757-8981. DOI: 10.1088/1757-899X/377/1/012167.

[107] O. L. Rodriguez et al. "Dynamic tensile behavior of electron beam additive manufactured Ti6Al4V". In: *Mater. Sci. Eng. A* 641 (2015), pp. 323–327. ISSN: 09215093. DOI: 10.1016/j.msea.2015.06.069.

[108] Refael Fadida, Amnon Shirizly, and Daniel Rittel. "Dynamic Tensile Response of Additively Manufactured Ti6Al4V With Embedded Spherical Pores". In: *J. Appl. Mech.* 85.4 (Apr. 2018), pp. 1–10. ISSN: 0021-8936. DOI: 10.1115/1.4039048.

[109] Bar Nurel et al. "Study on the dynamic properties of AM-SLM AlSi10Mg alloy using the Split Hopkinson Pressure Bar (SHPB) technique". In: *EPJ Web Conf.* Ed. by E. Buzaud et al. Vol. 183. EDP Sciences, Sept. 2018, p. 04005. ISBN: 9782759890538. DOI: 10.1051/epjconf/201818304005.

[110] D. R. Jones et al. "Spall fracture in additive manufactured Ti-6Al-4V". In: *J. Appl. Phys.* 120.13 (Oct. 2016), p. 135902. ISSN: 0021-8979. DOI: 10.1063/1.4963279.

[111] E. Zaretsky, A. Stern, and Nahum Frage. "Dynamic response of AlSi10Mg alloy fabricated by selective laser melting". In: *Mater. Sci. Eng. A* 688.February (Mar. 2017), pp. 364–370. ISSN: 09215093. DOI: 10.1016/j.msea.2017.02.004.

[112] D. R. Jones et al. "Spall fracture in additive manufactured tantalum". In: *J. Appl. Phys.* 124.22 (Dec. 2018), p. 225902. ISSN: 0021-8979. DOI: 10.1063/1.5063930.

[113] M. Laurençon et al. "Effects of additive manufacturing on the dynamic response of AlSi10Mg to laser shock loading". In: *Mater. Sci. Eng. A* 748.December 2018 (Mar. 2019), pp. 407–417. ISSN: 09215093. DOI: 10.1016/j.msea.2019.02.001.

[114] A. Charmi et al. "Mechanical anisotropy of additively manufactured stainless steel 316L: An experimental and numerical study". In: *Mater. Sci. Eng. A* 799.June 2020 (Jan. 2021), p. 140154. ISSN: 09215093. DOI: 10.1016/j.msea.2020.140154.

[115] Michał Zietala et al. "The microstructure, mechanical properties and corrosion resistance of 316L stainless steel fabricated using laser engineered net shaping". In: *Mater. Sci. Eng. A* 677 (Nov. 2016), pp. 1–10. ISSN: 09215093. DOI: 10.1016/j.msea.2016.09.028.

[116] Minh-Son Pham, Bogdan Dovgyy, and P.A. Hooper. "Twinning induced plasticity in austenitic stainless steel 316L made by additive manufacturing". In: *Mater. Sci. Eng. A* 704.July (Sept. 2017), pp. 102–111. ISSN: 09215093. DOI: 10.1016/j.msea.2017.07.082.

[117] Chola Elangeswaran et al. "Effect of post-treatments on the fatigue behaviour of 316L stainless steel manufactured by laser powder bed fusion". In: *Int. J. Fatigue* 123.February (June 2019), pp. 31–39. ISSN: 01421123. DOI: 10.1016/j.ijfatigue.2019.01.013.

[118] Holly D. Carlton et al. "Damage evolution and failure mechanisms in additively manufactured stainless steel". In: *Mater. Sci. Eng. A* 651 (Jan. 2016), pp. 406–414. ISSN: 09215093. DOI: 10.1016/j.msea.2015.10.073.

[119] Anne Mertens et al. "Microstructures and Mechanical Properties of Stainless Steel AISI 316L Processed by Selective Laser Melting". In: *Mater. Sci. Forum* 783-786.3 (May 2014), pp. 898–903. ISSN: 1662-9752. DOI: 10.4028/www.scientific.net/MSF.783-786.898.

[120] T. Niendorf et al. "Highly Anisotropic Steel Processed by Selective Laser Melting". In: *Metall. Mater. Trans. B* 44.4 (Aug. 2013), pp. 794–796. ISSN: 1073-5615. DOI: 10.1007/s11663-013-9875-z.

[121] Tomasz Kurzynowski et al. "Correlation between process parameters, microstructure and properties of 316 L stainless steel processed by selective laser melting". In: *Mater. Sci. Eng. A* 718.January (Mar. 2018), pp. 64–73. ISSN: 09215093. DOI: 10.1016/j.msea.2018.01.103.

[122] M. A. Bevan et al. "Mechanical Properties and Behavior of Additive Manufactured Stainless Steel 316L". In: *Miner. Met. Mater. Ser.* Vol. Part F7. February. 2017, pp. 577–583. ISBN: 9783319513812. DOI: 10.1007/978-3-319-51382-9_63.

[123] Patrick R. Carlson et al. "Mechanical behaviour and high strain rate deformation of stainless steel 316L processed by selective laser melting". In: *Int. J. Rapid Manuf.* 9.1 (2020), p. 84. ISSN: 1757-8817. DOI: 10.1504/IJRAPIDM.2020.10026158.

[124] Jie Chen et al. "Dynamic mechanical properties of 316L stainless steel fabricated by an additive manufacturing process". In: *J. Mater. Res. Technol.* 11 (2021), pp. 170–179. ISSN: 22387854. DOI: 10.1016/j.jmrt.2020.12.097.

[125] G.T. Gray III et al. "Structure/property (constitutive and dynamic strength/damage) characterization of additively manufactured 316L SS". In: *EPJ Web Conf.* 94 (Sept. 2015). Ed. by E. Cadoni, p. 02006. ISSN: 2100-014X. DOI: 10.1051/epjconf/20159402006.

[126] S. Tsopanos et al. "The Influence of Processing Parameters on the Mechanical Properties of Selectively Laser Melted Stainless Steel Microlattice Structures". In: *J. Manuf. Sci. Eng.* 132.4 (Aug. 2010), pp. 0410111–04101112. ISSN: 1087-1357. DOI: 10.1115/1.4001743.

[127] B. Gorny et al. "In situ characterization of the deformation and failure behavior of non-stochastic porous structures processed by selective laser melting". In: *Mater. Sci. Eng. A* 528.27 (Oct. 2011), pp. 7962–7967. ISSN: 09215093. DOI: 10.1016/j.msea.2011.07.026.

[128] F. Brenne, T. Niendorf, and H.J. Maier. "Additively manufactured cellular structures: Impact of microstructure and local strains on the monotonic and cyclic behavior under uniaxial and bending load". In: *J. Mater. Process. Technol.* 213.9 (Sept. 2013), pp. 1558–1564. ISSN: 09240136. DOI: 10.1016/j.jmatprotec.2013.03.013.

[129] Martin Jäcklein et al. "Dynamic compression of 3D printed metallic mesostructures with in-situ X-ray imaging". In: *Proc. ISIE 2019 10th Int. Symp. Impact Eng.* Gmunden: Trauner Verlag, 2019.

[130] Jean-Pierre Kruth et al. "Consolidation phenomena in laser and powder-bed based layered manufacturing". In: *CIRP Ann.* 56.2 (2007), pp. 730–759. ISSN: 00078506. DOI: 10.1016/j.cirp.2007.10.004.

[131] Dirk Herzog et al. "Additive manufacturing of metals". In: *Acta Mater.* 117 (Sept. 2016), pp. 371–392. ISSN: 13596454. DOI: 10.1016/j.actamat.2016.07.019.

[132] Todd M. Mower and Michael J. Long. "Mechanical behavior of additive manufactured, powder-bed laser-fused materials". In: *Mater. Sci. Eng. A* 651 (Jan. 2016), pp. 198–213. ISSN: 09215093. DOI: 10.1016/j.msea.2015.10.068.

[133] J.P. Oliveira, A.D. LaLonde, and J. Ma. "Processing parameters in laser powder bed fusion metal additive manufacturing". In: *Mater. Des.* 193 (Aug. 2020), p. 108762. ISSN: 02641275. DOI: 10.1016/j.matdes.2020.108762.

[134] G. Asala, J. Andersson, and O. A. Ojo. "Improved dynamic impact behaviour of wire-arc additive manufactured ATI 718Plus®". In: *Mater. Sci. Eng. A* 738.May (Dec. 2018), pp. 111–124. ISSN: 09215093. DOI: 10.1016/j.msea.2018.09.079.

[135] G. Asala, J. Andersson, and O. A. Ojo. "Analysis and constitutive modelling of high strain rate deformation behaviour of wire–arc additive-manufactured ATI 718Plus superalloy". In: *Int. J. Adv. Manuf. Technol.* 103.1-4 (July 2019), pp. 1419–1431. ISSN: 0268-3768. DOI: 10.1007/s00170-019-03616-2.

[136] C.M Sellars and W.J. McTegart. "On the mechanism of hot deformation". In: *Acta Metall.* 14.9 (Sept. 1966), pp. 1136–1138. ISSN: 00016160. DOI: 10.1016/0001-6160(66)90207-0.

[137] Y.C. Lin, Xiao-Min Chen, and Ge Liu. "A modified Johnson–Cook model for tensile behaviors of typical high-strength alloy steel". In: *Mater. Sci. Eng. A* 527.26 (Oct. 2010), pp. 6980–6986. ISSN: 09215093. DOI: 10.1016/j.msea.2010.07.061.

[138] Yanhua Zhao et al. "A comparative study on Johnson-Cook and modified Johnson-Cook constitutive material model to predict the dynamic behavior laser additive manufacturing FeCr alloy". In: *J. Alloys Compd.* 723 (Nov. 2017), pp. 179–187. ISSN: 09258388. DOI: 10.1016/j.jallcom.2017.06.251.

[139] Arman Ahmadi et al. "Finite Element Modeling of Selective Laser Melting 316L Stainless Steel Parts for Evaluating the Mechanical Properties". In: *Vol. 2 Mater. Biomanufacturing; Prop. Appl. Syst. Sustain. Manuf.* American Society of Mechanical Engineers, June 2016, pp. 1–5. ISBN: 978-0-7918-4990-3. DOI: 10.1115/MSEC2016-8594.

[140] T. Wang et al. "Grain morphology evolution behavior of titanium alloy components during laser melting deposition additive manufacturing". In: *J. Alloys Compd.* 632 (May 2015), pp. 505–513. ISSN: 09258388. DOI: 10.1016/j.jallcom.2015.01.256.

[141] Benjamin Thomas Spencer Cousins. "Development of Improved Numerical Techniques for High Strain Rate Deformation Behaviour of Titanium Alloys". PhD thesis. 2016.

[142] Oana Cazacu and Frédéric Barlat. "A criterion for description of anisotropy and yield differential effects in pressure-insensitive metals". In: *Int. J. Plast.* 20.11 (Nov. 2004), pp. 2027–2045. ISSN: 07496419. DOI: 10.1016/j.ijplas.2003.11.021.

[143] Douglas J. Bammann et al. *On the formulation, parameter identification and numerical integration of the EMMI model :plasticity and isotropic damage.* Tech. rep. Report No. SAND2006-0200. Albuquerque, NM, and Livermore, CA (United States): Sandia National Laboratories (SNL), Jan. 2006. DOI: 10.2172/883488.

[144] Douglas J. Bammann. "An internal variable model of viscoplasticity". In: *Int. J. Eng. Sci.* 22.8-10 (1984), pp. 1041–1053. ISSN: 00207225. DOI: 10.1016/0020-7225(84)90105-8.

[145] Livermore Software Technology Corporation (LSTC). *LS-DYNA Keyword User's Manual*. R12 Vol. 2. Livermore Software Technology Corporation, 2020. URL: https://www.lstc.com/download/manuals.

[146] R. Hill. "A theory of the yielding and plastic flow of anisotropic metals". In: *Proc. R. Soc. London. Ser. A. Math. Phys. Sci.* 193.1033 (May 1948), pp. 281–297. ISSN: 0080-4630. DOI: 10.1098/rspa.1948.0045.

[147] Michael A. Slawinski. *Waves and Rays in Elastic Continua*. WORLD SCIENTIFIC, Sept. 2010, pp. 1–583. ISBN: 978-981-4289-00-9. DOI: 10.1142/7486.

[148] John Frederick Nye. *Physical properties of crystals: their representation by tensors and matrices*. Oxford university press, 1985. ISBN: 9780198511656. URL: https://global.oup.com/academic/product/physical-properties-of-crystals-9780198511656?cc=gb%7B%5C&%7Dlang=en%7B%5C&%7D.

[149] R v. Mises. "Mechanik der festen Körper im plastisch- deformablen Zustand." In: *Nachrichten von der K. Gesellschaft der Wissenschaften.* 1 (1913), pp. 582–592. URL: http://gdz.sub.uni-goettingen.de/dms/resolveppn/?PPN=GDZPPN002503697.

[150] Heinrich Hencky. "Zur Theorie plastischer Deformationen und der hierdurch im Material hervorgerufenen Nachspannungen". In: *ZAMM - Zeitschrift für Angew. Math. und Mech.* 4.4 (Jan. 1924), pp. 323–334. ISSN: 00442267. DOI: 10.1002/zamm.19240040405.

[151] R. Hill. "Theoretical plasticity of textured aggregates". In: *Math. Proc. Cambridge Philos. Soc.* 85.1 (Jan. 1979), pp. 179–191. ISSN: 0305-0041. DOI: 10.1017/S0305004100055596.

[152] R. Hill. *The Mathematical theory of plasticity*. 11th ed. Oxford: Oxford University Press, 1998. ISBN: 9780198503675. URL: https://global.oup.com/academic/product/the-mathematical-theory-of-plasticity-9780198503675.

[153] Prasad Dasappa, Kaan Inal, and Raja Mishra. "The effects of anisotropic yield functions and their material parameters on prediction of forming limit diagrams". In: *Int. J. Solids Struct.* 49.25 (2012), pp. 3528–3550. ISSN: 00207683. DOI: 10.1016/j.ijsolstr.2012.04.021.

[154] G.R. Johnson and W.H. Cook. "A constitutive model and data for metals subjected to large strains, high strain rates and high temperatures." In: *Proc. 7th Int. Symp. Ballist.* The Hague The Netherlands, 1983, pp. 541–547.

[155] G.R. Johnson and W.H. Cook. "Fracture characteristics of three metals subjected to various strains, strain rates, temperatures and pressures". In: *Eng. Fract. Mech.* 21.1 (Jan. 1985), pp. 31–48. ISSN: 00137944. DOI: 10.1016/0013-7944(85)90052-9.

[156] E Orowan. "Problems of plastic gliding". In: *Proc. Phys. Soc.* 52.1 (Jan. 1940), pp. 8–22. ISSN: 0959-5309. DOI: 10.1088/0959-5309/52/1/303.

[157] Jean-Paul Poirier. *Creep of Crystals*. Cambridge University Press, Feb. 1985. ISBN: 9780521261777. DOI: 10.1017/CBO9780511564451.

[158] Daniele Versino and Kane C. Bennett. "Generalized radial-return mapping algorithm for anisotropic von Mises plasticity framed in material eigenspace". In: *Int. J. Numer. Methods Eng.* 116.3 (2018), pp. 202–222. ISSN: 10970207. DOI: 10.1002/nme.5921.

[159] J.C. Simo and R. L. Taylor. "A return mapping algorithm for plane stress elastoplasticity". In: *Int. J. Numer. Methods Eng.* 22.3 (1986), pp. 649–670. ISSN: 10970207. DOI: 10.1002/nme.1620220310.

[160] J.C. Simo. "A framework for finite strain elastoplasticity based on maximum plastic dissipation and the multiplicative decomposition. Part II: Computational aspects". In: *Comput. Methods Appl. Mech. Eng.* 68.1 (May 1988), pp. 1–31. ISSN: 00457825. DOI: 10.1016/0045-7825(88)90104-1.

[161] V.A. Lubarda. "Mechanics of Materials: Plasticity". In: *Ref. Modul. Mater. Sci. Mater. Eng.* March 2015. Elsevier, 2016. ISBN: 9780128035818. DOI: 10.1016/B978-0-12-803581-8.02841-1.

[162] William John Macquorn Rankine. "XV. On the thermodynamic theory of waves of finite longitudinal disturbance". In: *Philos. Trans. R. Soc. London* 160 (Jan. 1870), pp. 277–288. ISSN: 0261-0523. DOI: 10.1098/rstl.1870.0015.

[163] H Hugoniot. "Mémoire sur la propagation du mouvement dans un fluide indéfini (seconde Partie)". In: *J. Math. Pures Appl.* 4 (1888), pp. 153–168. URL: https://eudml.org/doc/233955.

[164] Jerry W Forbes. *Shock Wave Compression of Condensed Matter*. Berlin, Heidelberg: Springer Berlin Heidelberg, 2012. ISBN: 978-3-642-32534-2. DOI: 10.1007/978-3-642-32535-9.

[165] S A Novikov and A G Ivanov. "Failure of steel, aluminium and copper under explosive shock loading". In: *Fiz. Met. i Metalloved.* 21.4 (1966), pp. 608–615.

[166] G. V. Stepanov. "Spalling produced by elastoplastic waves in metals". In: *Strength Mater.* 8.8 (Aug. 1976), pp. 942–947. ISSN: 0039-2316. DOI: 10.1007/BF01529805.

Part II

Experimental Methods & Results

In order to interrogate the dynamic responses of additively manufactured material experimental work must be undertaken. This section details the construction of assemblies to record this data, the data itself and analyses, and discussion of the analysed results in the context of the current literature.

Chapter 5

Manufacturing & Characterisation

5.1 Manufacture

Additively manufactured samples were produced in two distinct batches using a Renishaw AM250 SLM printer and commercially available 316L steel powder. Print parameters were defined by a set of 5 quantities: the laser power, layer thickness, hatch spacing, point distance, and exposure time. This set of parameters varies slightly from other common laser based powder bed devices, with the norm to define a scanning speed in place of the ratio between point distance and exposure time such that,

$$v_{Scan} = \frac{d_{Point}}{t_{Exposure}}, \tag{5.1}$$

where v_{Scan} represents the scanning speed, $t_{Exposure}$ the exposure time, and d_{Point} the point distance. This substitution is required as the Renishaw AM250 uses a pulsed laser source, contrasting the majority of SLM printers that employ continuous wave lasers. To obtain an energy density we must start from the widely used continuous wave form, then modifying to include the point distance and exposure time such that:

$$E = \frac{P}{v_{Scan}\, h_{Layer}\, s_{Hatch}} = \frac{P\, t_{Exposure}}{d_{Point}\, h_{Layer}\, s_{Hatch}}, \tag{5.2}$$

where E represents energy density, P the laser power, h_{Layer} the layer height, and s_{Hatch} the hatch spacing. With these parameters as defined above, the parameter set used for each of the two print batches are given in table 5.1, with an effective scanning velocity calculated from the ratio of point distance to exposure time as defined in equation 5.1.

As can be seen in table 5.1 almost identical parameter sets were used for each print batch, with the drastic difference in resultant defect distributions, quantified

	1st Print Batch	2nd Print Batch
Powder size	$(10-45)\,\mu m$	$(15-45)\,\mu m$
Laser power	200 W	195 W
Spot size	$65\,\mu m$	$65\,\mu m$
Exposure time	$80\,\mu s$	$80\,\mu s$
Point distance	$60\,\mu m$	$60\,\mu m$
Scanning velocity	$750\,mm\,s^{-1}$	$750\,mm\,s^{-1}$
Hatch spacing	$110\,\mu m$	$110\,\mu m$
Layer height	$50\,\mu m$	$50\,\mu m$

Table 5.1: Powder and print parameters used for each print run.

in sections 5.2 and 5.3 stemming from the build volume geometry. As shown by Williams *et al.* [167], variation in *inter-layer cooling time*, can drastically alter the thermal environment of the powder bed during manufacture, affecting the resultant bulk material.

Within the initial print batch a singular densely packed build was used, increasing the inter-layer cooling time and therefore increasing the susceptibility of the produced component to lack-of-fusion type defects. For the first batch, the build volume following printing is not shown as components were supplied following removal from the build plate. In the second print batch components were printed across two separate build volumes and in isolation from any printed parts separate to this research. The pair of comparatively sparsely packed build plates can be seen in figure 5.1 following manufacture. By reducing the amount of material in each layer the inter-layer cooling time was simultaneously decreased, therefore ensuring the thermal environment remained at a higher temperature, in turn reducing susceptibility to lack-of-fusion defects. Of note is that whilst other modes of defect formation are possible, here the relatively low energy density used, when compared to results from Cherry *et al.* [26], predisposed printed components to lack-of-fusion defects above all other sources of porosity.

Following printing of each batch of material, parts were removed from the build plate using electrodischarge wire machining. Following this, the subtractive manufacture of specimens was carried out, negating surface layer effects upon the recorded

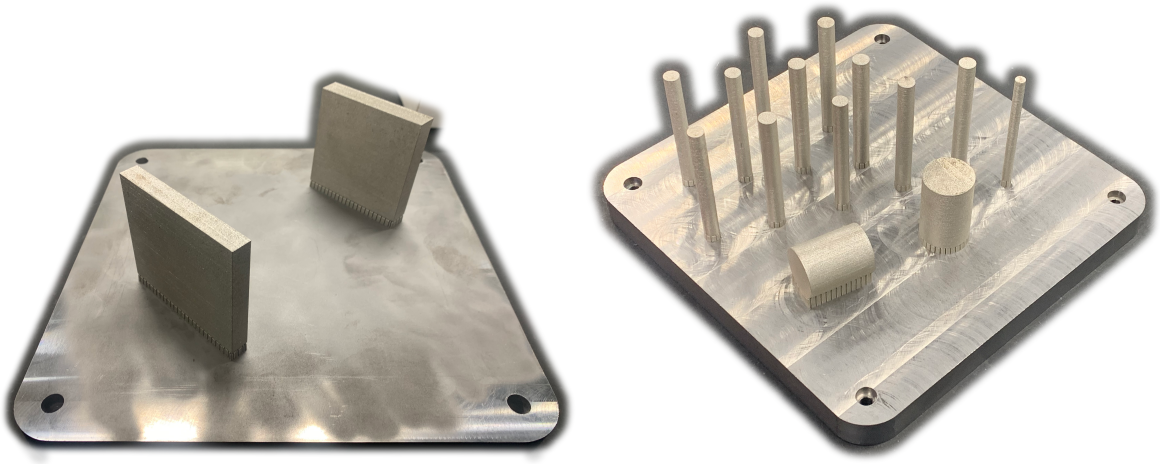

(a) Horizontal Samples (b) Vertical Samples

Figure 5.1: Build plates following manufacture in the 2nd print batch. Noted here is that while figure 5.1b contains primarily vertical samples, a horizontally printed cylinder is shown in the foreground. This division of parts between build plates was undertaken to minimise disparities in the inter-layer cooling time throughout the second batch of printed material.

material responses.

In the first batch of printed material, not shown in figure 5.1, all samples were produced in cylindrical form. The resultant parts closely resembled those shown in figure 5.1b albeit with additionally horizontally oriented cylinders and components produced simultaneously that were not used in this study. From here, as-built cylindrical samples in each orientation were machined via lathe to provide samples representative of bulk additively manufactured material.

In the second print batch, horizontal samples, seen in figure 5.1a, were printed as cuboids. These were then cut, again with electrodischarge wire, into intermediary cylinders prior to being turned on a lathe to reach their final geometry. Vertically oriented samples in the second batch were machined similarly to the first print batch, again using a lathe to directly machine the samples from the printed pieces. The end result of this machining were two groups of cylindrical samples, effectively consistent in geometry and surface finish but with variations in both orientation and thermal histories.

Alongside these samples corresponding conventionally manufactured equivalents

were produced from commercial 316L stainless steel bar stock. The bar stock was manufactured via hot rolling, with solution annealing then undertaken at 1060 °C for 4 h preceding a water quench. The material was then turned to the requested 1 in. diameter and polished prior to delivery, with the as-received bar then undergoing further subtractive machining via both electrodischarge wire and lathe to produce samples indistinguishable from equivalent additive specimens in both geometry and surface finish.

5.2 Microscopy

Microscopy offers a convenient method for characterising microstructure across a two dimensional plane of a sample, at a range of scales from mm to µm using optical and electron based techniques. Initial attempts to quantify porosity in AM specimens relied on visible light optical microscopy, allowing fast analysis of porosity across a limited sample size. These attempts are detailed below, focusing on a comparison in porosity between the first batch of AM 316L stainless steel and CM equivalents.

The preparation of additive samples for microscopy involved first splitting vertically and horizontally oriented cylinders of as built material into individual smaller cylinders, as shown for the vertical case in figure 5.2. From here both additively manufactured samples and conventional equivalents were mounted inside conductive resin pucks exposing their upper circular face. The samples were then ground using progressively smaller sized abrasives; achieving a highly planar surface suitable for both visible light and scanning electron microscopy techniques including electron back scatter diffraction.

Optical micrographs were recorded for samples, with each individual micrograph sampling a small area of a polished cross-section before being stitched together using post-processing methods within the ImageJ software package. From here composite micrographs, as displayed in figure 5.3a, were imported into MATLAB with the circular region of interest isolated from the surrounding mounting material. The intensity distribution of this circular region was then sampled and approximated using two

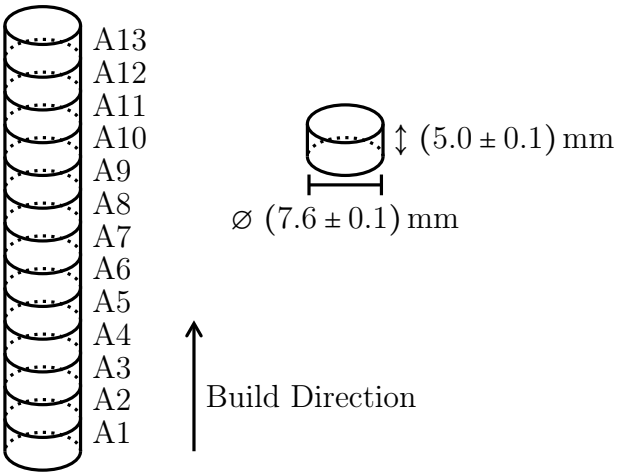

Figure 5.2: Positioning and orientation of additively manufactured microscopy specimens. Approximate dimensions are provided for samples as mounted into larger conductive pucks.

independent gaussian profiles, the first to represent a population of bulk material, and second a population of pores, resulting in binarised images as seen in figure 5.3b.

Quantifying the composite images, measured porosity fractions from vertically oriented additive samples A1, A3, A5, through A13, themselves from various heights within the build volume as seen in figure 5.2, are presented with comparison to CM material in figure 5.4. Porosity fractions measured within all AM samples, both horizontally and vertically oriented, were found to exceed the reference CM sample in all cases, however no obvious trend in porosity levels between AM samples was observed, nor any indication of a specific spatial distribution of voids.

To look further at AM and CM sample pore populations, individual and composite micrographs of both materials are shown in figure 5.5. Here, looking at pores morphology in AM samples in figure 5.5b the irregular shapes shown are clear examples of lack-of-fusion porosity [69] whilst the absence of thin cracks within any of the AM micrographs suggest a lack of thermal cracking [83] during solidification and further cooling. However, as these micrographs are all recorded in the same orientation, such cracking could have occurred out of plane. Considering the conventionally manufactured material in figure 5.5a, such irregular lack-of-fusion pores are not seen, with this expected given the fundamentally different manufacture route. Instead, roughly

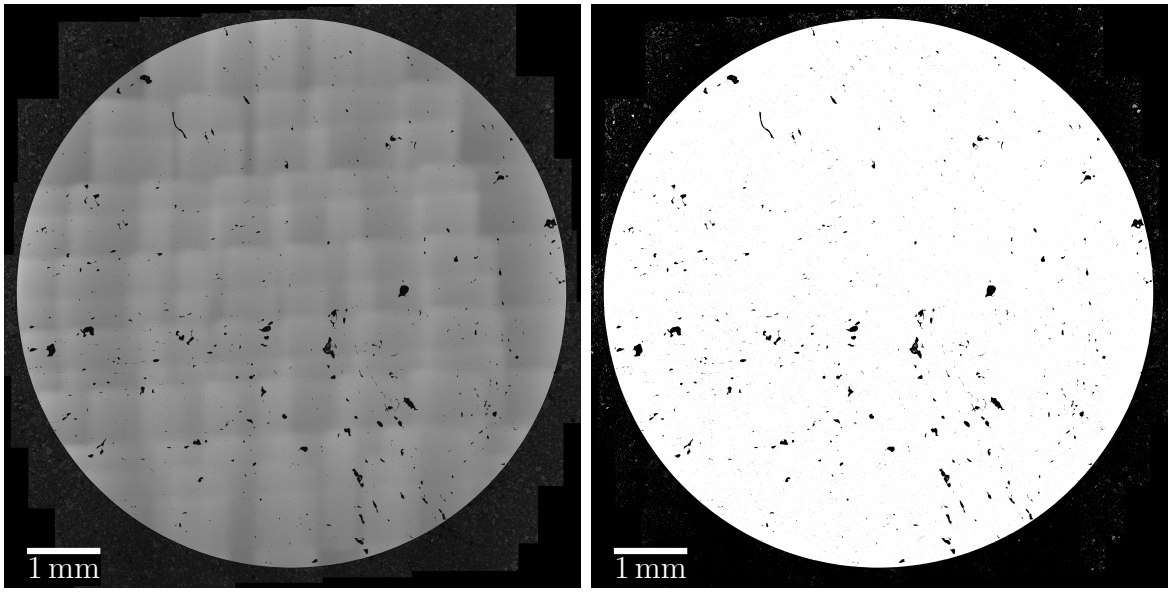

(a) Raw composite image. (b) Binary image.

Figure 5.3: Processing of optical micrographs.

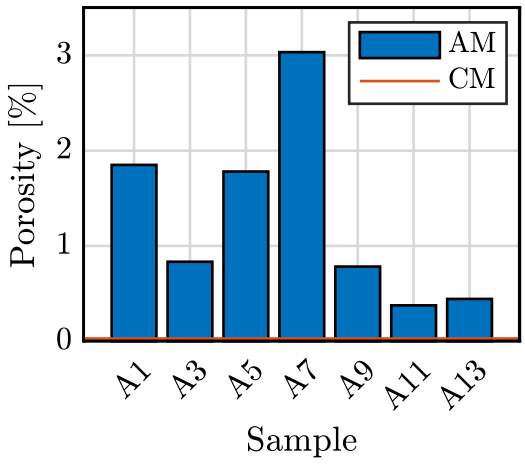

Figure 5.4: Porosity levels for each AM sample, seen with an overall porosity of (1.30 ± 0.97) % given as one standard deviation, with a comparison to CM reference, itself with a measured porosity of 0.03 %.

spherical pores are seen, with the source of this minor porosity fraction undetermined.

In summarising this microscopy, it is clear that a significantly elevated degree of porosity is present within the first batch of additively manufactured samples when compared to conventional equivalents. This porosity undoubtedly is formed by lack-of-fusion during manufacture, likely attributable to the combination of insufficient energy density and prolonged inter-layer cooling times. Furthermore, the porosity observed in additively manufactured samples display no clear spatial distribution, albeit with only a limited spatial sampling frequency throughout the material.

5.3 Tomography

As concluded previously, considering the optical micrographs of both the initial batch of additive and comparative conventional samples, it was clear the level of porosity within the additive material was fundamentally different to that existing in conventional samples. A drastically increased level of porosity was found in the initial batch of additive samples with this additive porosity showing the characteristic irregular profile associated to lack-of-fusion mode formation [86, 168]. Whilst optical microscopy reveals the presence of raised levels of porosity in additive samples, even using several sectioned scans it is limited in the ability to identify potential spatial distributions of the observed porosity, to this end micro computerised tomography (**µCT**) [169] offered a solution. The use of µCT to investigate porosity distributions prior to, after, and even during testing is well documented within literature [118, 170]. Studies have demonstrated that not only are the volumetric distribution of pores and overall fraction calculable, but also the pore characteristics. The latter is achievable providing the measurement carried out presents a sufficient signal to noise ratio to clearly differentiate pores, and a sufficient resolution to avoid undersampling the pore structure.

Here, the results of µCT scans of cylindrical samples from both batches of additively manufactured 316L stainless steel samples are presented. These scans were undertaken

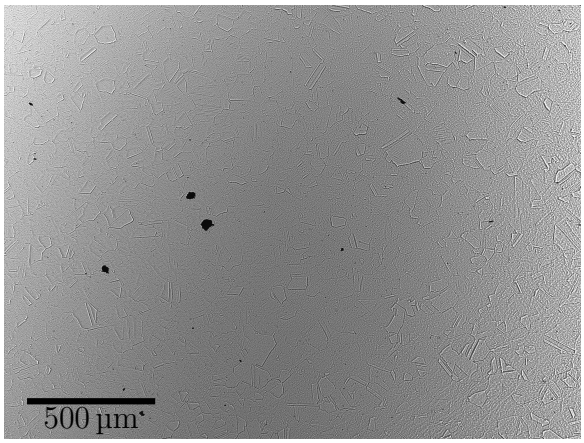

(a) CM sample single image.

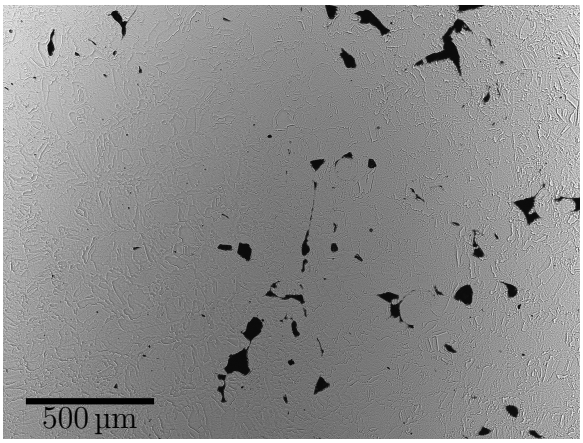

(b) AM sample single image.

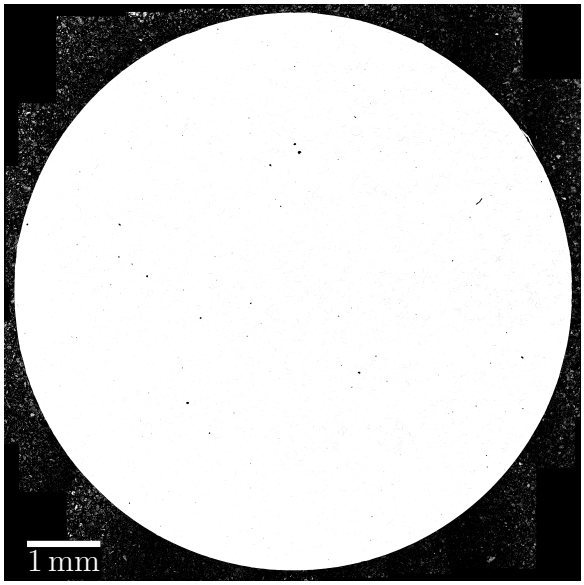

(c) CM composite image.

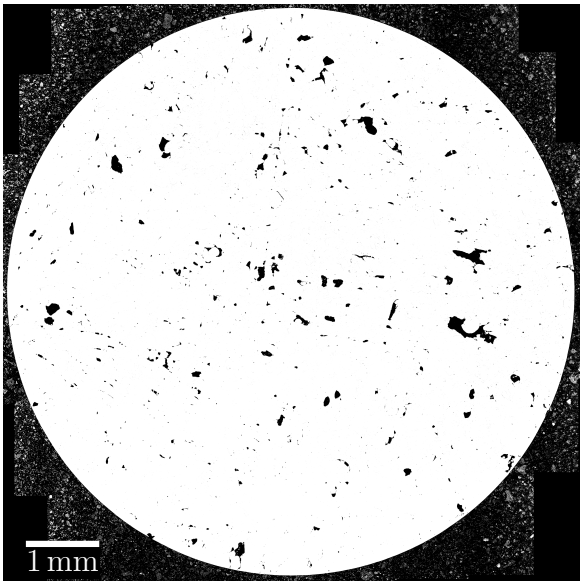

(d) AM composite image.

Figure 5.5: Optical micrographs of CM and AM 316L samples.

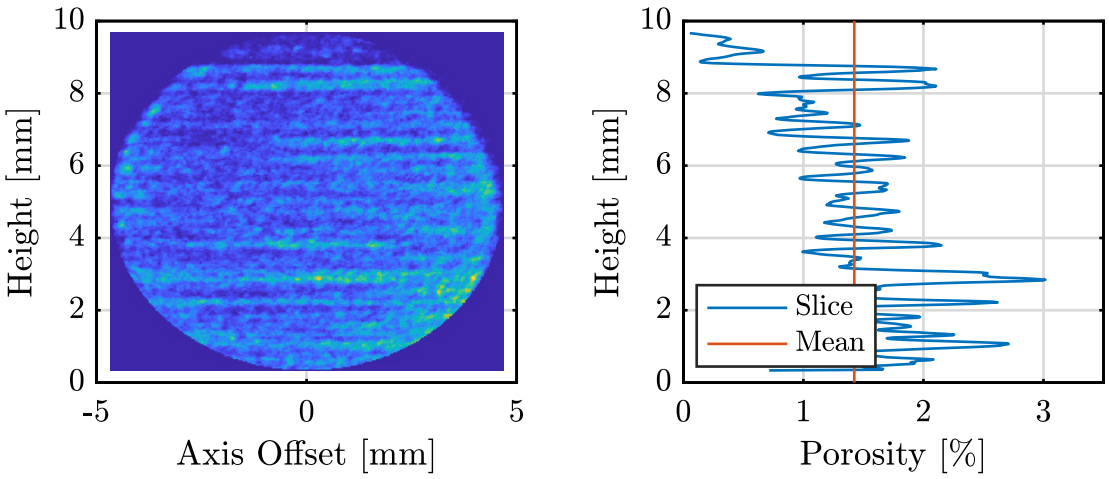

(a) Porosity heatmap.

(b) Porosity profile.

Figure 5.6: Horizontally layered porosity distributions existing within horizontally oriented samples in the initial batch of additively manufactured 316L stainless steel.

within the materials characterisation group at AWE Plc., with data provided in the form of large batches (several thousand) of cross-sectional images sequentially progressing through the samples along the axis of symmetry. Each image is interpreted as containing the information from a layer of voxels within the overall scanned volume.

Using each data set, flat-field corrections were applied to equalise the intensity of bulk material, assuming the bulk intensity profile remained consistent across small spreads of layers normal to the sample axis. From these homogenised scans of density, one of two methods was used to identify porosity within the volume.

Firstly, where a significant population of voids were observed, a whole sample binary threshold was computed via Otsu's method [171] with this minimising the intraclass variance of a two population classification of the density values. With this threshold, a binary volume was created with zeros representing the lighter (bulk) population of voxels and ones representing the darker (void) population of voxels. This scenario was found in scans of the initial batch of printed material, with the recorded distributions presented in figures 5.6 and 5.7.

Where a far smaller population of voids were present, as observed in scans of the second batch of printed material, an alternate method was necessary. Here the porosity was identified through location of outlier voxels, themselves identified from

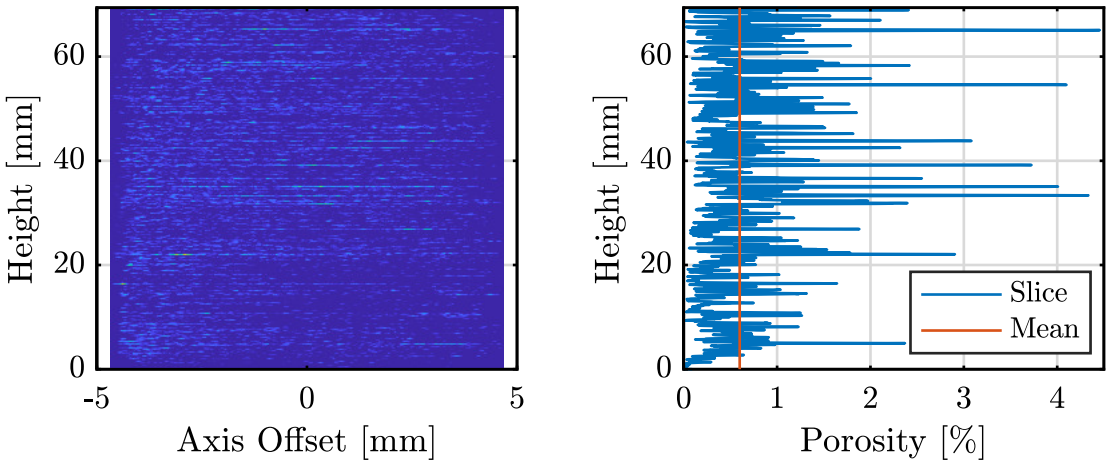

(a) Porosity heatmap.

(b) Porosity profile.

Figure 5.7: Horizontally layered porosity distributions existing within vertically oriented samples in the initial batch of additively manufactured 316L stainless steel.

a localised median absolute deviation sampled along the z-axis, that also displayed lower than average characteristic intensity. This secondary method was employed as use of the first routine created a significant number of false positives, attributable to significant variance in the characteristic density (the intensity of the imported image pixel, and therefore three-dimensional voxel) of clearly solid material. Given a comparatively small population of void voxels, the evaluation of a global threshold was dominated by the intra-population variance in the bulk solid, remaining insensitive to the inter-population variance between the pores and the bulk solid. Using this alternate algorithm, the resulting distributions are presented in figures 5.8 and 5.9.

From figures 5.6–5.9 the difference in prevalence in porosity is stark. Initial print samples contain porosity fractions approximately two orders of magnitude above print samples from the latter print batch, with these disparities quantified in table 5.2. Despite the marked difference in porosity fraction identified in table 5.2, a similarity is seen in the recorded data between the two batches of additively manufactured material. This similarity is found in the spatial distribution of the porosity, where structured horizontally layered distributions of voids are found in all scanned AM samples. Given the layer-wise manufacturing process such a distribution is undoubtedly linked to the inter-layer bonding within the material bulk. Whilst the same lack-of-fusion voids

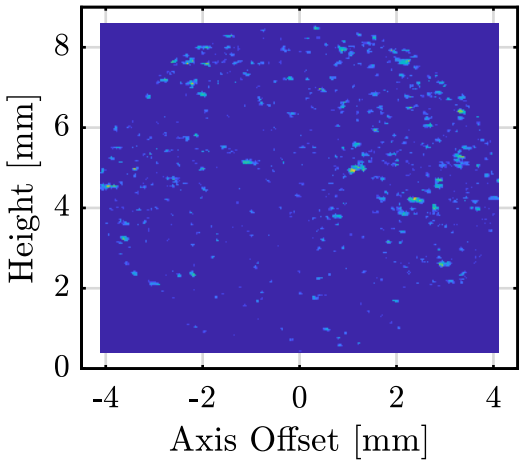

(a) Porosity heatmap.

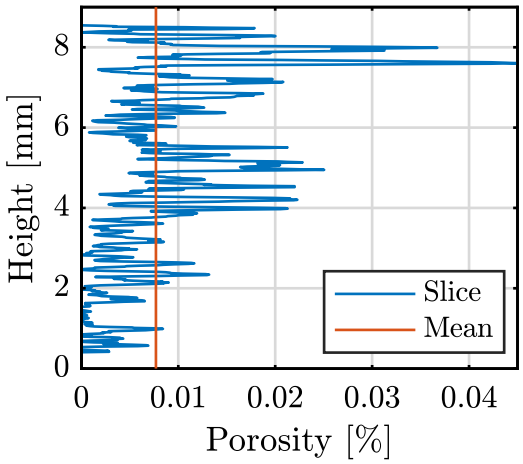

(b) Porosity profile.

Figure 5.8: Negligible horizontally layered porosity distributions existing within horizontally oriented samples in the latter batch of additively manufactured 316L stainless steel.

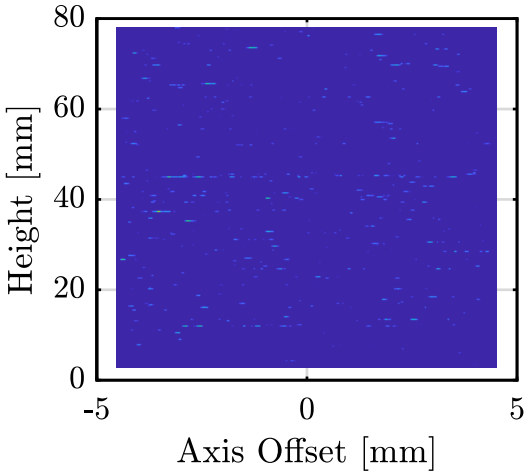

(a) Porosity heatmap.

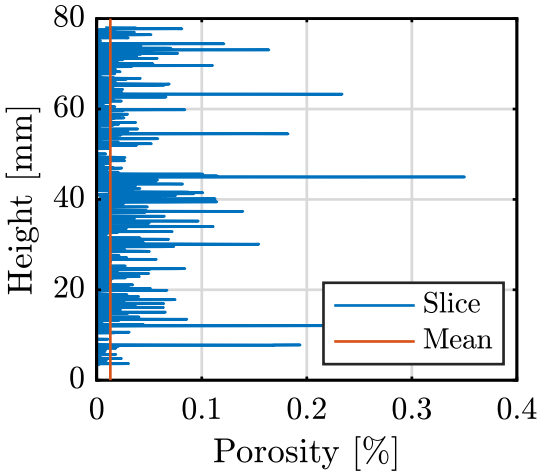

(b) Porosity profile.

Figure 5.9: Negligible horizontally layered porosity distributions existing within vertically oriented samples in the latter batch of additively manufactured 316L stainless steel.

	Microscopy Porosity Fraction [%]	Tomography Porosity Fraction [%]
1st Horizontal		1.445
1st Vertical	1.300	0.594
2nd Horizontal		0.008
2nd Vertical		0.013
Conventional	0.028	

Table 5.2: Average porosity fractions quantified from both microscopy and tomography techniques in both batches of additively manufactured material and conventional equivalents.

(with large volumes and irregular morphology) are not seen in the second batch of material, the steep thermospatial gradients and competitive epitaxial growth may still induce the formation of porosity on a smaller scale through other processes.

Chapter 6

Photon Doppler Velocimetry

First implemented in 2005 [172, 173] and now widely used throughout scientific fields investigating dynamic material behaviour [174, 175], Photon Doppler Velocimetry (**PDV**) facilitates measuring surface motion with a temporal resolution below 1 µs. The diagnostic adapts earlier free space interferometry techniques [176], based upon fundamental interference principles [177] to calculate the frequency of light collected from a moving surface. PDV itself uses a derived beat frequency produced from the superposition of the reflected light with a second frequency assumed to be static throughout the duration of the measurement. Below a brief explanation of this diagnostic is offered, covering two common subtly different implementations of the technique that were both employed during the research presented in this thesis. Following the introduction to the underpinning theory and experimental setup of PDV, a novel data cleansing technique theorised and implemented within these studies to improve the robustness of signal analyses is detailed.

6.1 Superposition & The Doppler Effect

Following from the overview, it is possible to consider an individual source of coherent monochromatic light with an associated time varying electric field, $\mathrm{E_i}(\mathrm{t})$, given by,

$$\mathrm{E_i}(\mathrm{t}) = \mathrm{E_{i0}} \cos\left(\omega_\mathrm{i} \mathrm{t} + \phi_\mathrm{i}\right),$$

where $\mathrm{E_{i0}}$ represents the peak amplitude of the electric field, ω the radial frequency, and ϕ an arbitrary static phase offset at a given location and time.

Were this light source split and propagated along two distinct optical paths prior to being recombined, the resultant electric field after recombination would be given by

[177–179]:

$$E(t) = E_1 \cos(\Phi_1) + E_2 \cos(\Phi_2),$$

where Φ_i represents the optical phase incurred along respective paths. The resultant superposition would contain an oscillatory electric field with the original frequency and a cycle averaged intensity, $I(t)$, of,

$$I(t) = I_0 + I_1 + 2\sqrt{I_0 I_1}\cos(\Phi_\delta). \tag{6.1}$$

Here Φ_δ is the relative phase shift incurred between light traversing alternate optical paths, with I_i the cycle averaged intensity of each light source prior to recombination. By enforcing that one optical path remains of constant length, and that the second path includes a round trip reflection from a moving surface (as the only region where the optical path difference may change), it is then possible to consider Φ_δ as a time varying property. With Φ_δ now time dependent, its differential with respect to time, $\frac{d\Phi_\delta}{dt}$, can be interpreted as imprinting a characteristic beat frequency, ω_B, upon the cycle averaged intensity. This imprinted beating is represented by the $\cos(\Phi_\delta)$ term found within equation 6.1, and can be related to the velocity of the surface upon which the second optical path reflects, v_S, such that [172, 177],

$$\frac{d\Phi_\delta}{dt} = \omega_B(t) = 4\pi\frac{v_S(t)}{\lambda_0},$$

where λ_0 is the initial frequency of light passed into the setup. This interpretation, using a path length argument, may alternatively be considered using a Doppler shift incurred within the second path upon reflection at the moving surface, and by ignoring the initial phase offsets, Φ_1 and Φ_2. If it is reasonable that the surface velocity does itself not vary drastically $\left(\Delta v_S < 1\,m\,s^{-1}\right)$ across a small number (< 10) cycles $\left(\Delta t_{Cycle} \approx 1\,ns\right)$ of the characteristic beat frequency, ω_B, then the same result is achieved such that,

$$\nu_B(t) = 2\frac{v_S(t)}{c_0}\nu_0 = 2\frac{v_S(t)}{\lambda_0},$$

where ν_0 and ν_B are the frequencies corresponding to λ_0 and ω_B respectively and where non-radial frequencies have been used to cast the result to a more conventional form. For completeness, c_0 is the speed of light. The definition of this characteristic beat frequency is the underpinning of conventional homodyne PDV.

Given the above, it is possible to imagine a similar system with two separate coherent, monochromatic, and stable light sources at differing frequencies where the resultant superposition would generate a stable non-zero characteristic beat frequency. Again, should light within the second optical path undergo a change in frequency upon reflection at a moving surface, then the resultant change in characteristic beat frequency following superposition will again follow such that,

$$\Delta\nu_B(t) = 2\left(\frac{\Delta v_S(t)}{c_0}\right)\nu_0.$$

This can then be simply rearranged, with the initial offset ignored for convenience, to give an expression for the motion of the surface as above such that [172],

$$v_S(t) = \frac{1}{2}\frac{\nu_B(t)\,c_0}{\nu_0} = \frac{1}{2}\nu_B(t)\,\lambda_0. \tag{6.2}$$

This alternate scenario, that begins with two distinct frequencies instead of a single source, is representative of frequency shifted, heterodyne, PDV [178, 180].

To measure this beating mode, or that of the original homodyne signal, a high-speed photodetector measures the intensity of the superposed light sources, with a high bandwidth digitiser recording the voltage across the photodetector giving a high-frequency sinusoidal signal similar to figure 6.1a. This voltage trace mirrors the beating, such that the evolution of the dominant beat frequency is calculable using sequential time windowed Fourier transforms of the voltage trace. The output of these sequential transforms is known as a spectrogram, an example of which is shown in figure 6.1c, with a Hamming window [181] used for all sampling. Considering this spectrogram, it is noted that a frequency shifted setup with two distinct wavelengths was used, as the initial dominant beat frequency, reflecting upon an initially static sur-

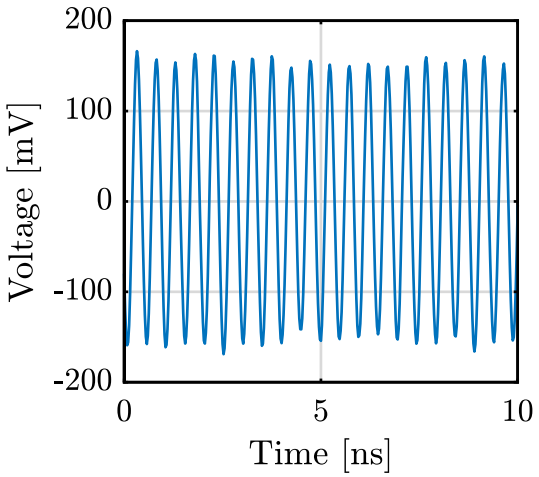

(a) Raw digitiser signal.

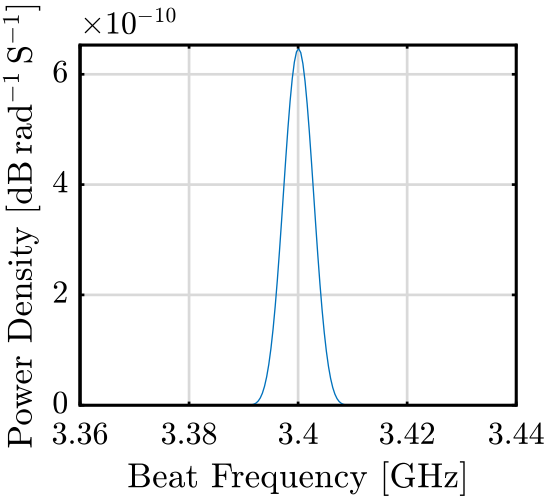

(b) Resultant Fourier spectrogram.

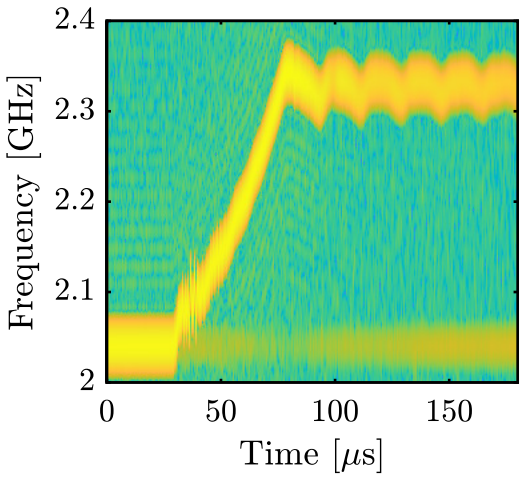

(c) Resultant Fourier spectrogram.

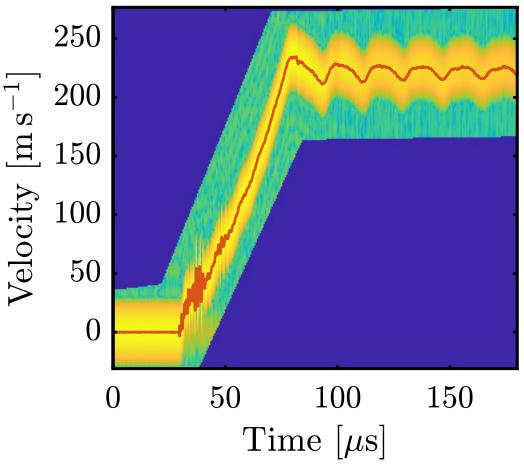

(d) Velocity profile.

Figure 6.1: Example PDV signal during analysis from raw interference pattern to velocity trace. In figure 6.1a a greatly cropped signal is shown to visualise the sinusoidal raw signal.

face, is non-zero, with this requiring a linear translation in velocity space to counteract the deliberate frequency offset.

In order to extract the velocity from a spectrogram a Gaussian fit is applied to the resultant Fourier spectrum within each window of the spectrogram. The use of such a fit is clearly valid given the example spectrum seen within figure 6.1b. This transform serves to identify the dominant frequency in the spectrum, with the subsequent conversion to velocity as given in equation 6.2. The end result, as seen in figure 6.1d, is a velocity trace of the surface motion along the probe axis with a sub µs temporal resolution and a margin of error less than 1 % [182]. Both versions of PDV, conventional and frequency shifted, were implemented using 1550 nm tunable lasers during this research. The latter, frequency shifted variant, was used in the majority of cases due to its improved resolution at low velocities and increased ease of use thanks to observable beating generated upon reflection from static surfaces. The implementations of both variants are given below, along with a detailed overview of the experimental setup.

6.2 Conventional (Homodyne) Implementation

The original implementation of PDV [172], as visualised in figure 6.3, requires use of a single laser and a critical optical component called a circulator. A circulator is an optical component with 3 or 4 ports that serves to redirect light depending on the direction of propagation of that light [183]. Visualised in figure 6.2, light entering the device into port A is passed to port B, with light incident upon port B passed to port C instead of port A. This redirection of light is often used within optical communications equipment to allow bidirectional information transfer within an optical fibre, however this ability also has other applications, including within PDV. The light from the singular laser is coupled into a fibre and passed to a circulator with as yet unshifted light progressing onwards to a probe. Light is then propagated from this probe, reflecting off a surface oriented normal to the probe axis, before being coupled back into the same probe. This reflected, and now potentially shifted, light

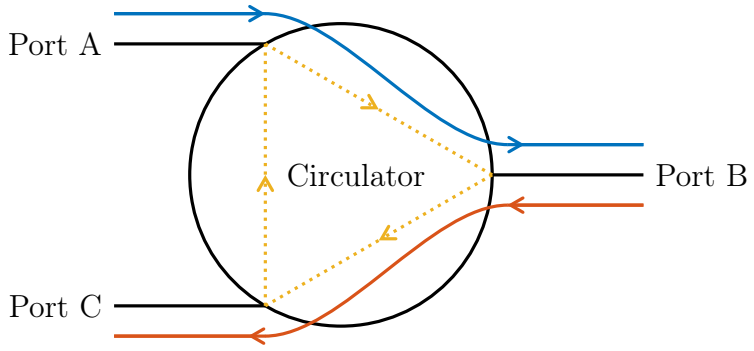

Figure 6.2: Simplified schematic of a 3 port optical circulator, the optical paths (given in blue) can be seen with physical optical fibres themselves shown in black. Where represented elsewhere an arrow is often provided to clarify the direction of optical transmission.

travels back along the probe fibre into the circulator and onwards, from the third port, along a third fibre to the photodetector.

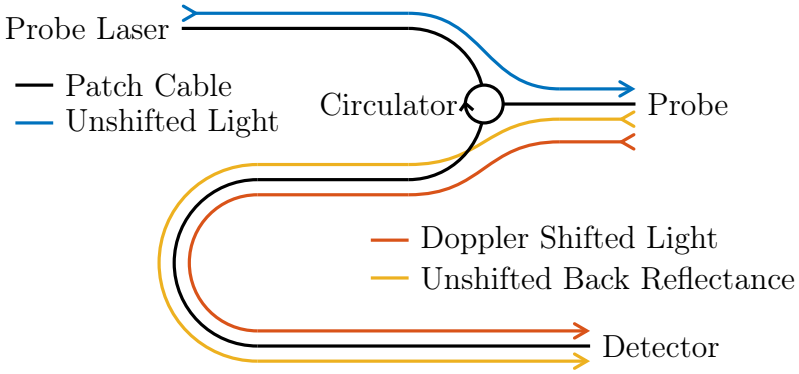

Figure 6.3: Diagram of homodyne photon Doppler velocimetry set-up.

During this process a back reflection is deliberately introduced at the optical probe from which the unshifted light is both launched and collected. This back reflection, alongside other lesser (and often unintentional) back reflections, provide a constant source of unshifted light (as the interfaces seeding these back reflections are themselves static) to the photodetector and hence serve to generate a beating frequency from the homodyne interference should the light reflected from the surface undergo a frequency shift. A key limitation of this technique is a lack of observable beating when the probe is normal to a static surface, limiting the ability to align the probe precisely to the surface normal using the generated voltage signal. A second limitation of this technique

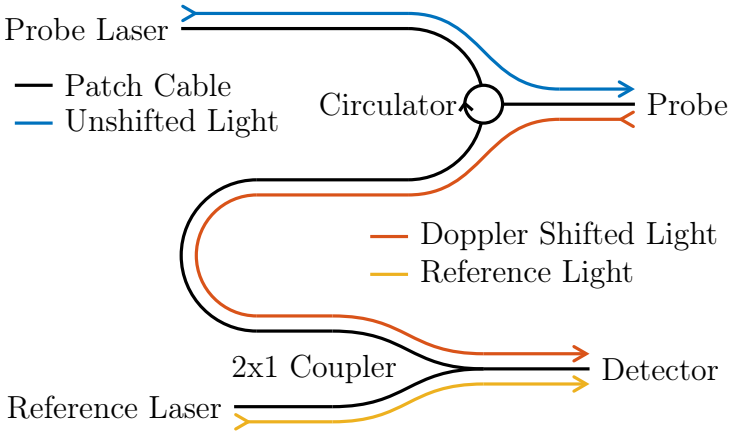

Figure 6.4: Diagram of frequency shifted, heterodyne, photon Doppler velocimetry set-up.

is the comparatively low beat frequencies induced at low surface velocities. Here the reduced rate of phase change within the signal hinders the accuracy of the Fourier transform during short time periods. These issues are partially mitigated through use of a frequency shifted implementation.

6.3 Frequency Shifted (Heterodyne) Implementation

Frequency shifted PDV, as seen in figure 6.4, expands upon the original setup by introducing a second independent laser operating at a marginally different wavelength. The addition of this second laser, known as the reference laser, generates a beat pattern when the measured surface is static. The reference laser is deliberately tuned to provide an appropriate disparity in frequency, allowing the experimenter to not only align the probe from the amplitude of induced beating, but also to generate high frequency beating at low surface velocities, improving diagnostic resolution. In order to add this second wavelength a 2x1 coupler [183] is used prior to the photodetector, with inline attenuators and power meters also included to enable the intensities of each light source to be varied in turn facilitating a greater degree of control over the observed beating.

One issue incurred with frequency shifted PDV is the presence of baseline interference, a by-product of the back reflections that are integral to a homodyne setup.

Owing to the independent second laser, these back reflections now induce their own beat frequency superposed atop the beating induced by the Doppler shifted light. As the surfaces spawning these spurious sources of unshifted light are stationary, a supplementary constant signal is generated at the beat frequency corresponding to $0\,\mathrm{m\,s^{-1}}$. This effect may be mitigated in two ways, firstly using clean angled FC-APC fibre couplings and probes with limited back reflection reduces the amplitude of the induced baseline, and secondly as this baseline is static, its amplitude, frequency, and phase may be calculated, with the inverted signal superposed to cancel out the baseline [180]. A widely observable everyday analogy to this computational approach is found in noise cancelling headphones, where inverted sound waves are added to the desired sound output of headphones to remove ambient noise. An example of such baseline removal via inverted superposition can be seen in figure 6.5.

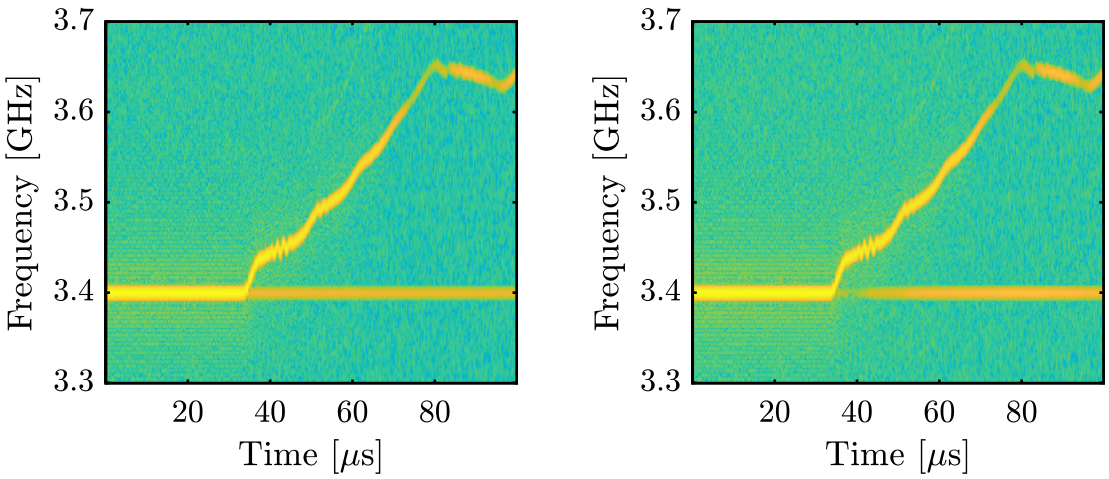

(a) With baseline.

(b) Without baseline.

Figure 6.5: An example of monochromatic baseline removal as first published by Dolan *et al.* in 2012 [180].

6.4 System Implementation

Given the above simplified descriptions of both conventional and frequency shifted PDV system designs, the real world implementation capable of functioning in both modes (conventional and frequency shifted) is detailed below to provide a complete overview of the route taken to produce velocimetry measurements presented later in



(a) Koheras Adjustik E15. (b) WaveMaster 808Zi.

Figure 6.6: Critical turnkey instruments within the setup. A pair of NKT Photonics Koheras Adjustik E15 1550 nm tunable continuous wave lasers provide the probe and reference light sources. The resulting interference signals are then recorded using a pair of Teledyne LeCroy WaveMaster 808Zi series 8 GHz/4 × 40 GS s^{-1} oscilloscopes.

this thesis. The starting point for any laser interferometer based velocimetry system is the laser(s), in this case a pair of lasers (often distinguished as the probe and reference lasers) are used so as to facilitate frequency shifted measurements. The lasers in question are NKT Photonics Koheras Adjustik units similar to that shown in figure 6.6a, which serve to provide a continuous source of ~1550 nm coherent light coupled into an FC-APC fibre. These lasers are tunable within an approximately 1 nm window, allowing a variable magnitude of frequency shift to be generated by deliberately detuning the reference laser source from its counterpart, and are specified to deliver a narrow Lorentzian linewidth not exceeding 100 Hz according to manufacturer specifications [184]. This tunable stability distinguishes these units as being ideal for interferometer based applications including PDV.

Using the coherent light provided by the pair of fibre coupled lasers, a fibre optic arrangement must be constructed following the form of a frequency shifted PDV channel as visualised in figure 6.4 with this allowing a homodyne diagnostic by simply removing any incident light from the reference laser path. This optical setup itself is seen in figures 6.7 and 6.8 with 8 independent channels of frequency shifted components combined with inline power meters and Variable Optical Attenuators (**VOAs**) that moderate the amount of laser light passing through the setup. The VOAs which serve to mediate laser propagation (as measured on inline power meters) through the system



(a) External assembly. (b) Internal view.

Figure 6.7: The optical fibre assembly. An upper 1U chassis splits both probe and reference lasers into the inputs for either 2, 4, or 8 channels of PDV. These inputs are then passed, via single mode patch fibre, to the rear of the lower 4U chassis, containing the circulators, 2X1 combiners, inline power meters, attenuators, and detectors. At the front of the 4U chassis 8 SMA terminals are located above 8 FC-APC fibre terminals, the upper grouping facilitating transmission of detector output to high-bandwidth digitiser with the lower grouping connecting the optical probes to the PDV fibre components via single mode patch fibre.

are themselves controlled by means of an in-house utility shown and detailed within figure 6.8 that also serves to display power meter readings, facilitating independent control of all 8 channels remotely and in real time. Following its passage through the optical components comprising the channel, the intended beating generated through wave interference is incident upon a Thorlabs DET08CFC/M InGaAs 5 GHz FC/PC fibre coupled photodetector. Sensitive to wavelengths from 800 nm to 1700 nm this photodetector easily covers the desired ~1550 nm light used within the setup and with a bandwidth suitable for measuring velocity changes of several $\mathrm{km\,s^{-1}}$ without resorting to advanced leapfrog techniques [175] or sacrificing temporal resolution with beat frequencies below 1 kHz. The electrical signals produced by these detectors are passed via SMA cable (owing to its increased bandwidth when compared to the commonplace BNC cable) to high bandwidth digitisers, specifically a pair of Teledyne LeCroy WaveMaster 808Zi series oscilloscopes. Each channel of these scopes is capable of recording PDV diagnostics at beat frequencies approaching the detector bandwidth without undersampling, allowing full utilisation of the 8 channels that could be fielded. Custom software was written within MATLAB to facilitate effective data ingest of recorded

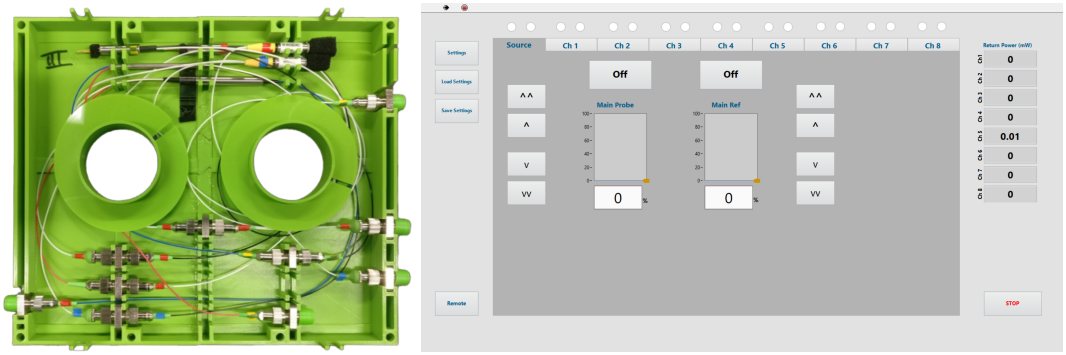

(a) Internal channel view. (b) Control interface.

Figure 6.8: Single channel setup shown alongside the control interface. Values reported from inline power meters located directly preceding the detector output are displayed to the right of the interface. The vertical bars in the center of the control interface report channel-specific VOA states with the arrows beside them mediating the respective attenuator. At the top of the interface a tab bar allows switching between channels to allow independent control of power levels on a channel by channel basis.

signals that could contain up to 128 MS of data recorded at an 8 bit vertical resolution per channel [185].

6.5 Phase Evolution Baseline Removal

As of this point in the description of the PDV diagnostic, theories are described following from the cited literature with the system assembly and implementation attributed to other members within the authors' research group. This information is presented to both effectively contextualised the nuances in recording velocimetry results presented later in this thesis, and to underpin an improvement to the baseline removal technique seen in figure 6.5, that was developed solely by the author within this research that is detailed in depth for the first time below.

In reality the use of a standard monochromatic numerical baseline correction [180] is hindered by the non-zero spectral Lorentzian linewidths of laser light passed into both probe and reference optical channels (as specified above for the chosen Koheras Adjustik E15 lasers this linewidth is sub 100 Hz), most likely resulting from subtle thermal variations within the laser itself and resulting in a population of frequencies closely packed around the desired wavelength.

In cases where the experimental duration lasts only a few microseconds the instability in the dominant baseline frequency within the population is negligible, however once longer durations of measurement are required this variation can no longer be ignored, with variances in the relative contributions of distinct frequencies within the inputted light hindering the effectiveness of the monochromatic baseline correction. The limitations of the monochromatic method when applied to longer durations is visualised previously in figure 6.5, where the resurgence of the baseline beyond 45 µs is symmetric about the baseline node (at approximately 40 µs) with the same baseline prevalent at earlier times including during breakout.

In order to circumvent this limitation an evolving baseline correction algorithm was developed, allowing the removal of such interference over durations many orders of magnitude greater than has been previously achievable. This method is based upon developing Dolan's traditional technique [180], to introduce a time varying phase offset, $\delta\phi(\mathrm{t})$, atop the correction specified by Dolan *et al.* such that the artificially superimposed correction signal follows the form,

$$\mathrm{I}(\mathrm{t}) = A\sin\left(2\pi\nu_{\mathrm{Baseline}}\mathrm{t} + \phi_0 + \delta\phi(\mathrm{t})\right). \tag{6.3}$$

Here amplitude A, baseline frequency ν_{Baseline}, and zeroth order phase offset ϕ_0 are calculated following Dolan's monochromatic method, where:

1. the dominant base frequency is calculated prior to breakout using a long duration Fourier transform,

2. both the amplitude and zeroth order phase offset evaluated in parallel using a non-linear optimisation seeking to minimise the spectral power within the baseline frequency range during a period proceeding separation of the signal and baseline modes.

These values are then applied to the signal, this producing a result similar to figure 6.5b that in this case is taken to be a partially corrected signal. From this state, a series

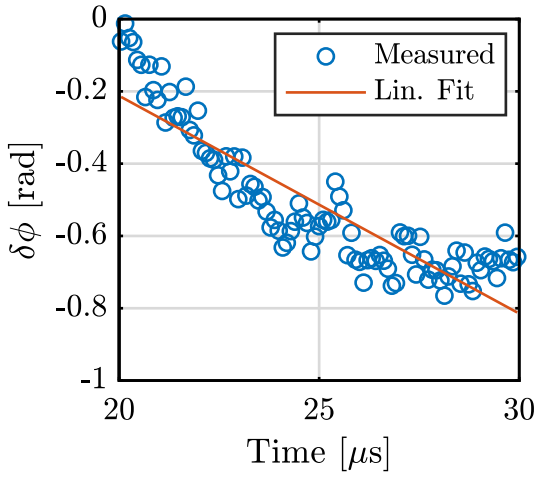

Figure 6.9: Characterising the evolution of $\delta\phi$ over a region of the signal directly proceeding breakout.

of further windowed evaluations of the phase offset are then calculated. These new phase offsets are evaluated (using the previously evaluated amplitude and baseline frequency as fixed terms) by again minimising baseline spectral power. However in this case the partially corrected signal is used in contrast to the raw signal used before. The evaluation of the new phase offsets are now however calculated from the partially corrected signal instead of the uncorrected signal as used within the monochromatic correction. Initially the evolution of the phase offset is quantified over a short region as seen in figure 6.9, with the goal of determining a suitable sampling frequency for the actual evaluation of phase offset evolution. A window is specified such that sequential non-overlapping windowed phase offsets are separated by $\delta\phi$ within the range $\frac{\pi}{8} < \delta\phi < \frac{\pi}{2}$. This range is chosen for the following reasons:

1. firstly to ensure a large enough window to minimise the likelihood of an evaluated phase offset becoming dominated by a signal crossing the baseline, which may then lead to the cancellation of the signal itself rather than the baseline;

2. and secondly to ensure a small enough window to minimise the potential of a full cycle of evolving phase offset going untracked with this leading to a lack of cancellation of the baseline.

Given the identification of a suitable window size for tracking the evolution of $\delta\phi$,

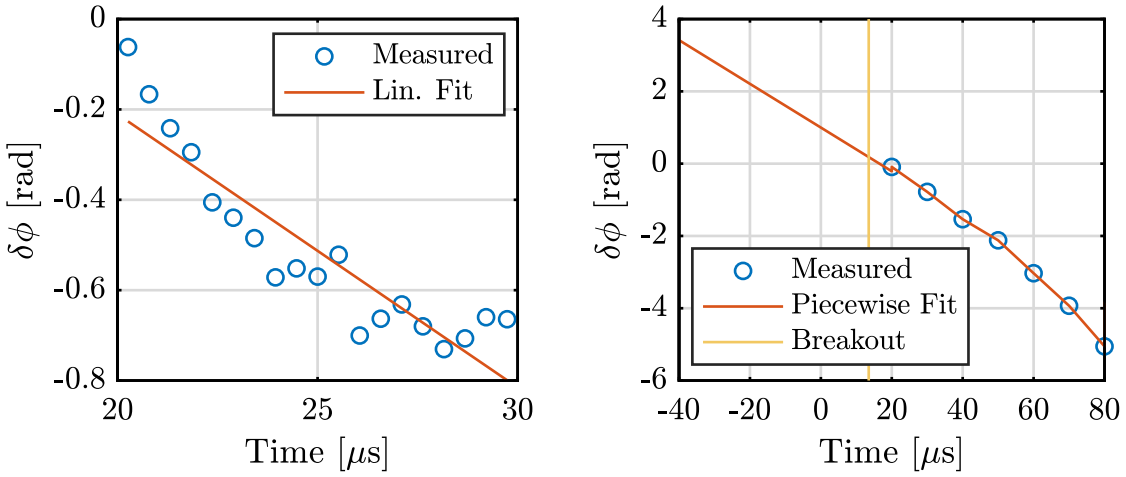

(a) Post breakout $\delta\phi$ evolution.

(b) Full correction.

Figure 6.10: Calculated evolution of baseline correction offset $\delta\phi$. Regions prior to breakout, which are seen preceding the first blue circle in the right hand figure, are predicted by the linear extrapolation shown in the left hand figure, with all other data predicted by linear interpolation. A negligible discontinuity in $\delta\phi$ is seen at the boundary of the interpolated domain, with this a result of the piecewise fitting.

a second set of phase offsets are calculated. This second set is calculated from a point after breakout (specifically the centre of the window within which the zeroth order phase offset was evaluated), to the end of the signal, in sequential non-overlapping windows sized per the above calculation. The evaluated values of phase offset are themselves confined within the region $0 < \delta\phi < 2\pi$, so they must then be sequentially offset, generating a series of continuous points as can be seen within the blue rings of figure 6.10b.

With the post-breakout baseline now well characterised, attention must be turned to the breakout region itself. Whilst the same method of direct phase offset evaluation is no longer feasible, owing to measured signal existing within the sample spectral region as the baseline, the gradual evolution of $\delta\phi$ may be again evaluated to predict a rate of phase shift, with units $\mathrm{rad\,s^{-1}}$, in the region directly proceeding breakout. The calculation of this evolution is seen in figure 6.10a, with the fit produced allowing for a linear extrapolation of $\delta\phi$ back into the breakout region, again using the initially determined amplitude, base frequency and zeroth order phase offset.

Using the recorded sequential evolution of phase offset throughout the post break-

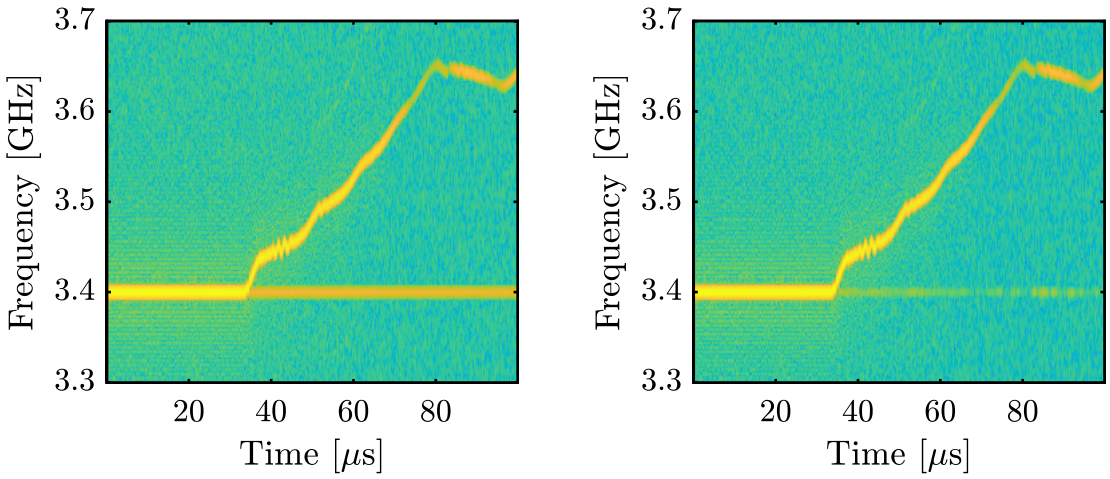

(a) Uncorrected.

(b) Corrected (Evolving).

Figure 6.11: Fully corrected signal shown alongside original uncorrected signal, here the improvements offered by the evolving baseline correction aid analysis around the breakout, where the extrapolated evolution improves the signal to background ratio. The benefits of the forward evolution of $\delta\phi$ using interpolation, are realised when tracking surfaces where the velocity trace passes back through the baseline later on during the experiment.

out region, the assumed continuous function $\delta\phi\,(\mathrm{t})$ is then upsampled to the rate of the original signal to provide a correction that accounts for the evolving phase shift post breakout at every time point within the partially corrected signal. For the partially corrected signal that exists during breakout, the aforementioned extrapolation is used to predict the phase shift prior to breakout, again upsampling to the partially corrected signal frequency. The end result, as seen in figure 6.10b is a map of effective extra phase offset that only assumes a lack of discontinuities in the rate of change in the phase offset. This correction is then applied to the partially corrected signal with the resulting filtered spectrogram visualised in figure 6.11.

In this research the ability to project an evolving phase offset was beneficial in maximising the signal to noise ratio within the breakout of spallation velocimetry traces, the ability to correct long durations of baseline to mitigate issues where a signal crossing this baseline would be obscured was not directly of use, however it has already seen use within other commercial projects and would have allowed for a more robust analysis routine were PDV diagnostics fielded upon split Hopkinson bar systems within this research. Whilst convoluted, the code itself is implemented within

a graphical PDV analysis program that is detailed below in section 6.6 to ensure its accessibility to others within the field.

A further planned development includes the use of a dedicated measurement of pure baseline (utilising a fibre coupled retroreflector) to negate the need to predict frequency or evolving phase offsets. This will be possible as a continuously varying baseline frequency is the underlying cause of the gradual phase offset evolution, so an evolving precise measurement of this varying frequency will require only the evaluation of an amplitude and zeroth order phase offset after breakout. The end result of this addition should be the ability to correct the entire signal, with only gradual baseline amplitude variations caused uniquely within a single channel remaining to hinder correction.

6.6 PDVTool

Due to the volume of PDV data recorded in this research, and the need for effective and repeatable analyses of any recorded data, a fully featured graphical interface was developed within the MATLAB programming package to handle processing of all PDV data recorded, with a screenshot of this seen in figure 6.12. The developed software package, named PDVTool and available freely [186], has now been adopted by others within the research group to improve the ease of handling this type of data, to effectively facilitate robust baseline correction, and to streamline the visualisation of PDV measurements within presentation materials.

Within the package, the aforementioned standard and evolving baseline corrections are fully integrated along with the capability to work with time and frequency multiplexed signals [174, 182, 187]. Atop the graphical interface and selection of analysis tools, the resulting data and analysis parameters are implicitly captured and stored, to allow effective re-analysis at a later date, or to facilitate access of exact analysis parameters if required when reporting results.

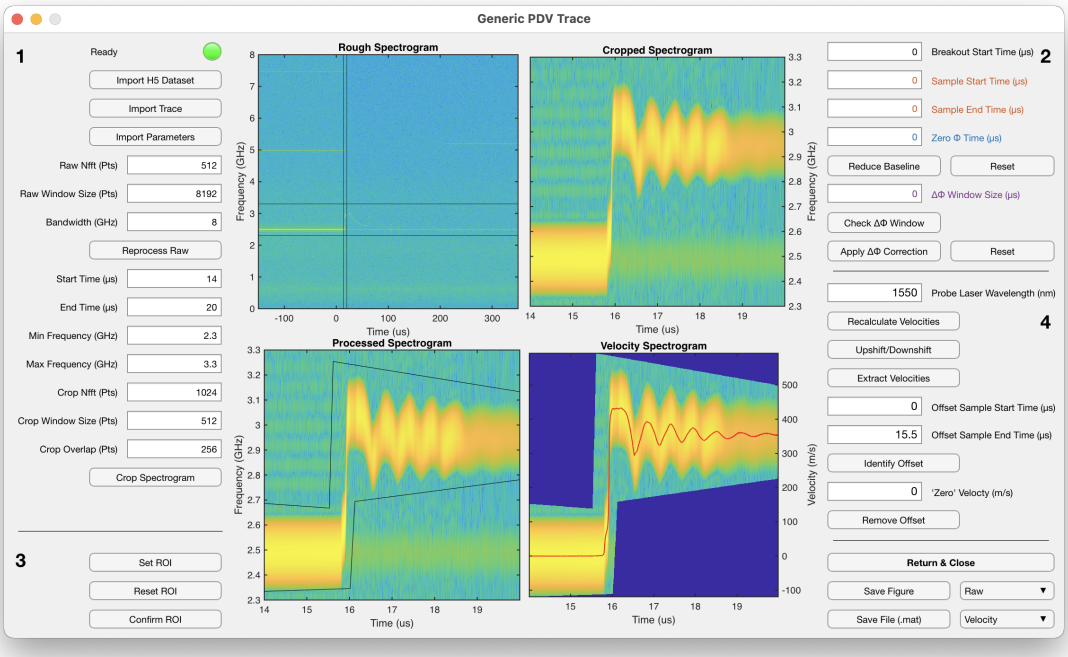

Figure 6.12: Screenshot of PDVTool with analysis of a PDV trace taken during a spallation impact in progress [186].

Chapter 7

Taylor Test Experimental Data

7.1 Overview

A large portion of the dynamic material testing in this body of work involved the Taylor impact test. First conducted by its namesake, G.I. Taylor in 1948 [188], the experiment involves the axially aligned impact of a cylindrical rod with an anvil assumed to be rigid, smooth, planar, and infinite. The rod is launched toward the anvil using a gas gun, providing control over the impact velocity and minimising tilt between the anvil surface normal and cylindrical rod axis. Upon impact the rod splays radially at its impact face and shortens axially, continuing to deform whilst the center of mass progressively decelerates, resulting in a gradient of deformation along a portion of the rod. These loading conditions subject the target to a diverse population of stress, strain and strain rate states, with rates up to $10^5\,\mathrm{s}^{-1}$ generated [36, 189]. This wide range of loading conditions make the Taylor impact test a particularly rigorous evaluation for the simulated dynamic response of a constitutive model. The difficulty in accurately simulating the observed deformation occurring across the diverse population of loading states has resulted in the Taylor impact test becoming widely used throughout the material testing world [36, 91, 190–192] as a method of validating rate dependent constitutive material models.

Early Taylor impact testing was solely focused on the measurement of the resulting post-impact shape, with analytical two-wave perfectly plastic interpretations used to infer a dynamic yield strength from known values of density, elastic properties, and the post impact profile (specifically the axial length reduction and the ratio of un-deformed to deformed regions along the length of the rod) [188, 193–195]. This post-impact technique was eventually augmented with ultra-high-speed imaging several decades

after the initial implementation [191, 196–198], with the extra knowledge of transient deformation profiles improving the rigour of the experiment and further highlighting issues with analytical solutions.

In the early 2000's, Rohr *et al.* [199] proposed a reversed layout for the Taylor impact experiment, building upon Taylor's original design. This alternate test involves the impact of an assumed rigid, smooth, and planar flyer plate into an axially aligned but now static target (this would have been the projectile in a standard Taylor impact). During impact the initially static rod undergoes similar deformation to a standard test, albeit in a decelerating reference frame (the frame here defined using the impact surface of the projectile). While this approach results in both sample and anvil existing in a state of motion after deformation has finished, complicating post impact recovery, it facilitates tracking the velocity of the rear of the target through laser based velocimetry techniques [176, 200] including PDV [172, 173] as described in depth in chapter 6 whilst still allowing for ultra-high-speed imaging.

Within this body of work a series of reverse Taylor impacts were conducted across a range of impact velocities and temperatures on both additively and conventionally manufactured 316L stainless steel. Additively manufactured samples were taken from two separate print runs of a Renishaw AM250 SLM printer in both horizontal and vertical orientations within the build volume. Conventionally manufactured samples were also tested alongside additive counterparts to provide a baseline response for 316L stainless steel. The full details of the samples tested can be seen in table 7.1, with an identifying tag listed in the leftmost column titled ShotID; these tags are used to distinguish between each reverse Taylor impact throughout this thesis when detailing experiment conditions, analysis parameters, and experimental results.

Studying the samples listed in table 7.1, a clear disparity is seen in the density of additive samples from the initial print run, which are identified using the POR subset in the ShotID column. Quantifying this disparity, porous samples were calculated as having a density of $(7735 \pm 36)\,\mathrm{kg\,m^{-3}}$ compared to the fully dense conventional samples that exhibited a significantly higher density of $(7940 \pm 5)\,\mathrm{kg\,m^{-3}}$. Here, uncertainties

ShotID	**Material (& Orientation)**	**Size** [mm] ($\varnothing \times \updownarrow$)	**Mass** [g]	**Density** [$\mathrm{kg\,m^{-3}}$]
CM RT TT 1	CM 316L	7.60×50.11	18.04	7940
AM H POR RT TT 1	AM 316L (Horizontal)	7.61×50.05	17.67	7760
AM V POR RT TT 1	AM 316L (Vertical)	7.60×50.09	17.44	7670
CM RT TT 2	CM 316L	7.60×49.98	18.01	7950
AM H POR RT TT 2	AM 316L (Horizontal)	7.61×50.07	17.66	7750
AM V POR RT TT 2	AM 316L (Vertical)	7.61×50.10	17.57	7710
CM RT TT 3	CM 316L	7.62×49.98	18.08	7930
AM H POR RT TT 3	AM 316L (Horizontal)	7.61×50.09	17.59	7720
AM V POR RT TT 3	AM 316L (Vertical)	7.61×50.09	17.72	7780
CM RT TT 4	CM 316L	7.64×49.78	18.13	7940
AM H POR RT TT 4	AM 316L (Horizontal)	7.61×50.08	17.71	7770
AM V POR RT TT 4	AM 316L (Vertical)	7.60×50.04	17.50	7710
AM V DEN RT TT 1	AM 316L (Vertical)	7.64×49.94	18.11	7910
AM V DEN RT TT 2	AM 316L (Vertical)	7.61×49.95	18.02	7930
AM H DEN RT TT 1	AM 316L (Horizontal)	7.60×49.98	18.00	7940
AM H DEN RT TT 2	AM 316L (Horizontal)	7.61×49.95	18.00	7920
AM H DEN HT TT 1	AM 316L (Horizontal)	7.61×49.95	18.00	7920
AM V DEN HT TT 1	AM 316L (Vertical)	7.60×49.94	17.96	7920
CM HT TT 1	CM 316L	7.62×50.05	18.14	7940

Table 7.1: Overview of samples used in reverse Taylor impacts, a clear change in density is seen in porous additive samples with this linked to the observed layered porosity within the material discussed in chapter 5. Dimensions of samples provided are given as diameter ($\varnothing$) multiplied by thickness ($\updownarrow$).

ShotID	Tank Vacuum [mTorr]	Temperature [K]	v_{Impact} [$m\,s^{-1}$]
CM RT TT 1	500	293	177.4
AM H POR RT TT 1	600	293	178.4
AM V POR RT TT 1	700	293	175.3
CM RT TT 2	800	293	242.6
AM H POR RT TT 2	1000	293	243.4
AM V POR RT TT 2	900	293	240.5
CM RT TT 3	216	293	304.5
AM H POR RT TT 3	180	293	303.4
AM V POR RT TT 3	215	293	304.5
CM RT TT 4	108	293	357.6
AM H POR RT TT 4	200	293	359.7
AM V POR RT TT 4	208	293	361.7
AM V DEN RT TT 1	800	293	219.0
AM V DEN RT TT 2	680	293	298.2
AM H DEN RT TT 1	255	293	195.1
AM H DEN RT TT 2	189	293	296.6
AM H DEN HT TT 1	234	613	284.0
AM V DEN HT TT 1	178	617	286.9
CM HT TT 1	254	608	287.1

Table 7.2: Summary of experimental conditions used for all reverse Taylor impacts conducted. Where a temperature of 293 K is seen, this was given as an assumed value of room temperature (nominally ~20 °C).

are given to be one standard deviation either side of the average. In the second print run it is clear that a significantly increased density was achieved with these evaluated to be $(7924 \pm 10)\,kg\,m^{-3}$, now within one standard deviation of the conventional value. This disparity in density is attributed to the significant lack-of-fusion porosity observed in additive samples as discussed in chapter 5.

Considering the testing of the samples, the experimental conditions for all reverse Taylor impacts are tabulated in table 7.2. Of note is the range of impact velocities from $177.4\,m\,s^{-1}$ to $361.7\,m\,s^{-1}$ and a trio of experiments conducted at elevated temperatures exceeding 600 K at the base of the table that were used to probe the thermal softening effects under dynamic loading.

Continuing from this table, the following section provides an overview of the experimental setups used for the listed reverse Taylor impacts, with the iterative modifications to the setup detailed and the resultant improvements in recorded data high-

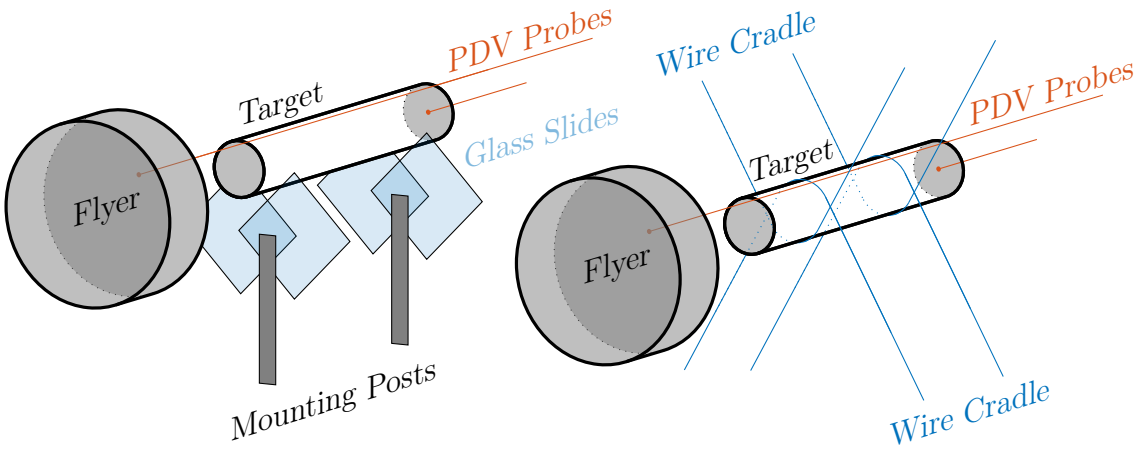

(a) Glass slide mounting. (b) Wire cradle mounting.

Figure 7.1: Example target mounting techniques. Earlier tests were conducted using the glass slide mounting with later tests using the more complex wire cradle that removed the glass debris cloud seen in the early tests. In both cases the flyer is shown to the left of the target with both target and flyer PDV probe traces shown in red.

lighted.

7.2 Experimental Setup

The initial challenge faced when conducting reverse Taylor impacts was ensuring the target could be mounted precisely in a concentric and coaxial position relative to the barrel of the gas gun. In order to facilitate this three generations of mount were used, each improving upon the prior, based on the two main techniques shown in figure 7.1.

The first of these techniques, identified as the glass slide technique, can be seen in figure 7.2. It used two pairs of microscope slides each glued together to form 'hourglass' shaped supports able to seat the target in a right angled grove. The limited out of plane strength and brittle behaviour of the glass served to provide a negligible impedance to any plastic deformation of the target rod, with each hourglass shattering shortly after impact. Each glass hourglass was glued atop a sacrificial plastic post, sized to approximately locate the target level with the barrel axis, with these mounted to a Thorlabs 5-axis optomechanical stage to provide the precise alignment capability required.

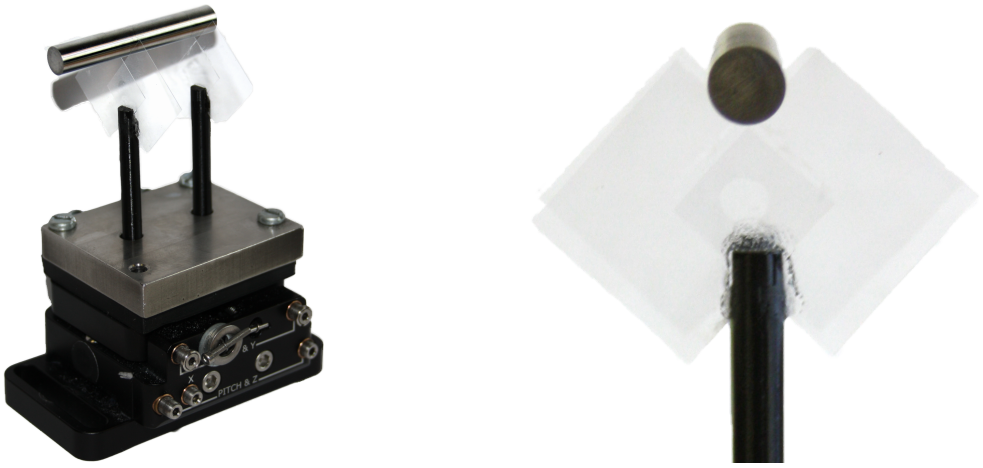

(a) Overview of mount. (b) Impact surface view.

Figure 7.2: Images showing a sample mounted upon glass slides. The two pairs of overlapping glass slides are glued to plastic rods with these attached to a 5-axis optomechanical mount that facilitates target alignment. The plastic rods are designed to ensure the target is suitably close to the barrel centreline prior to alignment as the range of height adjustment offered by the optomechanical mount is limited.

While this technique effectively facilitated alignment of the target, and did not significantly hinder plastic deformation, it did have two key issues that necessitated a new design, with it subsequently superseded by the more complex wire array technique for the 2nd and 3rd iterations of implemented target mounts. The first of these issues was the cloud of glass debris created upon impact; this can be seen forming in the final image of figure 7.8 with it obscuring radial profiles along the lower edge of the target, requiring instead that profiles be inferred from the midline of the sample and the upper edge. The second issue was that neither the glued glass hourglass nor the plastic posts would survive elevated temperatures, with the target then losing alignment, rendering the technique wholly unsuitable for any heated testing. To address these, a wire cradle as visualised in figure 7.1b was constructed, similar to that used by Chapman *et al.* [201] and Walley *et al.* [202], avoiding the generation of debris that would obscure the lower sample edge.

Initially assembled and validated on a small scale, as seen in figure 7.3, this cradle was then scaled up to a much larger assembly in order to incorporate an integrated infrared furnace (visualised in figure 7.4 and shown with a target mounted in figures 7.5

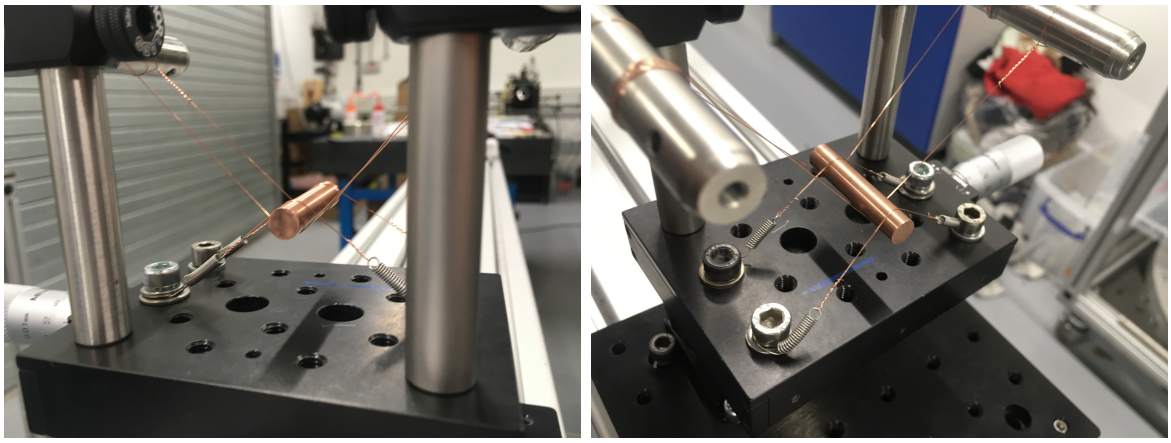

(a) Target impact surface view. (b) View from above of rear of target.

Figure 7.3: Example of 1st generation of wire cradle mounts. The target shown is a copper sample not directly related to this work, however the mounting method is the same. Springs attached to the lower set of wires ensure the wire array remains taught, while adjusting the length of the upper wires allows for adjustment of pitch and yaw. Lateral and vertical adjustment is achieved using two linear stages.

and 7.6) to allow the accessing of the desired elevated temperatures.

The larger wire array forwent the copper wiring seen in figure 7.3, instead using either 50 µm nichrome wire, that reduced the profile of the wires in imaging, or paired thermocouple wires that would facilitate the measurement of temperature without also spot welding a thermocouple to the target itself. By using a pair of thermocouples to replace both pairs of wires within the cradle, it was also possible to broadly gauge the uniformity of heating along the length of the rod, though no internal temperature continuity could be validated. Furthermore, this dual measurement allowed a degree of redundancy within the experimental setup, where a single measurement was required to automate the control of the oven, a second thermocouple read independently using a data logger would firstly retain measurement after the oven was powered down prior to firing the projectile, and secondly provide an ongoing measurement should the first thermocouple fail at any point during heating.

Alignment of all samples was achieved optically by reflecting a laser from the breech end of the gas launcher, aligned concentrically and coaxially within the barrel, against the impact face of the target. The target impact face itself was polished using a series of abrasive sheets finishing with the use of Thorlabs 3 µm optical paper to achieve a

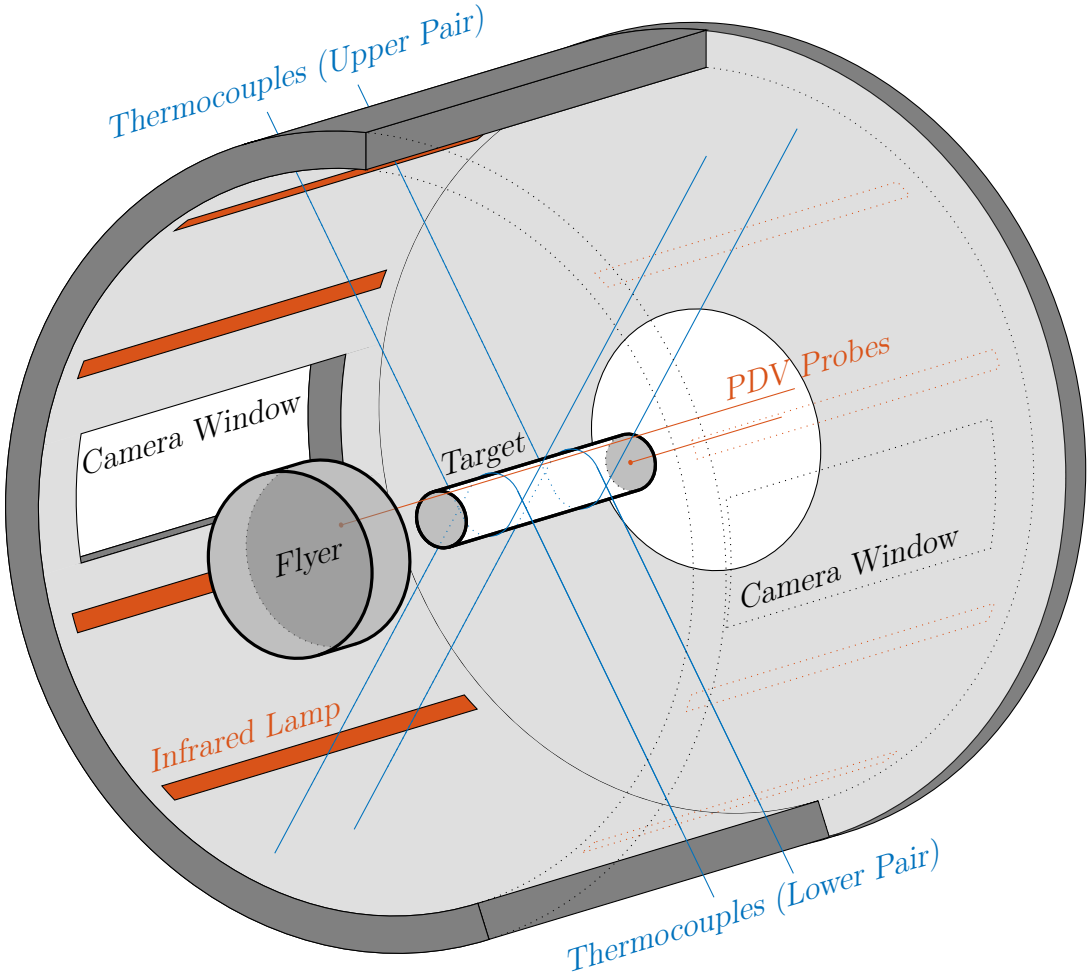

Figure 7.4: Diagram showing experimental setup used for reverse Taylor impact testing of samples at raised temperatures. The target is seen in the centre of an oven (partially cut-away) held within a wire cradle (shown in blue) and surrounded by a set of eight 750 W heating lamps (red rectangles). A rectangular opening in the side of the oven centered level to the target allows imaging of the impact event from the side. A pair of PDV probes (red lines) are fielded, with one measuring target response and a second recording the motion of the flyer (seen to the left of the target) impact face, to record both the impact time and velocity with high levels of precision.

suitably specular surface for optical reflection. The use of this alignment laser is seen in figure 7.6b, where the green class one alignment laser beam is seen reflecting from the target suspended within the oven.

During the alignment of the target, the impact frame was positioned roughly, usually within 5 mm, and secured to the breadboard mounted at the base of the target chamber. From here, subtle manipulation to the targets orientation was achieved by both varying the length and tension of wires suspending the target and by rotating the impact frame as a whole within the rotating optomechanical stage at its base. Adjustment to the wires was facilitated by anchoring the wires to linear stages mounted upon breadboards forming the upper and lower pieces of the rotating impact frame. This two stage process was repeated several times, re-centering the laser spot within the impact face to improve the concentricity, before then realigning the reflected laser along its initial beam path to in turn align the rod axis parallel to the barrel axis. Gradually, the adjustments required to regaining concentricity decreased, until coaxial, concentric alignment of the target was achieved to within 1 mm and 2 mrad respectively (assuming the beam deviated less than 5 mm from its original path over a 3 m distance). To validate the laser beam was returned along its initial path, therefore ensuring that the barrel and target were indeed coaxial, the laser spot was imaged upon an iris located in the beam path immediately ahead of the alignment laser diode itself, with this located at the breech end of the gas launcher.

7.3 Imaging

Imaging was attempted on all reverse Taylor impacts, with only one shot failing to capture images of the transient deformation states due to an anomalous trigger event stemming from the premature triggering of a light gate. As with the mounting techniques discussed above, the imaging setup changed iteratively over the course of the full set of tests, with various cameras, light sources, and imaging parameters used. These parameters are presented within table 7.3 to highlight the incremental revisions implemented within the imaging setup.

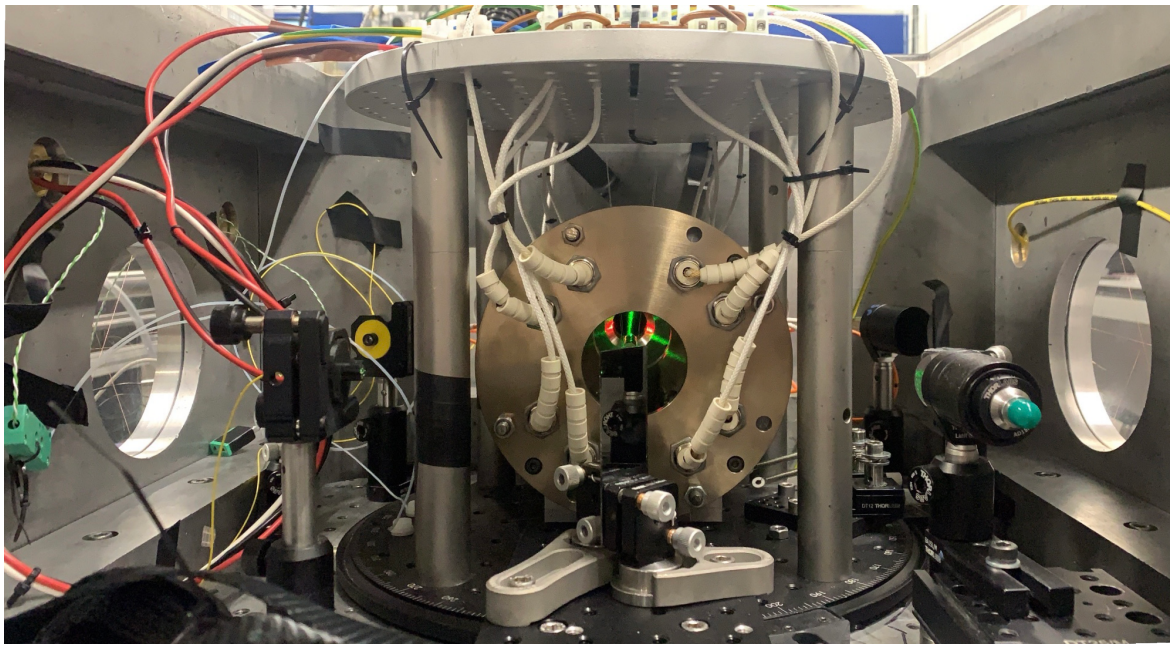

Figure 7.5: Rear view of heated Taylor impact frame. The rear of the oven is seen in the centre of the image, surrounded by the alignment frame comprised of four 25.4 mm diameter optical posts and two circular breadboards, the lower of which is combined with a rotating stage and attached to the base breadboard of the target chamber. Electrical wiring can be seen in red, white, and black entering the target chamber to the left of the image, with optical fibres seen in yellow to the right of image and to the left of alignment frame taped to the far face of the impact chamber. In the center a pair of sacrificial mirrors are aligned to a target and the barrel. The target is also aligned coaxially and concentrically to the barrel.

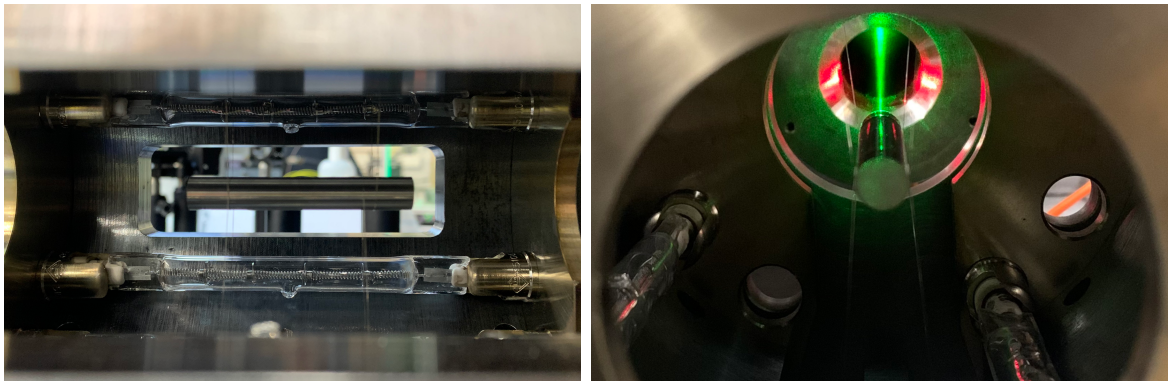

(a) View from side of oven. (b) View from rear of oven.

Figure 7.6: Views of a target suspended upon the larger 2nd generation wire cradle. In this case the larger cradle is shown in conjunction with the oven, to allow reverse Taylor impacts to be conducted at raised temperatures. In the rear view a laser is seen propagating along the centreline of the barrel and reflecting back from the target impact face. In the side view a layout similar to imaging sequences shown in figures 7.8–7.10 can be seen. This gives context to the imaging line, especially when imaging reverse Taylor impacts at elevated temperatures.

ShotID	Mounting Technique	Camera	Frame Rate [kfps]	Exposure Time [ns]	Pixel Size [µm px.$^{-1}$]
CM RT TT 1	Glass	IVV	200	1000	79
AM H POR RT TT 1	Glass	IVV	200	1000	79
AM V POR RT TT 1	Glass	IVV	200	1000	79
CM RT TT 2	Glass	IVV	200	1000	83
AM H POR RT TT 2	Glass	IVV	200	1000	75
AM V POR RT TT 2	Glass	IVV	200	1000	
CM RT TT 3	Copper Wire	Kirana	500	50	77
AM H POR RT TT 3	Copper Wire	Kirana	500	50	80
AM V POR RT TT 3	Copper Wire	Kirana	500	50	77
CM RT TT 4	Copper Wire	Kirana	500	50	77
AM H POR RT TT 4	Copper Wire	Kirana	500	50	77
AM V POR RT TT 4	Copper Wire	Kirana	500	50	77
AM V DEN RT TT 1	Nichrome Wire	SimX16	100	200	55
AM V DEN RT TT 2	Nichrome Wire	SimX16	100	100	55
AM H DEN RT TT 1	Nichrome Wire	SimX16	100	250	55
AM H DEN RT TT 2	Nichrome Wire	SimX16	100	250	55
AM H DEN HT TT 1	Thermocouples	SimX16	100	175	53
AM V DEN HT TT 1	Thermocouples	SimX16	100	175	53
CM HT TT 1	Thermocouples	SimX16	100	185	53

Table 7.3: Imaging parameters used for all shots, for CM RT TT 2 imaging was not captured due to an erroneous shutter trigger following the unintended coupling of an electromagnetic pulse emitted from the discharge of capacitors within a high powered flashlamp to a coaxial cable. This pulse was recorded on an oscilloscope channel used within the trigger for the camera.

7.3.1 Imaging Setup

Of key importance in measuring the transient deformation states of the Taylor rod was minimising any blurring of the radial profiles, accurately recording the time of the images, and minimising the effects of parallax. The easiest of these challenges to overcome was correctly recording the time of a given image following impact, with this accomplished simply by analysing a monitor output from the camera in use, taking the associated image time from the center of the period where the shutter was open for that frame, minus any delays stemming from transmission along cables. The center of the frame was chosen as on average this is when light captured at the sensor would have been traversing the sample, accepting that the passage of light through the setup is essentially negligible compared to the exposure time, and that the amount of light emitted from backlight for the experiment would remain constant over the duration of each exposure. This was then referenced to the impact time as given by velocimetry measurements of the flyer impact surface, which was also confirmed as matching that predicted by pre-impact imaging data showing the approach of the flyer to the target.

Parallax was minimised by carefully aligning the camera such that the imaging plane incorporated the axis of the sample, facilitated using a pair of mirrors to align a pair of reticles (each reticle centered inside circular windows located symmetrically within the sides of the target tank) within the camera frame. Finally blurring was mitigated simply by ensuring the exposure time was less than the time taken for an object to traverse a distance equal to the pixel size, were it travelling at the planned impact velocity. Working around this constraint and a suitable lens choice, in this case a Nikon Micro-Nikkor 200 mm f/4.0 owing to its ability to provide a suitable magnification, the aperture(s) of optics within the imaging line were minimised (to improve the resulting angular resolution) while maintaining a suitable exposure given the availability of light. Due to the short exposure times and high frame rates that were necessary to capture the event images were lit artificially. This backlighting

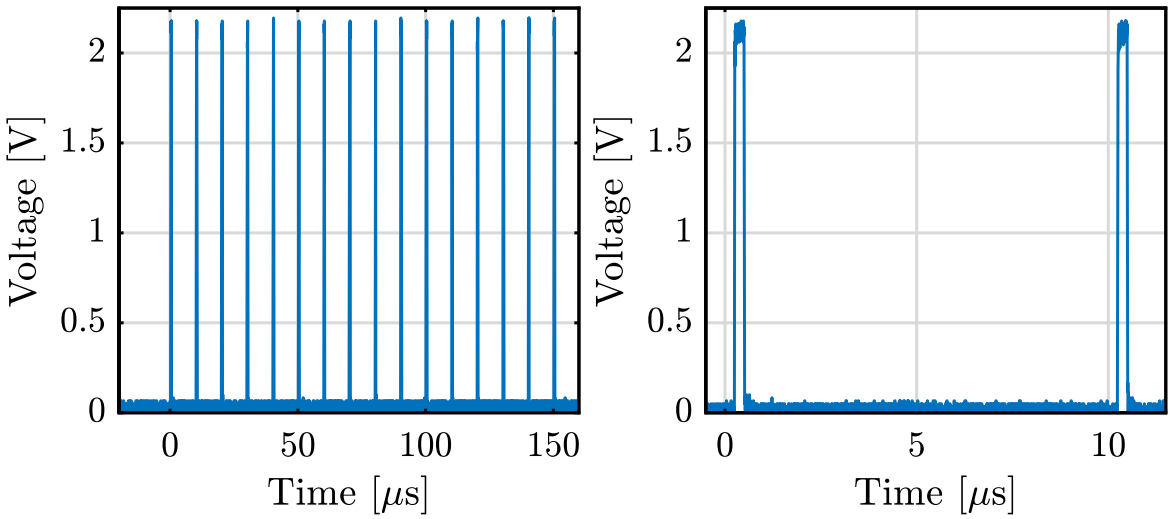

(a) Complete pulse sequence.

(b) Detail of two pulses.

Figure 7.7: Example monitor signal from a Specialised Imaging SimX16 framing camera showing 16 pulses located from 0 µs to 150 µs, corresponding to the 16 frames available within the camera. Each pulse has a gate width of 250 ns corresponding to the exposure time, with a 9.75 µs period directly after and prior to the proceeding frame, matching the imaging parameters given in table 7.3.

was achieved by means of either a Bowens Gemini 1500 Pro BW3955 flashlamp or Cavitar CAVILUX pulsed class 3B visible laser system [203], with the latter allowing an effective 50 ns exposure time equal to the pulse width of the light source. Where the pulsed laser backlight was used, the monitor signal from this was used in place of the camera monitor to record the time of exposure for each frame, as it was this pulsed source of light that provided essentially all of the light within each exposure.

7.3.2 Sample Images

Within this section, in figures 7.8–7.10, sample image sequences are shown for each of the three imaging/mounting combinations used. It is from imaging sequences such as these that measurements of sample length evolution were recorded with these then used for comparison against simulated length evolution.

In the initial series of images, taken using an IVV framing camera, the issues with the glass slide mounting technique are seen. Firstly, the slides hamper any measurement of the lower profile of the rod, and secondly in the final image the glass slides are obscuring not only radial measurements but also the flyer impact face, with a small

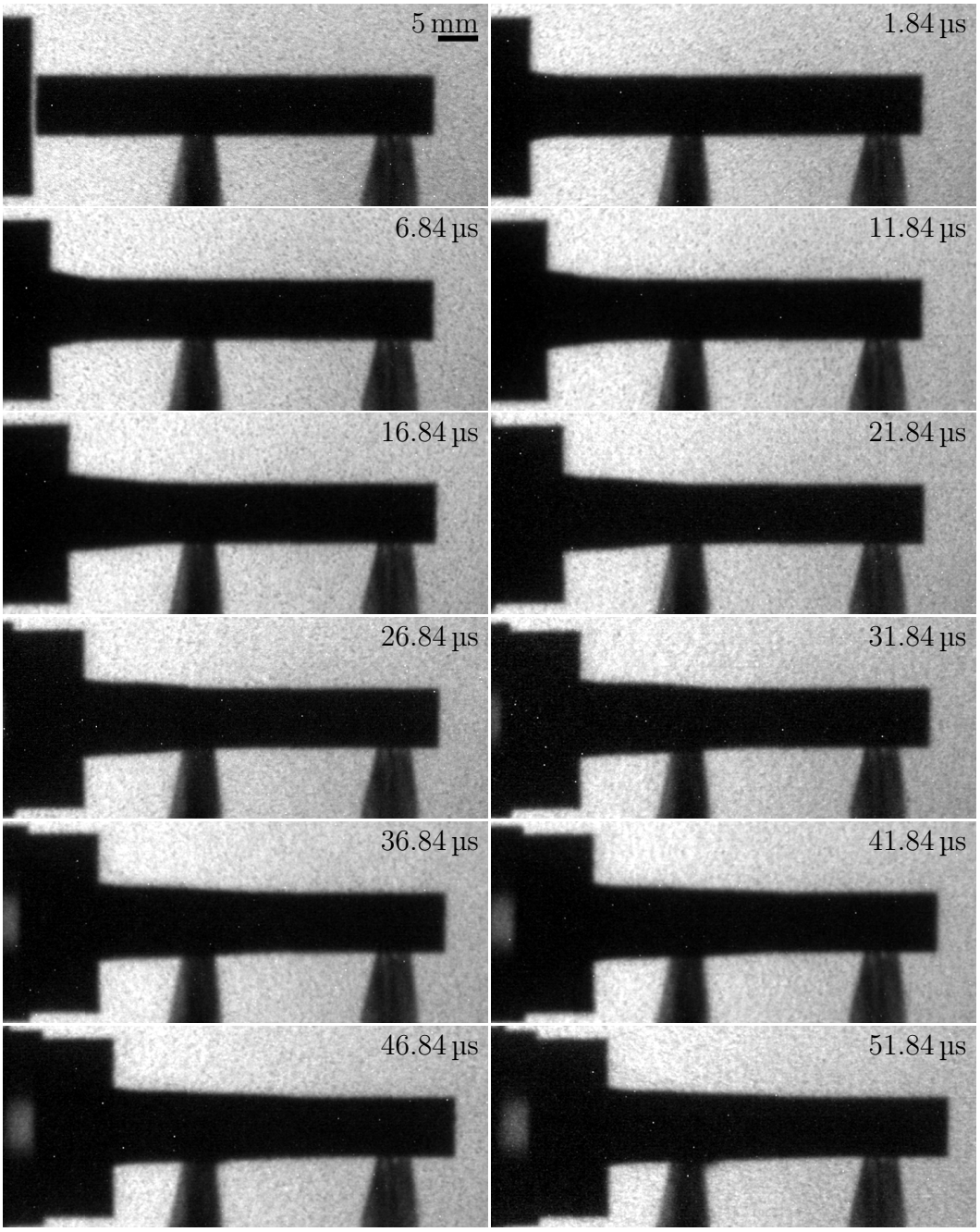

Figure 7.8: Sample IVV image series with the target mounted using glass slides as seen in figure 7.2, as was used for all tests where the IVV was fielded to image the impact.

cloud of debris seen forming from the forwardmost pair of overlapping slides. After this, as seen in figure 7.9, a series of images using the smaller wire cradle and imaged using a Kirana may be seen. These images show a reduction in noise, stemming from the use of a pulsed laser to light the scene, in turn facilitating a reduction to both the amplification of the digital sensor response and the lens aperture in the imaging system, resulting in improvements to the definition of the sample edges. This refinement is likely a symptom of the internal optics within a framing camera, as these optics (if set-up without particularly narrow apertures) will lead to significant loss of image quality. The series of images also highlights a ghosting issue that is inherent to the use of the Kirana camera, a feature that drove the use of a SimX16 in the final series of experiments.

Looking forward to the final series of images, the gradual improvements to imaging and alignment setup are seen, with a low noise image, nearly invisible wire cradle, and a reduced pixel size if also considering table 7.3.

7.3.3 Length Evolution

Drawing quantitative measurements from the imaging of transient deformation states existing during Taylor impacts was first introduced by Erlich and Shockey in 1983 [196], with Snyder and House amongst early adopters thereafter [191, 197, 198, 204]. These works either, with several assumptions, track the propagation of radial deformation from the impact face to generate stress-strain pairs, or compare measured radial profiles to computationally simulated equivalents.

Unfortunately non-isotropic dynamic behaviour convolves radial profile measurement as non-circular cross sections (expected within additive samples due to the transverse orthotropy known to exist within the microstructure) cannot be recorded from only a single profile. Instead, to map non-uniform radial profile evolution requires at least a trio of synchronous measurements recorded at known orientations, as conducted by Wielewski *et al.* [205] on traditional Taylor impacts. The replication of this technique, in a reverse Taylor impact setup, under vacuum and potentially at temperature,

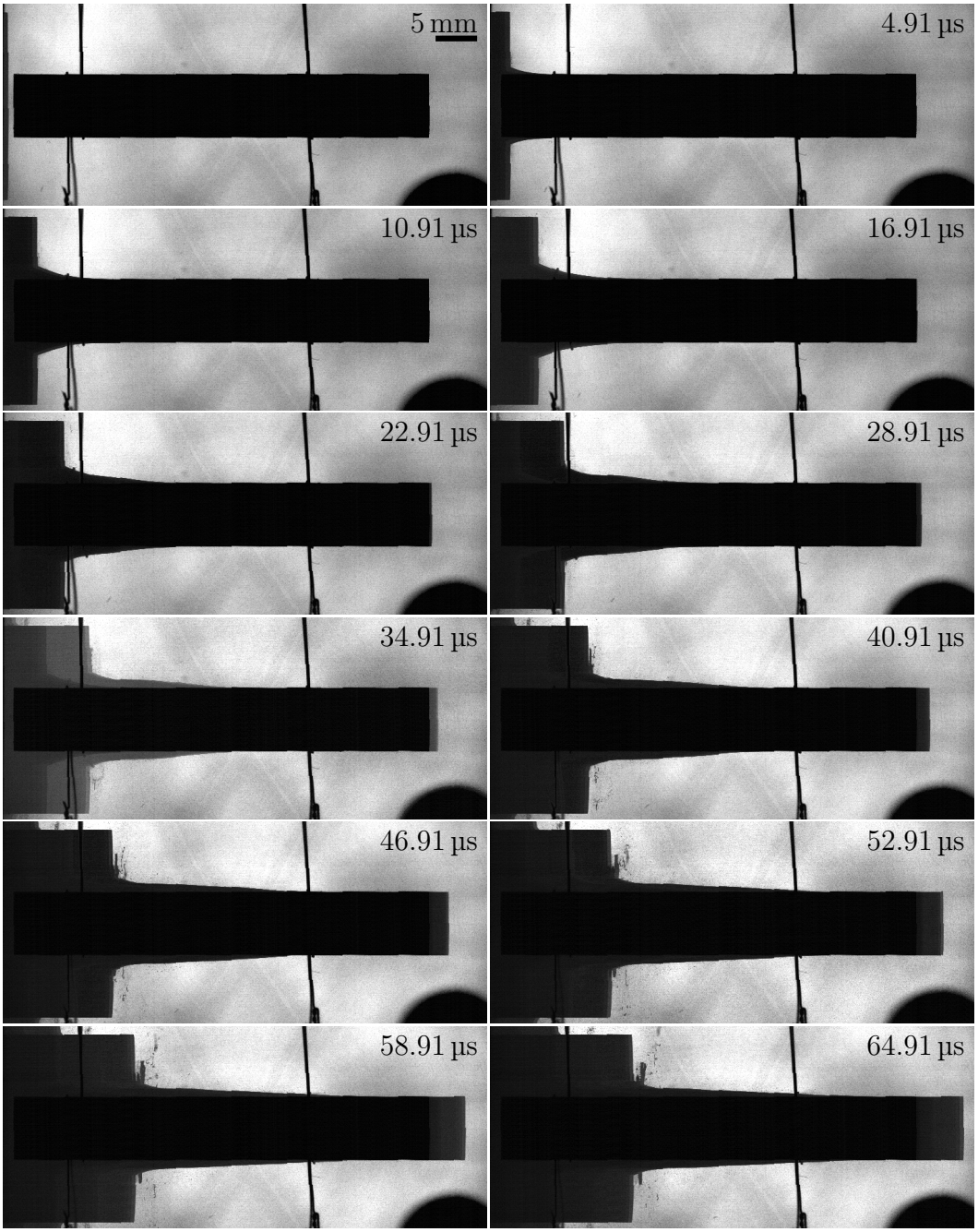

Figure 7.9: Sample Kirana image series, with the target mounted using the small wire cradle seen in figure 7.3. An example of the characteristic intermittent severe ghosting can be seen in the 7th frame, at 34.91 µs post impact, with minor ghosting visible on several other frames.

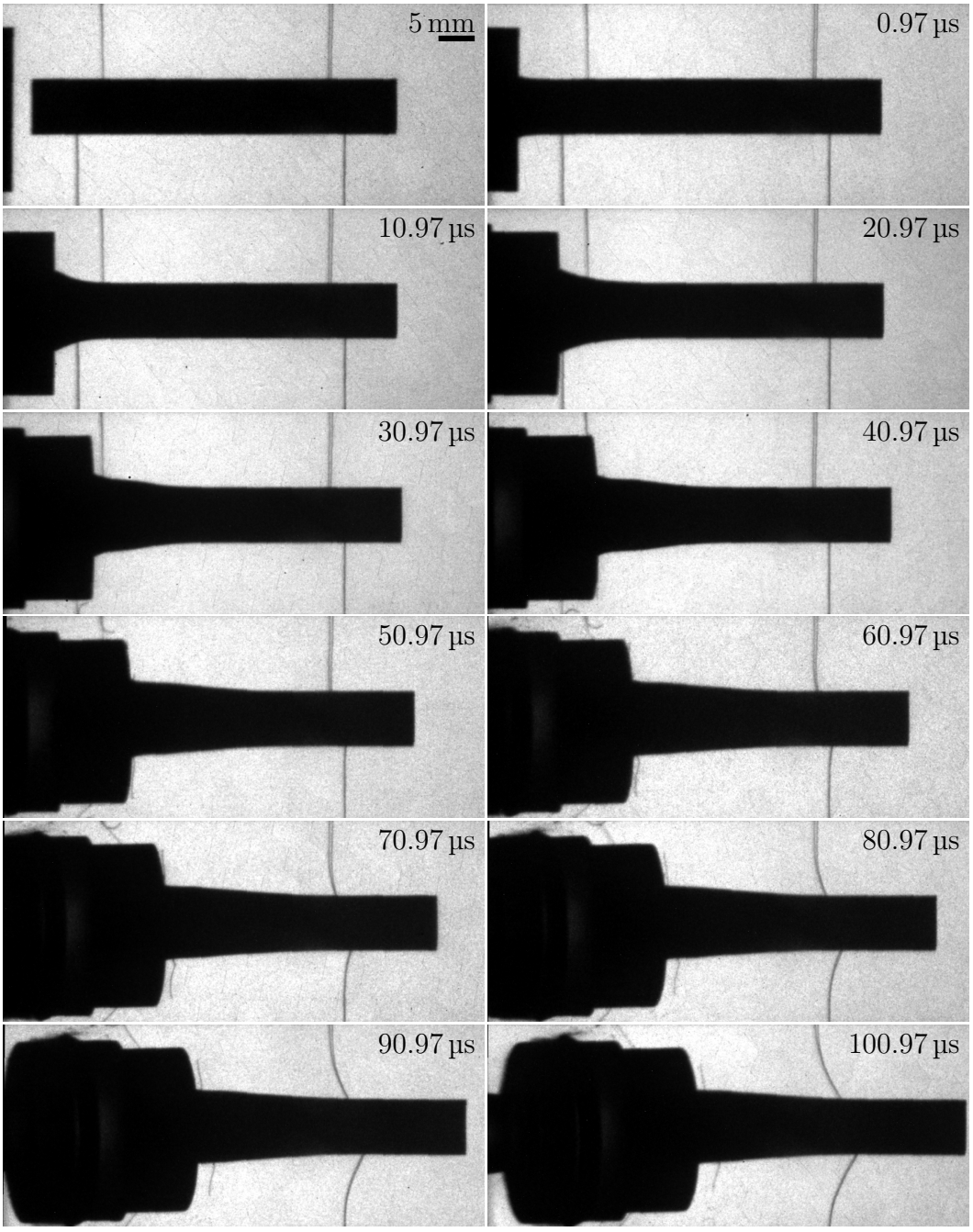

Figure 7.10: Sample SimX16 image series with the target mounted in the larger wire array seen in figures 7.4 and 7.6.

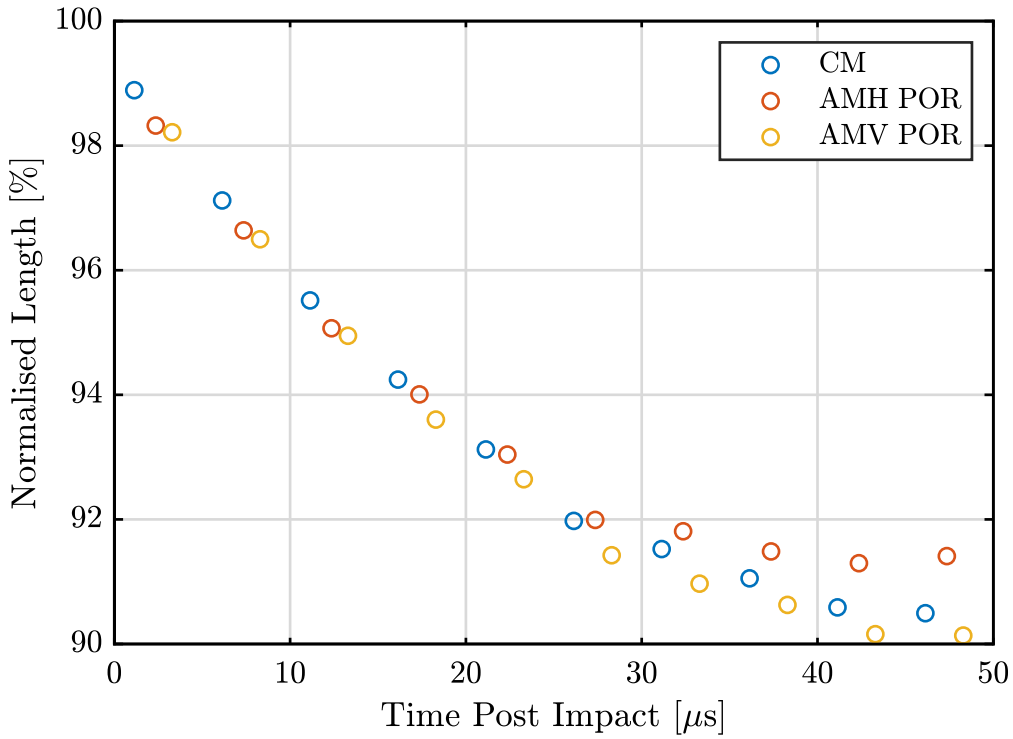

Figure 7.11: Length evolution of porous additive and conventional Taylor samples following impact at approximately 177 m s^{-1}.

was considered, however ultimately the measurement of length evolution from a single recorded imaging profile was preferred given the already challenging diagnostic array fielded.

In order to measure the length evolution from recorded imaging data, a series of steps were taken. Firstly, images from before and during the impact were rotated such that the target axes aligned to the image axes, correction of non-rotational distortion was avoided following the parallax mitigation discussed in section 7.3.1. From here, effective pixel sizes were computed using the known target dimensions. Armed with this calibration the position of both the front surface of the flyer and rear surface of the target could be tracked. These positions were then mapped over time with sample length determined from the separation between faces, producing a set of results similar to that seen in figure 7.11.

Due to the similarity in behaviour observed within the length evolution results there is limited ability to effectively draw conclusions from these measurements alone, albeit with an awareness that late stage disparity in the observed AM horizontally

oriented response may suggest increased strength at some state of effective plastic strain. However, to draw more than broad conclusions from such a result would require significant assumptions. Instead, it was decided to pass the full set of results through to augment the population of measured behaviour, against which constitutive models could be optimised against. This strategy ensured the use of the recorded behaviour to form valid conclusions, whilst also highlighting the effectiveness with which PDV can be used to reveal subtle variations in material response.

7.4 Rear Surface Velocity

Whilst imaging provides an excellent diagnostic for recording profiles, the measuring of radial or axial deformation shows limited, if any, sensitivity to the behaviour of elastic waves within the sample, instead highlighting the deformative effect of plastic waves traversing the rod. In contrast to this, laser velocimetry offers a clear measurement of both elastic and plastic waves as they traverse the sample, with the measurement of rear surface motion the primary reason for conducting this experiment in a reverse configuration. To this end the rear surface velocity of the sample was recorded in every reverse Taylor impact conducted, in addition to the velocity of the flyer impact face. This secondary measurement quantified both the impact time and velocity to the high levels of precision needed for creating an accurate digital twin and facilitating the comparison of the simulated sample rear surface response of said digital twin to the experimentally recorded dataset.

7.4.1 Optical Setup & Example Data

In practice the recording of these quantities involved fielding two frequency shifted PDV diagnostics, the theory underpinning which is detailed in chapter 6. These diagnostic measurements were located as shown in figures 7.1 and 7.4, producing results of the form seen in figures 7.12 and 7.13. In earlier tests a pair of 0.4 mm spot size collimating optical probes were used to field the pair of velocimetry measurements, however in later experiments a focusing probe with a 1 in. diameter and 250 mm focal

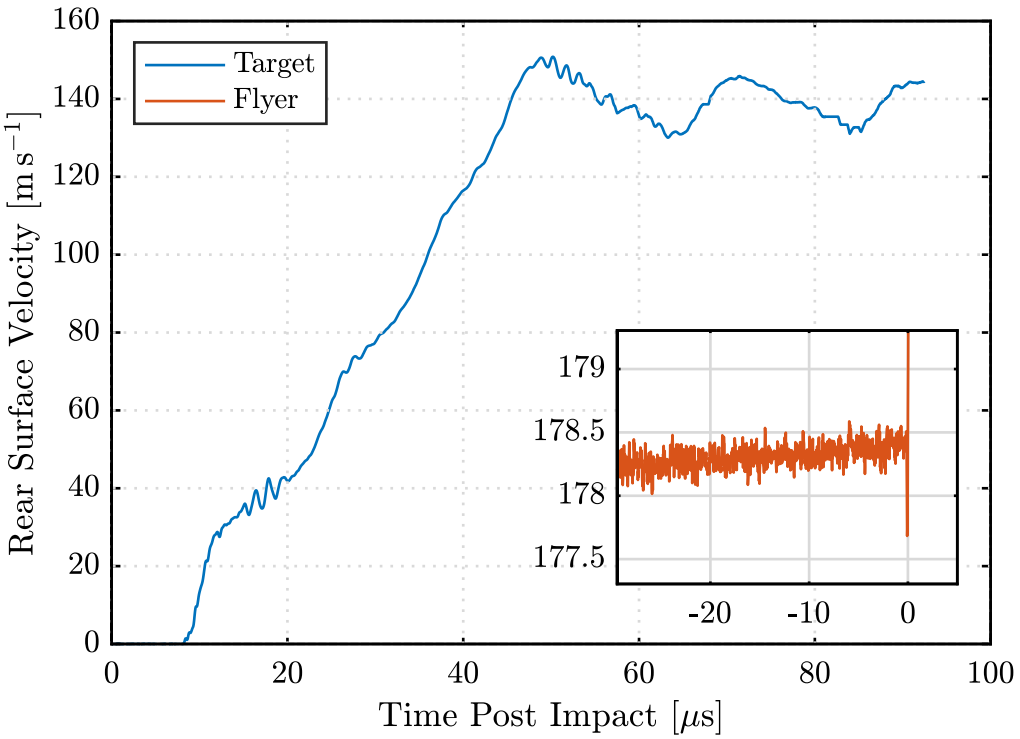

Figure 7.12: Surface velocity traces from reverse Taylor impact on an additively manufactured, horizontally oriented sample with significant layered porosity.

length was used to record target motion. The change in probe reduced the sensitivity of the target velocimetry to the adverse effects of tilt during impact. Specifically, careful positioning and alignment of the probe ensured the target rear surface passed through the lens focus approximately halfway through the impact event, with the large diameter of the probe retaining sufficient return signal at tilts well beyond that supported by the initial collimating probes. Whilst this alteration was not necessitated by a lack of effective measurement from the original setup, the improvements allowed for a reduction to the window size used during sequential fourier analyses, improving the overall temporal precision of the diagnostic.

Considering the observed rear surface motion in both of these examples, a characteristic sloped stepped form is seen in the response with the surface accelerating sequentially upon the longitudinal reverberation of the dominant elastic wavefront traversing the sample. This stepped acceleration shows a gradual loss of coherence consistent with the dispersion of the elastic wavefront, likely due to interactions with the ever increasing region of plastic deformation in the frontal half of the sample, and

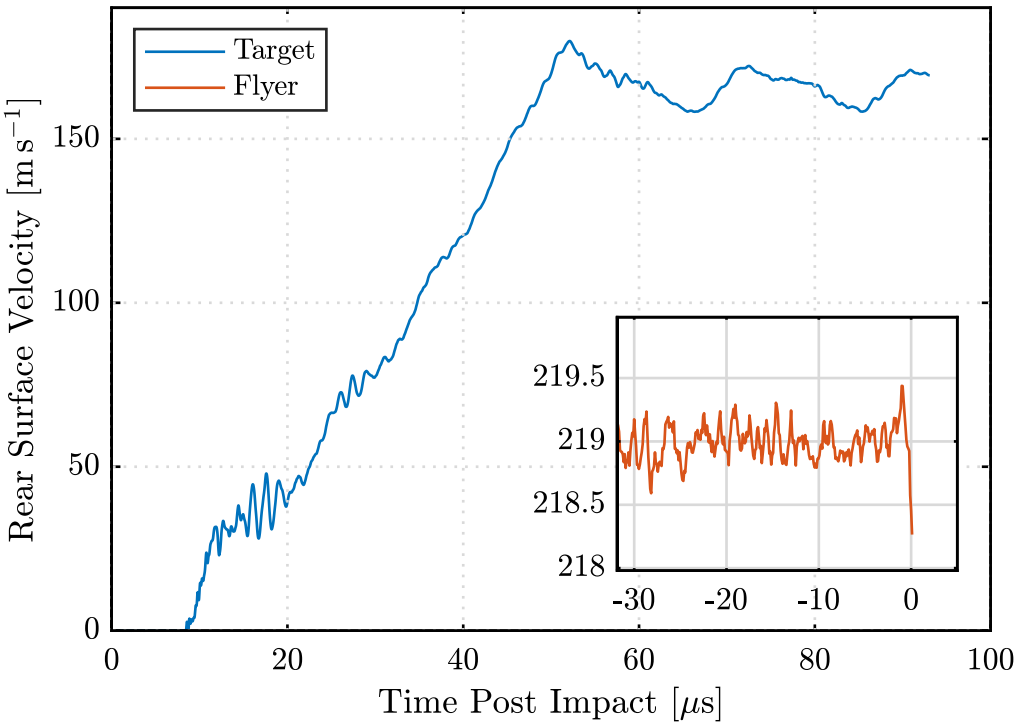

Figure 7.13: Surface velocity traces from reverse Taylor impact on an additively manufactured, vertically oriented sample without significant layered porosity.

due to radial release effects that are also seen to drive high frequency modes in the early stages of the rear surface acceleration [206]. Upon the completion of deformation within the sample, and separation between the sample and the projectile, a steady state periodic motion is seen, with this corresponding to the longitudinal reverberation of remaining elastically supported waves within the sample. Data following the same form as figures 7.12 and 7.13 was recorded for every Taylor impact experiment, albeit with a less stepped from seen at elevated temperatures, and is presented in full in section 13.2.

7.4.2 Radial Mode Dampening

Considering the behaviour of Taylor sample rear surfaces during the initial post-breakout period, as visualised for 6 impacts in figure 7.14, an unequal magnitude of high-frequency radial release oscillations are seen superposed atop the characteristic stepped wave profile. In the observed response of conventional samples, prior literature results [199, 207] considering the rear surface motion of a sample during reverse Taylor impact, and in finite element simulations, clear high frequency radial modes

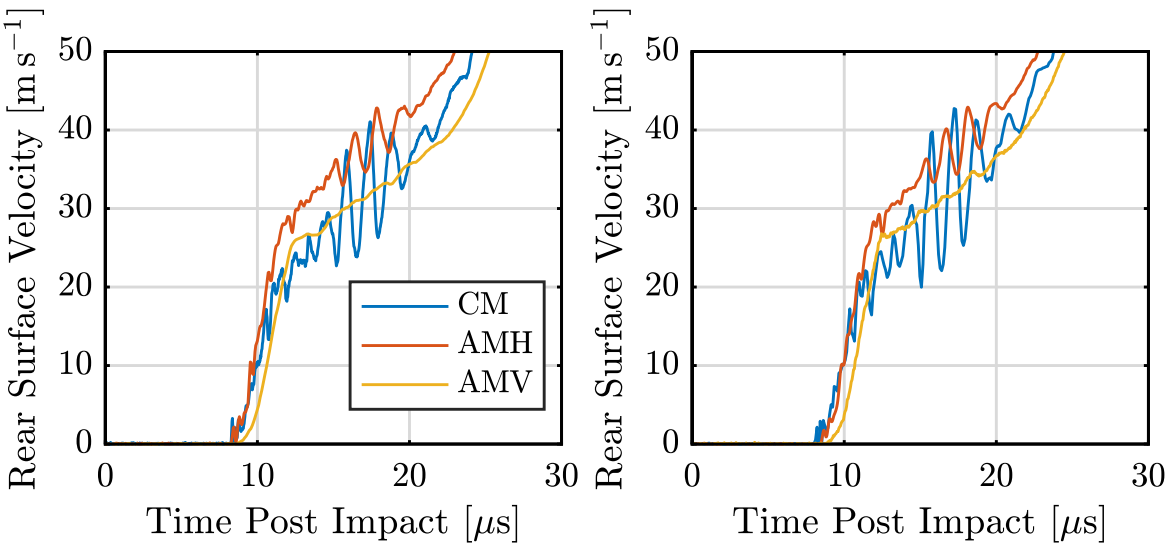

(a) $v_{Imp} = (177 \pm 3)\,m\,s^{-1}$ (b) $v_{Imp} = (242 \pm 3)\,m\,s^{-1}$

Figure 7.14: Initial response of porous additive samples and conventional counterparts. Disparities in the amplitude of high frequency radial modes in the initial elastic plateau within the period from 10 µs to 20 µs highlight the role of porosity, partially structured porosity, in the dissipation of elastic wave structure.

are observed. The consistency with which these modes exist strongly suggest that a form of damping is likely occurring within porous additive samples.

Considering the measured porosity existing within these samples, as detailed in chapter 5, possessing a horizontally layered structure, it seems logical that these layers of porosity are impairing the propagation of coherent elastic wavefronts throughout the samples, leading to the observed atypical attenuated response. Similar trends are also seen with the atypical responses observed during spallation testing of porous additive samples, detailed in chapter 8, and in literature on split Hopkinson pressure bar loading of sintered additive materials [32], lending support to the hypothesis that this effect is driven by the porosity distributions. Furthermore, within the subset of additively manufactured samples, increased damping of the high frequency radial modes is observed in vertically oriented cases. Here it is hypothesised that successive layers of repeated scattering, the effects of which are observed in axially oriented motion, are exacerbating dissipation of the elastic wavefront. In horizontally oriented cases the presence of relatively (in comparison to vertically oriented samples) dense planes of material that contain the rod axis, may serve to mitigate the complete

annihilation of the high frequency modes upon the initial reflection at the rear surface.

7.4.3 Initial Elastic Wavefront

Whilst quantitative measurements have been proposed for the Taylor impact test based upon post-impact geometry [188, 193, 194] and upon imaging data [195, 206], the most direct link between measured response and material properties was made using the amplitude of the initial elastic wavefront traversing the rod by Rohr *et al.* [199, 208, 209] and Bagusat *et al.* [210]. This method uses traditional one-dimensional theory, as discussed in chapter 4, to convert the velocity jump of this wave to an associated stress using the relation:

$$\sigma = \frac{1}{2}\rho\, c_L\, (\Delta u_{FS})\,,$$

where ρ is material density, Δu_{FS} the change in free surface velocity at the rear of the Taylor rod upon reflection of the wavefront, and c_L the longitudinal sound speed, used here given that the wave itself is elastic. Values for material density were calculated geometrically, with longitudinal sound speed taken from literature published by Gray *et al.* [125].

The use of one-dimensional relations here is notwithstanding the obvious lack of one-dimensional conditions observed during impact and the low sample aspect ratios, given axial length is many times greater than diameter of the impacted cylinder. As such, the stress evaluated using this method is interpreted as a lower bound on the supported elastic stress in the sample, with lateral release effects reducing the pressure state within the initial elastic wavefront as it traverses the length of the rod. This release in turn reduces the magnitude of resultant acceleration induced upon reflection, and therefore the calculated associated stress that is ultimately reported in table 7.4.

It is entirely reasonable however, to compare the magnitude of supported elastic stress at the rear of the rod between samples undergoing impact at similar velocities. An arbitrary threshold for the impact velocity disparity of $<5.0\,\mathrm{m\,s^{-1}}$ was considered within the bounds for similarity, with awareness that slight scatter in impact velocity

ShotID	PDV Temporal Resolution [ns]	Δv_{Init} [m s^{-1}]	Density [kg m^{-3}]	Associated Stress [MPa]
CM RT TT 1	25.6	21.0	7940	475
AM H POR RT TT 1	51.2	28.6	7760	637
AM V POR RT TT 1	102.4	24.8	7670	545
CM RT TT 2	102.4	21.7	7950	491
AM H POR RT TT 2	29.8	28.0	7750	622
AM V POR RT TT 2	51.2	25.4	7710	561
CM RT TT 3	51.2	21.6	7930	489
AM H POR RT TT 3	102.4	26.8	7720	593
AM V POR RT TT 3	51.2	26.5	7780	590
CM RT TT 4	25.6	20.0	7940	452
AM H POR RT TT 4	102.4	27.8	7770	619
AM V POR RT TT 4	102.4	24.9	7710	550
AM V DEN RT TT 1	25.6	29.1	7910	660
AM V DEN RT TT 2	25.6	28.6	7930	649
AM H DEN RT TT 1	51.2	28.8	7940	657
AM H DEN RT TT 2	51.2	26.9	7920	611
AM H DEN HT TT 1	51.2	20.3	7920	460
AM V DEN HT TT 1	51.2	17.9	7920	406
CM HT TT 1	102.4	12.7	7940	289

Table 7.4: Data pertaining to the evaluation of initial pulse height stresses in reverse Taylor impacts. The specific analysis parameters for the PDV traces themselves are provided in the appendices.

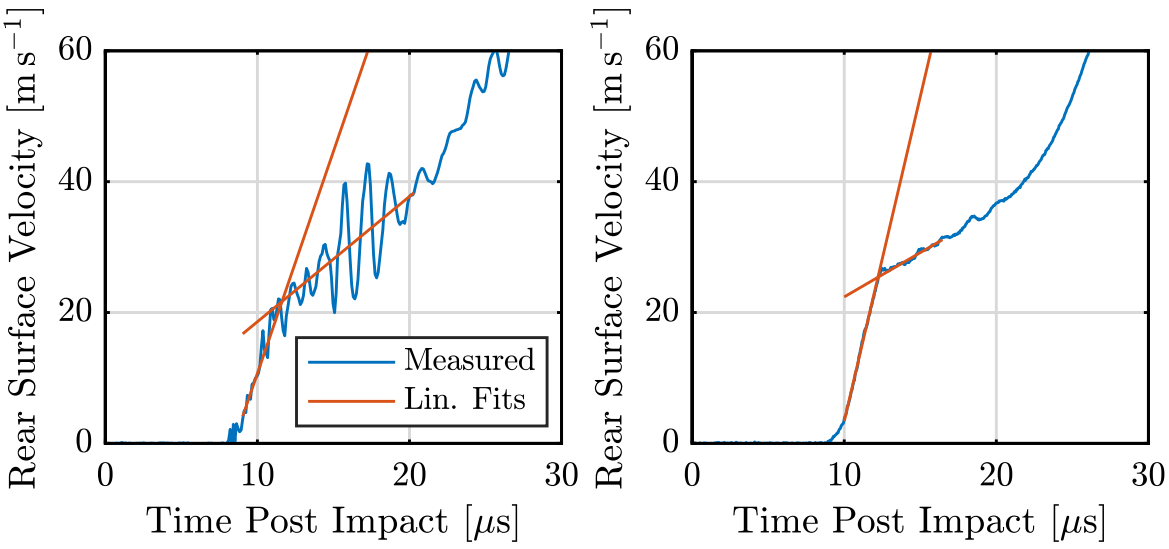

(a) CM RT TT 2 (b) AMV POR RT TT 2

Figure 7.15: Example calculation of the initial velocity jump from measured target rear surface motion during Taylor impact. The height of the jump is taken from the intersection of the pair of linear fits seen within each figure.

is inherent to gas gun loading with single experiment impacts[1]. Considering this, it is possible to compare the stress jump observed at three distinct velocities: $(177 \pm 5)\,\mathrm{m\,s^{-1}}$, $(286 \pm 5)\,\mathrm{m\,s^{-1}}$ and $(301 \pm 5)\,\mathrm{m\,s^{-1}}$

Firstly, considering the trio of impacts conducted at approximately $177\,\mathrm{m\,s^{-1}}$ a clear increased associated stress is seen in both porous additive samples compared to the conventional equivalents. This increase is recorded despite the known layered porosity distribution existing within the additive samples that would undoubtedly decrease the resultant stress in the initial elastic wavefront due to scattering and plasticity occurring within stress concentrations induced around pores upon arrival of the wavefront. The increase in supported stress present within additive samples, particularly the horizontally oriented samples that exhibit associated stresses exceeding vertically oriented equivalents, follow observed behaviour within literature [125, 132], with the increase attributed to the complex hierarchical grain structure, including additional low angle grain boundaries [86] atop that expected within conventional wrought 316L stainless steel.

Secondly, considering the five impacts conducted at approximately $301\,\mathrm{m\,s^{-1}}$, all additively manufactured samples again show a clear improvement in specific strength when compared to the conventional baseline, with dense additively manufactured samples showing a further increase in associated stress when compared to porous additively manufactured equivalents. Interestingly, the directionality observed in porous samples is reversed in the dense samples, with vertically oriented dense samples showing the greatest associated stress, higher than the horizontally oriented counterpart. This flipped relationship, paired with the apparent increase in associated stress in both dense horizontal and vertical specimens at lower impact velocities respectively, suggest that differences below $1\,\mathrm{m\,s^{-1}}$ may in fact be negligible, with these differences potentially stemming from subtle amounts of tilt or even inherent mechanical heterogeneities within the bulk materials.

Finally, considering the trio of impacts conducted at elevated temperatures at ap-

[1]Gun loading on large bore gas guns can facilitate the simultaneous impact of several targets at a single velocity, however conducting such experiments would be prohibitively costly.

proximately $286\,\mathrm{m\,s^{-1}}$, the improved specific strength of additive samples, including the directional behaviour seen in additive samples at lower velocities, is again replicated at elevated temperatures. This lends support to the hypothesis that the thermal softening exhibited is isotropic, and independent of manufacture route. This is not unexpected, as the underlying microstructural lattices of both additive and conventional steel will be the same (in terms of atomic arrangement and electromagnetic potentials), such that the similarity of atomic potentials will in turn enforce similar thermal softening behaviour.

7.5 Conclusions

Reverse Taylor impact testing subjects material to complex loading scenarios with strain rates in excess of $10^3\,\mathrm{s^{-1}}$, revealing some interesting behaviour and contextualising trends in dynamic AM 316L response within the wider field of AM mechanical performance. The population of dynamic response data presented in this thesis represents significant experimental work, with iterative improvements generating data that may be used to parametrise directional rate-sensitive constitutive material strength models effectively.

The first clear conclusion of this testing is the increase in specific strength offered by all AM samples above CM counterparts across strain rates, orientations, and temperatures, as seen in the elevated elastic wavefront amplitudes supported by AM samples. This trend has been seen in other studies, though the observation has been conducted at lower strain rates using either quasi-static testing frames or split Hopkinson pressure bar apparatuses.

Expanding on the above conclusion, elevated specific strengths come with the clear caveat of directionality in samples that show significant porosity. This porosity, observed separately to exist in a layered distribution, serves to reduce performance in general, with a greater suppression of performance observed when loading along the build direction. Despite this, all AM samples showed significant strength improvements above CM equivalents. The presence of directionality is not immediately apparent in

near fully dense AM samples, though this was further studied through the use of digital twins in iterative inverse modelling routines discussed later.

Finally, where present porosity also serves to to disperse localised stress fronts propagating through the samples. This effect is seen in the attenuation of radial release modes, which posses higher frequencies than their longitudinal counterparts. This attenuation is particularly prevalent in vertically oriented samples where layered porosity exists oriented normal to the target axis, highlighting the geometrical influence of the porosity distribution upon wave dynamics.

Chapter 8

Spallation Testing: Atypical Behaviour

8.1 Overview

As discussed in chapter 2, a small amount of spallation testing has already been conducted on AM material, with results suggesting improved spallation strength in 316L stainless steel [125], titanium [110], and tantalum [112] alongside a directionally dependent spallation strength in the latter two. Currently a gap exists in the literature concerning the directional response of additively manufactured 316L stainless steel when subjected to dynamic tensile loading at strain rates above $10^4\,\mathrm{s}^{-1}$, and in the effect that porosity could have on this response. In this work testing was done on both porous and dense AM 316L stainless steel samples, as detailed in table 8.1, in both horizontal and vertical orientations. These were paired with comparison to CM equivalents to contextualise observed responses.

8.2 Initial Campaign: Porous Response

Testing was conducted in two campaigns with improvements in experimental configuration, implemented between campaigns, detailed later in this chapter. In the first round of testing a setup was used partially inspired by Jonsson *et al.* [211], with a target design as shown in figure 8.1. This design used a pair of polycarbonate discs, also referred to as rings. In the forwardmost of these the target was mounted whilst diagnostics were located behind, facilitating the recording of a single rear surface velocity trace, and measurement of the stress through standard one-dimensional shock methods [43, 44, 212] as discussed in chapter 4.

The impact tilt was intended to be calculated using impact times and velocities as recorded on three 120° spaced tilt probes set at a PCD of 16.0 mm from the centre of the

ShotID	Material (& Orientation)	Size [mm] (⌀ × ↕)	Mass [g]	Target Form
CM SP 1	CM 316L	9.50 × 2.00	1.12	Fig. 8.1
AM V POR SP 1	AM 316L (Vertical)	9.75 × 2.08	1.19	Fig. 8.1
AM H POR SP 1	AM 316L (Horizontal)	9.56 × 1.99	1.10	Fig. 8.1
CM SP 2	CM 316L	9.52 × 2.00	1.12	Fig. 8.1
AM V POR SP 2	AM 316L (Vertical)	9.69 × 2.00	1.13	Fig. 8.1
AM H POR SP 2	AM 316L (Horizontal)	9.56 × 1.99	1.11	Fig. 8.1
CM SP2 1	CM 316L	26.71 × 2.94	13.09	Fig. 8.4
AM H DEN SP2 1	AM 316L (Horizontal)	26.95 × 2.98	13.43	Fig. 8.4
AM V DEN SP2 1	AM 316L (Vertical)	26.96 × 3.01	13.60	Fig. 8.4
CM SP2 2	CM 316L	26.70 × 2.94	13.09	Fig. 8.4[1]

Table 8.1: Overview of spallation sample manufacture process and dimensions, which are given as diameter (⌀) multiplied by thickness (↕). Experimental configurations are given showing two variants of setup, with these referencing either figure 8.1 or 8.4 where each setup is detailed.

target. Using these measurements, expected to echo flyer behaviour in reverse Taylor impacts as presented in figure 7.12, offset locations representing the flyer surface could be calculated at each tilt probe location according to its impact time and velocity. Reconstructing the flyer surface from these three points, the impact tilt could then be evaluated using simple vectorial expressions, with impact time evaluated using the calculated offset at the centre of the target. This impact time could then be used to align rear surface velocity measurements between experiments.

With figure 8.1 showing an idealised setup, the images in figure 8.2 show the setup in practice. Both rings were attached, using nylon screws, to an interfacing metal mounting piece that was itself concentrically threaded onto the muzzle of the barrel. Using small malleable O-Rings as spacers sandwiched between polycarbonate rings, the rear diagnostic disc could be deliberately tilted by varying the relative engagement of the nylon screws. This control allowed alignment of the velocity probe, mounted centrally in the rear diagnostic disc, to the rear surface of the target. Alignment was quantified using the round trip signal loss of the velocity probe, with minimisation of this maximising the amount of light coupled back into the probe following reflection,

[1]Here only a single diagnostics ring similar to figure 8.1 was used with a single centered probe, allowing comparison between offset and centered probe measurements.

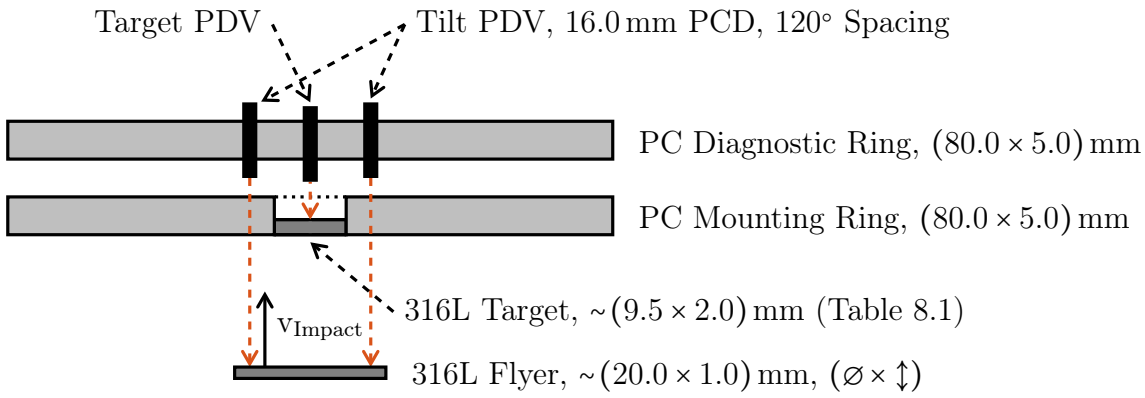

Figure 8.1: Experimental setup for first round of spallation experiments with a stainless steel target mounted inside a polycarbonate ring, backed by a second polycarbonate diagnostics ring containing PDV probes. Dimensions of the sample, target, and rings are given as approximate values for diameter (⌀) multiplied by thickness (↕). Precise values for target dimensions are available in table 8.1 as detailed in the above figure, precise values for the flyer dimensions were recorded and are provided in the appendix.

thus effectively aligning it to the target rear surface normal assuming an approximately specular reflection.

Augmenting velocimetry, a pair of light gates were mounted ahead of target, within the interfacing metal mounting piece threaded to the muzzle, to provide a trigger signal for data acquisition. These are not shown within this section for concision, however an example of this diagnostic as used in both reverse Taylor and spallation testing is provided in section 13.1 for completeness.

No alignment capability was implemented for tilt probes due to the use of a bare FC-PC fibre connectors as probes themselves. It was believed the inherent divergence of these bare fibres, paired with the need for only a brief measurement from a specular surface in close proximity moving towards the probe, would negate the need for independent alignment beyond that achieved for the velocity probe mounted within the same diagnostic disc. The error in location of these probes can be reasonably assumed below 100 µm with this attributed to the manufacturing tolerances of the diagnostic discs themselves.

Using the setup as described six impacts were conducted, three at both $344\,\mathrm{m\,s^{-1}}$ and $446\,\mathrm{m\,s^{-1}}$, with the measured rear surface velocities presented in figure 8.3. Un-

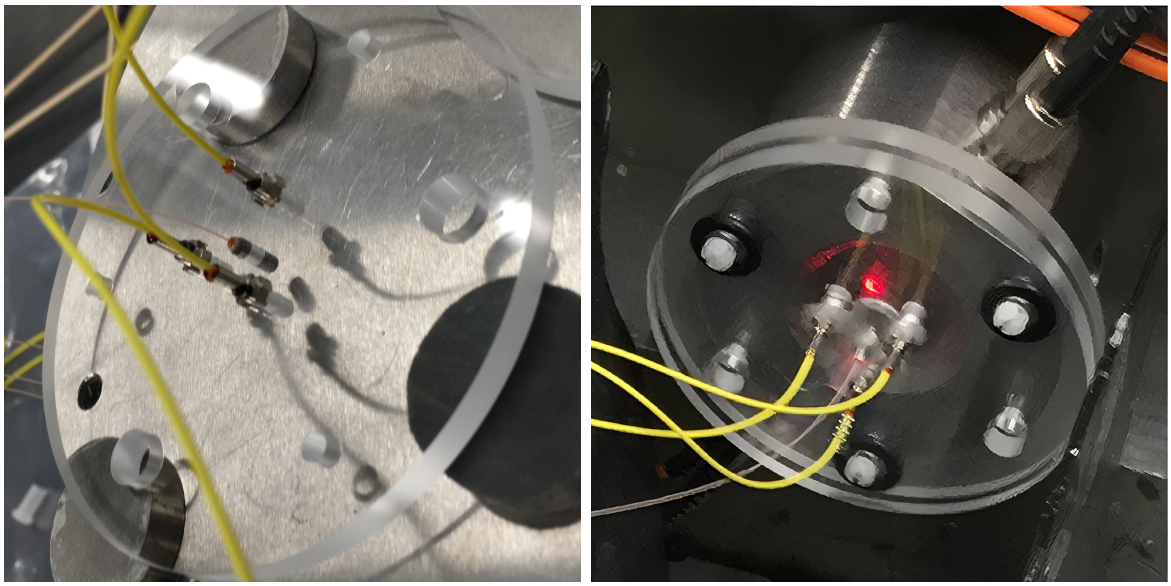

(a) Diagnostic ring prior to mounting. (b) Setup mounted to muzzle of barrel.

Figure 8.2: Example images of the setup detailed in figure 8.1. In both images three tilt probes (identified by yellow sleeved fibre optics) can be seen radially spaced at 120° intervals surrounding a singular velocity probe (identified by bare fibre optic).

fortunately, suitably precise measurement of the impact times were not achieved due to both significant round trip loss within tilt probes (limiting signal to noise ratios and in turn the temporal resolution of the sequential fourier transform analysis) and a limited flyer velocity change immediately following impact with the polycarbonate target ring. Noted here is the gap of over 3 mm between the center of each tilt probe and the edge of the comparatively dense target. The presented velocity traces are therefore aligned using the breakout of the rear surface, with later impacts rectifying the issues encountered.

Reviewing figure 8.3, while the response of CM samples clearly include a characteristic pull-back signal from around 0.6 µs to 0.75 µs after breakout, the same cannot be seen for any of the AM samples tested at either velocity. This lack of pull-back signal is attributed to the presence of porosity, with this also dispersing the plastic compressive wavefront and slightly reducing the peak compressive stress state compared to conventional responses. The reasoning for this is similar to that found in recently published spallation testing on Ti-6Al-4V [40], with an ensemble of dispersive effects drastically suppressing the coherence of generated wavefronts as they interact

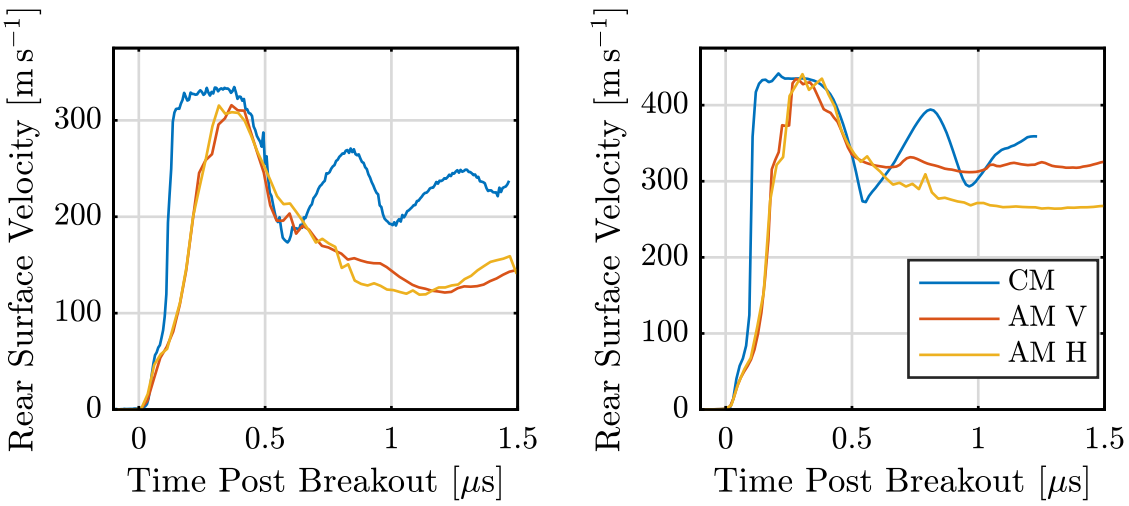

(a) $v_{Imp} \approx 344\,m\,s^{-1}$ (b) $v_{Imp} \approx 446\,m\,s^{-1}$

Figure 8.3: Rear surface velocity profiles for spallation tests conducted on conventional and porous additively manufactured 316L stainless steel in the first series of spallation tests, times are given post breakout due to issues in mitigating cable delays.

with the internal free surfaces of the preexisting porosity.

The same pores would then also interact with the reflected release fans, dispersing both forwards and backwards moving characteristics and seeding compressive pulses at internal free surfaces. Scattering to both groups of tensile release fan characteristics would alter measured rear surface motion in the post-plateau region, causing the atypical signal that understandably displays no clear compressive spallation pull-back feature. It is suggested that the lack of a clear pull-back signal not only stems from the above dispersive effects, but also a diverse spread of defect driven failure locations, with these limiting initial coherence in the compressive characteristics generated following failure. Further convolving the dispersed compressive pulse, characteristics may then interact with preexisting porosity or further nascent failure sites as they propagate towards the rear surface of the target, further inhibiting formation of the classical spallation waveform.

Considering the form of the post-plateau regions within porous additive responses, there is some evidence to support attributing the atypical response to porosity. The comparatively prolonged tail of post-plateau deceleration observed in the horizon-

tal additive response in figure 8.3b, over the equivalent vertically oriented response, suggests increased wave scattering within the horizontal sample. Given that a horizontally layered porosity distribution is known to exist in these samples, an elevated coherence would exist in the through-thickness positioning of failure sites within vertically printed samples, where the layers of porosity themselves align to the excited failure plane. Conversely, within horizontal samples the layers of pores would fall along the through-thickness direction. With such an alignment, a layer of pores could successively convolve failure driven reflected compressive pulses, leading to a further reduction in any semblance of observed pull-back.

The lack of similarity in the post-plateau additive responses in figure 8.3a does not support the assertion, however it does not suggest the converse. It is possible that this variance could stem from inconsistencies within the spatial distribution of manufactured porosity inherent to the subtle inconsistencies within the additive manufacturing process.

Unfortunately, given the collected data, it is difficult to offer firm conclusions as to the observed atypical response as the behaviour of elastic waves and evolution of failure itself is not directly measured, rather the resultant effects of these waves following reflection at the rear surface of the target. The potential to interrogate such mechanisms *in situ* using subsurface X-ray phase contrast imaging techniques [213–216] does exist, however there are significant challenges to overcome before measurements of incoherent failure features could be obtained. This is the case for materials such as steel alloys where the high material density limits direct transmission of X-ray sources, requiring a source with a suitably high brilliance to capture dynamic events using ultra-high-speed imaging.

8.3 Second Campaign: Dense Response

Moving forward with the testing of additive material, a series of changes were implemented that sought to tackle the issues encountered when determining the impact tilt and impact time in the first round of spallation tests, and to improve both the

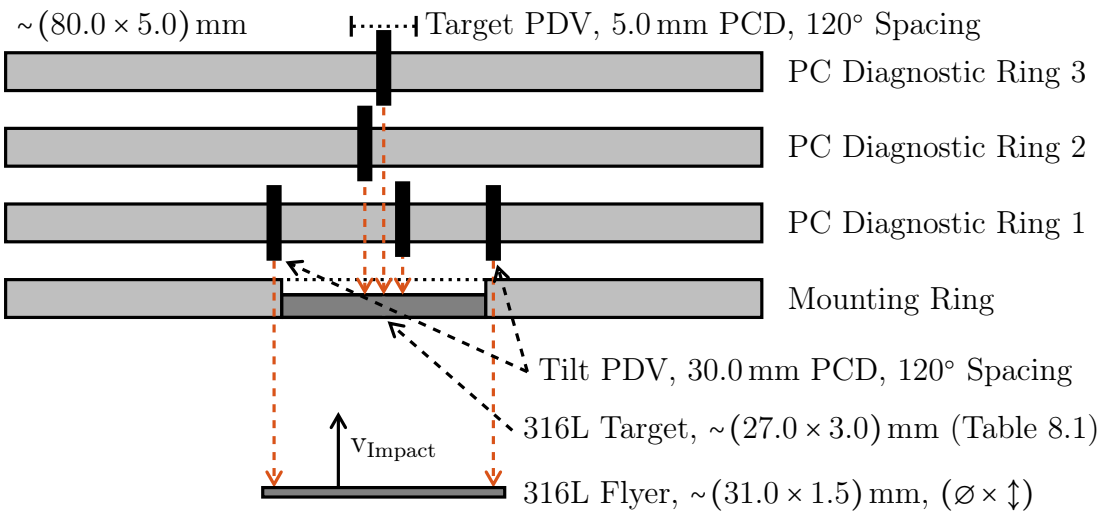

Figure 8.4: Setup for second round of spallation experiments. Developments included increasing the sample diameter, dimensions again given as diameter, ⌀, multiplied by thickness, ↕, to prolong the duration of one-dimensional conditions, and tripling the number of rear-surface PDV probes to increase the amount of recorded data. Each diagnostics ring was suspended from the mounting ring, with holes in the preceding rings both maintaining a clear laser paths to the target and ensuring independence in the alignment of each ring.

quality and quantity of captured data. With figure 8.4 showing the idealised setup, and figure 8.5 the real world implementation, the changes themselves are discussed below.

The first major change was to add two further specimen velocity probes, with the now trio of measurements set at 120° spacings in a close circular packing at a PCD of 5.0 mm, as seen in figure 8.5. The use of multiple closely packed probes is similar to recent use of PDV array probes [217] where several traces may be recorded over a given area, albeit using widely available and comparatively inexpensive components. Each velocity probe was mounted in a different diagnostic disc, with this allowing independent alignment of the probes to the target rear surface. The use of multiple rear surface velocity measurements would in turn serve to better validate the target response in the case of a similar atypical behaviour in the additive samples.

A trio of bare FC-PC fibre connectors were again mounted within the forwardmost diagnostic ring to record impact time, velocity and tilt as before, however this time

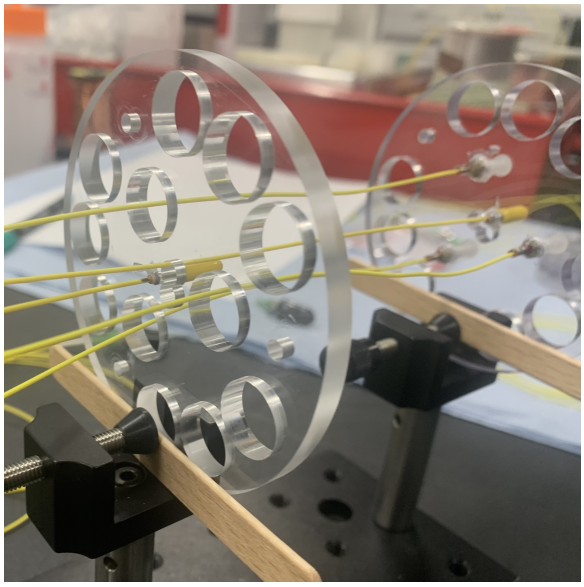

(a) Assembly of diagnostic rings.

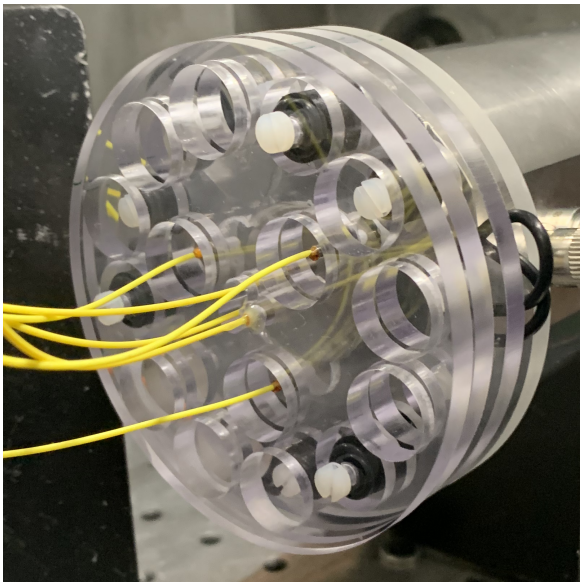

(b) Rings mounted to muzzle.

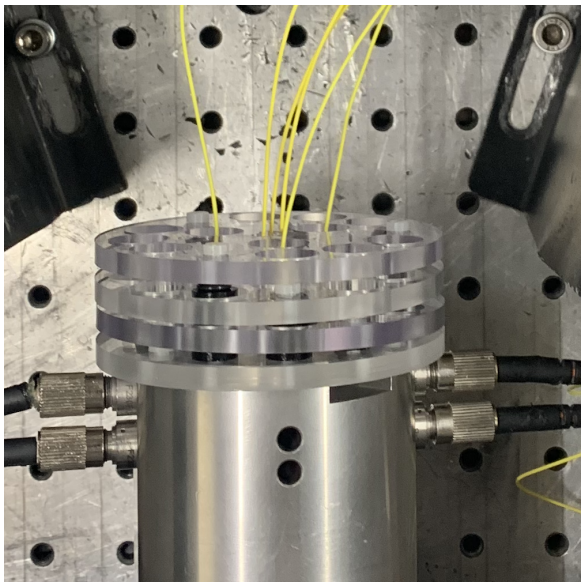

(c) View of target from above.

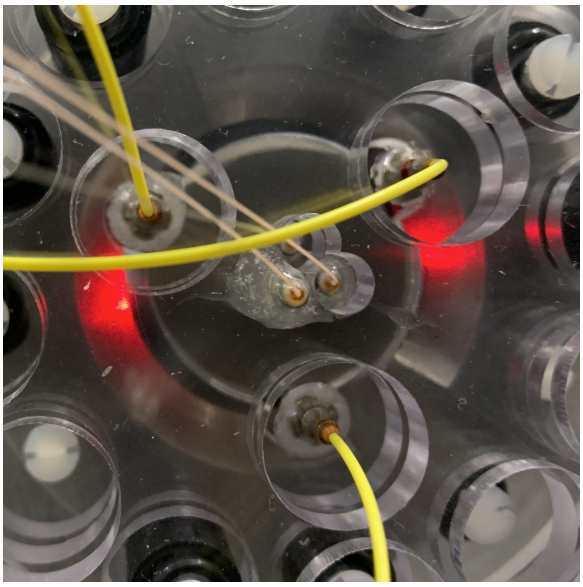

(d) Detailed view of PDV probes.

Figure 8.5: Example images of the setup detailed in figure 8.4 being constructed and after mounting to the interfacing piece. During setup velocity probes were fixed in individual diagnostic discs with fibre optic patch cables carefully threaded prior to assembly. Once assembled, three tilt probes can be seen radially spaced at 120° intervals at a PCD of 30.0 mm surrounding a trio of 120° spaced velocity probes. The velocity probes sit at a PCD of 5.0 mm offset by 60° from the tilt probes surrounding them. A pair of light gates are mounted ahead of target within the interfacing piece that is threaded to the muzzle. These provided a triggering mechanism and a redundant measurement of both impact velocity and approximate impact time.

ShotID	v_{Imp} [m s^{-1}]	Tilt [mrad]
CM SP 1	352.3 ± 0.6	
AM V POR SP 1	337.8 ± 0.7	
AM H POR SP 1	342.7 ± 0.7	
CM SP 2	441.5 ± 0.4	
AM V POR SP 2	449.5 ± 0.7	
AM H POR SP 2	449.3 ± 0.4	
CM SP2 1	440.0 ± 1.2	1.5 ± 0.3
AM H DEN SP2 1	446.7 ± 0.3	3.7 ± 0.3
AM V DEN SP2 1	442.8 ± 1.2	3.1 ± 0.3
CM SP2 2	438.8 ± 1.0	2.4 ± 0.2

Table 8.2: Overview of impact velocities and tilt of spallation impact tests conducted. Of note is that tests using the latter setup visualised in figure 8.4, where impact tilt was calculable and is therefore reported, all exhibit impact tilts of below 5 mrad, which is widely considered a benchmark for planarity within plate impact experiments.

two alterations were implemented to improve impact detection. Firstly the impact surface of the flyer was mirrored using 5 µm grade optical finishing papers in addition to, and following on from, the previously used coarser abrasives, with this drastically reducing round trip loss for the tilt probes. Secondly, the probes were now mounted at a PCD only 3.0 mm larger than the diameter of the target. By positioning the probes closer to the edge of the target itself, an increased deviation in velocity would likely be observed upon impact, given the higher density of the steel target compared to the polycarbonate mounting disc. These improvements allowed for a drastic improvement in the quality of data, facilitating confident measurement of impact tilt, with these values listed in table 8.2.

Alongside improvements to diagnostics, the aspect ratio of the samples was increased to delay the arrival of lateral release waves within the sample. Whilst this did not appear to be an issue with the first round of experiments, given the CM sample response, increasing both the aspect ratio and sample thickness would ensure a more standard experimental configuration for spallation testing and reduce potential late stage convolution of target rear surface motion stemming from the arrival of lateral rarefaction waves.

In addition to the updates for the experimental setup in the second round of experi-

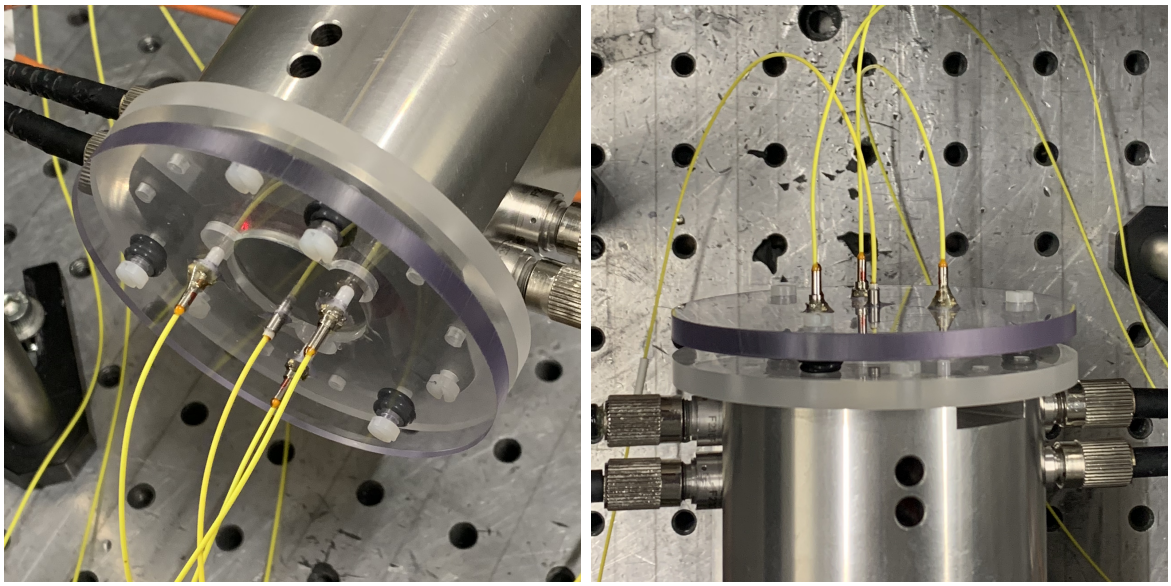

(a) Rear view. (b) View from above.

Figure 8.6: Modified setup from second round with single central rear surface velocity probe, as used in CM SP2 2.

ments, a single probe variant was designed to mimic the diagnostic setup from the first round of tests, albeit using the revised target geometry characterised by an increased aspect ratio. This single probe setup would serve to validate the triple probe variant, as were lateral release effects significantly altering the measured rear surface velocity history, a disparity would be seen when comparing single and triple probe responses in CM material. Images from this single probe setup can be seen in figure 8.6, showing the single velocity probe aligned to the centre of the target rear surface. The three tilt probes are visible located just beyond the ~ 27 mm diameter of the target at a PCD of 30 mm so as to record flyer motion at the edges of the larger 31 mm diameter flyer as described for the revised triple velocity probe target variant.

The data recorded on the rear surface velocity probes from this second round of testing can be seen in figure 8.7, with clear pull-back signals shown in all cases from 1 µs to 1.25 µs after impact, shown in detail in figure 8.7b. The similarity in the measured response of additive samples on all three probes fielded on each experiment suggest development of similar spallation responses in the material below that targeted by each probe. Furthermore, the designed presence of a one-dimensional response

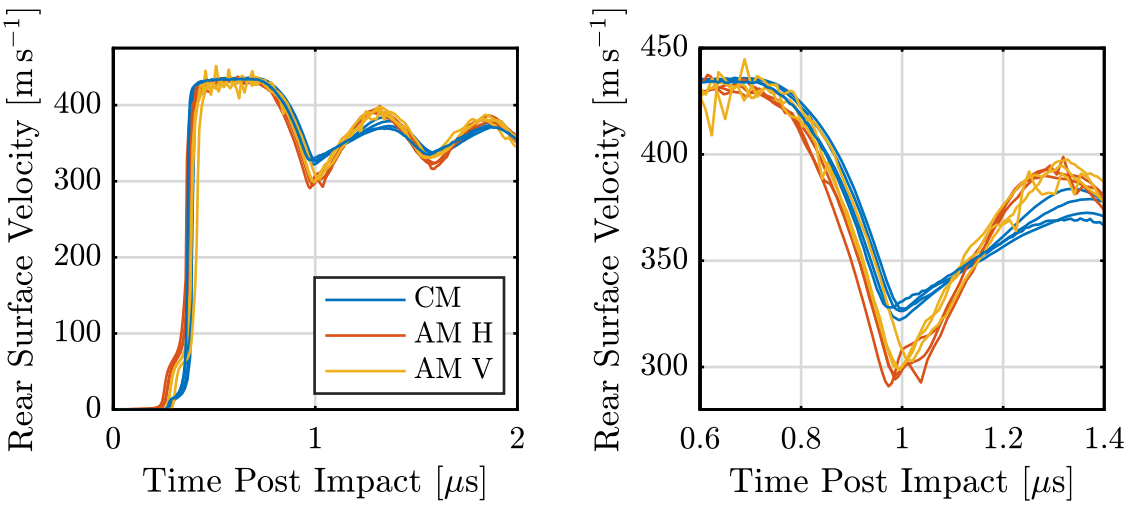

(a) Overview. (b) Pull back detail.

Figure 8.7: Rear surface velocity profiles for spallation tests conducted at $\sim 445\,\mathrm{m\,s^{-1}}$ on conventional and fully dense additively manufactured 316L stainless steel.

over this region throughout the spallation process in turn suggests the formation of a spallation plane that spans all three probes. This follows, as had an incomplete zone of spallation occurred within this region it is reasonable to assume that one of the probes would have captured a disparate response. It is suggested that the subtly increased spread of pull-back gradients observed in CM traces, as seen in figure 8.7b may stem from the formation and spread of a failure plane. The increased depth of the pull-back troughs, quantified later, in additive samples compared to CM equivalents are indicative of elevated spallation stress. Alongside this, the increased gradient of the pull-back (from 1 µs to 1.25 µs) in additively manufactured samples is indicative of a more sudden, brittle failure [218] compared to the comparably ductile conventional sample response.

Using the pull-back method given by Kanel and Gluzman *et al.* [43, 44] as discussed in chapter 4, a traditional one dimensional spallation analysis with elastoplastic correction may be considered, with the spallation rupture strength given such that,

$$\sigma_{\mathrm{Spall}} = \frac{1}{2}\rho_0\, c_B \left(\Delta u_{FS} + \left(\frac{H_S}{c_B} - \frac{H_S}{c_L} \right) \frac{\left| \left(\frac{d(u_{FS})}{dt} \right)_{\downarrow} \left(\frac{d(u_{FS})}{dt} \right)_{\uparrow} \right|}{\left| \left(\frac{d(u_{FS})}{dt} \right)_{\downarrow} \right| + \left(\frac{d(u_{FS})}{dt} \right)_{\uparrow}} \right),$$

ShotID	$\sigma_{\mathbf{Spall}}$ [GPa]		
	Probe 1	**Probe 2**	**Probe 3**
CM SP2 1	2.09	2.18	2.04
AM H DEN SP2 1	2.76	2.82	2.74
AM V DEN SP2 1	2.67	2.53	2.66
CM SP2 2	1.99		

Table 8.3: Spallation rupture strengths calculated from rear surface velocity profiles presented in figure 8.7.

with this as defined in equation 4.7. Of note here are the signs of each term, with both Δu_{FS} and $\left(\frac{d(u_{FS})}{dt}\right)_{\downarrow}$ negative, whilst $\left(\frac{H_S}{c_B} - \frac{H_S}{c_L}\right)$ is evaluated to be positive, with this leading to a negative value of σ_{Spall}. This corresponds to the tensile loading configuration, however the values presented here are swapped in sign for clarity. Applying this analysis to the measured signals yields the results as presented in table 8.3, with the increase in additive spallation strength quantified compared to the reference conventional 316L stainless steel.

Looking at the tabulated results, a small but significant directional dependency is observed in the rupture stress between horizontally and vertically oriented additively manufactured samples, matching that seen in both Ti-6-Al-4V [110] and tantalum [112] by Jones *et al.* . It was suggested by Jones that such a directional variance in failure could be attributed to tensile loading along interlayer interfaces resulting from the layered manufacturing process. This work supports the assertion, with improvements to spallation rupture strength stemming from the refined underlying directional microstructure of additively manufactured metals. Despite this agreement however, the clear disparity between porous and dense AM spallation responses highlights the key role that defects, particularly those with spatial coherence, can play in influencing dynamic response and failure.

Considering a second region of figure 8.7, a disparity is seen between additive and conventional samples in the velocity history of the HEL upon reflection at the rear surface. Looking at this closely in figure 8.8, the conventional specimens show a significantly decreased HEL magnitude, and therefore stress amplitude, compared to

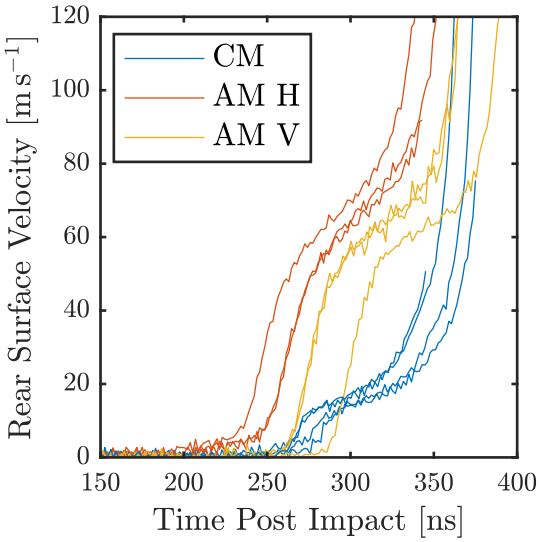

Figure 8.8: Hugoniot elastic limit wave profiles for spallation tests conducted at ~ 445 m s^{-1} on conventional and fully dense additively manufactured 316L stainless steel.

additive counterparts.

Quantifying the disparity shown in figure 8.8, the intersection of a linear fit and an exponent was used, with this effectively capturing the linear acceleration of the initial elastic stress jump and the gradual transition into the main plastic shock front following the elastic precursor. An example of this can be seen in figure 8.9 with paired fittings presented for both AM and CM elastic precursors atop the underlying raw data.

From the produced fits a velocity of the elastic precursor shoulder could be measured for each velocity trace at the intersection of the linear and exponential fits. This velocity was then converted to stress using traditional one-dimensional theory as covered in chapter 4 such that,

$$\sigma = \frac{1}{2}\,\rho_0\,c_L\,(\Delta u_{FS})\,,$$

where ρ_0 represents the material density, c_L the longitudinal sound speed (in this case used instead of the bulk sound speed as the wave is elastic instead of plastic), and Δu_{FS} the jump in normal free surface velocity as measured at the rear of the target. The density was calculated geometrically using values presented in table 8.1 with

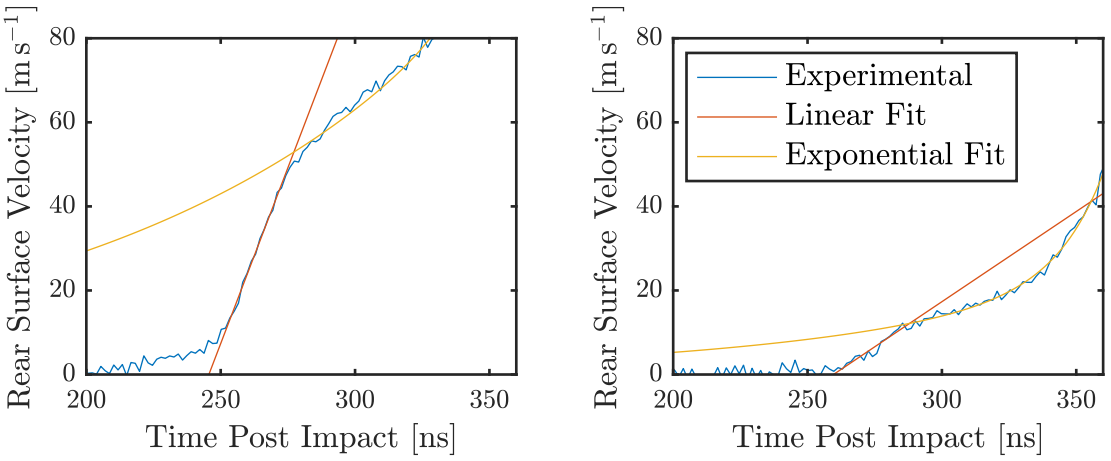

(a) Additive sample.

(b) Conventional sample.

Figure 8.9: Example measurement of the characteristic velocity of the elastic precursor in spallation tests.

longitudinal sound speed taken from Gray *et al.* [125] to be 5734 m s^{-1} and 5722 m s^{-1} for AM and CM samples respectively.

The calculated density, measured velocity jump, and associated HEL stress are presented in table 8.4, with the increase in HEL stress of AM samples significant, at approximately quadruple the measured CM response. Quantifying this; the vertically printed sample exhibited 417 % of its conventional counterpart (averaging CM SP2 1), with horizontal additive samples showing a 398 % increase. It is noted that the HEL of conventionally manufactured 316L appears lower than expected, raising questions as to the validity of this result. Defending this, firstly the similarity in spallation strength and HEL stress between both second round CM samples tested in this work refutes a variation in loading conditions, and secondly the relative similarity, well inside of 10 %, in observed CM 316L spallation strength to Gray *et al.* further aid validity. However an interesting question remains as to the cause of the degraded HEL magnitude in conventional samples, with the appearance of elevated HEL stress in AM samples unsurprising but the magnitude of the disparity well above expectation.

8.4 Conclusions

Spallation experimental results have furthered understanding into the behaviour of as-built AM 316L under dynamic uniaxial tensile strain conditions, beyond that

ShotID	ρ [kg m^{-3}]	σ_{HEL} [GPa]		
		Probe 1	**Probe 2**	**Probe 3**
CM SP2 1	7943	0.28	0.31	0.29
AM H DEN SP2 1	7903	1.20	1.18	1.13
AM V DEN SP2 1	7904	1.19	1.27	1.21
CM SP2 2	7941	0.23		

Table 8.4: Measured Hugoniot elastic limit stresses during initial compressive pulses of spallation tests on 316L stainless steel samples.

presented by Gray *et al.* in 2015 [125]. Whilst Gray *et al.* presented information on the effects of heat treatment, this work focused instead on the effects of both porosity and orientation. Application of traditional spallation analyses, where one-dimensional conditions are assumed present, did not allow effective analysis of porous responses. In place of this a qualitative approach considering wave dynamics offered some insight.

Firstly during the propagation of the compressive plastic characteristics through porous AM samples, the wavefront, ordinarily found to steepen, is dispersed from a shock to a ramp wave. This dispersion limits the duration of the peak compressive stress state in the material and slightly decreases the magnitude of achieved peak compressive stress as well.

Secondly, following the interaction of tensile plastic release fans, no coherent compressive elastic spallation pulse is recorded, indicative of an incoherent failure plane that suggests the dominance of defect driven failure modes. Similar behaviour has been observed by Carlton *et al.* in 2016 [118] at low rates, however this research presents the first validation of the trend at strain rates exceeding $10^3\,s^{-1}$ where wave dynamics convolve failure behaviour.

These conclusions highlight the change in wave dynamics stemming from defect distributions in AM materials. The need to consider this at high strain rates is imperative, as the response of porous components to high strain rate plasticity is markedly different from both CM and dense AM behaviour. Building upon the conclusions of reverse Taylor impact testing, the performance threshold of porous AM materials may still exceed CM counterparts, however defect driven behaviour will certainly dominate

tensile failure modes.

With respect to dense AM spallation responses, a more positive outlook is possible. Echoing the conclusions of Gray *et al.* [125], traditional spallation waveforms are seen in the velocity history of the target rear surface, thus facilitating one-dimensional analyses. These analyses suggest an increase in spallation strength of approximately 30 % above CM baselines in AM dense samples averaged across orientations, a value that is above existing literature conclusions of approximately 10 %. Such variation is not concerning, given the limited published results, complexity of spallation testing and analyses, and the knowledge that even slight defects can significantly limit resultant performance in AM samples. Furthermore, a small but significant directional disparity of approximately 5 % in spallation rupture strength is observed between horizontally and vertically oriented dense AM samples. This disparity, with horizontally oriented samples outperforming vertically oriented equivalents, mirrors observations in literature on other additively manufactured material including titanium [110] and tantalum [112], though the limited extent of testing does leave potential for further validation of this trend.

Contrasting previous responses seen in literature, a significant disparity in HEL stresses between CM and dense AM samples is observed. The exact cause of such a large disparity is not clear, however increased HEL stresses in AM samples would be expected due to the microstructural refinement driven by exposure to steep thermo-spatio-temporal gradients during manufacture. It is evident that further testing with metallographic analysis before and after loading of both CM and dense AM samples would be of significant value.

References

[26] J. A. Cherry et al. "Investigation into the effect of process parameters on microstructural and physical properties of 316L stainless steel parts by selective laser melting". In: *Int. J. Adv. Manuf. Technol.* 76.5-8 (Feb. 2015), pp. 869–879. ISSN: 0268-3768. DOI: 10.1007/s00170-014-6297-2.

[32] H. Nahme, E. Lach, and R. Rohr. "Dynamic materials behavior of a porous pressureless sintered steel and a HIPped steel". In: *J. Phys. IV* 134 (Aug. 2006), pp. 1047–1051. ISSN: 1155-4339. DOI: 10.1051/jp4:2006134160.

[36] ASM Handbook Committee. *Mechanical Testing and Evaluation*. English. Vol. 8. 1. [Metals Park, Ohio]: ASM International, 2000. ISBN: 978-0-87170-389-7. URL: https://www.asminternational.org.

[40] Yihang Cui et al. "Effect of Porosity on Dynamic Response of Additive Manufacturing Ti-6Al-4V Alloys". In: *Micromachines* 13.3 (Mar. 2022), p. 408. ISSN: 2072-666X. DOI: 10.3390/mi13030408.

[43] V D Gluzman and G. I. Kanel. "Measurement of the tensile stresses behind a spalling plane". In: *J. Appl. Mech. Tech. Phys.* 24.4 (1984), pp. 582–585. ISSN: 0021-8944. DOI: 10.1007/BF00907912.

[44] G. I. Kanel. "Distortion of the Wave Profiles in an Elastoplastic Body upon Spalling". In: *J. Appl. Mech. Tech. Phys.* 42.2 (2001), pp. 358–362. ISSN: 1573-8620. DOI: 10.1023/A:1018804709273.

[69] Michael Cloots, Peter J. Uggowitzer, and Konrad Wegener. "Investigations on the microstructure and crack formation of IN738LC samples processed by selective laser melting using Gaussian and doughnut profiles". In: *Mater. Des.* 89 (Jan. 2016), pp. 770–784. ISSN: 02641275. DOI: 10.1016/j.matdes.2015.10.027.

[83] Zhongji Sun et al. "Selective laser melting of stainless steel 316L with low porosity and high build rates". In: *Mater. Des.* 104 (Aug. 2016), pp. 197–204. ISSN: 02641275. DOI: 10.1016/j.matdes.2016.05.035.

[86] Y. Morris Wang et al. "Additively manufactured hierarchical stainless steels with high strength and ductility". In: *Nat. Mater.* 17.1 (Jan. 2018), pp. 63–71. ISSN: 1476-1122. DOI: 10.1038/nmat5021.

[91] Elton N. Kaufmann. *Characterization of Materials: Volume 1*. Ed. by Elton N. Kaufmann. Hoboken, NJ, USA: John Wiley & Sons, Inc., Oct. 2003. ISBN: 0471266965. DOI: 10.1002/0471266965.

[110] D. R. Jones et al. "Spall fracture in additive manufactured Ti-6Al-4V". In: *J. Appl. Phys.* 120.13 (Oct. 2016), p. 135902. ISSN: 0021-8979. DOI: 10.1063/1.4963279.

[112] D. R. Jones et al. "Spall fracture in additive manufactured tantalum". In: *J. Appl. Phys.* 124.22 (Dec. 2018), p. 225902. ISSN: 0021-8979. DOI: 10.1063/1.5063930.

[118] Holly D. Carlton et al. "Damage evolution and failure mechanisms in additively manufactured stainless steel". In: *Mater. Sci. Eng. A* 651 (Jan. 2016), pp. 406–414. ISSN: 09215093. DOI: 10.1016/j.msea.2015.10.073.

[125] G.T. Gray III et al. "Structure/property (constitutive and dynamic strength/damage) characterization of additively manufactured 316L SS". In: *EPJ Web Conf.* 94 (Sept. 2015). Ed. by E. Cadoni, p. 02006. ISSN: 2100-014X. DOI: 10.1051/epjconf/20159402006.

[132] Todd M. Mower and Michael J. Long. "Mechanical behavior of additive manufactured, powder-bed laser-fused materials". In: *Mater. Sci. Eng. A* 651 (Jan. 2016), pp. 198–213. ISSN: 09215093. DOI: 10.1016/j.msea.2015.10.068.

[167] Richard J. Williams et al. "In situ thermography for laser powder bed fusion: Effects of layer temperature on porosity, microstructure and mechanical properties". In: *Addit. Manuf.* 30.March (Dec. 2019), p. 100880. ISSN: 22148604. DOI: 10.1016/j.addma.2019.100880.

[168] M. Naveed Ahsan, Robert Bradley, and Andrew J. Pinkerton. "Microcomputed tomography analysis of intralayer porosity generation in laser direct metal deposition and its causes". In: *J. Laser Appl.* 23.2 (May 2011), p. 022009. ISSN: 1042-346X. DOI: 10.2351/1.3582311.

[169] Fiorello Losano et al. "Computed tomography in the automotive field. Development of a new engine head case study". In: *Comput. Tomogr. Ind. Appl. Image Process. Radiol.* 1999, pp. 65–73. URL: https://www.dgzfp.de/Portals/24/PDFs/BBonline/bb%7B%5C_%7D67-CD/bb67%7B%5C_%7Dv10.pdf.

[170] A. Thompson, I. Maskery, and R. K. Leach. "X-ray computed tomography for additive manufacturing: a review". In: *Meas. Sci. Technol.* 27.7 (July 2016), p. 072001. ISSN: 0957-0233. DOI: 10.1088/0957-0233/27/7/072001.

[171] Nobuyuki Otsu. "A Threshold Selection Method from Gray-Level Histograms". In: *IEEE Trans. Syst. Man. Cybern.* 9.1 (Jan. 1979), pp. 62–66. ISSN: 0018-9472. DOI: 10.1109/TSMC.1979.4310076.

[172] Oliver T. Strand et al. "Velocimetry using heterodyne techniques". In: *26th Int. Congr. High-Speed Photogr. Photonics*. Ed. by Dennis L. Paisley et al. Vol. 5580. Mar. 2005, p. 593. DOI: 10.1117/12.567579.

[173] Oliver T. Strand et al. "Compact system for high-speed velocimetry using heterodyne techniques". In: *Rev. Sci. Instrum.* 77.8 (Aug. 2006), p. 083108. ISSN: 0034-6748. DOI: 10.1063/1.2336749.

[174] E. A. Moro. "New developments in photon Doppler velocimetry". In: *J. Phys. Conf. Ser.* 500.14 (May 2014), p. 142023. ISSN: 1742-6596. DOI: 10.1088/1742-6596/500/14/142023.

[175] D. H. Dolan. "Extreme measurements with Photonic Doppler Velocimetry (PDV)". In: *Rev. Sci. Instrum.* 91.5 (2020). ISSN: 10897623. DOI: 10.1063/5.0004363.

[176] L. M. Barker and R. E. Hollenbach. "Interferometer Technique for Measuring the Dynamic Mechanical Properties of Materials". In: *Rev. Sci. Instrum.* 36.11 (Nov. 1965), pp. 1617–1620. ISSN: 0034-6748. DOI: 10.1063/1.1719405.

[177] Max Born et al. *Principles of Optics: Electromagnetic Theory of Propagation, Interference and Diffraction of Light*. 7th ed. Cambridge University Press, Oct. 1999. ISBN: 9780521642224. DOI: 10.1017/CBO9781139644181.

[178] Tommy Ao and Daniel H Dolan. *SIRHEN : a data reduction program for photonic Doppler velocimetry measurements.* Tech. rep. June. Albuquerque,

NM, and Livermore, CA (United States): Sandia National Laboratories (SNL), June 2010, pp. 1–66. DOI: 10.2172/989357.

[179] Daniel H Dolan. *Velocimetry signal synthesis with fringen.* Tech. rep. February. Albuquerque, NM, and Livermore, CA (United States): Sandia National Laboratories (SNL), Feb. 2011. DOI: 10.2172/1008143.

[180] D. H. Dolan, T. Ao, and O. Hernandez. "Note: Frequency-conversion photonic Doppler velocimetry with an inverted circulator". In: *Rev. Sci. Instrum.* 83.2 (Feb. 2012), p. 026109. ISSN: 0034-6748. DOI: 10.1063/1.3688851.

[181] R W Hamming. *Digital Filters (3rd Ed.)* Dover Publications, 1989. ISBN: 9780486650883. URL: https://store.doverpublications.com/048665088x.html.

[182] D. H. Dolan. "Accuracy and precision in photonic Doppler velocimetry". In: *Rev. Sci. Instrum.* 81.5 (May 2010), p. 053905. ISSN: 0034-6748. DOI: 10.1063/1.3429257.

[183] Harry J R Dutton. *Understanding Optical Communications.* Tech. rep. IBM Corporation, 1998.

[184] NKT Photonics GmbH. *Koheras AdjustiK E15 Datasheet.* 2022. URL: https://www.photonicsolutions.co.uk/upfiles/AdjustiK-E15.pdf (visited on 11/24/2022).

[185] Teledyne Lecroy. *WaveMaster 8 Zi-B Oscilloscopes.* 2022. URL: https://teledynelecroy.com/oscilloscope/wavemaster-sda-dda-8-zi-b-oscilloscopes/wavemaster-808zi-b (visited on 11/24/2022).

[186] Liam C. Smith. *PDVTool.* 2022. URL: https://github.com/liamcsmith/PDVTool.

[187] D. B. Holtkamp. "Survey of Optical Velocimetry Experiments - Applications of PDV, A Heterodyne Velocimeter". In: *2006 IEEE Int. Conf. Magagauss Magn. F. Gener. Relat. Top.* IEEE, Nov. 2006, pp. 119–128. ISBN: 978-1-4244-2061-2. DOI: 10.1109/MEGAGUSS.2006.4530668.

[188] Geoffrey Taylor. "The use of flat-ended projectiles for determining dynamic yield stress I. Theoretical considerations". In: *Proc. R. Soc. London. Ser. A. Math. Phys. Sci.* 194.1038 (Sept. 1948), pp. 289–299. ISSN: 0080-4630. DOI: 10.1098/rspa.1948.0081.

[189] D. J. Allen, W. K. Rule, and S.E. Jones. "Optimizing material strength constants numerically extracted from taylor impact data". In: *Exp. Mech.* 37.3 (Sept. 1997), pp. 333–338. ISSN: 0014-4851. DOI: 10.1007/BF02317427.

[190] Paul J. Maudlin et al. "On the modeling of the Taylor cylinder impact test for orthotropic textured materials: experiments and simulations". In: *Int. J. Plast.* 15.2 (Mar. 1999), pp. 139–166. ISSN: 07496419. DOI: 10.1016/S0749-6419(98)00058-8.

[191] J.W. House et al. "Film data reduction from Taylor impact tests". In: *J. Strain Anal. Eng. Des.* 34.5 (July 1999), pp. 337–345. ISSN: 0309-3247. DOI: 10.1243/0309324991513678.

[192] A. Mishra. "Reverse Taylor Tests on Ultrafine Grained Copper". In: *AIP Conf. Proc.* Vol. 845. 2006. AIP, 2006, pp. 757–760. ISBN: 0735403414. DOI: 10.1063/1.2263433.

[193] J.B. Hawkyard. "A theory for the mushrooming of flat-ended projectiles impinging on a flat rigid anvil, using energy considerations". In: *Int. J. Mech.*

Sci. 11.3 (Mar. 1969), pp. 313–333. ISSN: 00207403. DOI: 10.1016/0020-7403(69)90049-6.

[194] S.E. Jones, Peter P. Gillis, and Joseph C. Foster. "On the equation of motion of the undeformed section of a Taylor impact specimen". In: *J. Appl. Phys.* 61.2 (1987), pp. 499–502. ISSN: 00218979. DOI: 10.1063/1.338249.

[195] S.E. Jones, Paul J. Maudlin, and Joseph C. Foster. "An engineering analysis of plastic wave propagation in the Taylor test". In: *Int. J. Impact Eng.* 19.2 (Feb. 1997), pp. 95–106. ISSN: 0734743X. DOI: 10.1016/S0734-743X(96)00020-6.

[196] D.C. Erlich and D.A. Shockey. "Dynamic flow curve of 4340 steel as determined by the symmetric rod impact test". In: *Shock Waves Condens. Matter 1983*. Elsevier, 1984, pp. 129–132. DOI: 10.1016/B978-0-444-86904-3.50030-0.

[197] Joel W. House. *Taylor Impact Testing*. Tech. rep. September. 1989, p. 120. URL: https://apps.dtic.mil/sti/pdfs/ADA215018.pdf.

[198] Donald R. Snyder, Leonard L. Wilson, and Joel W. House. "Analysis Of High Speed Framing Camera Data For The Development Of Material Models Used In Penetration Mechanics." In: *Ultrah. Speed High Speed Photogr. Photonics, Videogr. '89 Seventh a Ser.* 1155.January 1990 (1990), p. 34. ISSN: 1996756X. DOI: 10.1117/12.962401.

[199] I. Rohr, H. Nahme, and K. Thoma. "A modified TAYLOR-test in combination with numerical simulations - a new approach for the determination of model parameters under dynamic loads". In: *J. Phys. IV* 110 (Sept. 2003), pp. 513–518. ISSN: 1155-4339. DOI: 10.1051/jp4:20020745.

[200] L. M. Barker and R. E. Hollenbach. "Laser interferometer for measuring high velocities of any reflecting surface". In: *J. Appl. Phys.* 43.11 (Nov. 1972), pp. 4669–4675. ISSN: 0021-8979. DOI: 10.1063/1.1660986.

[201] David J. Chapman et al. "Shock induced void nucleation during Taylor impact". In: *Int. J. Fract.* 134.1 (July 2005), pp. 41–57. ISSN: 0376-9429. DOI: 10.1007/s10704-005-7151-1.

[202] S.M. Walley et al. "A novel technique for performing symmetric Taylor impact". In: *EPJ Web Conf.* 94 (Sept. 2015). Ed. by E. Cadoni, p. 01029. ISSN: 2100-014X. DOI: 10.1051/epjconf/20159401029.

[203] Cavitar Ltd. *Cavitar Products*. 2022. URL: https://www.cavitar.com/products.

[204] Joel W. House, Leonard L. Wilson, and Michael E. Nixon. "High Strain-Rate Material Behavior Using Taylor Anvil Experiments". In: *Mech. Behav. Mater. VI, Proc. Sixth Int. Conf. Kyoto, Japan, 29 July - 2 August 1991*. Ed. by Masahiro Jono and Tatsuo Inoue. Kyoto: Elsevier, 1992, pp. 343–349. DOI: 10.1016/B978-0-08-037890-9.50061-2.

[205] E. Wielewski et al. "A method for the in situ measurement of evolving elliptical cross-sections in initially cylindrical Taylor impact specimens". In: *J. Strain Anal. Eng. Des.* 45.6 (Aug. 2010), pp. 429–437. ISSN: 0309-3247. DOI: 10.1243/03093247JSA639.

[206] Daniel E. Eakins and N.N. Thadhani. "Analysis of dynamic mechanical behavior in reverse Taylor anvil-on-rod impact tests". In: *Int. J. Impact Eng.* 34.11 (Nov. 2007), pp. 1821–1834. ISSN: 0734743X. DOI: 10.1016/j.ijimpeng.2006.11.001.

[207] Daniel E. Eakins and N.N. Thadhani. "Instrumented Taylor anvil-on-rod impact tests for validating applicability of standard strength models to transient deformation states". In: *J. Appl. Phys.* 100.7 (Oct. 2006), p. 073503. ISSN: 0021-8979. DOI: 10.1063/1.2354326.

[208] I. Rohr, H. Nahme, and K. Thoma. "Material characterization and constitutive modelling of ductile high strength steel for a wide range of strain rates". In: *Int. J. Impact Eng.* 31.4 (Apr. 2005), pp. 401–433. ISSN: 0734743X. DOI: 10.1016/j.ijimpeng.2004.02.005.

[209] I. Rohr et al. "Material characterisation and constitutive modelling of a tungsten-sintered alloy for a wide range of strain rates". In: *Int. J. Impact Eng.* 35.8 (Aug. 2008), pp. 811–819. ISSN: 0734743X. DOI: 10.1016/j.ijimpeng.2007.12.006.

[210] F. Bagusat and I. Rohr. "Modified Taylor-tests with miniaturized samples". In: *EPJ Web Conf.* 26 (Aug. 2012), p. 01007. ISSN: 2100-014X. DOI: 10.1051/epjconf/20122601007.

[211] J. C. Jonsson et al. "Effect of texture on elastic precursor decay in magnesium alloy AZ31B". In: *AIP Conf. Proc.* 2272.November (2020). ISSN: 15517616. DOI: 10.1063/12.0000818.

[212] Cyril L. Williams, K. T. Ramesh, and D. P. Dandekar. "Spall response of 1100-O aluminum". In: *J. Appl. Phys.* 111.12 (June 2012), p. 123528. ISSN: 0021-8979. DOI: 10.1063/1.4729305.

[213] Michael E. Rutherford et al. "Probing the early stages of shock-induced chondritic meteorite formation at the mesoscale". In: *Sci. Rep.* 7.1 (May 2017), p. 45206. ISSN: 2045-2322. DOI: 10.1038/srep45206.

[214] Emilio M. Escauriza et al. "Ultra-high-speed indirect x-ray imaging system with versatile spatiotemporal sampling capabilities". In: *Appl. Opt.* 57.18 (2018), p. 5004. ISSN: 1559-128X. DOI: 10.1364/ao.57.005004.

[215] Emilio M. Escauriza et al. "Ultra-high-speed X-ray imaging of shock-induced cavity collapse in a solid medium". In: *AIP Conf. Proc.* 2272.November (2020). ISSN: 15517616. DOI: 10.1063/12.0000933.

[216] Lukasz Farbaniec et al. "In-situ visualisation of dynamic fracture and fragmentation of an L-type ordinary chondrite by combined synchrotron X-ray radiography and microtomography". In: *Icarus* 359.December 2020 (2021), p. 114346. ISSN: 10902643. DOI: 10.1016/j.icarus.2021.114346.

[217] Robert M. Malone et al. "Photonic Doppler velocimetry probe used to measure grain boundaries of dynamic shocked materials". In: *Opt. Syst. Alignment, Toler. Verif. XI*. Ed. by José Sasián and Richard N. Youngworth. Vol. 1037704. August 2017. SPIE, Aug. 2017, p. 3. ISBN: 9781510612112. DOI: 10.1117/12.2276436.

[218] G. D. Owen et al. "Spall behaviour of single crystal aluminium at three principal orientations". In: *J. Appl. Phys.* 122.15 (Oct. 2017), p. 155102. ISSN: 0021-8979. DOI: 10.1063/1.4999559.

Part III

Modelling & Optimisations

Within the following section the development of a predictive constitutive capability tailored to the observed experimental responses is detailed. To begin with an algorithmic overview of the model is given, with the parametrisation of the model to experimental data presented thereafter.

Chapter 9

Orthotropic Material Model

In this chapter the mathematical framework and computational algorithmic implementation of the developed orthotropic Johnson-Cook strength model are detailed. Initially the mathematical framework is given, specifying the construction of directionally dependent parameters that can be used to seed an orthotropic, strain, strain rate, and temperature sensitive plastic potential. This plastic potential is also used to form the yield surface of the model such that it may be considered associative, as is commonplace for the numerical modelling of strength in metals [219–223]. Following this, a multilevel algorithm is presented to explicitly combine the eigenspace mapping technique of Versino and Bennett [158] with the novel orthotropic potential. This algorithm was implemented successfully into a user-defined material subroutine within a finite element multi-physics software package, specifically LS-Dyna [145, 224, 225]. This implementation required the use of FORTRAN77 and was done with a highly modular approach that separates the eigenspace mapping, subspace radial return, and plastic potential evaluation within the subroutine. It is this modularity that will also allow the model to be easily adapted to alternate plastic potentials, increasing its applicability to a wide range of preexisting orthotropic modelling scenarios.

9.1 Johnson-Cook Parameters

To develop an orthotropic plastic potential with strain, strain rate and temperature sensitivities, six independent Johnson-Cook responses will be used to define the flow stress along the set of directions $\{11, 22, 33, ', '', '''\}$, with these directions as defined in figure 3.2. Using these six functions a corresponding set of flow stresses, calculated at the beginning of each time-step in every element, will then define the anisotropy matrix $\mathbf{A}$, in turn defining the yield criterion. Where experimental data was not measured,

notably along the $\{',''',''''\}$ directions, a linear transition of parameters was assumed as the stress state rotated between principle directions $\{11, 22, 33\}$, such that:

$$\mathrm{x}_\mathrm{i}' = \frac{1}{2}\left((\mathrm{x}_\mathrm{i})_{22} + (\mathrm{x}_\mathrm{i})_{33}\right),$$

with other off axis terms following from symmetry. Whilst an anisotropy matrix $\mathbf{A}$ is calculable to satisfy the Hill yield criterion for a material of state $\left\{\epsilon_\mathrm{p}^\mathrm{eff}, \dot{\epsilon}_\mathrm{p}^\mathrm{eff}, \mathrm{T}\right\}$, the plastic potential poses a more complex issue as it can depend on the relative contributions of both the absolute value and the gradient of each Johnson-Cook model so is itself directionally dependent, consequently:

$$\begin{aligned}
\neg\,\square\left(\frac{\mathrm{d}}{\mathrm{d}\boldsymbol{\sigma}_\mathrm{n}}\frac{\partial f}{\partial\left(\epsilon_\mathrm{p}^\mathrm{eff}\right)} = 0\right),\\
\neg\,\square\left(\frac{\mathrm{d}}{\mathrm{d}\boldsymbol{\sigma}_\mathrm{n}}\frac{\partial f}{\partial\left(\dot{\epsilon}_\mathrm{p}^\mathrm{eff}\right)} = 0\right),\\
\neg\,\square\left(\frac{\mathrm{d}}{\mathrm{d}\boldsymbol{\sigma}_\mathrm{n}}\frac{\partial f}{\partial \mathrm{T}} = 0\right).
\end{aligned}$$

With these expressions formalising the possibility of a dependence between the stress tensor and the rate of change of the yield threshold with respect to the effective plastic strain, effective plastic strain rate, or temperature (given that $\neg\square$ symbolises a lack of necessity in the truth of the proceeding condition). For example, a plastic potential valid at a given effective plastic strain rate may vary with changes in the stress state, even when the magnitude of the stress tensor, effective plastic strain, effective plastic strain rate, and temperature remain constant.

To calculate the plastic potential given the material, $\left\{\epsilon_\mathrm{p}^\mathrm{eff}, \dot{\epsilon}_\mathrm{p}^\mathrm{eff}, \mathrm{T}\right\}$, and loading state, $\left\{\boldsymbol{\sigma}_\mathrm{n}, \Delta\boldsymbol{\epsilon}_\mathrm{p}\right\}$, the parameter set $\mathbf{x}$ as defined in section 3.3 for on axis cases can be mapped to five independent six-dimensional hyperellipsoids (one per parameter x_i of the traditional isotropic Johnson-Cook seen in equation 3.26). These hyperellipsoids may then be sampled analogously to the the Hill yield criterion in matrix form (originally

presented in equation 3.12) such that:

$$f_{\text{Hill}} = \mathbf{s}^{\mathsf{T}}\mathbf{A}\mathbf{s},$$

with a projection along a suitable vector. In this case, instead of using the deviatoric stress $(\mathbf{s})$, the deviatoric strain increment $\left(\text{dev}\left(\Delta\boldsymbol{\epsilon}\right)\right)$ is the appropriate choice, as this is collinear to the deviatoric stress within the stress eigenspace. Furthermore, as only the direction is of interest, a normalisation must be applied to account for scaling by the magnitude of the projection vector. This magnitude may be calculated analogously to the magnitude of the second invariant of the deviatoric stress such that with implied Einstein summation:

$$\left|\Delta\boldsymbol{\epsilon}_{\text{p}}\right|^2 = \frac{3}{2}\left(\Delta\epsilon_{\text{p}}\right)_{\text{ij}}\left(\Delta\epsilon_{\text{p}}\right)_{\text{ij}}.$$

Each component of the effective Johnson-Cook, x_i, during the interval $\text{t}_\text{n} \rightarrow \text{t}_{\text{n}+1}$ is identified by $\left(\text{x}_\text{i}^{\text{eff}}\right)_\text{n}$. This variable is defined solely within the time interval for evaluation of the plastic potential within the stress eigenspace of that specific element, is calculated as follows:

$$\left(\text{x}_\text{i}^{\text{eff}}\right)_\text{n} = \frac{\left(\Delta\boldsymbol{\epsilon}_{\text{p}}\right)^{\mathsf{T}}\mathbf{A}_{\text{x}_\text{i}}\left(\Delta\boldsymbol{\epsilon}_{\text{p}}\right)}{\left|\Delta\boldsymbol{\epsilon}_{\text{p}}\right|^2}. \tag{9.1}$$

In the above expressions we see again an anisotropy matrix, $\mathbf{A}_{\text{x}_\text{i}}$, which is defined similarly to the Hill anisotropy matrix such that:

$$\mathbf{A}_{\text{x}_\text{i}} = \begin{bmatrix} G_{\text{x}_\text{i}} + H_{\text{x}_\text{i}} & -H_{\text{x}_\text{i}} & -G_{\text{x}_\text{i}} & 0 & 0 & 0 \\ -H_{\text{x}_\text{i}} & F_{\text{x}_\text{i}} + H_{\text{x}_\text{i}} & -F_{\text{x}_\text{i}} & 0 & 0 & 0 \\ -G_{\text{x}_\text{i}} & -F_{\text{x}_\text{i}} & F_{\text{x}_\text{i}} + G_{\text{x}_\text{i}} & 0 & 0 & 0 \\ 0 & 0 & 0 & 2L_{\text{x}_\text{i}} & 0 & 0 \\ 0 & 0 & 0 & 0 & 2M_{\text{x}_\text{i}} & 0 \\ 0 & 0 & 0 & 0 & 0 & 2N_{\text{x}_\text{i}} \end{bmatrix},$$

with the coefficients of $\mathbf{A}_{x_i}$ defined as:

$$
\begin{aligned}
F_{x_i} &= \frac{1}{2}\left((x_i)_{22} + (x_i)_{33} - (x_i)_{11}\right), \\
G_{x_i} &= \frac{1}{2}\left((x_i)_{33} + (x_i)_{11} - (x_i)_{22}\right), \\
H_{x_i} &= \frac{1}{2}\left((x_i)_{11} + (x_i)_{22} - (x_i)_{33}\right), \\
L_{x_i} &= 2\,(x_i)' - \frac{1}{2}(x_i)_{11}, \\
M_{x_i} &= 2\,(x_i)'' - \frac{1}{2}(x_i)_{22}, \\
N_{x_i} &= 2\,(x_i)''' - \frac{1}{2}(x_i)_{33}.
\end{aligned}
$$

Given the projection defined in equation 9.1 it is then possible to use the effective Johnson-Cook coefficient set to seed a plastic potential with the following form:

$$
f_{\text{eff}}\left(\epsilon_p^{\text{eff}}, \epsilon^*, T\right) = \left(x_1^{\text{eff}} + x_2^{\text{eff}}\left(\epsilon_p^{\text{eff}}\right)^{x_3^{\text{eff}}}\right)\left(1 + x_4^{\text{eff}} \ln\left(\epsilon^*\right)\right)\left(1 - \left(T^*\right)^{x_5^{\text{eff}}}\right).
$$

This plastic potential has implicit directional sensitivities to strain, strain rate and temperature, provided by the effective parameter set, and can mediate the exchange between excess elastic strain energy in and increases in the effective plastic strain of an element such that the yield criterion remains satisfied but not exceeded at the end of the time step. The exact implementation of this exchange into an algorithm, which then was implemented into a user subroutine within LS-Dyna, is detailed below in section 9.2.

9.2 Pseudocode Algorithm

9.2.1 Overview

The algorithm detailed below consists of three broad sections; an overall subroutine algorithm (figure 9.1), an outer element-wise loop (figure 9.2), and an inner element-wise iterative eigenspace loop (figure 9.3). Each loop, accompanied with an associated flowchart, is detailed in a separate section with the outer algorithm shown first directly

below.

1. Input variables for the model including on axis Johnson-Cook parameters and elastic stiffness matrix components are initially parsed from input arrays and mapped to appropriate structures including $\mathbf{C}$.

2. The eigendecomposition of $\mathbf{C}$ is computed, this single eigendecomposition holds for every element for all time steps. Despite values for $\mathbf{Q_C}$ and $\mathbf{\Gamma_C}$ only being used when plastic deformation occurs, their consistency across elements mandates that the most efficient placement of this calculation remain outside the element-wise loop. It was however decided to calculate this for every time step to reduce variable passing between time steps at the expense of negligible computational overhead.

3. Each Johnson-Cook parameter matrix must then be computed as described in section 9.1. Similarly to the eigendecomposition of $\mathbf{C}$, it is most efficient to calculate this outside of the element-wise loop at the start of each time step.

4. For each element defined using the model, the stress and effective plastic strain must be updated. This process is detailed in the element-wise algorithm (figure 9.2).

5. The updated stress and effective plastic strain values for each element are then returned to the main finite element code, alongside this history variables are also recorded for every element to allow retrospective analysis.

Element-wise Algorithm

The outer element-wise loop is entered at every time step, with this responsible for updating the stress state and effective plastic strain state (should plastic deformation occur) of every element within the current time step.

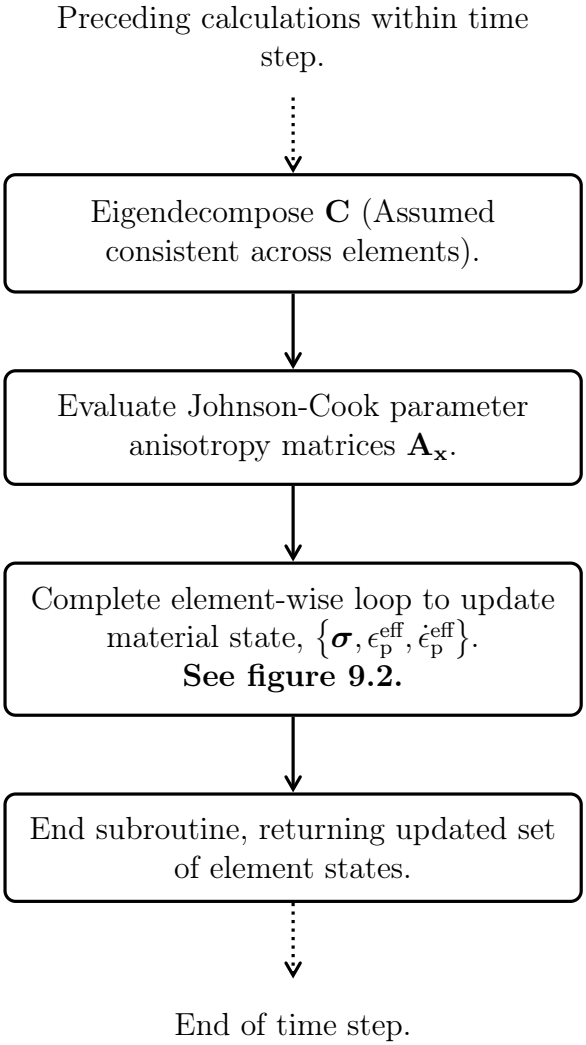

Figure 9.1: Overall material subroutine algorithm.

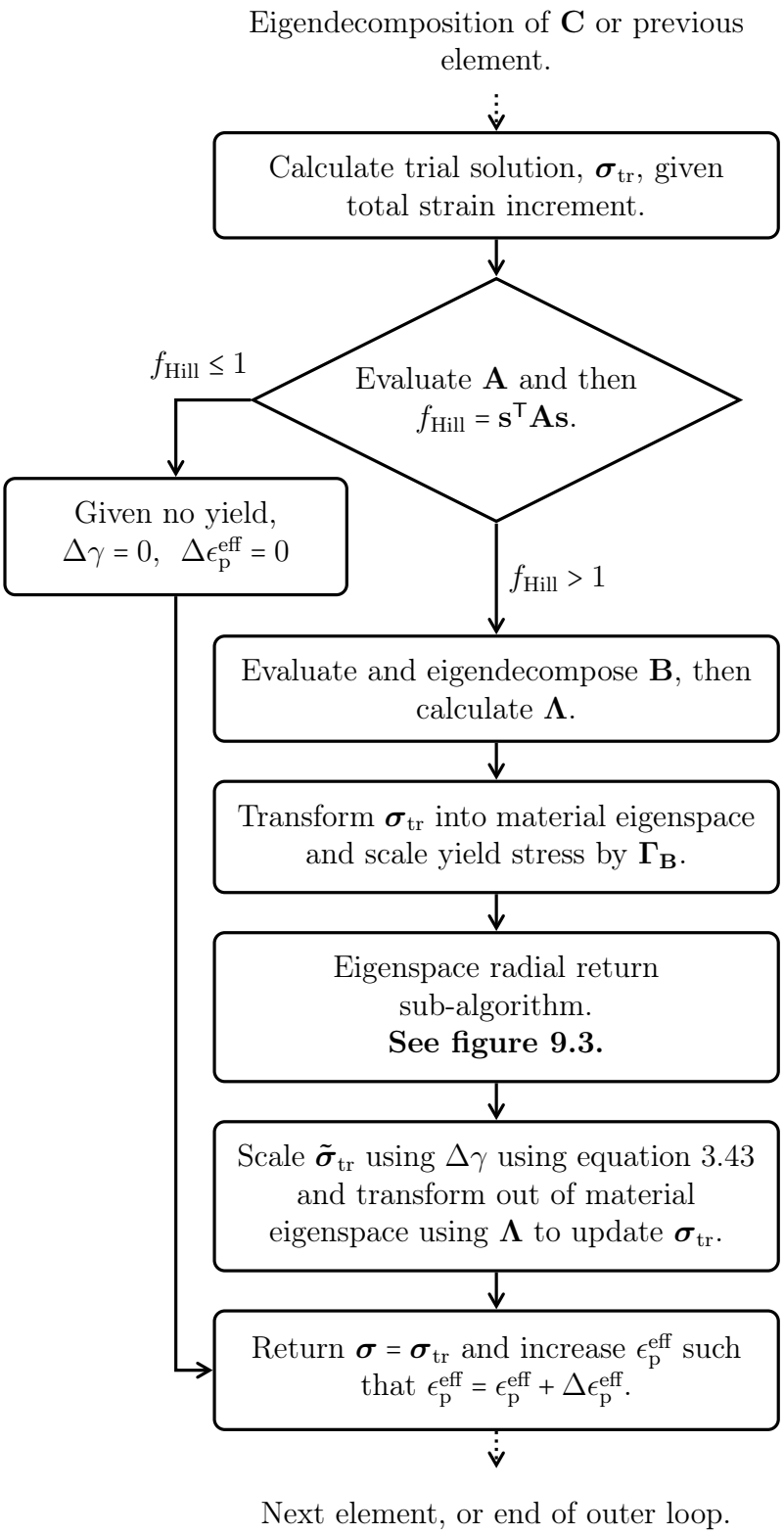

Figure 9.2: Outer element-wise loop.

1. First the trial solution is calculated, assuming that during the time-step there is no plastic deformation. This step aligns to equation 3.34, albeit with the assumption that $\Delta\gamma = 0$.

2. Using the on-axis Johnson-Cook coefficients and material state, specifically $\left\{\left(\epsilon_{\mathrm{p}}^{\mathrm{eff}}\right)_{\mathrm{n}}, \mathrm{T}_{\mathrm{n}}\right\}$, the anisotropy matrix $\mathbf{A}$ is created, defining the threshold for elastic deformation and the state of anisotropy.

3. The yield criterion, $f_{\mathrm{Hill}} = \left(\mathbf{s}_{\mathrm{n}}\right)^{\mathsf{T}} \mathbf{A}\mathbf{s}_{\mathrm{n}} \leq \sigma^{\mathrm{Y}}$, is evaluated. Here $\mathbf{s}_{\mathrm{n}}$ is the deviatoric trial stress state as defined using equations 3.3–3.6 and 3.34.

4. If the yield criterion is satisfied such that $f_{\mathrm{Hill}} > \sigma^{\mathrm{Y}}$ then the trial elastic solution is not valid. In this case correct non-zero values for $\left\{\Delta\gamma, \Delta\epsilon_{\mathrm{p}}^{\mathrm{eff}}\right\}$ will need to be calculated.

   (a) The eigenspace defined by $\mathbf{\Lambda}$ and $\mathbf{\Gamma_B}$ is calculated, as described previously using equations 3.35 and 3.43.

   (b) The deviatoric trial stress state and the yield stress is transformed into the eigenspace by multiplying by $\left(\mathbf{\Lambda}\right)^{-1}$ using equation 3.42 and dividing the yield stress by $\mathbf{\Gamma_B}$. Division of σ^{Y} by $\mathbf{\Gamma_B}$ is required to correct for the scaling of stress within the eigenspace that would in turn affect the effective stress within the eigenspace, ω.

   (c) One dimensional radial return is performed within the eigenspace using an algorithm detailed in section 9.2.1 and figure 9.3.

   (d) Following evaluation of the plastic multiplier within the eigenspace, the trial stress state for the element is scaled by $\Delta\gamma$ within the eigenspace preceding transformation out of the eigenspace.

5. The evaluated (and potentially scaled if yielding occurred) trial stress state is then passed back to the element with any accrued plastic strain incremented atop the preexisting amount. The incrementing of $\epsilon_{\mathrm{p}}^{\mathrm{eff}}$ ensures that strain dependent responses are feasible similarly to conventional material strength models.

Eigenspace Algorithm

This loop, the innermost within the model, is only entered when an element is unable to support the trial stress state elastically during a time step. Within this loop, an associated deviatoric stress subspace is evaluated such that the yield surface normal is collinear to the transformed deviatoric stress state, thus reducing the evaluation of resultant stress for a given plastic multiplier to a one dimensional problem.

This one-dimensional problem is equivalent to that tackled by conventional strength models that are both isotropic and associative, usually employing a single 1st order Newton-Raphson estimation to predict plastic evolution. Due to the added complexity of the problem introduced by the directionality, an iterative first order Newton-Raphson iteration is employed (with user defined termination limits) instead of a single prediction to ensure robust convergence in a less favourable optimisation space.

1. Given the current estimate of $\Delta\gamma$, calculate $\boldsymbol{\kappa}$ using equation 3.44. If in the first iteration then $\Delta\gamma$ is instantiated to an arbitrary small value of 1×10^{-60}.

2. Given the current estimations of $\left\{\epsilon_{\mathrm{p}}^{\mathrm{eff}}, \Delta\epsilon_{\mathrm{p}}^{\mathrm{eff}}, \Delta\mathrm{t}, \mathrm{T}\right\}$, compute the effective yield function:

$$f_{\mathrm{eff}}\left(\epsilon_{\mathrm{p}}^{\mathrm{eff}}, \epsilon^{*}, \mathrm{T}^{*}\right) = \left(\left(\mathrm{x}_{1}^{\mathrm{eff}}\right)_{\mathrm{n}} + \left(\mathrm{x}_{2}^{\mathrm{eff}}\right)_{\mathrm{n}}\left(\epsilon_{\mathrm{p}}^{\mathrm{eff}}\right)^{\left(\mathrm{x}_{3}^{\mathrm{eff}}\right)_{\mathrm{n}}}\right) \left(1 + \left(\mathrm{x}_{4}^{\mathrm{eff}}\right)_{\mathrm{n}} \ln\left(\epsilon^{*}\right)\right)\left(1 - \left(\mathrm{T}^{*}\right)^{\left(\mathrm{x}_{5}^{\mathrm{eff}}\right)_{\mathrm{n}}}\right),$$

   and calculate its derivative $\frac{\partial f_{\mathrm{eff}}}{\partial\left(\Delta\epsilon_{\mathrm{p}}^{\mathrm{eff}}\right)}$ to allow estimation of the yield function following a finite amount of deformation via Taylor expansion.

3. Construct a convergence inequality defined for the loading state $\omega\left(\tilde{\boldsymbol{\sigma}}_{\mathrm{tr}}, \Delta\gamma\right)$ and material state $f_{\mathrm{eff}}\left(\epsilon_{\mathrm{p}}^{\mathrm{eff}}, \Delta\epsilon_{\mathrm{p}}^{\mathrm{eff}}, \Delta\mathrm{t}, \mathrm{T}\right)$. This inequality is defined to be:

$$f_{\Delta\gamma} \coloneqq \left|\frac{f_{\mathrm{eff}}}{\omega} - 1\right| < \delta,$$

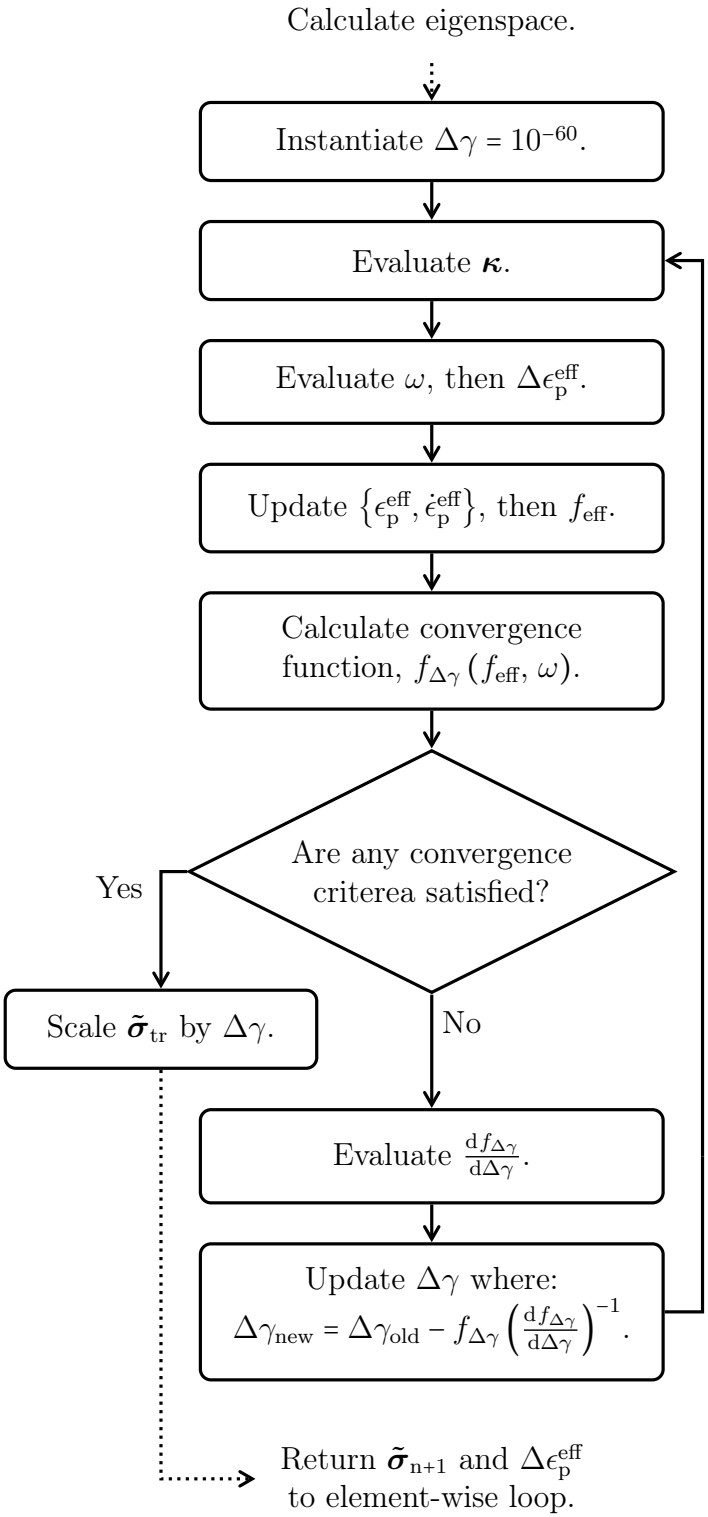

Figure 9.3: Inner eigenspace algorithm.

where δ is a user defined threshold for accepting convergence. If this inequality is satisfied then the predicted values $\left\{\Delta\gamma, \Delta\epsilon_{\mathrm{p}}^{\mathrm{eff}}\right\}$ are deemed valid and the sub algorithm should return and exit the loop.

4. If reaching this point in the loop then the inequality has not been satisfied and an updated prediction of $\Delta\gamma$ will be required. To do this a Newton-Raphson iteration will be computed to update the prediction of $\Delta\gamma$ by an increment $\Delta(\Delta\gamma)$ such that $\Delta(\Delta\gamma) = -f_{\Delta\gamma}\left(\frac{\partial f_{\Delta\gamma}}{\partial(\Delta\gamma)}\right)^{-1}$. The evaluation of the gradient $\frac{\partial f_{\Delta\gamma}}{\partial(\Delta\gamma)}$ increment involves a series of steps detailed in section 9.2.2.

9.2.2 Newton-Raphson Gradient

Whilst not complex, the calculation of the gradient $\frac{\partial f_{\Delta\gamma}}{\partial(\Delta\gamma)}$ is detailed below for completeness. Initially the equivalent yield function is separated via the chain rule such that:

$$\frac{\partial f_{\Delta\gamma}}{\partial(\Delta\gamma)} = \frac{\partial}{\partial(\Delta\gamma)}\left(\frac{f_{\mathrm{eff}}}{\omega} - 1\right) = \frac{1}{\omega}\frac{\partial f_{\mathrm{eff}}}{\partial(\Delta\gamma)} - \frac{1}{\omega^2}\frac{\partial\omega}{\partial(\Delta\gamma)}\left(f_{\mathrm{eff}}\right) \tag{9.2}$$

From here the differential of ω is evaluated by considering the dependence of each term on $\Delta\gamma$ such that:

$$\frac{\partial\omega}{\partial(\Delta\gamma)} = \frac{\partial}{\partial(\Delta\gamma)}\left(\sqrt{\frac{1}{2}\tilde{\boldsymbol{\sigma}}_{\mathrm{tr}}{}^{\mathsf{T}}\boldsymbol{\kappa}\tilde{\boldsymbol{\sigma}}_{\mathrm{tr}}}\right) = \frac{1}{2}\left(\frac{1}{2}\tilde{\boldsymbol{\sigma}}_{\mathrm{tr}}{}^{\mathsf{T}}\frac{\partial\boldsymbol{\kappa}}{\partial(\Delta\gamma)}\tilde{\boldsymbol{\sigma}}_{\mathrm{tr}}\right)\frac{1}{\omega} \tag{9.3}$$

where $\tilde{\boldsymbol{\sigma}}_{\mathrm{tr}}$ is the trial stress within the eigenspace assuming $\Delta\gamma = 0$ and where,

$$\frac{\partial\boldsymbol{\kappa}}{\partial\Delta\gamma} = -2\frac{\boldsymbol{\Gamma}_{\mathbf{B}}\boldsymbol{\kappa}}{\left(\mathbf{I} + \Delta\gamma\boldsymbol{\Gamma}_{\mathbf{B}}\right)}. \tag{9.4}$$

From here the effective plastic potential can be differentiated by chain rule:

$$\frac{\partial f_{\mathrm{eff}}}{\partial(\Delta\gamma)} = \frac{\partial f_{\mathrm{eff}}}{\partial\left(\Delta\epsilon_{\mathrm{p}}^{\mathrm{eff}}\right)}\frac{\partial\left(\Delta\epsilon_{\mathrm{p}}^{\mathrm{eff}}\right)}{\partial(\Delta\gamma)}. \tag{9.5}$$

Here $\frac{\partial\left(\Delta\epsilon_p^{eff}\right)}{\partial(\Delta\gamma)}$ is calculable from equations 3.31 and 3.33 with use of the product rule such that:

$$\frac{\partial\left(\Delta\epsilon_p^{eff}\right)}{\partial(\Delta\gamma)} = \frac{\partial}{\partial(\Delta\gamma)}\left(2\left(\Delta\gamma\right)\omega\right) = 2\omega + 2\left(\Delta\gamma\right)\frac{\partial\omega}{\partial(\Delta\gamma)}, \tag{9.6}$$

and $\frac{\partial f_{eff}}{\partial\left(\Delta\epsilon_p^{eff}\right)}$ may then be calculated directly from the definition of f_{eff} in equation 3.26. This final differential is taken using product rule such that

$$\begin{aligned}\frac{\partial f_{eff}}{\partial\left(\Delta\epsilon_p^{eff}\right)} &= \frac{\partial}{\partial\left(\Delta\epsilon_p^{eff}\right)}\left(\left(x_1 + x_2\left(\epsilon_p^{eff}\right)^{x_3}\right)\left(1 + x_4\ln\left(\epsilon^*\right)\right)\left(1 - \left(T^*\right)^{x_5}\right)\right) \\ &= \left[\frac{\partial\left(x_1 + x_2\left(\epsilon_p^{eff}\right)^{x_3}\right)}{\partial\left(\Delta\epsilon_p^{eff}\right)}\left(1 + x_4\ln\left(\epsilon^*\right)\right)\right. \\ &\quad \left. + \frac{\partial\left(1 + x_4\ln\left(\epsilon^*\right)\right)}{\partial\left(\Delta\epsilon_p^{eff}\right)}\left(x_1 + x_2\left(\epsilon_p^{eff}\right)^{x_3}\right)\right]\left(1 - \left(T^*\right)^{x_5}\right),\end{aligned} \tag{9.7}$$

where the differential of the rate-based term is a piecewise non-continuous function. The rate term differential is evaluated using equation 3.27 such that

$$\frac{\partial\left(1 + x_4\ln\left(\epsilon^*\right)\right)}{\partial\left(\Delta\epsilon_p^{eff}\right)} = \begin{cases} \frac{x_4}{\dot{\epsilon}_p^{eff}\Delta t} & \dot{\epsilon}_p^{eff} > \dot{\epsilon}_{p0}^{eff} \\ 0 & \dot{\epsilon}_p^{eff} \leq \dot{\epsilon}_{p0}^{eff}. \end{cases} \tag{9.8}$$

Given the set of equations 9.6–9.8 it is possible to construct the differential in equation 9.2 with this then used to compute the updated estimate of $\Delta\gamma$.

9.3 Model Validation

In order to validate the orthotropic model detailed in chapter 9, a series of simulations would need to be constructed allowing each dependency to be tested along a range of directions. To this end a cube formed from a $(4 \times 4 \times 4)$ set of hexahedral elements, visualised in figure 9.4, was simulated in LS-DYNA. A pair of one dimensional displacement constraints were applied to nodes on the top and base faces of the hypercube with the enforced displacement evolution moderating the resultant strain rate of the elements in the cube. Nodes with enforced displacements along the Z axis were allowed to move freely in the XY plane, with this allowing isochoric plastic

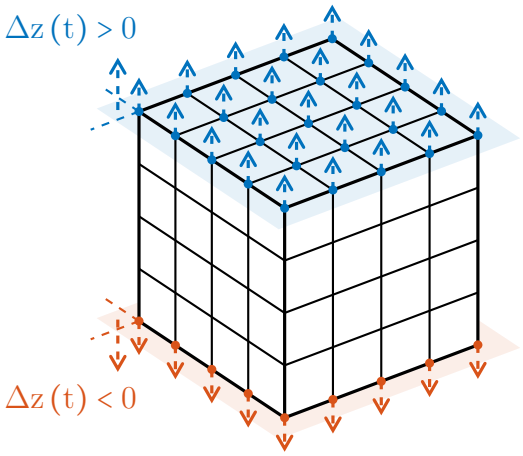

Figure 9.4: Validation simulation setup used to interrogate the behaviour of the orthotropic model in comparison to the pre-existing isotropic implementation of the Johnson-Cook.

deformation following a standard elastic response.

Following the completion of a simulation, terminated upon the global strain state (known from the predefined constrained face displacements) reaching an equivalent plastic strain of 40 %, the material state during the simulation was sampled from the gaussian points associated with the central $(2 \times 2 \times 2)$ element volume. This choice of sampling was taken to ensure measurements of the simulated response were isolated from both the displacement constraints at the top and bottom faces that could influence behaviour and from the side faces where the free surface could also influence the results. The sampled data was averaged across the gaussian points in the $(2 \times 2 \times 2)$ element sub-hypercube with errors recorded, these errors are not displayed in this section as they are negligible, as would be expected for a deterministic material model that is subjected to essentially homogeneous loading conditions.

In order to interrogate the directional dependence of the model each simulation would need to be repeated whilst the direction of applied plastic deformation was altered. It was decided to sweep through 180° ranges in YZ, ZX, and XY planes, as visualised in figure 9.5. This choice of angles ensured that tests would remain normal to one axis, ensuring that the influence of that direction upon the simulation was kept constant, and therefore isolating a subset of dependencies to better highlight those

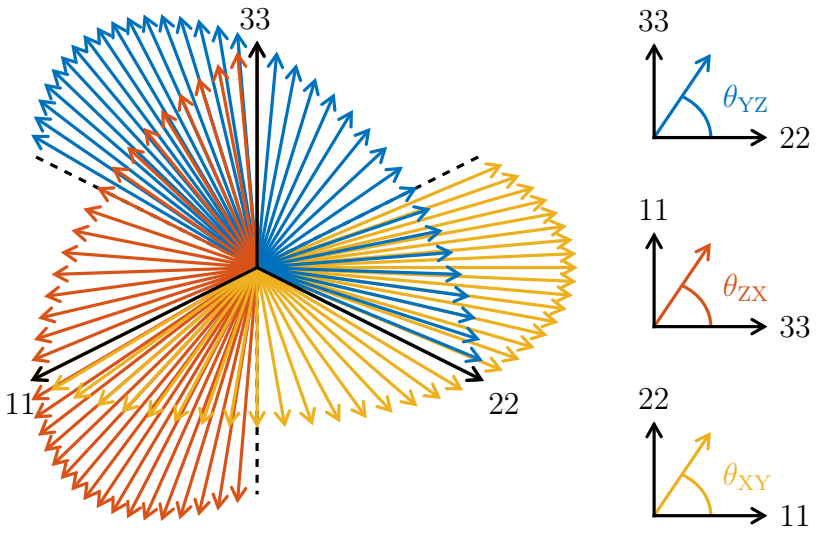

Figure 9.5: The angular domain that was interrogated throughout the material model validation. Each coloured line in the isometric view is spaced in 5° increments to match the simulations completed. Axes are displayed in black, on each positive axis duplicate tests were conducted and are not displayed in this figure. To the right in-plane views are shown detailing the in-plane angle that is used in in-plane simulations.

being sampled.

As can be seen in figure 9.5, a total of 36 directions were mapped for each of the three planes. This set of directions were simulated at 5 strain rates logarithmically spaced between $0.1\,\mathrm{s}^{-1}$ up to $1000\,\mathrm{s}^{-1}$ for each material parameter set. Given isotropic responses were simulated along with variation of each parameter (aside from x_5) this validation totalled 2700 individual simulations. The compilation of results was achieved using a data pipeline framework, first converting proprietary binary encoded output files from each simulation to HDF5 containers. These archives were then imported into a single object-oriented analysis framework where the responses were available at the gaussian-point level. Nested statistics for each object were used to propagate and combine results and errors, allowing the reduction of 180 simulations to a single figure, such as in figure 9.12.

Direction	$\mathbf{x_1}$ [MPa]	$\mathbf{x_2}$ [MPa]	$\mathbf{x_3}$	$\mathbf{x_4}$	$\mathbf{x_5}$
11	525	1180	0.6220	0.0099	0.5201
22	525	1180	0.6220	0.0099	0.5201
33	525	1180	0.6220	0.0099	0.5201
′	525	1180	0.6220	0.0099	0.5201
″	525	1180	0.6220	0.0099	0.5201
‴	525	1180	0.6220	0.0099	0.5201

Table 9.1: Parameter set used to validate the isotropic degenerate response of the orthotropic model matches the pre-existing isotropic model implementation.

9.3.1 Isotropy

In the first validation step for the model it was decided to replicate the behaviour of the pre-existing isotropic Johnson-Cook that is implemented in the LS-DYNA finite element code. In order to do this the orthotropic model was sampled alongside the pre-existing isotropic implementation, with both models seeded using the parameter set in table 9.1. These parameter values were taken from various literature sources studying both CM and AM 316L stainless steel [122, 125, 226–228], with application of the traditional isotropic Johnson-Cook [154].

The results from a subset of the 540 isotropically seeded simulations are shown in the series of figures below, initially individual on-axis responses are seen in figures 9.6–9.8, with sub-figures presenting individual strain rates from the logarithmically spaced set that was simulated. In each figure the orthotropic response, at the specified direction and strain rate, is plotted alongside the isotropic response from the same simulation, therefore mirroring both strain rate and strain tensor evolution between models.

From these results it is seen that the on-axis response of the orthotropic model does indeed recreate the pre-existing isotropic response when seeded using equal parameters across all directions. The slight instability seen in figures 9.6d, 9.7d and 9.8d, highlighting responses at strain rates of $100\,\mathrm{s}^{-1}$, is attributed to the simulation rather than the model itself as the instability is also present in both isotropic and orthotropic responses, with the isotropic response taken from the preexisting, and widely validated,

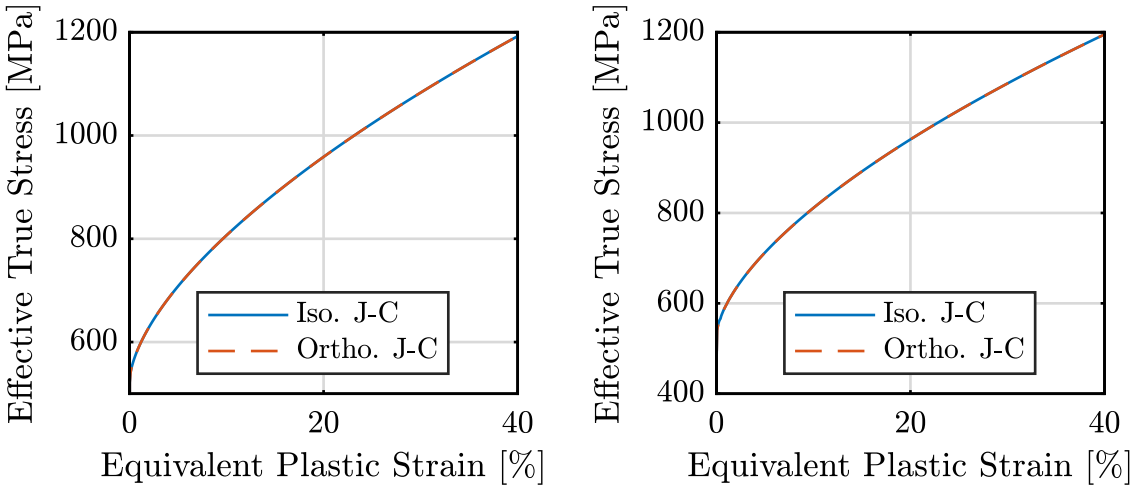

(a) $0.1\,\mathrm{s}^{-1}$.

(b) $1\,\mathrm{s}^{-1}$.

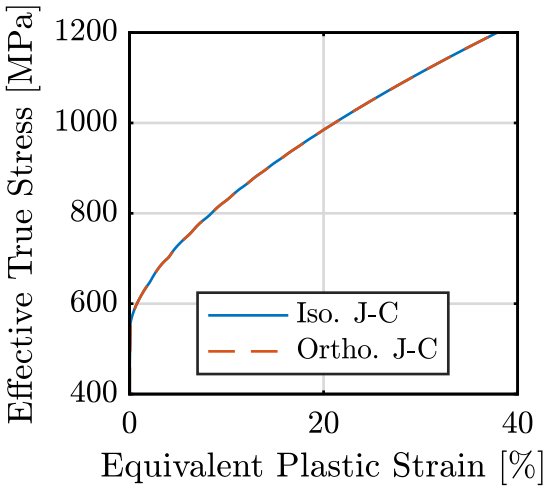

(c) $10\,\mathrm{s}^{-1}$.

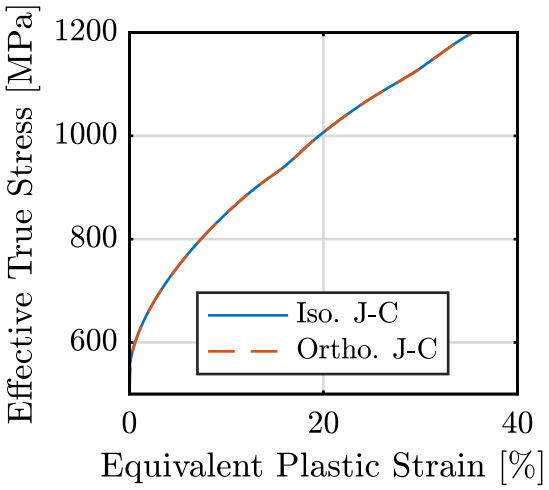

(d) $100\,\mathrm{s}^{-1}$.

Figure 9.6: Example model response along Y-Axis under enforced isotropic conditions compared to pre-existing isotropic Johnson-Cook implementation. Series of figures represents set of strain rates.

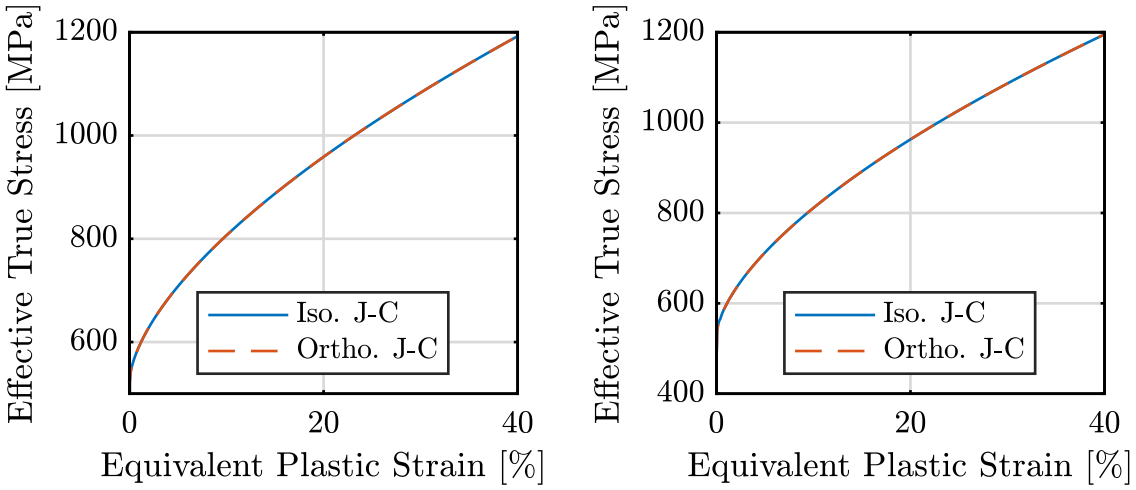

(a) $0.1\,\mathrm{s}^{-1}$.

(b) $1\,\mathrm{s}^{-1}$.

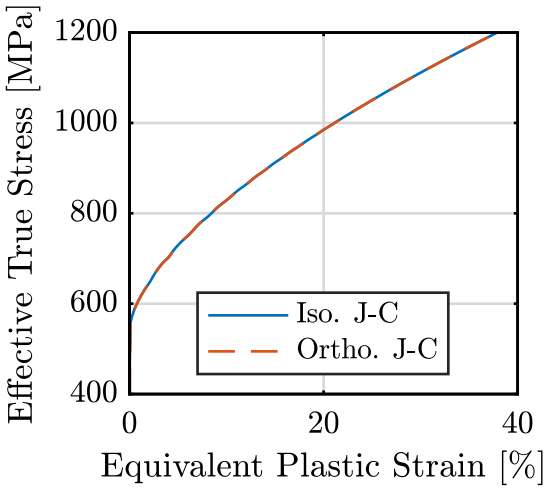

(c) $10\,\mathrm{s}^{-1}$.

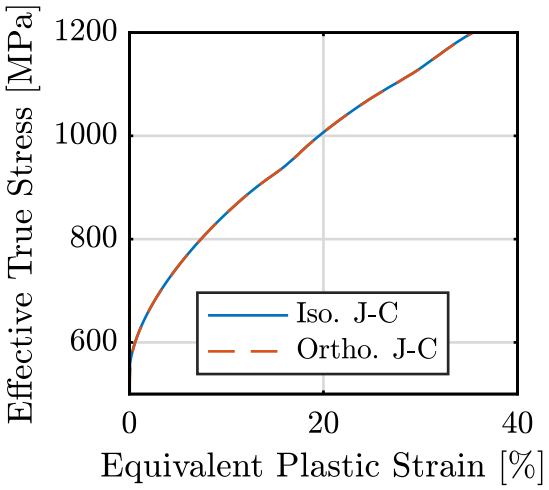

(d) $100\,\mathrm{s}^{-1}$.

Figure 9.7: Example model response along Z-Axis under enforced isotropic conditions compared to pre-existing isotropic Johnson-Cook implementation. Series of figures represents set of strain rates.

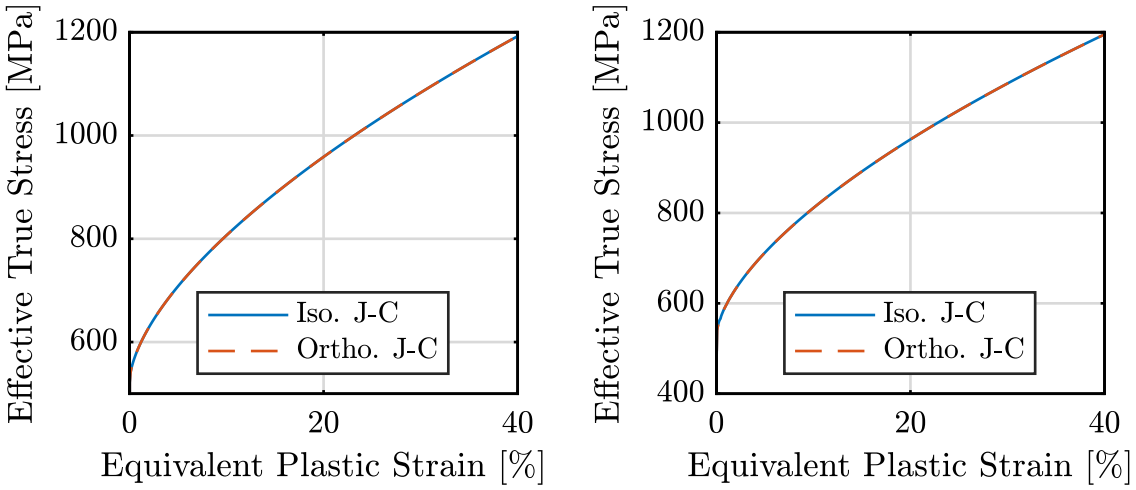

(a) $0.1\,\mathrm{s}^{-1}$.

(b) $1\,\mathrm{s}^{-1}$.

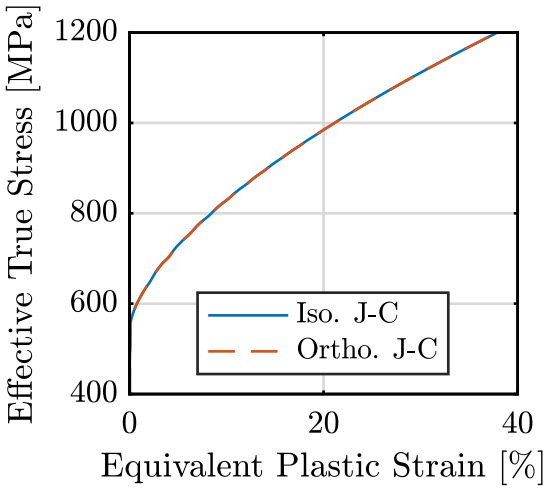

(c) $10\,\mathrm{s}^{-1}$.

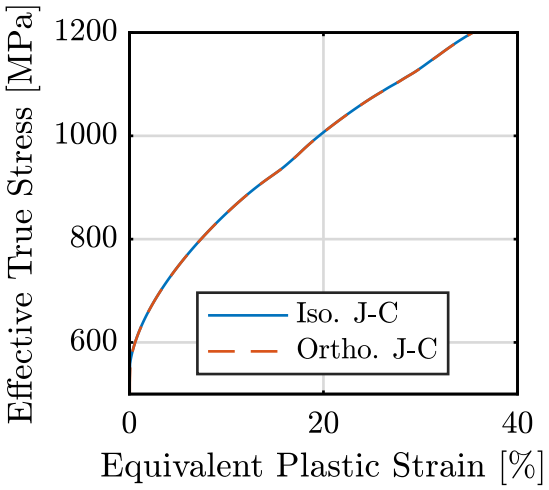

(d) $100\,\mathrm{s}^{-1}$.

Figure 9.8: Example model response along X-Axis under enforced isotropic conditions compared to pre-existing isotropic Johnson-Cook implementation. Series of figures represents set of strain rates.

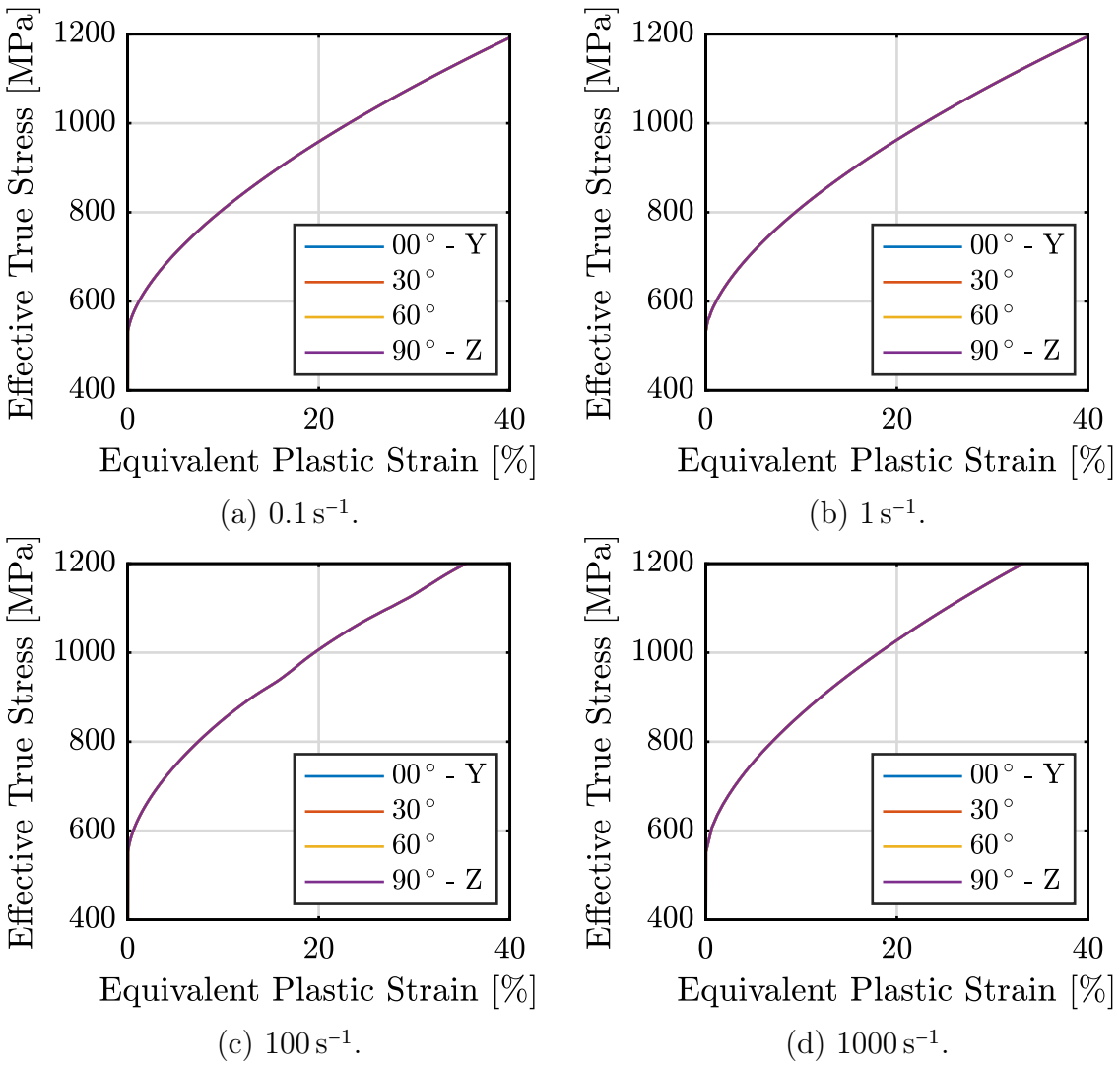

(a) $0.1\,\mathrm{s}^{-1}$. (b) $1\,\mathrm{s}^{-1}$.

(c) $100\,\mathrm{s}^{-1}$. (d) $1000\,\mathrm{s}^{-1}$.

Figure 9.9: Example model response with enforced isotropic conditions for groups of in-plane tests carried out across strain rates.

Johnson-Cook model implemented within LS-DYNA.

Continuing to look for disparities, figures 9.9–9.11 show in-plane orthotropic responses across a set of angles, here the model continues to demonstrate the intended isotropy in orthotropic material responses given the consistency regardless of angle, given the fact that all responses show the same behaviour.

As a final demonstration of the model successfully replicating the isotropic case, the effective stress present at range of equivalent plastic strains (ranging from 10 % up to 40 % in 5 % increments) was calculated for each simulation. The pre-existing isotropic responses were then plotted as contours with each plane, with the orthotropic model (seeded to replicate the pre-existing isotropic model) responses superposed atop

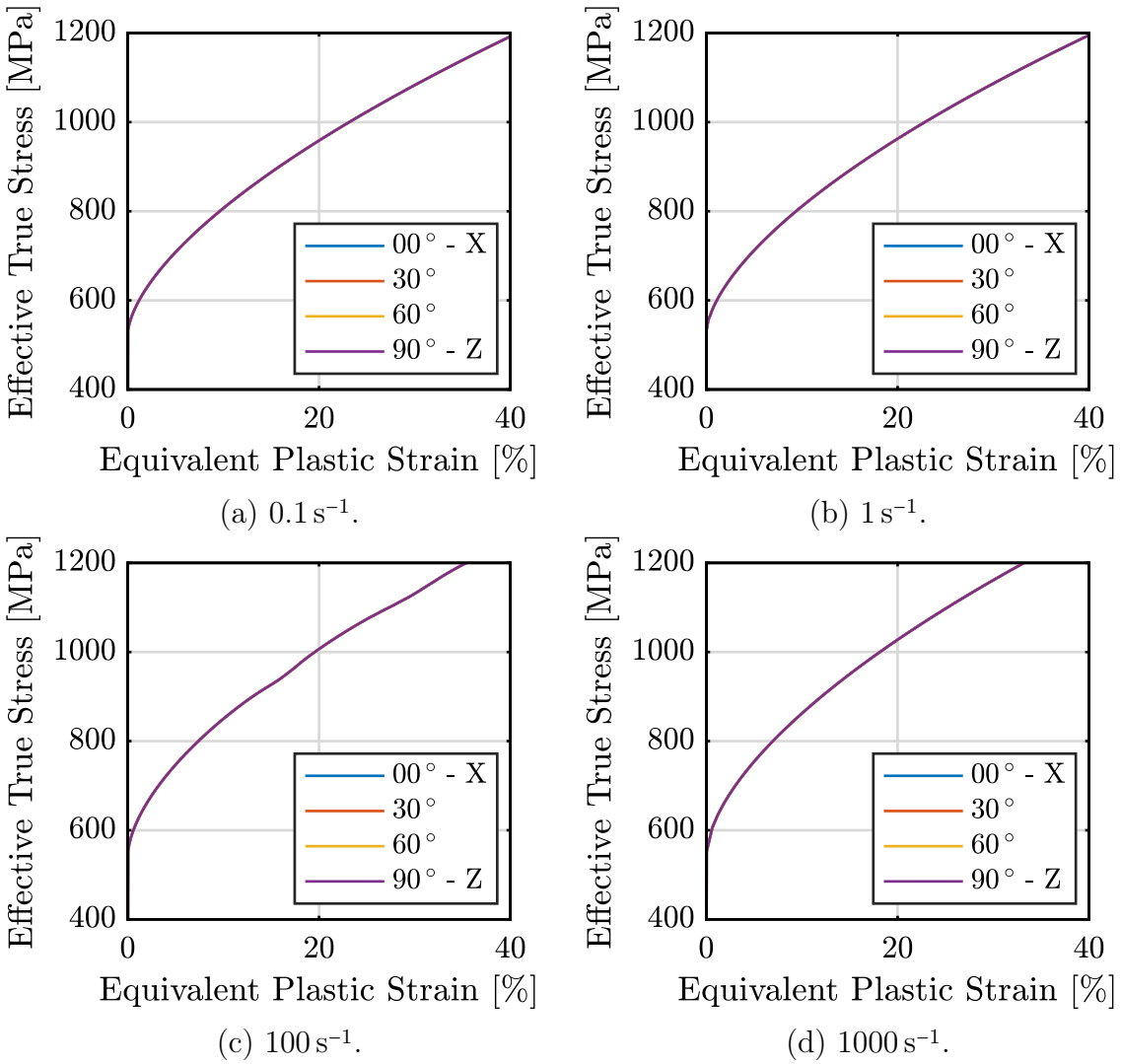

(a) $0.1\,\mathrm{s}^{-1}$.

(b) $1\,\mathrm{s}^{-1}$.

(c) $100\,\mathrm{s}^{-1}$.

(d) $1000\,\mathrm{s}^{-1}$.

Figure 9.10: Example model response with enforced isotropic conditions for groups of in-plane tests carried out across strain rates.

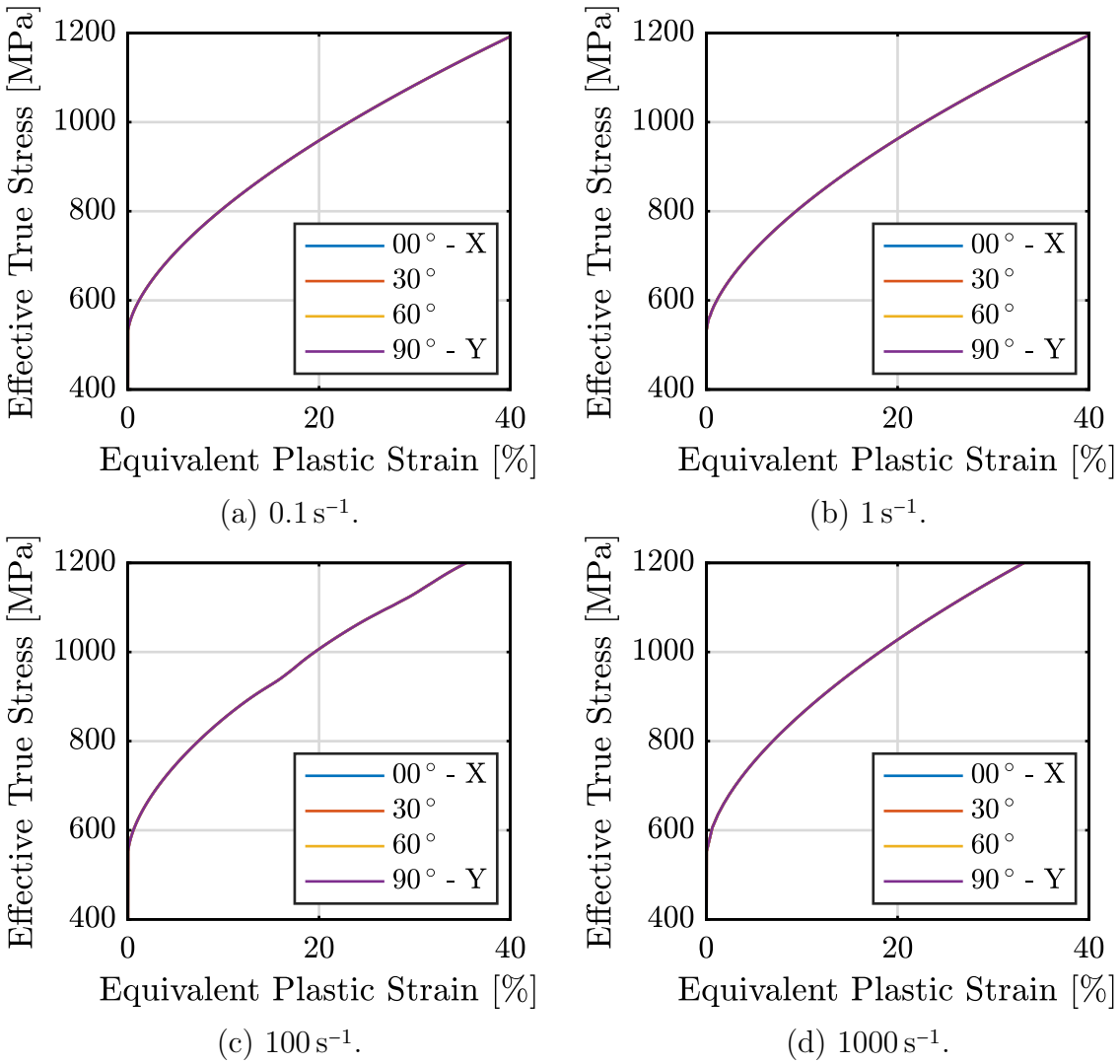

(a) $0.1\,\mathrm{s}^{-1}$.

(b) $1\,\mathrm{s}^{-1}$.

(c) $100\,\mathrm{s}^{-1}$.

(d) $1000\,\mathrm{s}^{-1}$.

Figure 9.11: Example model response with enforced isotropic conditions for groups of in-plane tests carried out across strain rates.

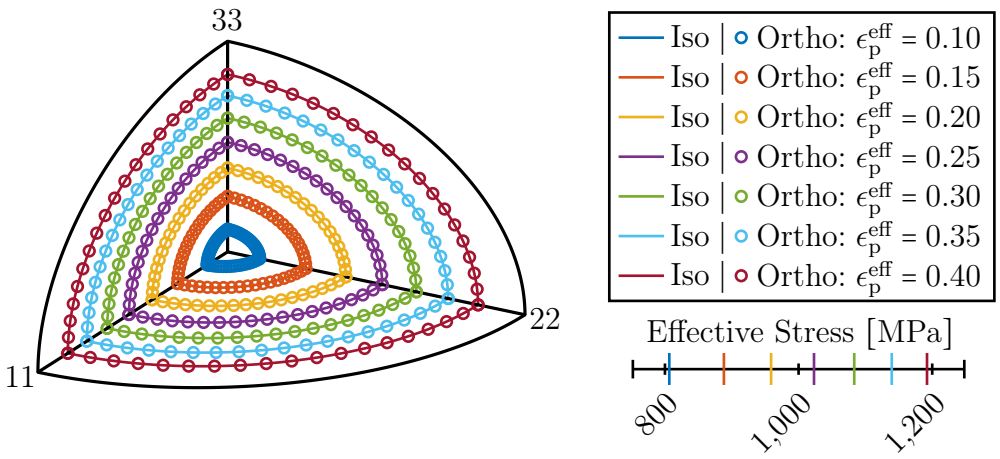

Figure 9.12: Example model response with enforced isotropic conditions across planes for tests carried out at $0.1\,s^{-1}$.

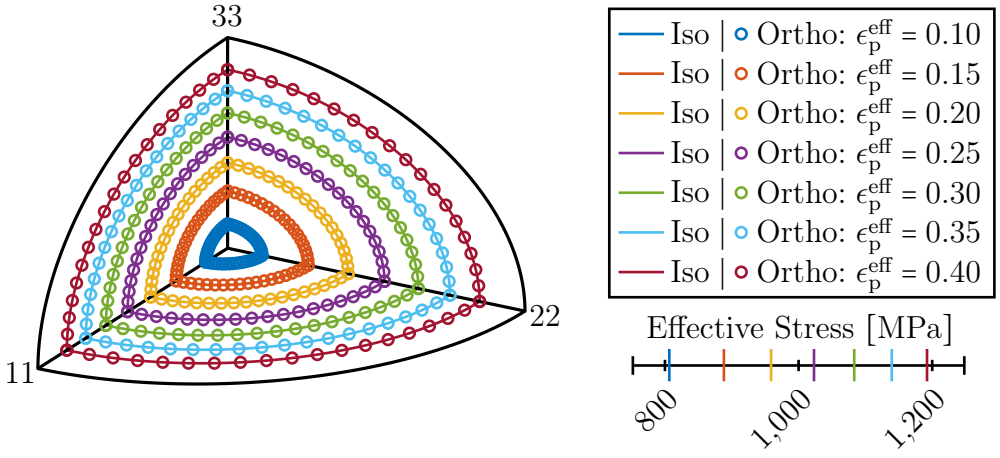

Figure 9.13: Example model response with enforced isotropic conditions across planes for tests carried out at $1\,s^{-1}$.

the contours using circles coloured so as to identify the respective isotropic contour against which they may be compared. Figures 9.12–9.14 show the behaviour across strain rates with the consistent replication of the pre-existing model clearly evident, as the orthotropic circles remain well aligned to their isotropic counterparts.

9.3.2 Yield Onset

Having demonstrated that the orthotropic model behaves equivalently to the pre-existing isotropic model when seeded using the same parameters in every direction, the next step was to investigate the effect of allowing the effective Johnson-Cook parameters to vary directionally. The first parameter to be allowed to vary was x_1,

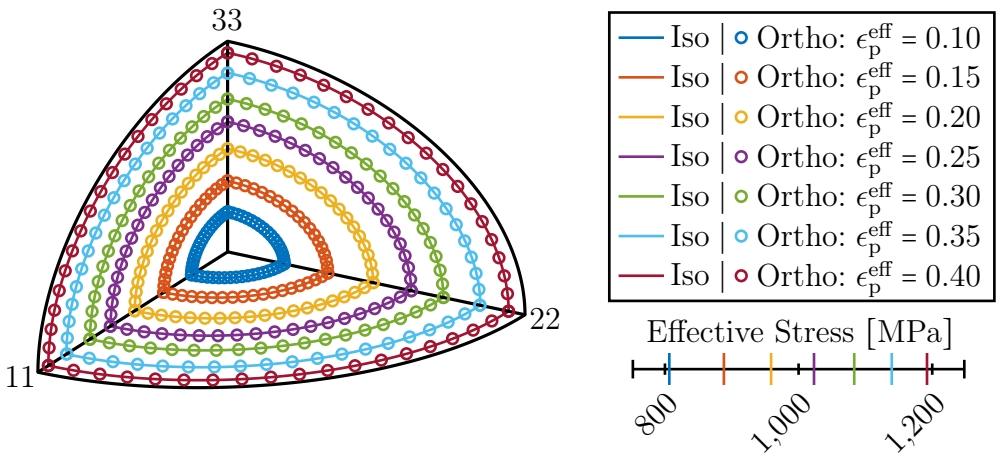

Figure 9.14: Example model response with enforced isotropic conditions across planes for tests carried out at $100\,s^{-1}$.

Direction	$\mathbf{x_1}$ [MPa]	$\mathbf{x_2}$ [MPa]	$\mathbf{x_3}$	$\mathbf{x_4}$	$\mathbf{x_5}$
11	525	1180	0.6220	0.0099	0.5201
22	525	1180	0.6220	0.0099	0.5201
33	577.5	1180	0.6220	0.0099	0.5201
/	551.25	1180	0.6220	0.0099	0.5201
//	551.25	1180	0.6220	0.0099	0.5201
///	525	1180	0.6220	0.0099	0.5201

Table 9.2: Parameter set used to interrogate the effects of implementing an orthotropic yield onset in the model.

highlighted in equation 9.9, with this affecting the initial onset of plastic deformation, to this end the model was seeded with the parameter set given in table 9.2.

$$\sigma^{Y} = \underbrace{\left(x_1}_{\text{Directional}} + x_2 \left(\epsilon_p^{eff}\right)^{x_3}\right)\left(1 + x_4 \ln\left(\epsilon^*\right)\right)\left(1 - \left(T^*\right)^{x_5}\right) \tag{9.9}$$

As can be seen in table 9.2 the increased values for x_1 in the /, //, and 33 directions were chosen to increase the simulated onset of yield as the direction of deformation gradually rotated from the 11-22 (XY) plane to the 33 direction. Once again the validation compares the orthotropic model against the preexisting isotropic model, which in this case is seeded with the parameters of the 11-22 plane. Skipping presentation of individual simulation results similar to figures 9.6–9.8, the behaviour of the orthotropic model across a set of angles in plane, across YZ, ZX, and XY planes, is

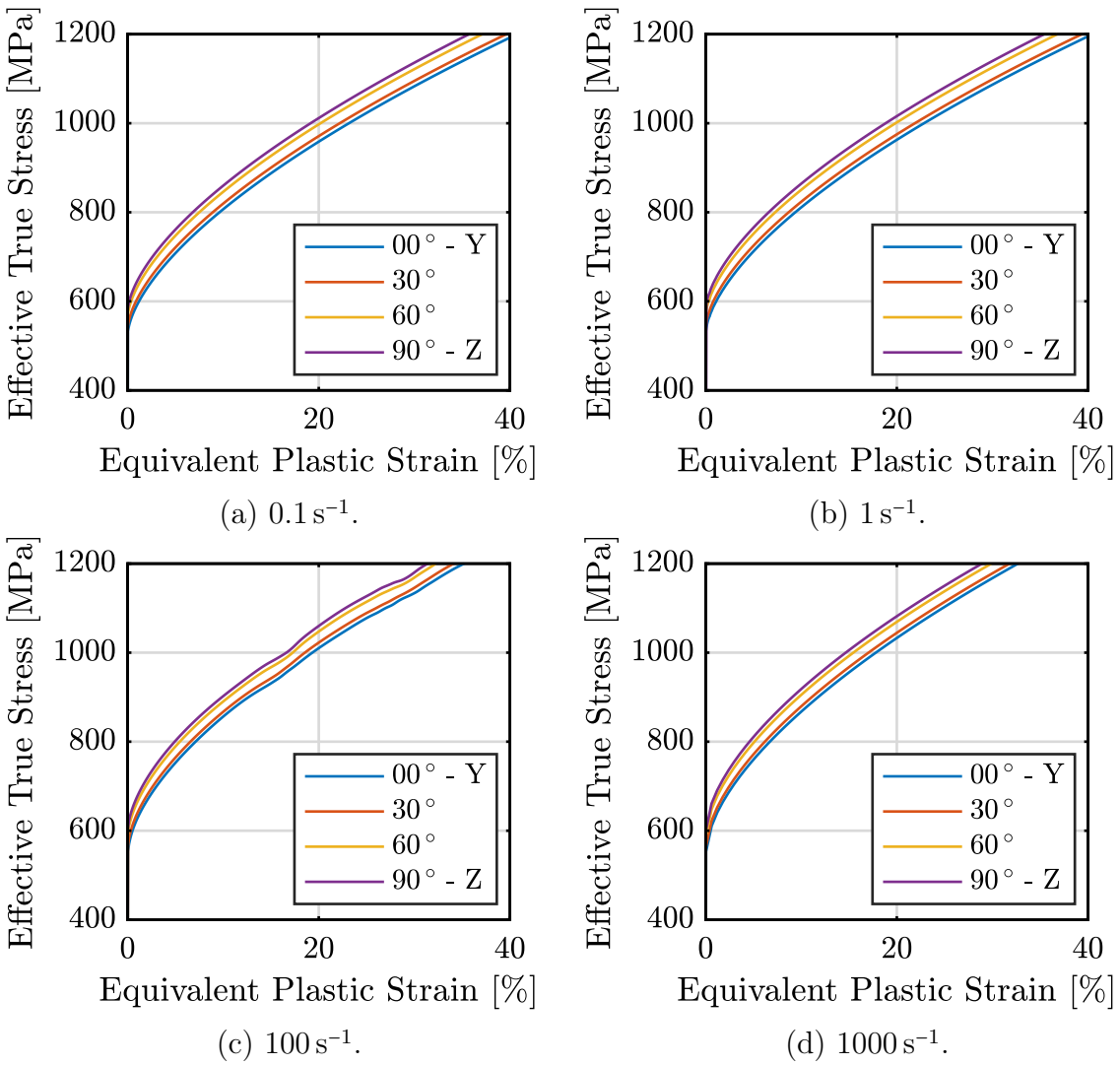

(a) $0.1\,\mathrm{s}^{-1}$. (b) $1\,\mathrm{s}^{-1}$.

(c) $100\,\mathrm{s}^{-1}$. (d) $1000\,\mathrm{s}^{-1}$.

Figure 9.15: Example model response with enforced anisotropic initial yield coefficients for groups of tests carried out across strain rates in the YZ plane.

shown in figures 9.15–9.17.

Considering the observed behaviour, a gradual shift in the curves is seen in responses that involve deformation partially along the 33 axis. The gradual shift in response curves is ordered such that as deformation direction changes to align more closely with the 33 axis the effective stresses increases with a consistent offset regardless of the magnitude of equivalent plastic strain. Carefully looking at the exact spacing of response curves in figures 9.15–9.17, an increased rate of change in yield stress between 30° and 60° is seen when compared to that in the regions around the axes, it is suggested that this follows from the squared-sinusoidal terms within the coordinate transform shown in equation 3.25. Finally for this parameter set, figures 9.18

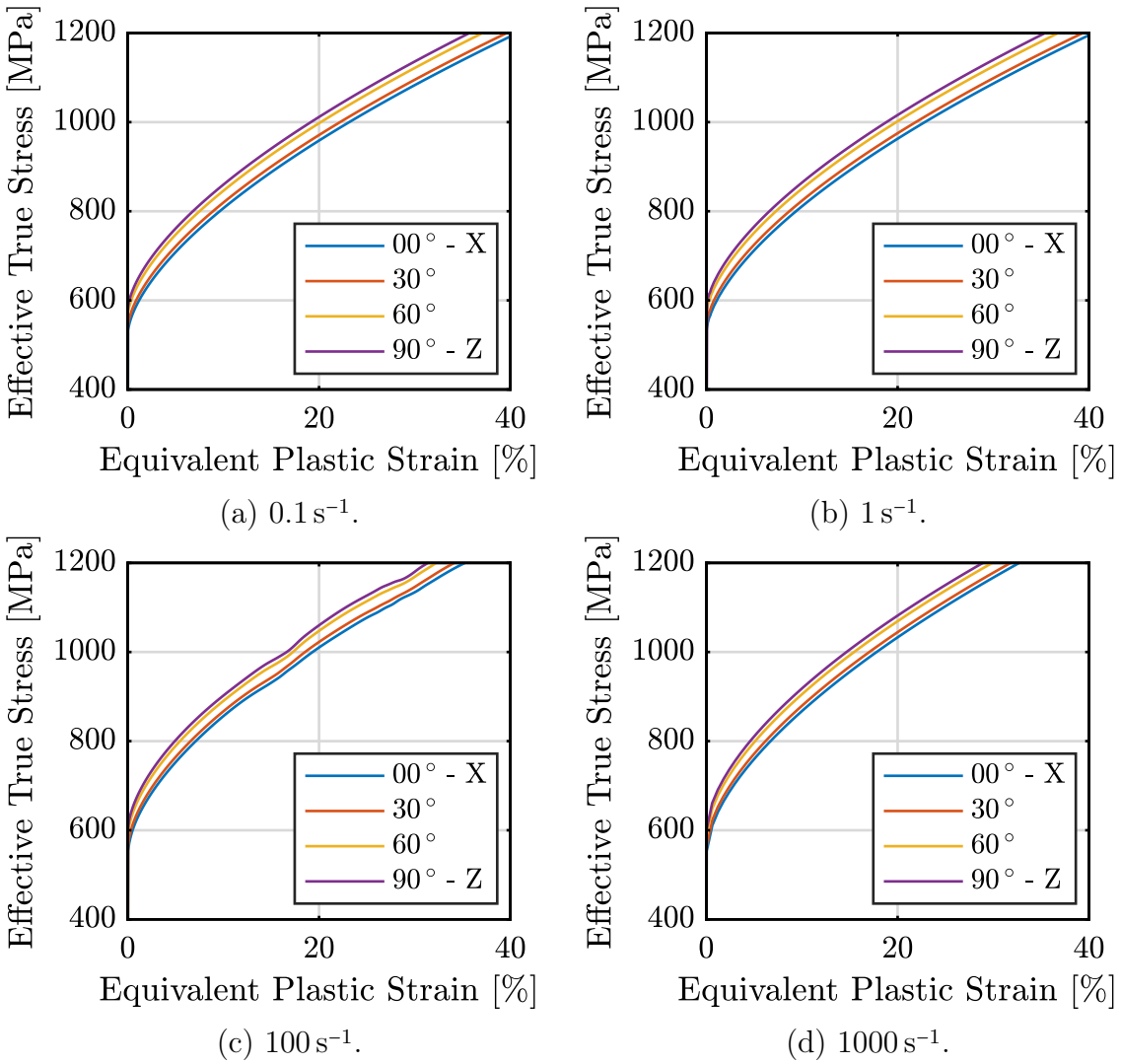

(a) $0.1\,\mathrm{s}^{-1}$.

(b) $1\,\mathrm{s}^{-1}$.

(c) $100\,\mathrm{s}^{-1}$.

(d) $1000\,\mathrm{s}^{-1}$.

Figure 9.16: Example model response with enforced anisotropic initial yield coefficients for groups of tests carried out across strain rates in the ZX plane.

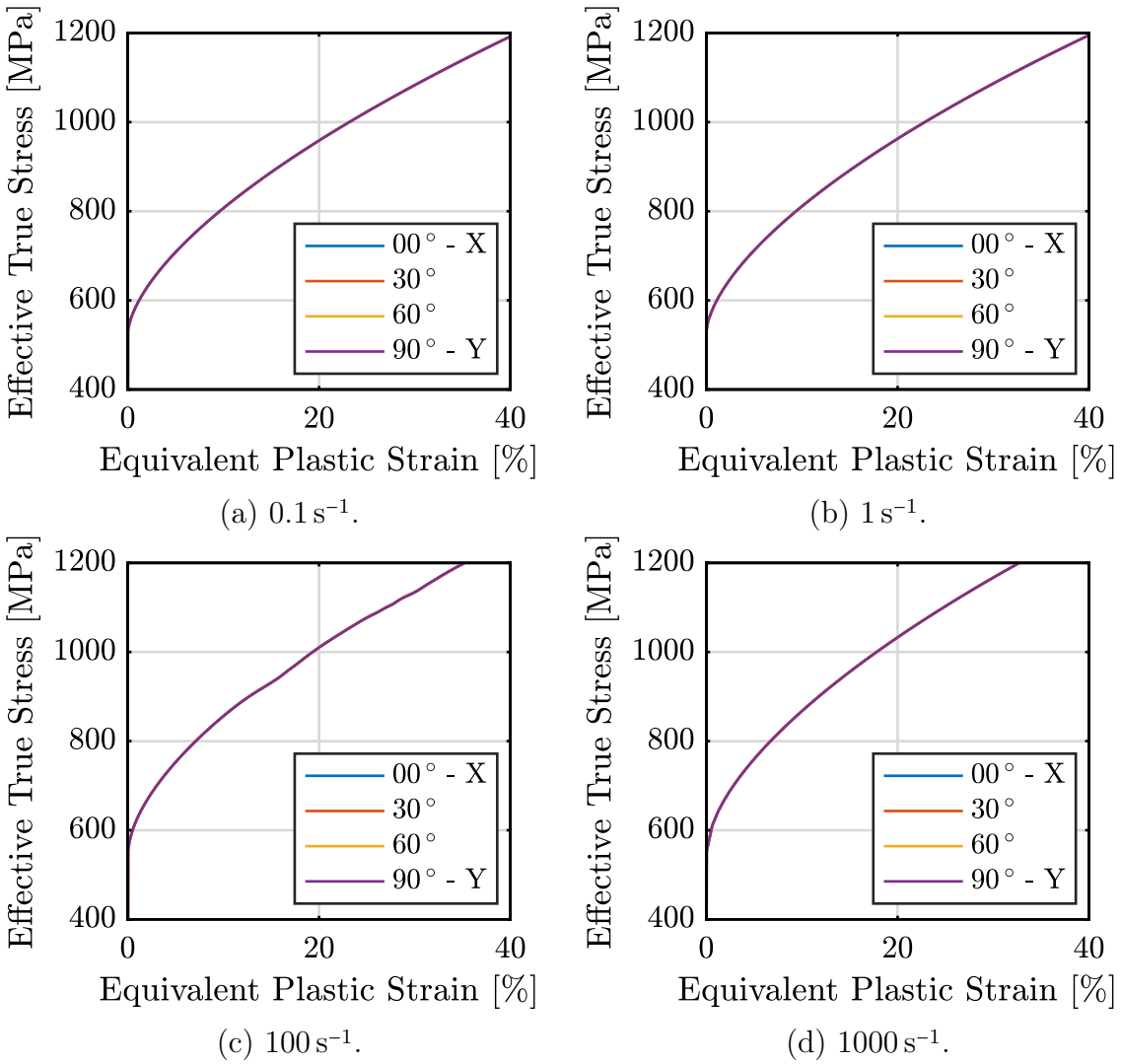

(a) $0.1\,\mathrm{s}^{-1}$.

(b) $1\,\mathrm{s}^{-1}$.

(c) $100\,\mathrm{s}^{-1}$.

(d) $1000\,\mathrm{s}^{-1}$.

Figure 9.17: Example model response with enforced anisotropic initial yield coefficients for groups of tests carried out across strain rates in the XY plane.

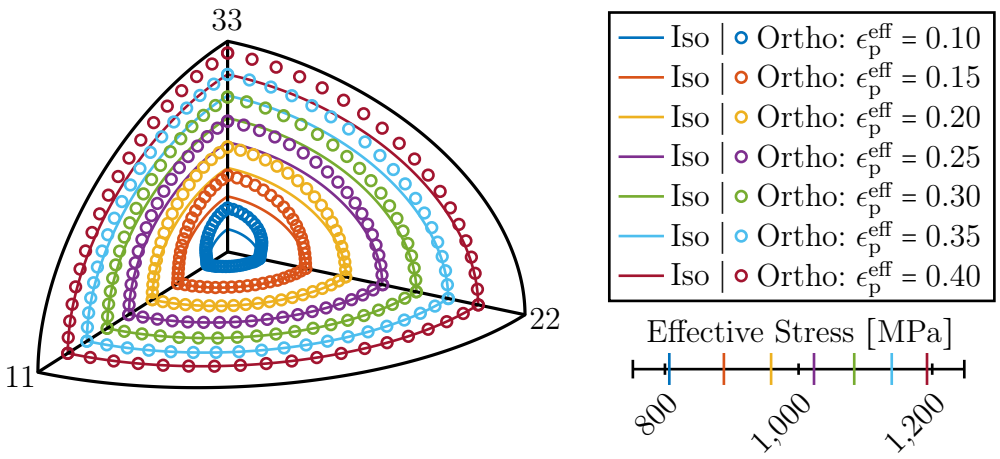

Figure 9.18: Example model response with enforced anisotropic initial yield coefficients across planes for tests carried out at $0.1\,s^{-1}$.

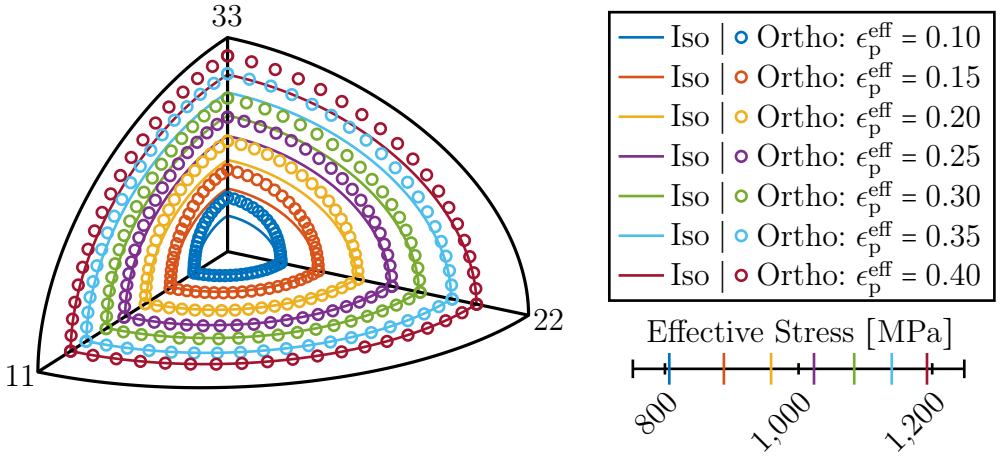

Figure 9.19: Example model response with enforced anisotropic initial yield coefficients across planes for tests carried out at $100\,s^{-1}$.

and 9.19 visualise the response across a range of directions at individual strain rates, with isotropic contours again presented using the same colours for equal strain levels again. Looking at these results, the intended orthotropy is seen in its entirety with a smooth transition in response moving from deformation occurring in the 11-22 plane identically to the isotropic response to that occurring along the plane normal where a greater effective stress is observed at each strain increment.

9.3.3 Strain Hardening

The Johnson-Cook model includes two parameters that mediate the strain hardening process. The first, x_2, is a coefficient that allows for linear variations in the

Direction	$\mathbf{x_1}$ [MPa]	$\mathbf{x_2}$ [MPa]	$\mathbf{x_3}$	$\mathbf{x_4}$	$\mathbf{x_5}$
11	525	1180	0.6220	0.0099	0.5201
22	525	1180	0.6220	0.0099	0.5201
33	525	1298	0.6220	0.0099	0.5201
/	525	1239	0.6220	0.0099	0.5201
//	525	1239	0.6220	0.0099	0.5201
///	525	1180	0.6220	0.0099	0.5201

Table 9.3: Parameter set used to interrogate the effects of implementing an orthotropic hardening coefficient in the model.

magnitude of strain hardening independent of the deformation state. The second, x_3, is an exponent that allows variation in the magnitude of strain hardening that is dependent on the amount of plastic strain, effectively moderating the curvature of the initial plastic response.

Linear

Considering the first strain hardening parameter, highlighted in the expression below,

$$\sigma^{Y} = \left(x_1 + \underbrace{x_2 \left(\epsilon_p^{eff}\right)^{x_3}}_{\text{Directional}}\right)\left(1 + x_4 \ln\left(\epsilon^*\right)\right)\left(1 - \left(T^*\right)^{x_5}\right).$$

The orthotropic response was seeded again to increase the chosen parameter (and therefore the degree of strain hardening) along the 33 (Z) axis with values as given in table 9.3. Figures 9.20 and 9.21, considering only the response in its entirety, show a clear gradual shift in behaviour is seen as tests become more aligned with the 33 axis. Whilst the there is again some instability in both preexisting isotropic and orthotropic models at $100\,s^{-1}$, attributed to the simulation parameters, comparing the orthotropic behaviour to the isotropic contours we see the additional orthotropic hardening shifting the effective stress well beyond the isotropic contours, with the disparities increasing at each increment in effective plastic strain as expected.

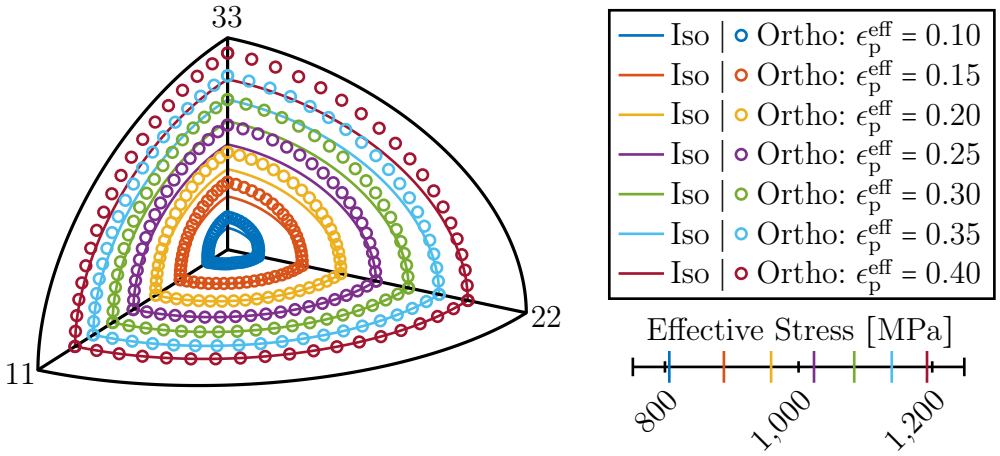

Figure 9.20: Example model response with enforced anisotropic hardening coefficients across planes for tests carried out at $0.1\,\mathrm{s}^{-1}$.

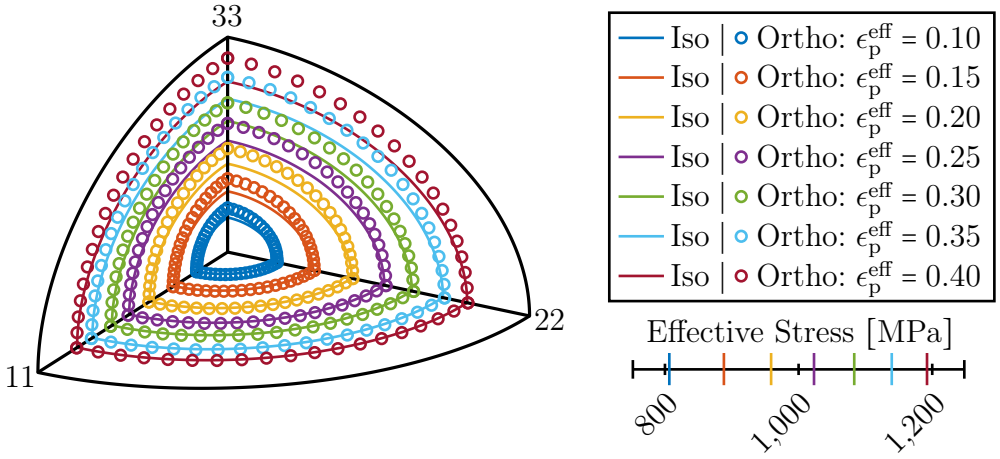

Figure 9.21: Example model response with enforced anisotropic hardening coefficients across planes for tests carried out at $100\,\mathrm{s}^{-1}$.

Direction	$\mathbf{x_1}$ [MPa]	$\mathbf{x_2}$ [MPa]	$\mathbf{x_3}$	$\mathbf{x_4}$	$\mathbf{x_5}$
11	525	1180	0.6220	0.0099	0.5201
22	525	1180	0.6220	0.0099	0.5201
33	525	1180	0.6842	0.0099	0.5201
′	525	1180	0.6531	0.0099	0.5201
″	525	1180	0.6531	0.0099	0.5201
‴	525	1180	0.6220	0.0099	0.5201

Table 9.4: Parameter set used to interrogate the effects of implementing an orthotropic hardening exponent in the model.

Exponential

Subtly differs from hardening coefficient variation in its effects, increases in the magnitude of the hardening exponent (highlighted below),

$$\sigma^{Y} = \left(x_1 + x_2\left(\epsilon_p^{eff}\right)^{\overbrace{x_3}^{\text{Directional}}}\right)\left(1 + x_4 \ln\left(\epsilon^*\right)\right)\left(1 - \left(T^*\right)^{x_5}\right),$$

usually serve to decrease the yield stress in contrast to increasing the hardening coefficient which boosts yield stress for a given plastic strain. This occurs as, in most conditions, both the exponent and equivalent plastic strain are less than 1, increases in the exponent also effectively reduce the curvature of the exponential, given that increases bring its magnitude closer to unity and a linear dependency. In order to highlight the effects of directional dependence of the hardening exponent, the parameter set in table 9.4 was seeded, showing an increased value of x_3 in the 33 direction, with this aiming to reduce the rate of hardening along the Z axis for a given plastic strain.

Looking at the resultant effects in groups of in-plane simulations across angles, the expected reduction in hardening along the Z axis is observed, with the development of anisotropy only present at lower strains, highlighting the differing effects of the strain hardening coefficient and exponent.

Again looking at the full range of directions a clear anisotropy is displayed with a gradual reduction in effective stress at specified equivalent plastic strains along the

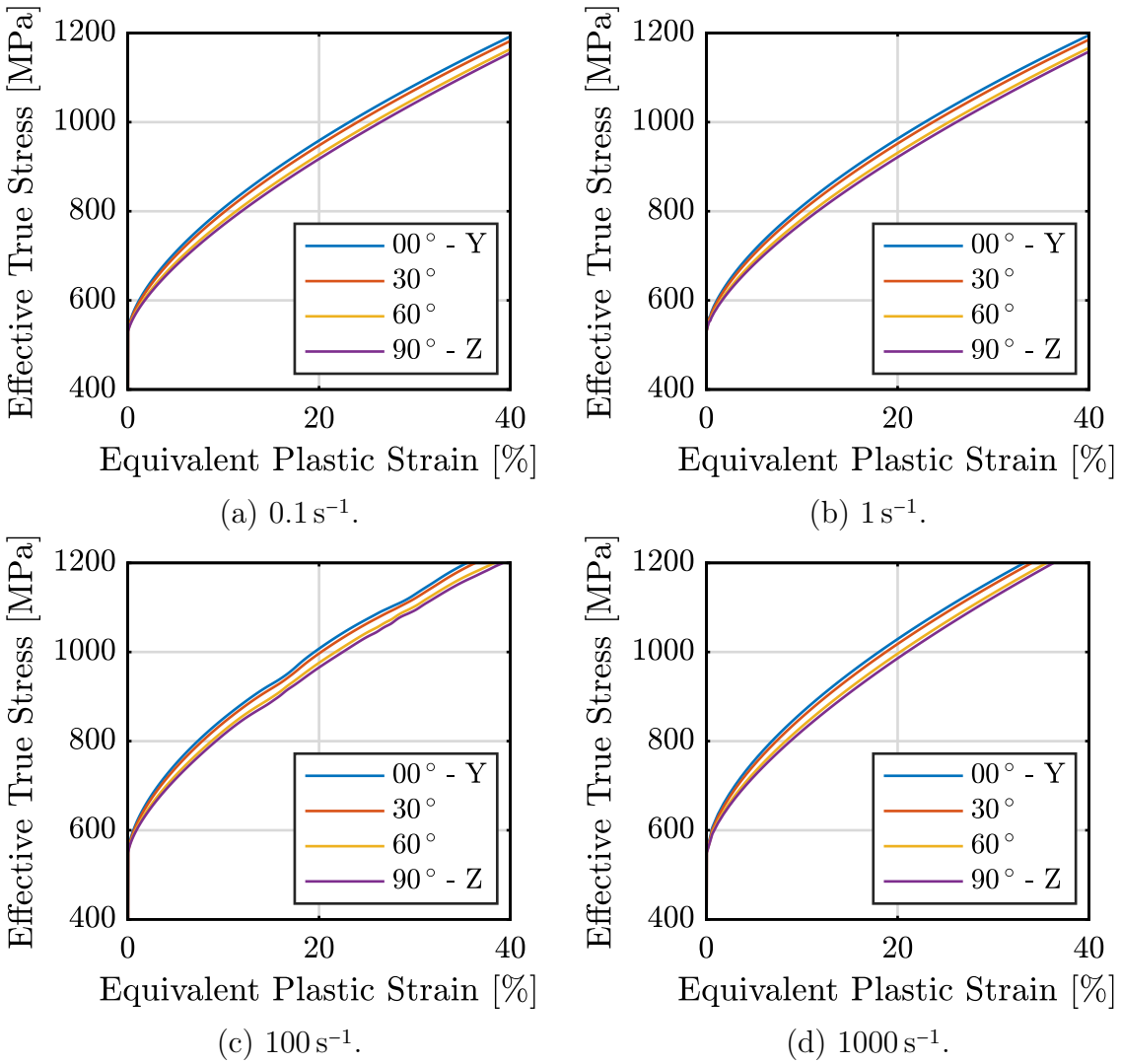

(a) $0.1\,\mathrm{s}^{-1}$.

(b) $1\,\mathrm{s}^{-1}$.

(c) $100\,\mathrm{s}^{-1}$.

(d) $1000\,\mathrm{s}^{-1}$.

Figure 9.22: Example model response with enforced anisotropic strain hardening exponents for groups of tests carried out across strain rates in the YZ plane.

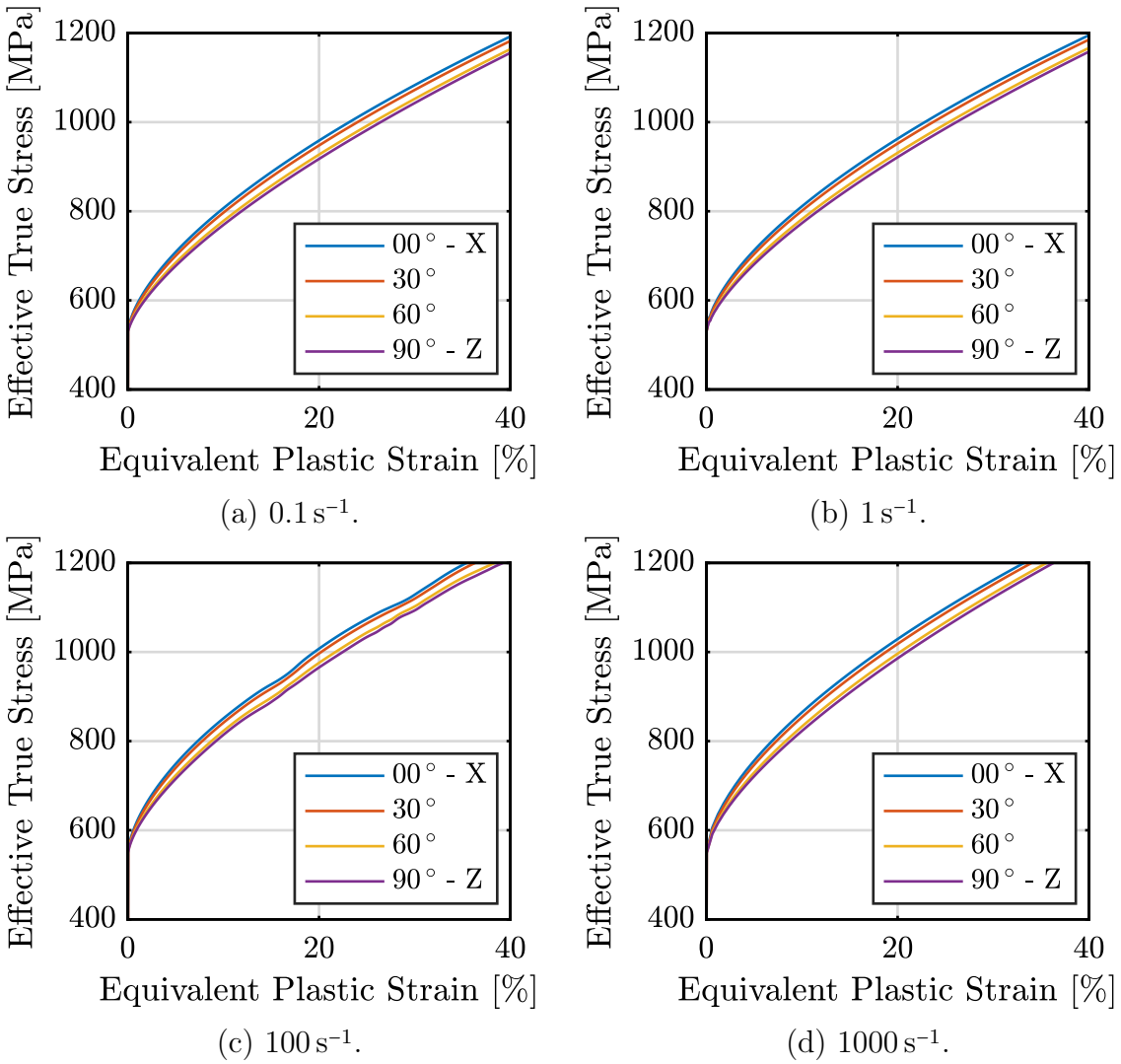

(a) $0.1\,\mathrm{s}^{-1}$.

(b) $1\,\mathrm{s}^{-1}$.

(c) $100\,\mathrm{s}^{-1}$.

(d) $1000\,\mathrm{s}^{-1}$.

Figure 9.23: Example model response with enforced anisotropic strain hardening exponents for groups of tests carried out across strain rates in the ZX plane.

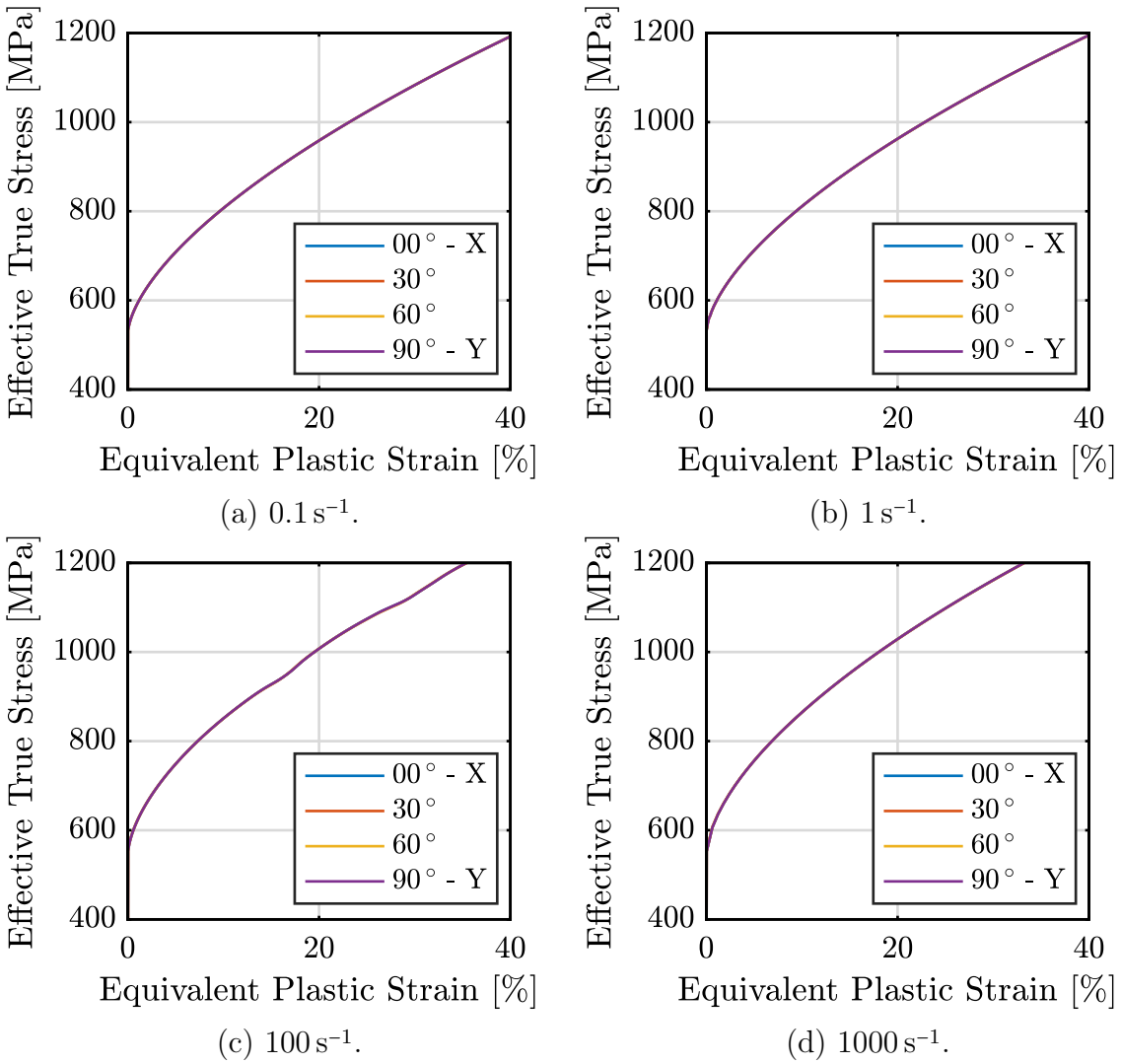

(a) $0.1\,\mathrm{s}^{-1}$.

(b) $1\,\mathrm{s}^{-1}$.

(c) $100\,\mathrm{s}^{-1}$.

(d) $1000\,\mathrm{s}^{-1}$.

Figure 9.24: Example model response with enforced anisotropic strain hardening exponents for groups of tests carried out across strain rates in the XY plane.

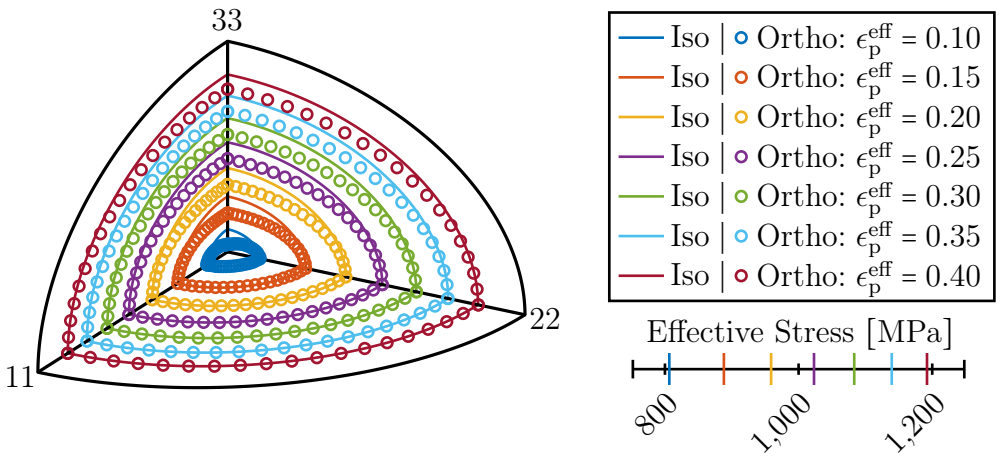

Figure 9.25: Example model response with enforced anisotropic hardening exponents across planes for tests carried out at $0.1\,s^{-1}$.

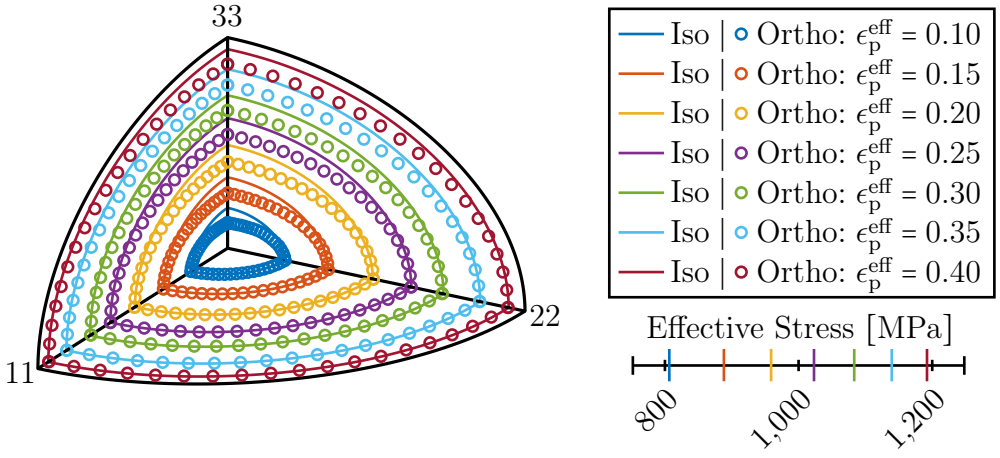

Figure 9.26: Example model response with enforced anisotropic hardening exponents across planes for tests carried out at $100\,s^{-1}$.

weakened Z axis. There is also a reassuring equivalence to the isotropic model maintained in the 11-22 (XY) plane, shown by the alignment of orthotropic circles to the isotropic contours.

9.3.4 Rate Hardening

Possibly the most interesting capability of the model is the potential to create rate-dependent orthotropic responses where the degree of orthotropy itself may depend on the rate of deformation, allowing the model to feasibly handle materials where the generation and propagation of dislocations (each distinct terms within the equation 3.29, the Orowan equation) exhibit differing levels of directionality. Seeding this is achieved

Direction	x_1 [MPa]	x_2 [MPa]	x_3	x_4	x_5
11	525	1180	0.6220	0.0500	0.5201
22	525	1180	0.6220	0.0500	0.5201
33	525	1180	0.6220	0.0575	0.5201
/	525	1180	0.6220	0.0538	0.5201
//	525	1180	0.6220	0.0538	0.5201
///	525	1180	0.6220	0.0500	0.5201

Table 9.5: Rate-dependent model orthotropy validation parameters.

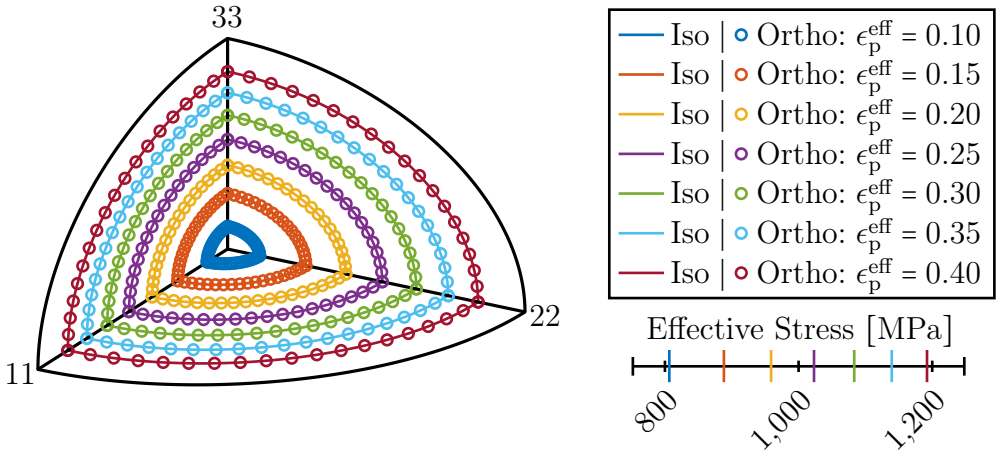

Figure 9.27: Example model response with enforced anisotropic rate-dependency across planes for tests carried out at $0.1\,\mathrm{s}^{-1}$.

by creating a directional dependency in x_4, with this identified below:

$$\sigma^{Y} = \left(x_1 + x_2\left(\epsilon_p^{eff}\right)^{x_3}\right)\Big(1 + \underbrace{x_4}_{\text{Directional}} \ln\left(\epsilon^*\right)\Big)\left(1 - \left(T^*\right)^{x_5}\right),$$

whilst maintaining the other dependencies in an isotropic state. The parameter set used for this scenario is presented in table 9.5, with the reference strain rate [154] set at $1\,\mathrm{s}^{-1}$ as is commonly used with the Johnson-Cook model.

To fully display the directional rate dependence, the behaviour across all planes and across the full logarithmically spaced set of sampled strain rates is presented in figures 9.27–9.31. Inspecting these figures the expected rate-dependency is observed, highlighting a capability that where implemented in other explicit codes, necessitates either tabulated datasets or overnumerous parametrisation.

Explicitly detailing the rate-dependence, fully isotropic behaviour is shown at strain

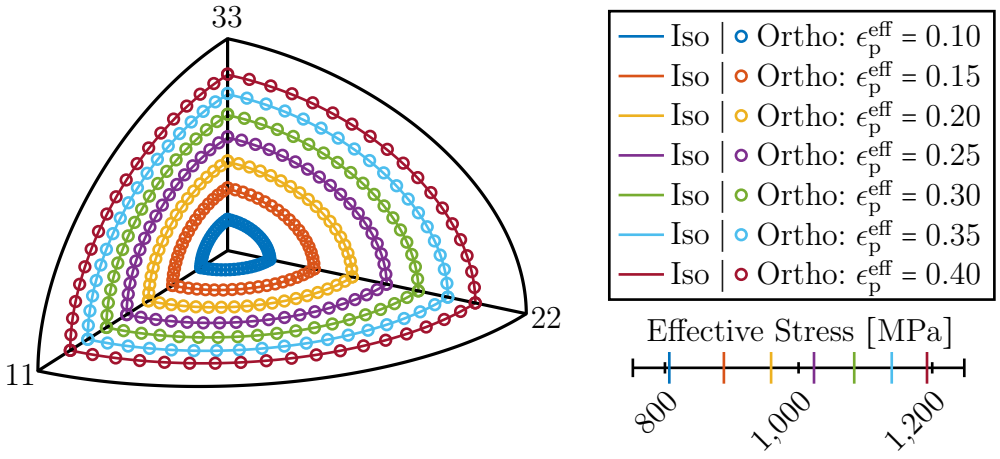

Figure 9.28: Example model response with enforced anisotropic rate-dependency across planes for tests carried out at $1\,s^{-1}$.

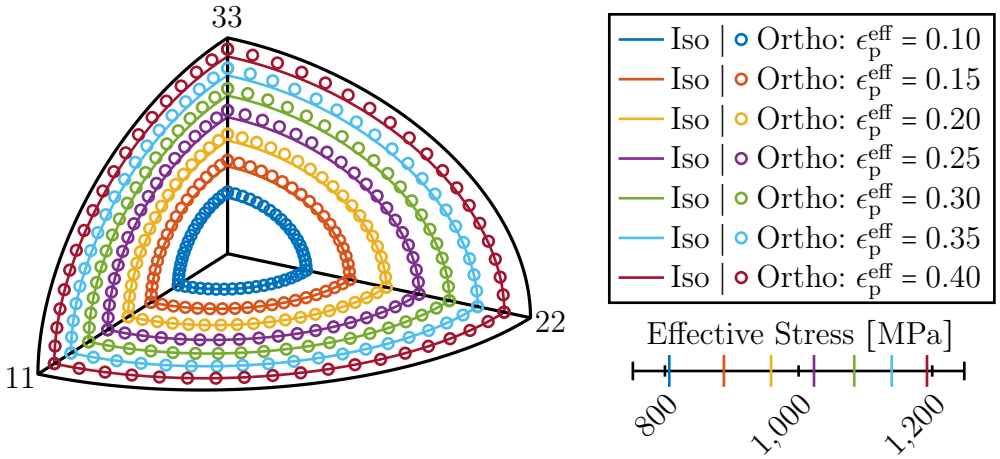

Figure 9.29: Example model response with enforced anisotropic rate-dependency across planes for tests carried out at $10\,s^{-1}$.

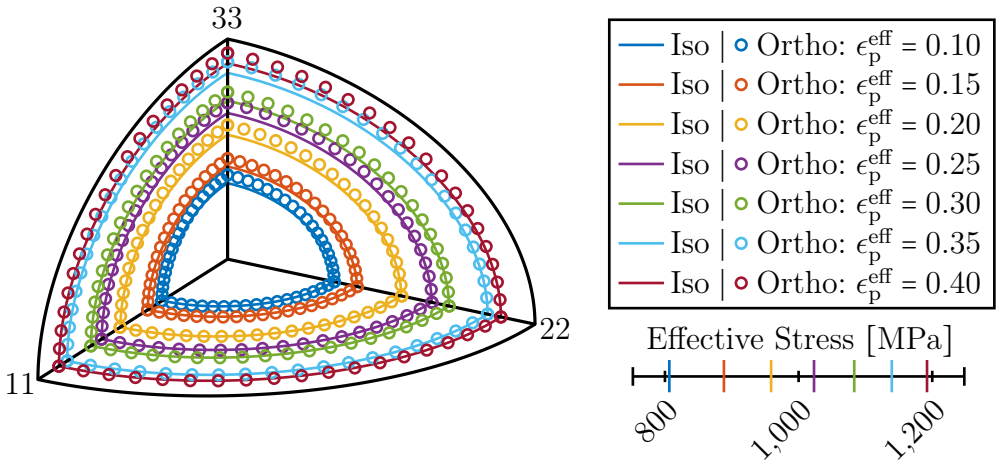

Figure 9.30: Example model response with enforced anisotropic rate-dependency across planes for tests carried out at $100\,s^{-1}$.

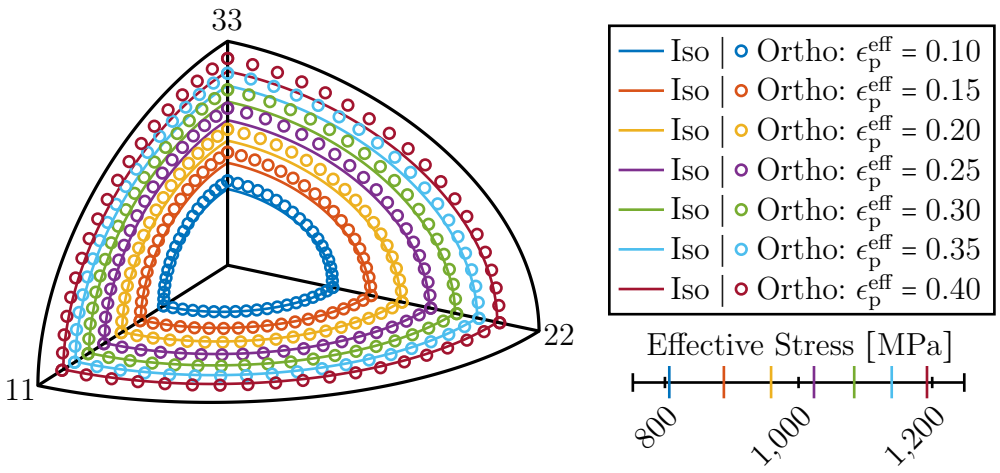

Figure 9.31: Example model response with enforced anisotropic rate-dependency across planes for tests carried out at $1000\,s^{-1}$.

rates not exceeding the reference strain rate ($0.1\,s^{-1}$ to $1\,s^{-1}$), with orthotropy present above this rate allowing the development of increased levels of anisotropy (due to increases in the logarithm of the normalised strain rate), as the strain rate climbs. Of note is the behaviour around the 11-22 (XY) plane at $1000\,s^{-1}$ with the material exhibiting slightly increased strength at higher strains, shown as the coloured orthotropic circles are marginally offset, to increased radii, from the isotropic contours. This increase in strength likely stems from both the rapid deformation inducing a confined state, in turn leading to out of plane stresses which incur slight increases in resultant effective stress and from poisson effects that manifest to become visible due to the increased degree of orthotropy.

9.4 Conclusions

Within this chapter, the numerical eigenspace algorithm detailed in section 3.4 has been developed further to include a directional plastic potential with the potential to implement directional sensitivities to strain, strain rate, and temperature. These directional dependencies have been evaluated with projection along the normalised deviatoric strain increment, passing this potential into the evaluated material eigenspace where traditional, and widely understood, radial return methods can be applied. The resultant hierarchical numerical algorithm, comprising of three layers, has been de-

tailed extensively with accompanying flowcharts. Following the description of the constitutive model, validation was undertaken by first demonstrating the ability to successfully recreate an isotropic Johnson-Cook response across both directions and strain rates when seeded with parameters matching the already implemented isotropic Johnson-Cook within LS-DYNA. Having validated the isotropic case, four distinct individual directional dependencies covering initial yield, hardening, and strain rate sensitivities were probed, with the expected responses observed in all cases. Given the successful validation of the model, the application to observed experimental responses is the logical next step, with this undertaken and described in chapter 10.

Chapter 10

Optimisations & Parametrisation

Following development of the orthotropic Johnson-Cook, its application to recreate recorded experimental responses would necessitate the identification of a suitable parameter set. The methodology and results of identifying the optimal parameter set are discussed herein.

10.1 Parameter Identification Routine

To identify the combination of parameters best able to recreate the observed range of experimental behaviour an iterative optimisation technique was used. This technique, also known as regression or inverse modelling, is suited to experimental data where a range of material and loading states are present such that robust analytical solutions to the undertaken experiments do not exist. The technique also allows for simultaneous optimisation against a series of experiments with varying experimental conditions, helping to mitigate against the difficulty in conducting repeats of complex dynamic impact events. Instead, by validating the result from a good agreement across the ensemble of conditions sampled the potential for parameter overfitting is reduced. By comparing the response of digital twins, simulations generated to mimic real world experiments, simultaneously across a range of strains, strain rates, and orientations the parameter set of the orthotropic material model may be robustly identified. It should be noted that an exact solution, perfectly recreating the observed responses, is not expected, instead inverse modelling seeks to identify the optimal parametrisation of the implemented material model, with the true material response approximated by this intermediary mathematical construct.

In practice this optimisation involved an iterative convergence routine, within the LS-OPT software package, as summarised in figure 10.1. Here an ensemble of trial pa-

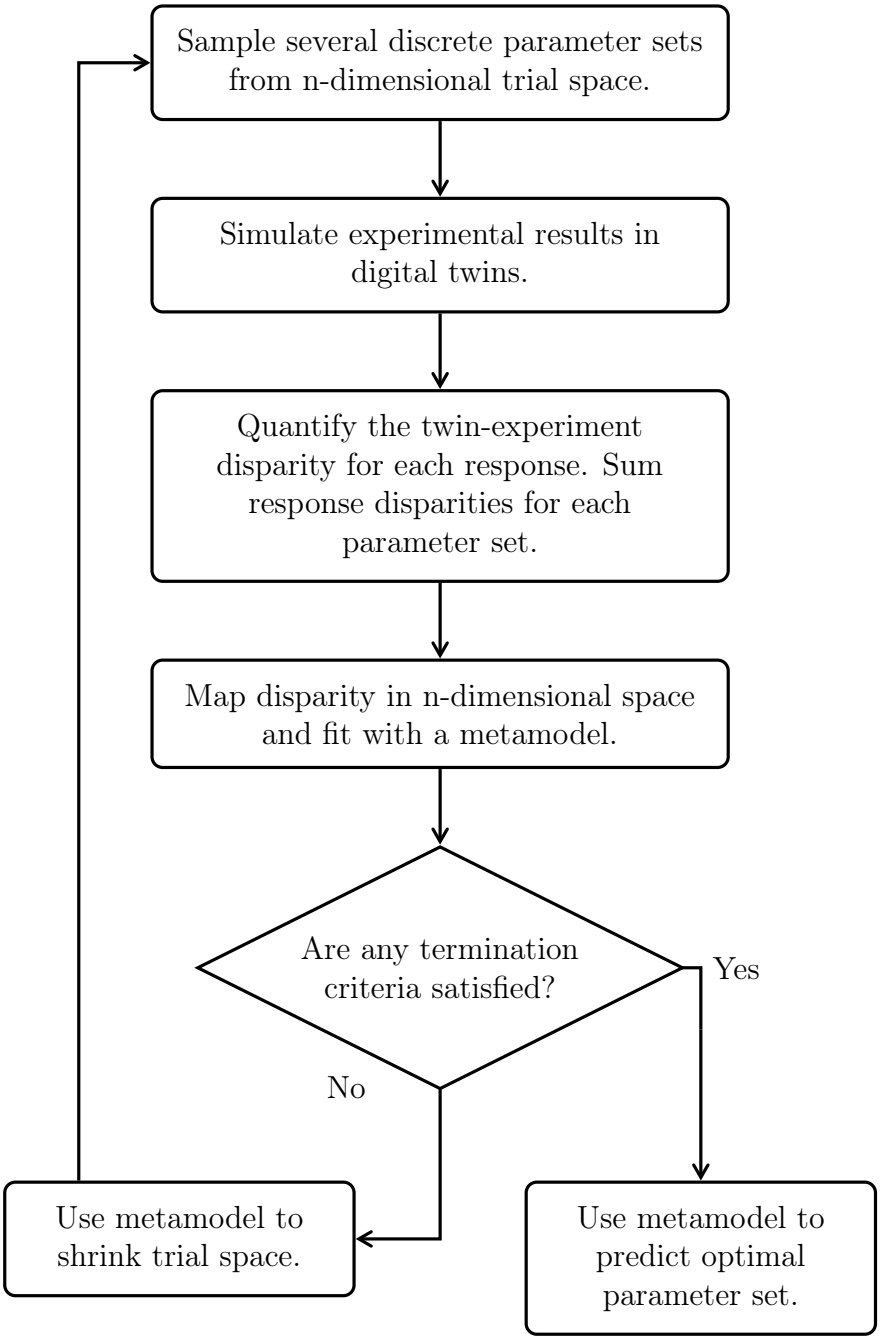

Figure 10.1: Parameter identification workflow within LS-OPT.

rameter sets are sampled from an n-dimensional parameter domain; the sampling technique used within this project was a standard D-Optimal technique [229], providing a robust and efficient sampling algorithm widely used within this class of multivariate non-linear problems [230]. Sampled trial parameter solutions were then implemented within the set of digital twins, with the simulated responses serving to populate an $(n+1)$-dimensional manifold. The absolute value, the "height" of the manifold in an abstract sense given that $n > 2$, of this manifold described the cumulative disparity across all responses of all the digital twins for that specific parameter solution. The combined measure of response convergence was chosen to be the summation of weighted mean square errors, with weightings ensuring the order of magnitude of responses were approximately equal. Whilst more involved algorithms could be implemented to gauge overall convergence, ensuring that there was no large disparity in response magnitude ensured that the optimisation would remain somewhat sensitive to all the histories throughout several iterations, driving continued convergence.

Upon completion of a given iteration, having explored a region of the n-dimensional parameter domain, the response was be mapped out in an $(n+1)$-dimensional space, with the response surface approximated using a low order polynomial metamodel. This metamodel served to simplify the non-linear surface and smooth out local variations. From here, the locating of regions exhibiting an increased disparity identified areas where less optimal parameter solutions were located. With unfavourable regions identified, the n-dimensional domain could be reduced in size, avoiding less optimal regions. Successive iterations served to map ever more favourable areas with an ever increasing sampling density.

10.2 Digital Twins

In the overview of the iterative optimisation routine, digital twins are described that served to recreate conducted experiments. For this optimisation the full suite of room temperature Taylor impact experiments were used to provide the set digital twins, with the combination of limited real world event scale, and short experiment

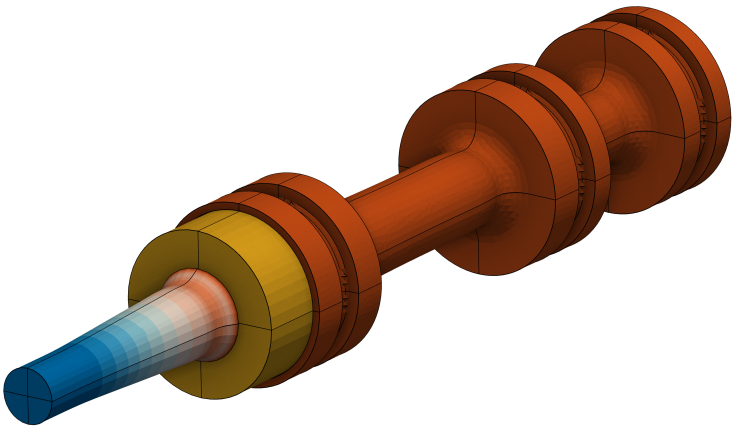

Figure 10.2: Quarter symmetry reverse Taylor impact simulation used as a template for digital twins in orthotropic Johnson-Cook optimisations. The simulation is shown mirrored along symmetry planes to give a full view. Both sabot and flyer are shown in a single colour with the target coloured proportional to the amount of incurred equivalent plastic strain in that simulation at that point in time.

duration reducing the computational demands of explicit simulations. These computational demands were a key concern given the complexity of the numerical algorithm underpinning the constitutive strength model being optimised.

The coupled evolution of the target length and the rear surface motion, each aligned temporally using the impact time derived from flyer surface motion, were chosen to optimise the material model within the iterative routine. These two experimental histories provided information on both the plastic and elastic responses, the rear surface motion specifically provided both, with elastic wave reverberations along the target convolved by the evolution of plastic deformation gradually propagating towards the rear surface of the Taylor rod.

Due to the directional nature of the material model, it was infeasible to reduce the computational demands by fully leveraging the axial geometric symmetry of the reverse Taylor impact experiment using a two-dimensional asymmetrical simulation. In order to avoid a full three dimensional simulation, a quarter symmetry digital twin was implemented, as shown in figure 10.2 with black lines highlighting axes of symmetry about which the rendering is reflected. This allowed for a reduction in the computational demands of each simulation, whilst still supporting the orthotropy within the implemented material model.

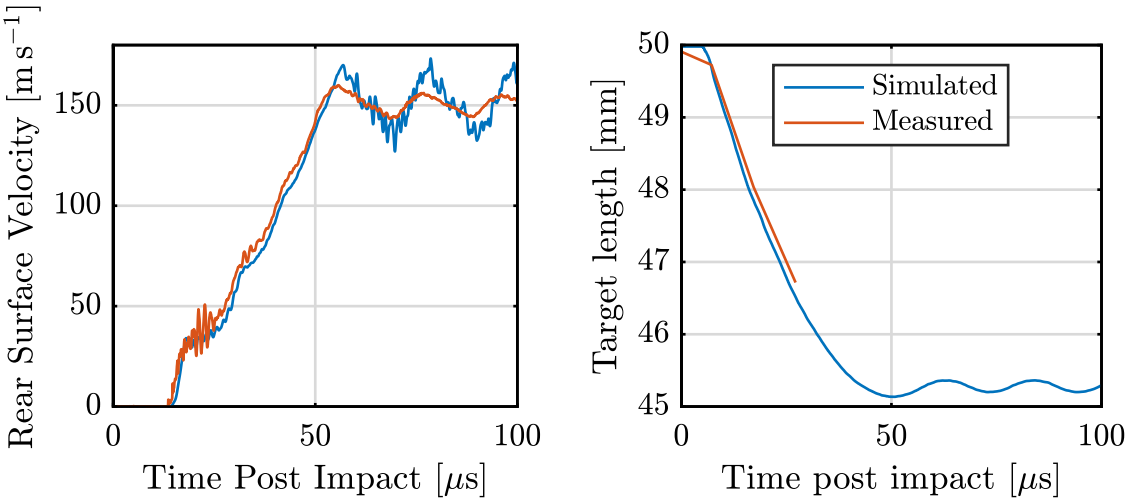

(a) Target rear surface motion.

(b) Target length evolution.

Figure 10.3: Example simulated histories produced from an initial ensemble of parameter sets used in an iterative optimisation. Here a discrepancy exists between the observed and predicted responses for several reasons, including the dependencies defining the mathematical form of the model and the values of parameters used to populate the model.

The evolution of rear surface motion was then recorded from nodes at the center of the rear surface to recreate measured data, whilst length evolution was recorded using the relative position of nodes along the faces at each end of the target, examples of each are visualised in figure 10.3. As stated in section 7.3, regression to radial profile histories was avoided due to the directionality of the implemented material model. Specifically, the variation in plastic responses parallel or perpendicular to the build direction would seed non-axisymmetric radial cross sections in Taylor impact testing of horizontally oriented samples, with elliptical cross sections generated by similarly orthotropic digital twins.

10.3 Porous AM 316L

The optimisation of the orthotropic model to porous additively manufactured 316L would require the evaluation of a set of directional responses where negligible variations in dynamic testing conditions,specifically impact velocity differences of a few m s^{-1}, paired with differing orientations led to a clear variance in the dynamic response. Seeding the n-dimensional parameter domain using the values given in table 10.1,

Name	Lower Bound	Value	Upper Bound
x_{1H}	5.00×10^{8}	5.50×10^{8}	6.50×10^{8}
x_{1V}	5.00×10^{8}	5.41×10^{8}	6.50×10^{8}
x_{2H}	5.00×10^{8}	1.16×10^{9}	1.40×10^{9}
x_{2V}	9.00×10^{8}	1.25×10^{9}	1.40×10^{9}
x_{4H}	5.00×10^{-3}	1.38×10^{-2}	3.00×10^{-2}
x_{4V}	5.00×10^{-3}	1.28×10^{-2}	3.00×10^{-2}
E	1.37×10^{11}	1.57×10^{11}	2.50×10^{11}
ν	2.00×10^{-1}	3.10×10^{-1}	4.00×10^{-1}
x_{3H}	3.00×10^{-1}	5.50×10^{-1}	7.00×10^{-1}
x_{3V}	3.00×10^{-1}	5.50×10^{-1}	7.00×10^{-1}

Table 10.1: Initial parameters for iterative optimisation of orthotropic Johnson-Cook to experimental behaviour of porous AM 316L steel. Where a parameter name ends with either an H or V, this is a Johnson-Cook model parameter for either vertical or horizontal directions assuming transverse isotropy about the vertical axis. E is given as the Young's modulus with ν given as the Poisson's ratio.

taken from values within the literature pertaining to conventionally manufactured 316L [226–228], a gradual convergence was seen across several iterations.

The gradual convergence to measured experimental histories is visualised in figures 10.4–10.7 with experimental histories given alongside the evaluated albeit non-normalised disparities between the simulations and the experiment.

Following convergence of the simulated response to the experimental histories, a single set of parameter values were identified as providing an optimal reconstruction of the set of observed experimental responses, presented in table 10.2. Here, considering the optimised set of parameters, the disparity in x_1 observed between horizontal and vertical directions echoes the analysis of initial pulse heights, with elevated initial yield strengths observed in the horizontal orientation. To draw further conclusions here, it is best to consider the results alongside the optimised parameter set returned from the separate regression to 316L without significant porosity.

10.4 Dense AM 316L

When optimising the orthotropic Johnson-Cook to experimental histories recorded for dense additively manufactured specimens, the parameter set was seeded from the same initial state given in table 10.1, with convergence achieved after several iterative

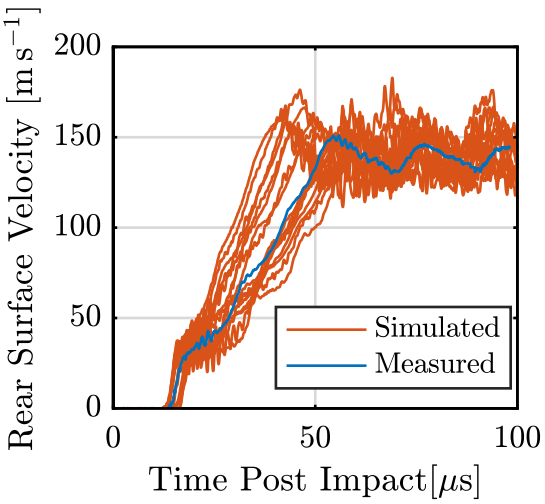

(a) Iteration 1.

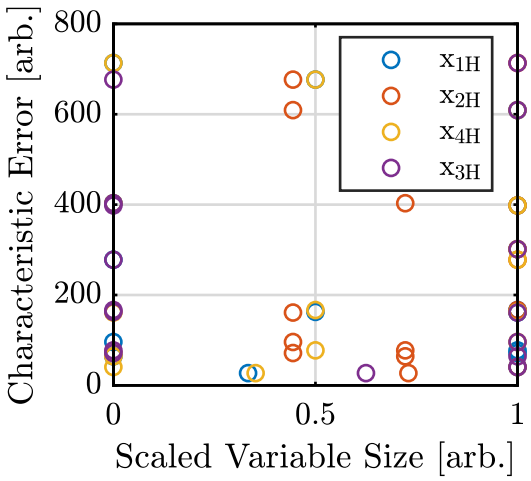

(b) Iteration 1.

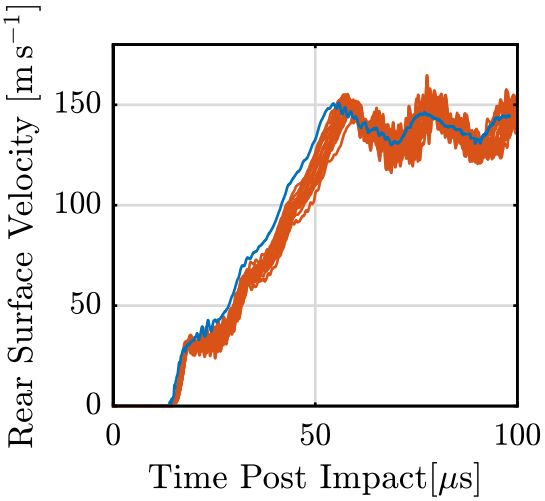

(c) Iteration 5.

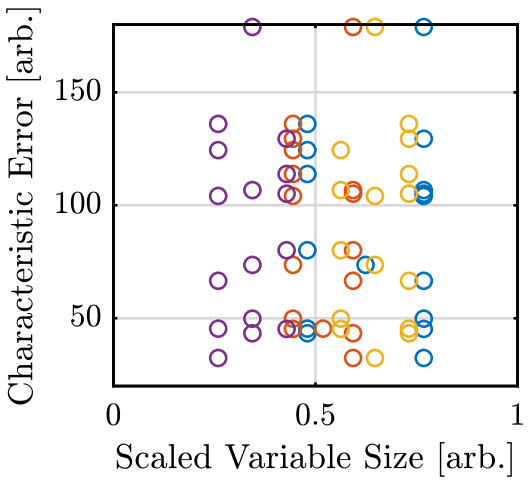

(d) Iteration 5.

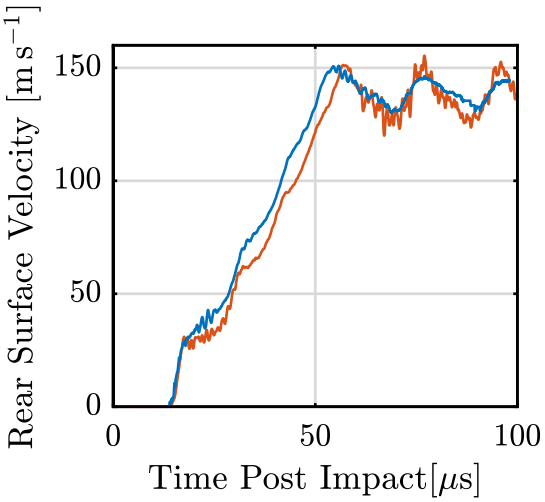

(e) Iteration 15.

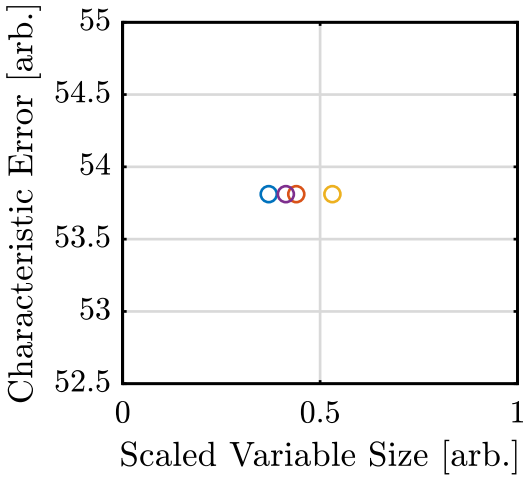

(f) Iteration 15.

Figure 10.4: Convergence of rear surface velocity histories for a horizontally oriented reverse Taylor impact digital twin to recorded experimental histories. The experiment in question is AM H POR RT TT 1, with an impact velocity of 177 m s^{-1}.

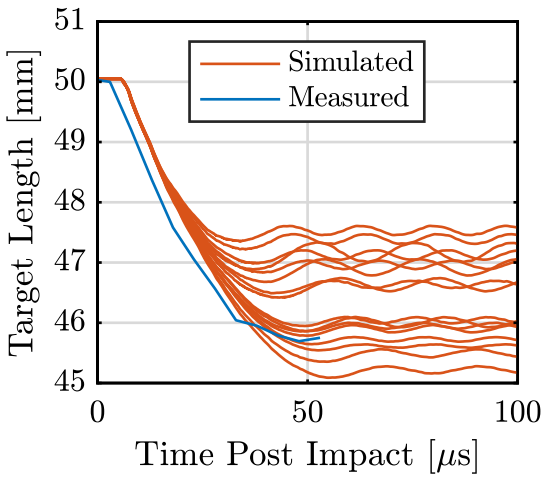

(a) Iteration 1.

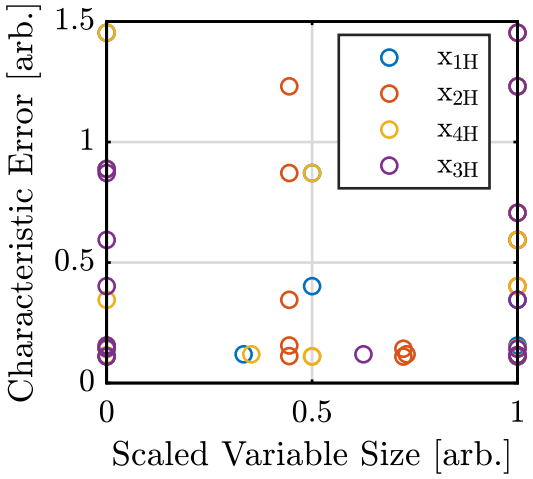

(b) Iteration 1.

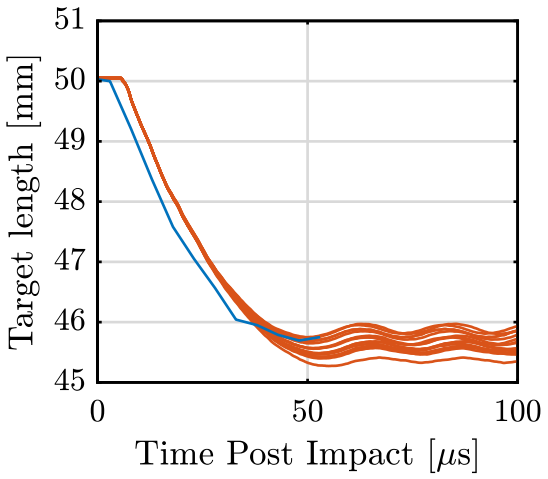

(c) Iteration 5.

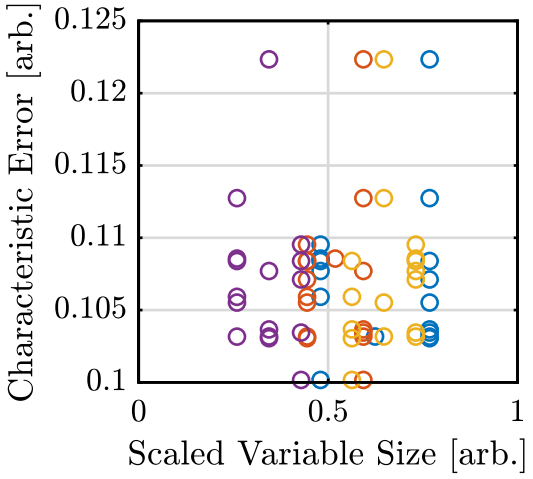

(d) Iteration 5.

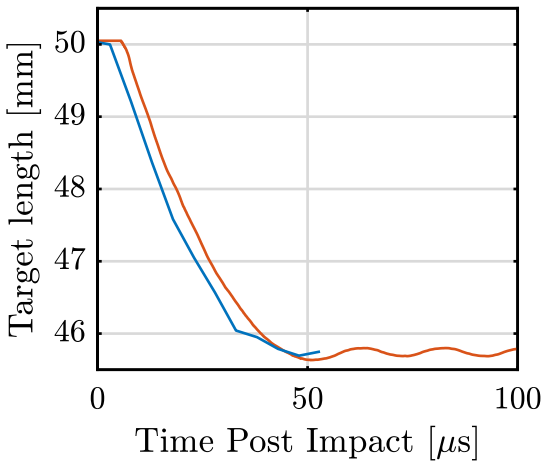

(e) Iteration 15.

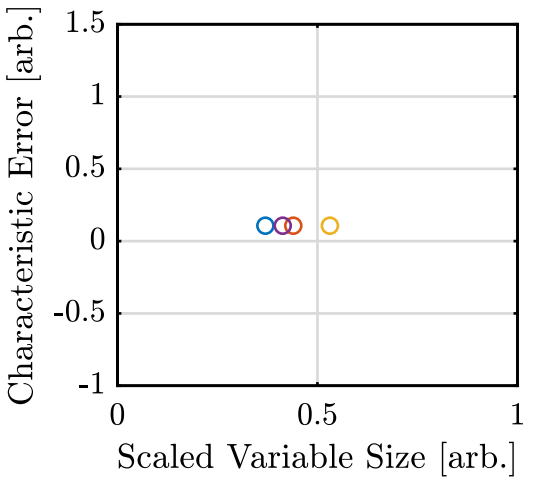

(f) Iteration 15.

Figure 10.5: Convergence of target length evolution histories for a horizontally oriented reverse Taylor impact digital twin to recorded experimental histories. The experiment in question is AM H POR RT TT 1, with an impact velocity of 177 m s^{-1}.

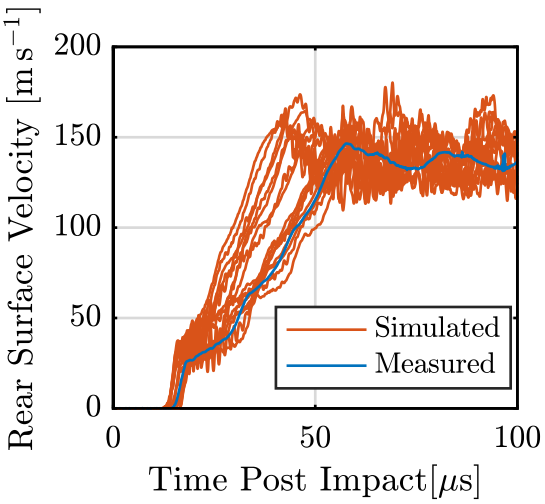

(a) Iteration 1.

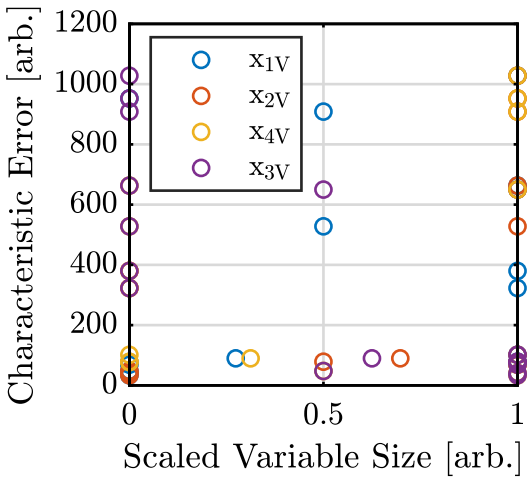

(b) Iteration 1.

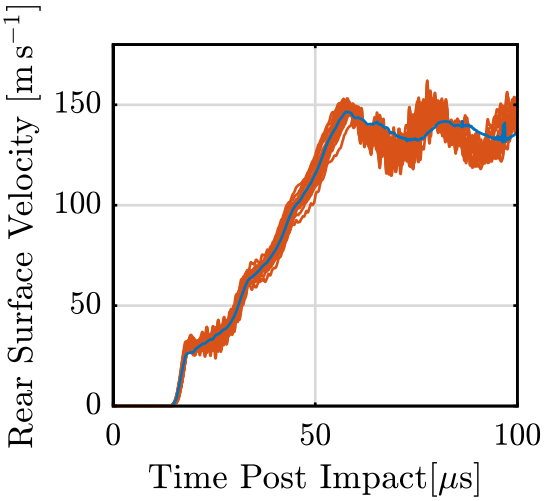

(c) Iteration 5.

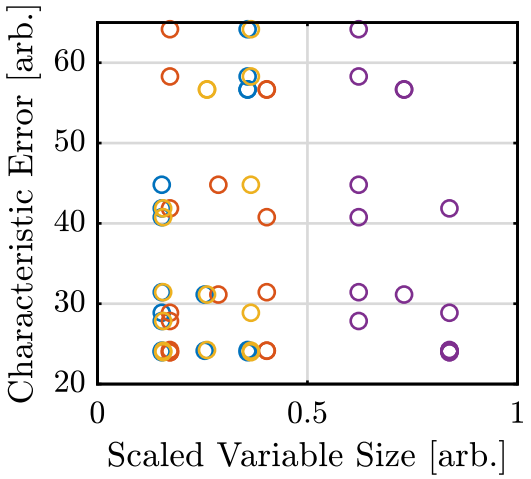

(d) Iteration 5.

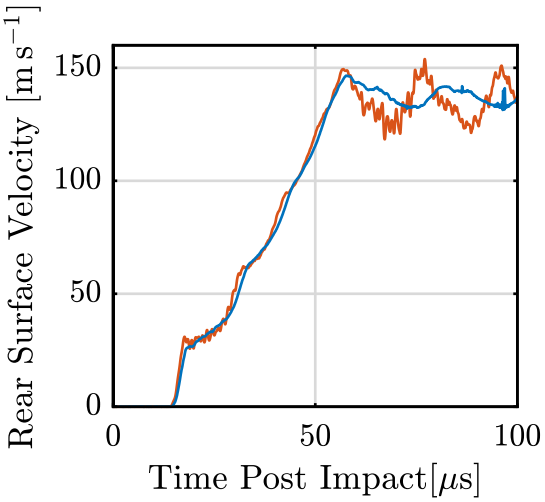

(e) Iteration 15.

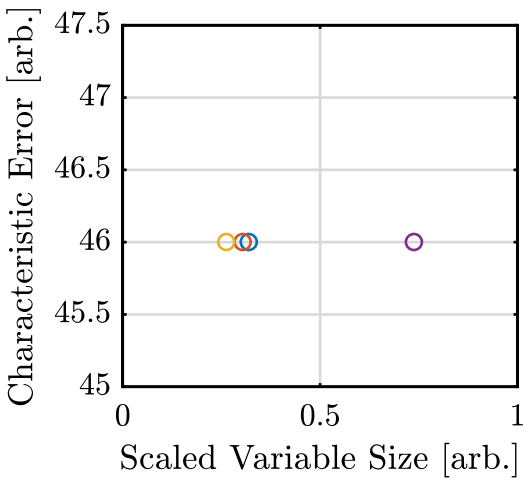

(f) Iteration 15.

Figure 10.6: Convergence of rear surface velocity histories for a vertically oriented reverse Taylor impact digital twin to recorded experimental histories. The experiment in question is AM V POR RT TT 1, with an impact velocity of 177 m s^{-1}.

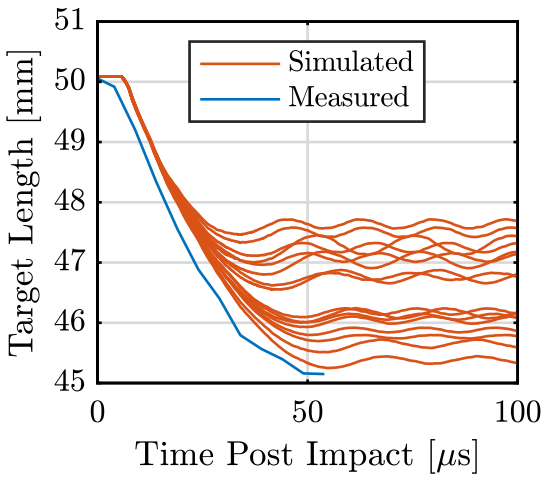

(a) Iteration 1.

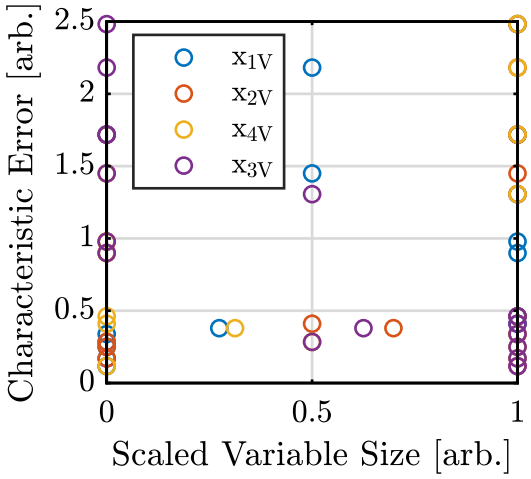

(b) Iteration 1.

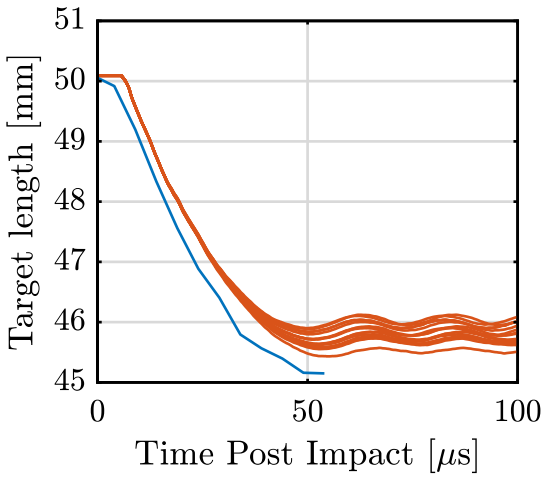

(c) Iteration 5.

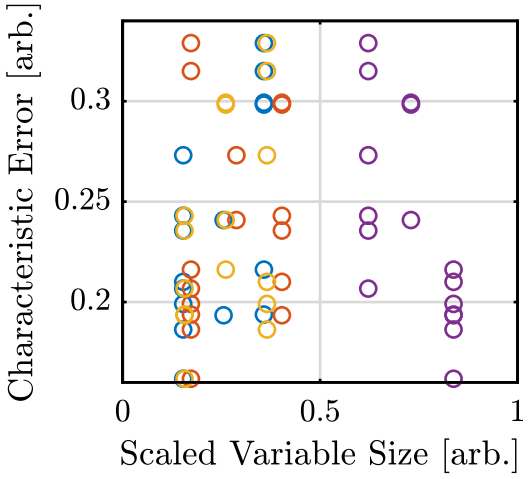

(d) Iteration 5.

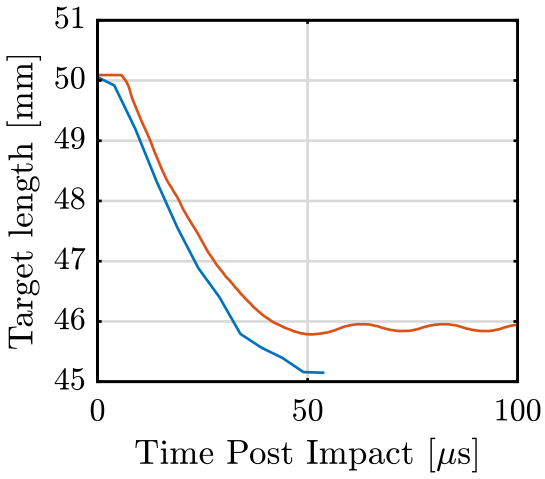

(e) Iteration 15.

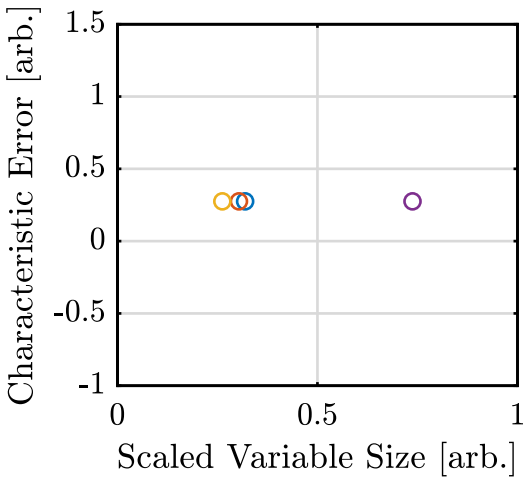

(f) Iteration 15.

Figure 10.7: Convergence of target length evolution histories for a vertically oriented reverse Taylor impact digital twin to recorded experimental histories. The experiment in question is AM V POR RT TT 1, with an impact velocity of 177 m s^{-1}.

Name	Lower Bound	Value	Upper Bound
x_{1H}	5.55×10^{8}	5.55×10^{8}	5.65×10^{8}
x_{1V}	5.46×10^{8}	5.48×10^{8}	5.48×10^{8}
x_{2H}	8.96×10^{8}	8.96×10^{8}	8.98×10^{8}
x_{2V}	1.05×10^{9}	1.05×10^{9}	1.06×10^{9}
x_{4H}	1.83×10^{-2}	1.83×10^{-2}	1.92×10^{-2}
x_{4V}	1.16×10^{-2}	1.16×10^{-2}	1.18×10^{-2}
E	1.88×10^{11}	1.88×10^{11}	1.93×10^{11}
ν	2.98×10^{-1}	2.98×10^{-1}	3.01×10^{-1}
x_{3H}	4.64×10^{-1}	4.65×10^{-1}	4.65×10^{-1}
x_{3V}	5.91×10^{-1}	5.95×10^{-1}	5.95×10^{-1}

Table 10.2: Optimised parameters for iterative optimisation of orthotropic Johnson-Cook to experimental behaviour of porous AM 316L steel.

cycles as before with the porous optimisation. As with the porous material, the convergence is visualised for reverse Taylor impacts digital twins of experiments on both horizontally and vertically manufactured targets in figures 10.8–10.11.

The optimised parameter set resulting from this regression is given in table 10.3 with similar trends observed in the relative magnitudes of the first four Johnson-Cook coefficients, with these identified as $\mathbf{x} = \left\{ x_i \mid i = 1, 2, 3, 4 \right\}$, between orientations in both dense and porous material datasets. To fully compare both optimised solutions, the resultant effective flow stress responses along each orientation were plotted, with the resulting curves presented in figure 10.12.

10.5 Conclusions

Given the consistent trends in parameter magnitude across directions within optimised datasets presented in this chapter, a consistent trend is observed in the relative evolution of plasticity across orientations. To better visualise the predicted response of optimised models, they are presented below in figure 10.12 with characteristic curves projected along both horizontal and vertical axes, at strain rates of $1\,s^{-1}$ and $1000\,s^{-1}$, and at effective plastic strains of up to $40\,\%$. These optimised results are presented alongside published isotropic Johnson-Cook curves for CM 316L within literature [226–228] to provide context to conventionally manufactured equivalents.

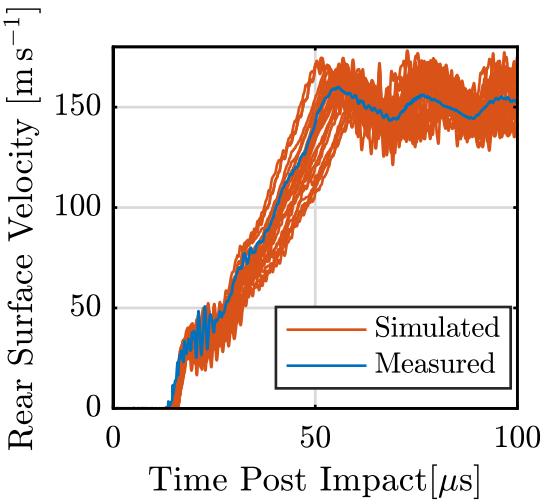

(a) Iteration 1.

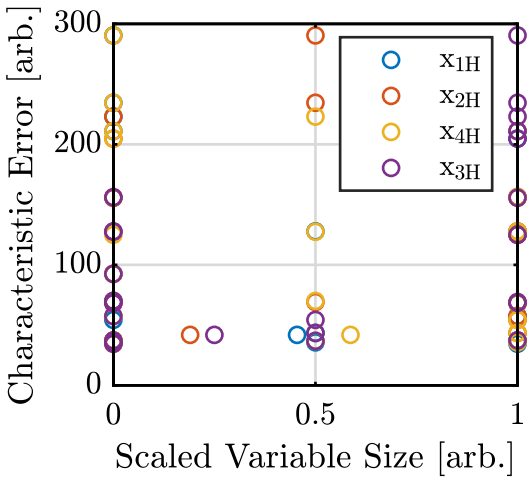

(b) Iteration 1.

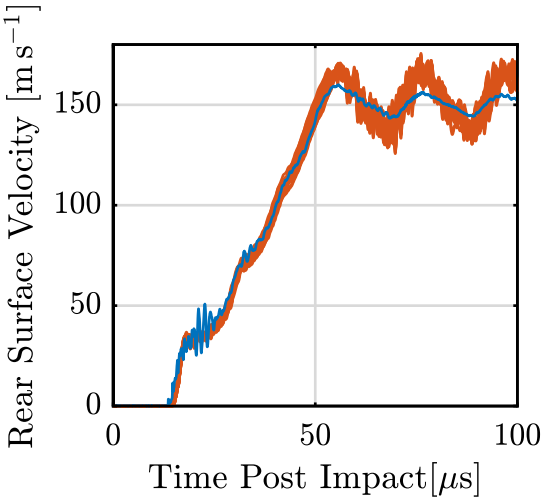

(c) Iteration 5.

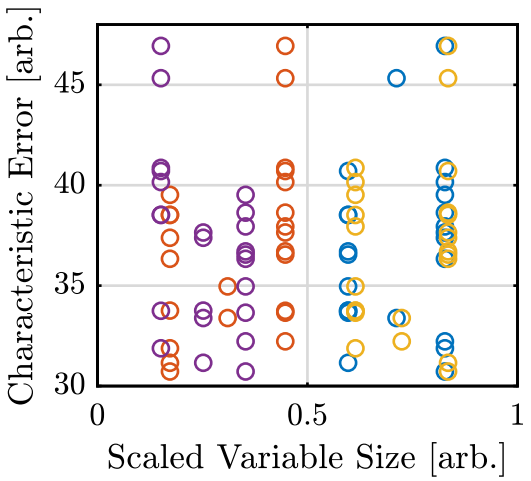

(d) Iteration 5.

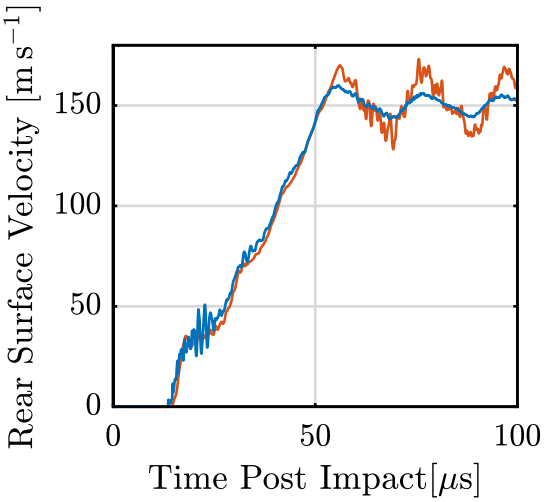

(e) Iteration 11.

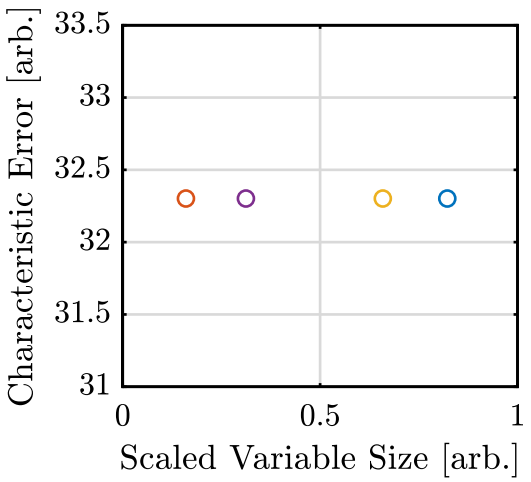

(f) Iteration 11.

Figure 10.8: Convergence of rear surface velocity histories for a horizontally oriented reverse Taylor impact digital twin to recorded experimental histories. The experiment in question is AM H DEN RT TT 1, with an impact velocity of 177 m s^{-1}.

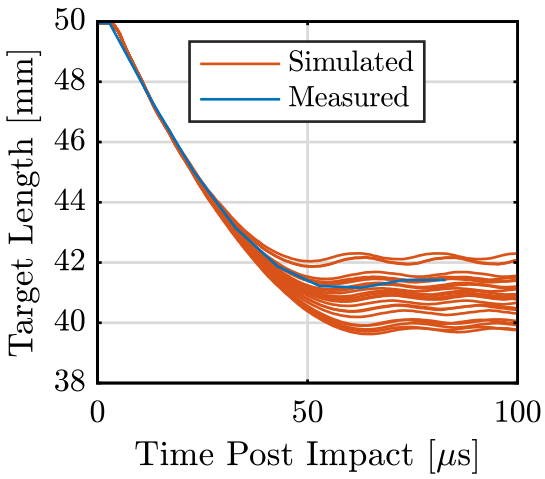

(a) Iteration 1.

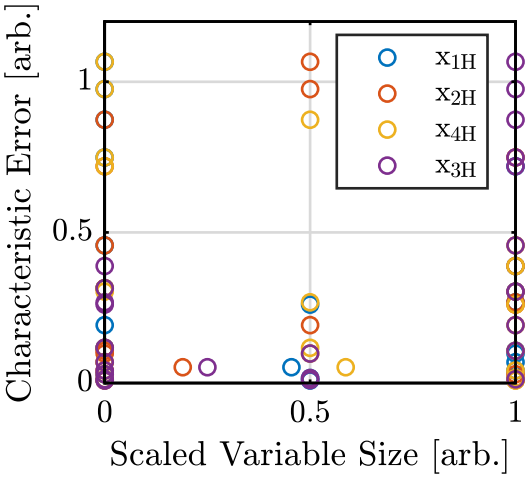

(b) Iteration 1.

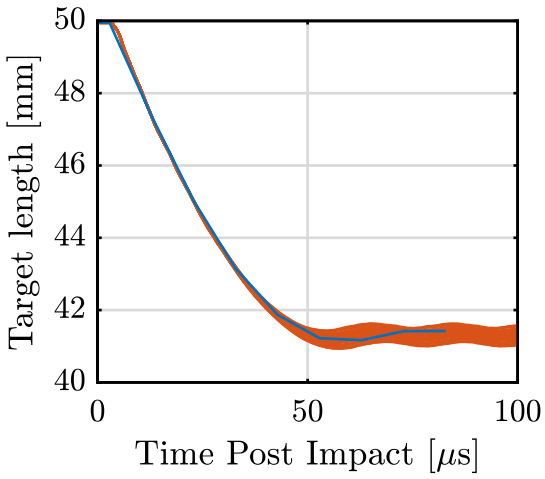

(c) Iteration 5.

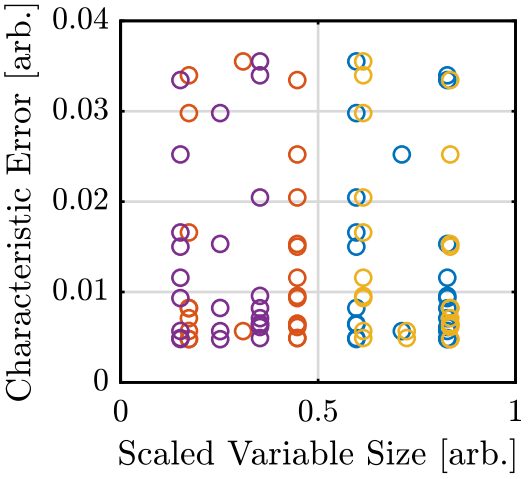

(d) Iteration 5.

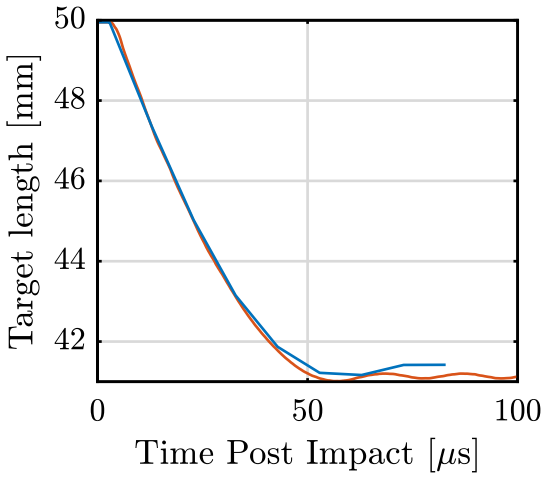

(e) Iteration 11.

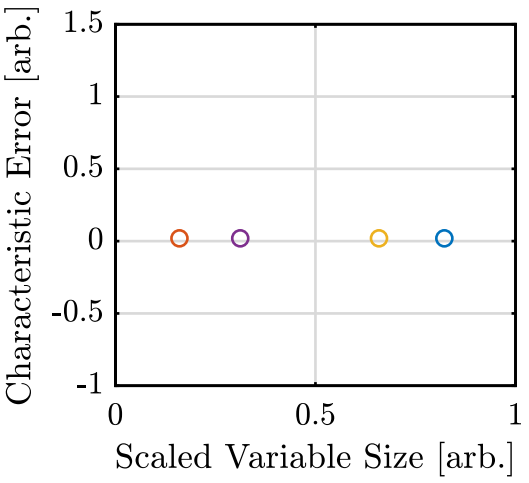

(f) Iteration 11.

Figure 10.9: Convergence of target length evolution histories for a horizontally oriented reverse Taylor impact digital twin to recorded experimental histories. The experiment in question is AM H DEN RT TT 2, with an impact velocity of 297 $\mathrm{m\,s^{-1}}$.

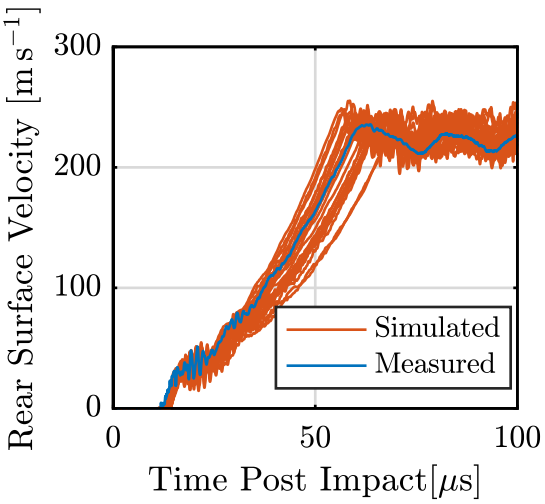

(a) Iteration 1.

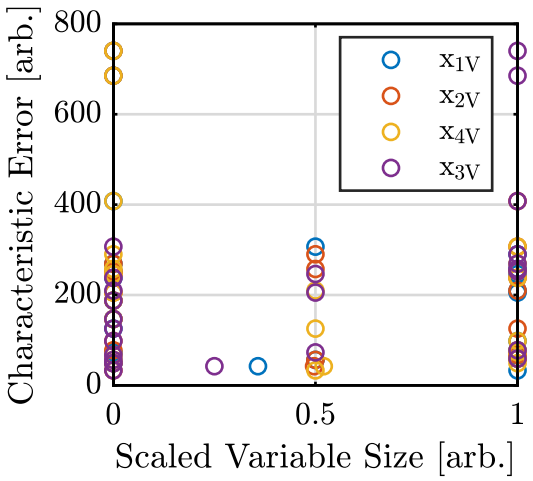

(b) Iteration 1.

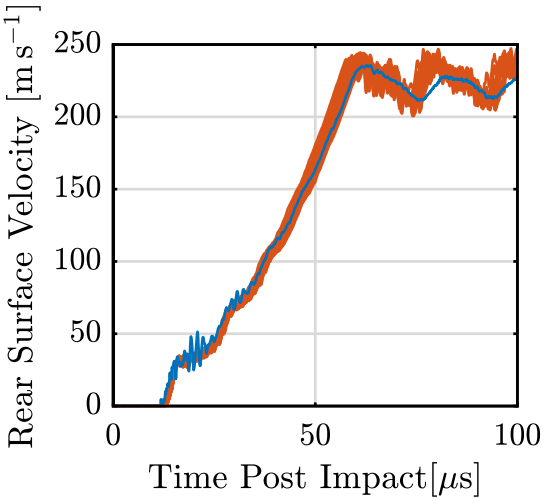

(c) Iteration 5.

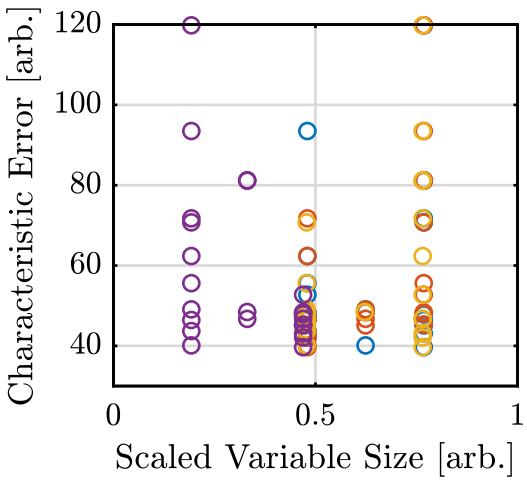

(d) Iteration 5.

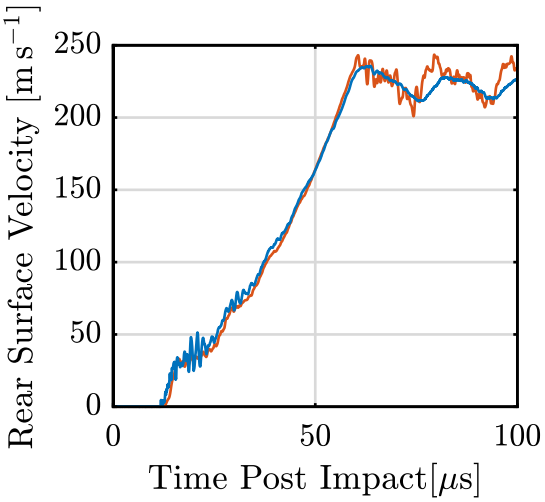

(e) Iteration 11.

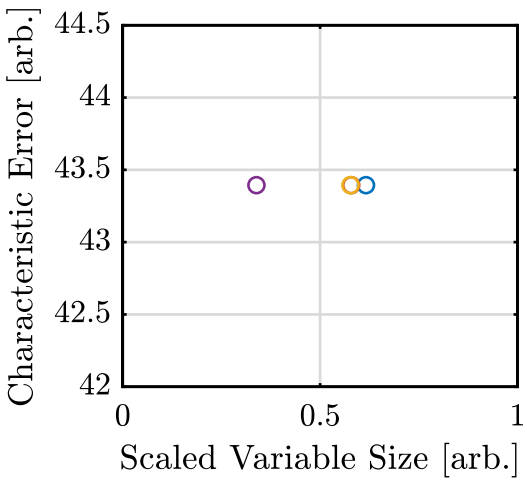

(f) Iteration 11.

Figure 10.10: Convergence of rear surface velocity histories for a vertically oriented reverse Taylor impact digital twin to recorded experimental histories. The experiment in question is AM V DEN RT TT 2, with an impact velocity of 298 m s^{-1}.

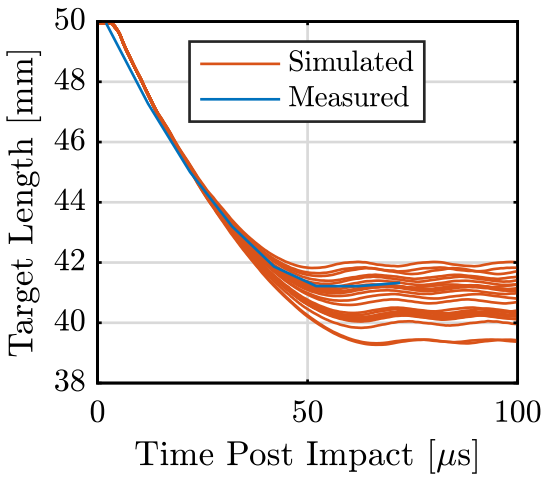

(a) Iteration 1.

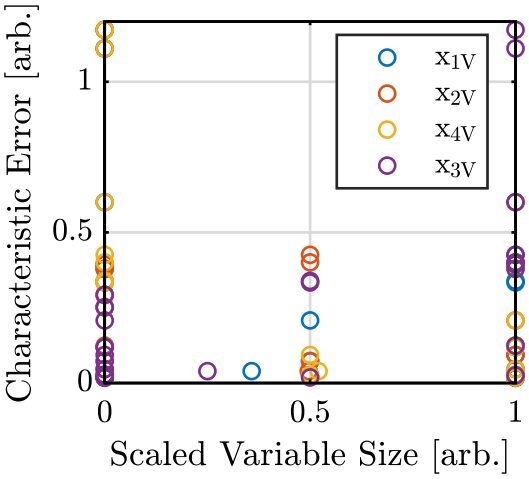

(b) Iteration 1.

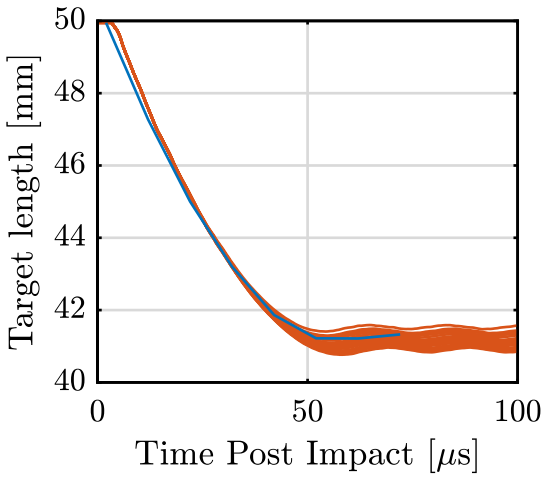

(c) Iteration 5.

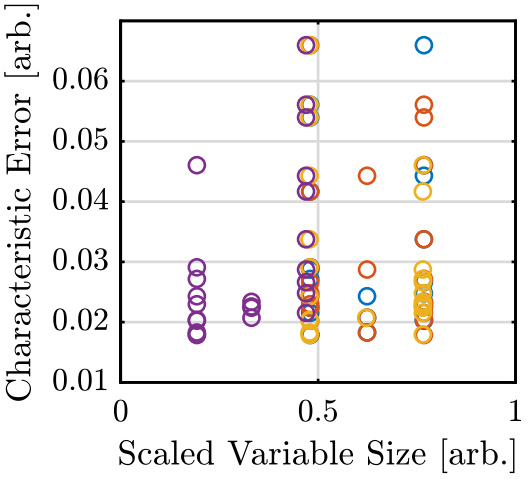

(d) Iteration 5.

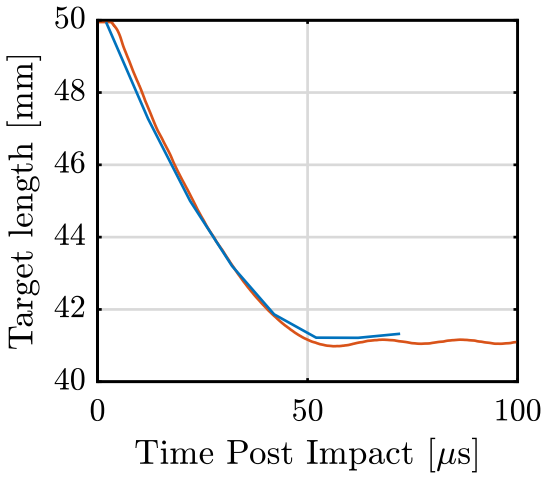

(e) Iteration 11.

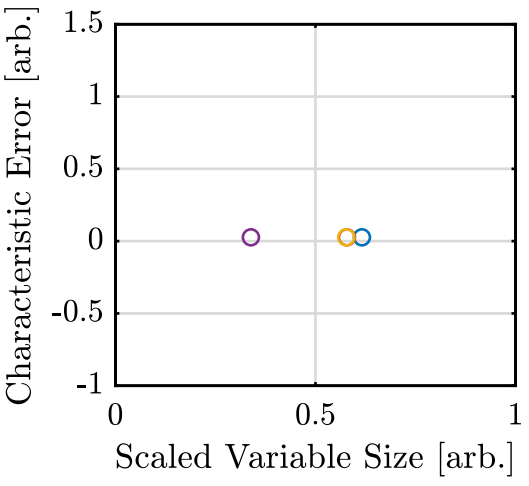

(f) Iteration 11.

Figure 10.11: Convergence of target length evolution histories for a vertically oriented reverse Taylor impact digital twin to recorded experimental histories. The experiment in question is AM V DEN RT TT 2, with an impact velocity of 298 $\mathrm{m\,s^{-1}}$.

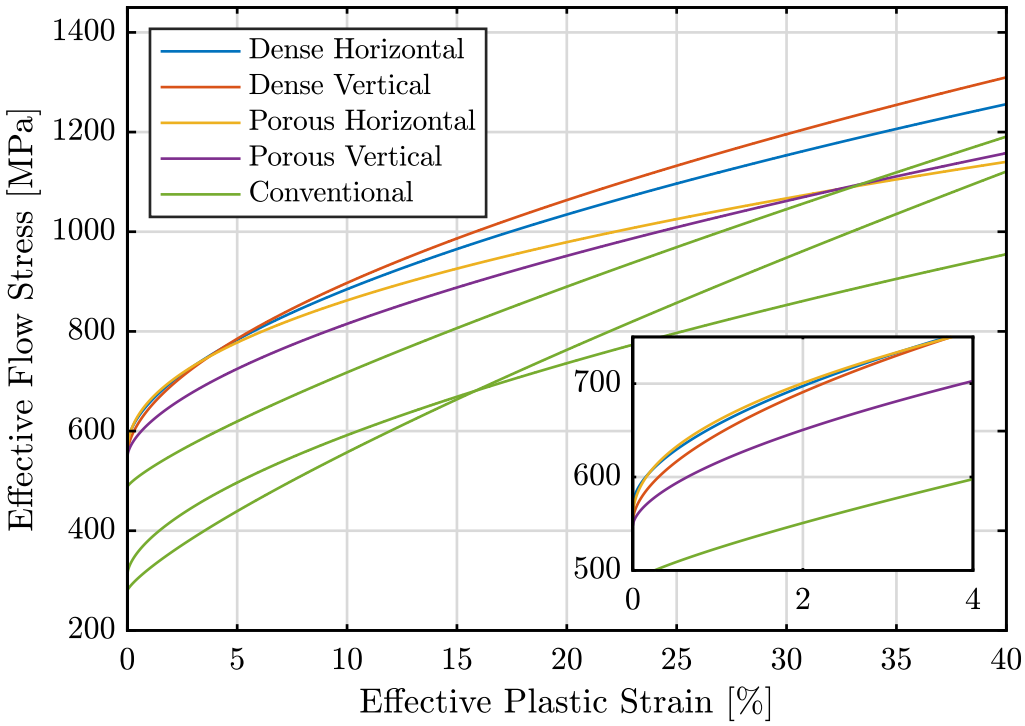

(a) $1\,\mathrm{s}^{-1}$

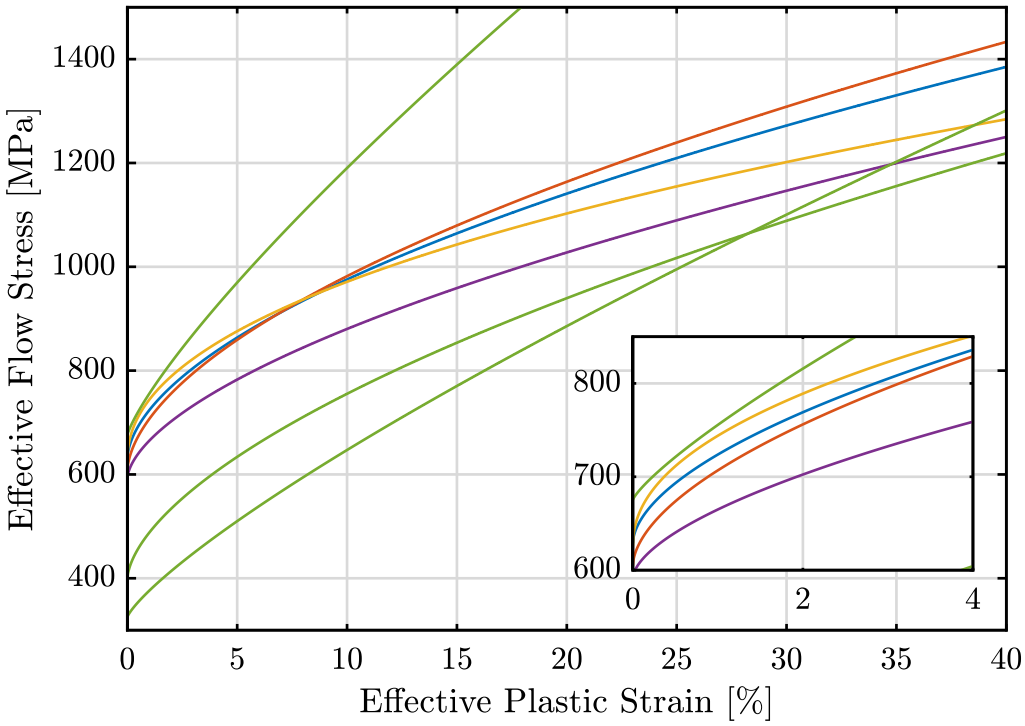

(b) $1000\,\mathrm{s}^{-1}$

Figure 10.12: A comparison of optimised Johnson-Cook responses within optimisations on both porous and dense additively manufactured 316L stainless steel in both horizontal and vertical orientations. It is noted that the uppermost conventional curve is parametrised by a reference strain rate of $10^{-3}\,\mathrm{s}^{-1}$. Such a reference strain rate is highly unusual for a Johnson-Cook model applicable to dynamic events limiting its suitability to events such as the Taylor impacts simulated.

Name	Lower Bound	Value	Upper Bound
x_{1H}	5.67×10^{8}	5.70×10^{8}	5.70×10^{8}
x_{1V}	5.51×10^{8}	5.53×10^{8}	5.53×10^{8}
x_{2H}	1.12×10^{9}	1.15×10^{9}	1.15×10^{9}
x_{2V}	1.27×10^{9}	1.27×10^{9}	1.28×10^{9}
x_{4H}	1.46×10^{-2}	1.49×10^{-2}	1.49×10^{-2}
x_{4V}	1.37×10^{-2}	1.37×10^{-2}	1.42×10^{-2}
E	1.63×10^{11}	1.63×10^{11}	1.68×10^{11}
ν	2.70×10^{-1}	2.83×10^{-1}	2.83×10^{-1}
x_{3H}	5.62×10^{-1}	5.62×10^{-1}	5.66×10^{-1}
x_{3V}	5.68×10^{-1}	5.68×10^{-1}	5.75×10^{-1}

Table 10.3: Optimal parameter set for iterative optimisation of orthotropic Johnson-Cook to experimental behaviour of dense AM 316L steel. Where a parameter name ends with either H or V, this is a Johnson-Cook model parameter for either vertical or horizontal directions assuming transverse isotropy about the vertical axis. E is given as the Young's modulus with ν given as the Poisson's ratio.

Considering both figures, the similarity between optimised AM behaviours at both strain rates indicate limited sensitivity to the rate of deformation. This similarity in response was not unexpected, especially given the population of experimental responses used to optimise the models lacked purely quasistatic measurements, and measurements inducing strain rates exceeding $10^{5}\,\mathrm{s}^{-1}$ where significant disparities between constitutive response would more likely be observed, in turn increasing the influence of the predicted rate dependency.

Looking within each figure, the mechanical performance of all AM 316L populations is shown exceeding published results for CM equivalents in nearly all cases at effective plastic strains below 40 %. This echoes the earlier quantitative conclusions following analysis of initial elastic wavefront magnitude under reverse Taylor impact. Furthermore this elevated performance is also observed widely within literature at lower rates.

In the case of each AM response, elevated mechanical performance is seen in the horizontal orientation initially, whilst this trend narrows before finally inverting following further deformation. Here the limitations of the Johnson-Cook are observed, where hardening behaviour is defined with only two parameters there is no capability

for variance in the form of hardening behaviour as plastic strain increases, although this simplification also reduces the model complexity and increases effective accessibility to industry. Considering the somewhat fixed form of response curves, the following hypotheses are suggested.

Firstly where no porosity is present, horizontally oriented specimens offer mildly elevated mechanical performance above that of vertically oriented counterparts both in the onset of yield and in performance at low magnitudes of deformation. However, as deformation increases the variance between these is seen to narrow, likely due to any preexisting microstructural characteristics being dwarfed by the microstructural evolution introduced by the deformation itself.

Secondly, where planar layered porosity is found to exist significant variance is found in the mechanical response. At effective plastic strains below 5 % and where loading occurs primarily in the plane of porosity, performance is similar to that of non-porous AM equivalents. However, beyond this initial stage the same performance is not maintained, with predicted effective flow stress trending towards that of similarly porous AM material being loaded out of plane. Regardless, and to conclude the hypotheses offered, it is observed that the performance of porous AM material is still predicted above that of conventional predictions, so that even with defect distributions the dynamic specific strength of AM 316L still exceeds that of CM equivalents.

References

[122] M. A. Bevan et al. "Mechanical Properties and Behavior of Additive Manufactured Stainless Steel 316L". In: *Miner. Met. Mater. Ser.* Vol. Part F7. February. 2017, pp. 577–583. ISBN: 9783319513812. DOI: 10.1007/978-3-319-51382-9_63.

[125] G.T. Gray III et al. "Structure/property (constitutive and dynamic strength/damage) characterization of additively manufactured 316L SS". In: *EPJ Web Conf.* 94 (Sept. 2015). Ed. by E. Cadoni, p. 02006. ISSN: 2100-014X. DOI: 10.1051/epjconf/20159402006.

[145] Livermore Software Technology Corporation (LSTC). *LS-DYNA Keyword User's Manual*. R12 Vol. 2. Livermore Software Technology Corporation, 2020. URL: https://www.lstc.com/download/manuals.

[154] G.R. Johnson and W.H. Cook. "A constitutive model and data for metals subjected to large strains, high strain rates and high temperatures." In: *Proc. 7th Int. Symp. Ballist.* The Hague The Netherlands, 1983, pp. 541–547.

[158] Daniele Versino and Kane C. Bennett. "Generalized radial-return mapping algorithm for anisotropic von Mises plasticity framed in material eigenspace". In: *Int. J. Numer. Methods Eng.* 116.3 (2018), pp. 202–222. ISSN: 10970207. DOI: 10.1002/nme.5921.

[219] Jacek J. Skrzypek and Artur W. Ganczarski. *Mechanics of Anisotropic Materials*. Ed. by Jacek J. Skrzypek and Artur W. Ganczarski. Engineering Materials. Cham: Springer International Publishing, 2015. ISBN: 978-3-319-17159-3. DOI: 10.1007/978-3-319-17160-9.

[220] William Prager. "Recent developments in the mathematical theory of plasticity". In: *J. Appl. Phys.* 20.3 (1949), pp. 235–241. ISSN: 00218979. DOI: 10.1063/1.1698348.

[221] D. C. Drucker. "Some implications of work hardening and ideal plasticity". In: *Q. Appl. Math.* 7.4 (1950), pp. 411–418. ISSN: 0033-569X. DOI: 10.1090/qam/34210.

[222] D. C. Drucker. "A more fundamental approach to plastic stress-strain relations". In: *Proc. 1st U.S. Natl. Congr. Appl. Mech.* 1951, pp. 487–491.

[223] D. C. Drucker, W. Prager, and H. J. Greenberg. "Extended limit design theorems for continuous media". In: *Q. Appl. Math.* 9.4 (1952), pp. 381–389. ISSN: 0033-569X. DOI: 10.1090/qam/45573.

[224] Livermore Software Technology Corporation (LSTC). *LS-DYNA Keyword User's Manual*. R12 Vol. 1. Livermore Software Technology Corporation, 2020. URL: https://www.lstc.com/download/manuals.

[225] Livermore Software Technology Corporation and (LSTC). *LS-DYNA Keyword User's Manual*. R12 Vol. 3. Livermore Software Technology Corporation, 2020. URL: https://www.lstc.com/download/manuals.

[226] N. Tounsi et al. "From the basic mechanics of orthogonal metal cutting toward the identification of the constitutive equation". In: *Int. J. Mach. Tools Manuf.* 42.12 (Sept. 2002), pp. 1373–1383. ISSN: 08906955. DOI: 10.1016/S0890-6955(02)00046-9.

[227] H. Chandrasekaran, R. M'Saoubi, and H. Chazal. "Modelling of material flow stress in chip formation process from orthogonal milling and split Hopkinson tests." In: *Mach. Sci. Technol.* 9.1 (Mar. 2005), pp. 131–145. ISSN: 1091-0344. DOI: 10.1081/MST-200051380.

[228] D. Umbrello, R. M'Saoubi, and J.C. Outeiro. "The influence of Johnson–Cook material constants on finite element simulation of machining of AISI 316L steel". In: *Int. J. Mach. Tools Manuf.* 47.3-4 (Mar. 2007), pp. 462–470. ISSN: 08906955. DOI: 10.1016/j.ijmachtools.2006.06.006.

[229] Anthony Atkinson, Alexander Donev, and Randall Tobias. *Optimum Experimental Designs, With SAS*. Vol. 34. OUP Oxford, 2007. ISBN: 9780199296606. URL: https://global.oup.com/academic/product/optimum-experimental-designs-with-sas-9780199296606.

[230] Nielen Stander et al. *LS-OPT User's Manual*. 4.1. December. Livermore Software Technology Corporation, 2010. URL: https://www.lstc.com/download/manuals.

Part IV

Conclusions & Future Work

Research is an iterative process, within this section the findings are summarised prior to a discussion of future avenues of potential work.

Chapter 11

Conclusions

The first of the two main challenges addressed within this thesis was the drawing of links between atypical additive microstructures of as-built AM 316L steel, an austenitic corrosion resistant stainless steel, and its dynamic strength and failure modes. To this end two distinct batches of additively manufactured 316L stainless steel were obtained, with these then characterised by means of optical microscopy or micro-computed tomography, including comparison to conventionally manufactured equivalents. Characterisation efforts identified clear disparities between batches of additively manufactured material. Whilst one batch exhibited a near fully dense bulk, the other contained a microstructure dominated by layered lack-of-fusion porosity. In comparison to conventionally manufactured 316L stainless steel, the porous batch of additive samples showed drastically increased levels of porosity, with the differences in porosity seen between additive material batches dwarfing that seen between the near fully dense batch of additively manufactured material and its conventional equivalent. Investigating the impacts of the observed variance in defect distributions, the testing of dynamic response was conducted using reverse Taylor impact and spallation plate impact techniques. Both experimental techniques involved multiple testing campaigns with iterative improvements implemented between each series of experiments.

Under reverse Taylor loading a diverse range of loading states were probed, with these used later within inverse modelling routines. Additionally a one dimensional analysis introduced by Rohr *et al.* [199] was applied to recorded rear surface motion of both additively and conventionally manufactured targets. The results of these analyses indicated elevated specific strength within additively manufactured samples above conventionally manufactured equivalents across orientations, temperatures, and a range of impact velocities. Within the recorded behaviour of additively manufactured samples

exhibiting layered porosity distributions, elevated strength was found in horizontally oriented samples compared to vertically oriented equivalents. This layered porosity was also found to drive directional attenuation of high frequency radial modes, with this matching a similar response identified under split-Hopkinson pressure bar loading by Nahme *et al.* [32].

Alongside Taylor impacts, spallation testing compared the dynamic tensile response of both additively and conventionally manufactured 316L samples. As with reverse Taylor impact testing, the layered porosity distributions within one of the batches of additively manufactured material affected the propagation of stress waves within the experiments. Whilst this hampered the ability to conduct traditional spallation analyses, a more qualitative analysis suggested defect driven failure modes, with spatial coherence between stress and porosity distributions further exacerbating this trend. Where near fully dense additively manufactured material was tested, traditional spallation waveforms were recovered and a increase of approximately 20 % in interlayer spallation strength was observed over conventional samples, with additive intralayer spallation strength exceeding additive interlayer values by approximately a further 5 %. Interestingly a significant increase in HEL stress was observed between dense additively manufactured material and conventional equivalents. Such is the magnitude of this disparity that it warrants further investigation, however the consistency in conventionally manufactured spallation strength between measured and literature values offers some support to the observed trend in measured HEL response.

Ultimately the experimental work subjected additively manufactured material both with and without layered porosity distributions to dynamic loading. The responses recorded have expanded the available data concerning the dynamic response of AM 316L, as well as highlighting the potential variation in wave dynamics that porosity distributions can induce. Preexisting analyses were applied to quantify aspects of the observed dynamic response with these found to echo trends observed in the results of inverse modelling efforts detailed below. Whilst current results leave room for further experimental investigation, the conclusions reached are linked back to microstructural

characterisation with an added awareness that modelling has in turn allowed for further interrogation of the observed dynamic response.

The second major challenge tackled within this thesis was to improve the foundations for effective adoption of as-built AM components into industrial applications where dynamic loading is of concern. This was to be achieved by developing predictive capabilities well suited to the modelling of as-built additive material. To this end an orthotropic development of the Johnson-Cook strength model was implemented within a commercially available finite element package. The model itself was developed atop a theoretical framework detailed by Versino and Bennett in 2018 [158] that leveraged eigendecomposition of the orthotropic quadratic Hill yield surface to identify isotropic subspaces. Implementing this theory and yield criterion whilst also introducing a plastic potential with parameters themselves derived using an orthotropic form similar to the yield surface, albeit with normalisation, allowed for the development of a modular orthotropic framework within which a strain, strain rate, and temperature dependent constitutive model allowed for the simulation of dynamic deformation events where the underlying material exhibited an orthotropic response. The plastic potential selected was the widely used Johnson-Cook, with this implemented such that under isotropic parametrisation the response of already preexisting implementations of the original isotropic form were recovered. This model was then shown to allow orthotropic descriptions of strain hardening and strain rate sensitivity as intended, with the validated model then applied to measured directional dynamic behaviour under reverse Taylor impact loading.

The parametrisation of the developed model necessitated a significant inverse modelling campaign using an ensemble of quarter symmetry digital twins, each one specifically tailored to recreate an undertaken reverse Taylor impact experiment, to provide a diverse population of dynamic material loading states for both porous and dense additively manufactured 316L stainless steel. An iterative optimisation with sequential domain reduction was implemented within the LS-OPT software package with convergence to observed Taylor rod rear surface motion and length evolution driving the

identification of optimal solutions.

Once converged, parameter sets were returned, with these further evidencing the elevated mechanical performance of additively manufactured 316L above conventionally manufactured equivalents under dynamic loading. Furthermore, consistent trends were observed within the relative magnitude of directional Johnson-Cook parameters. These trends highlighted the disparity in performance between the porous additively manufactured material and its dense equivalent, with elevated mechanical performance observed for the latter. The comparison of directional parameters within a single batch of material, either porous or dense additively manufactured 316L stainless steel, showed elevated performance during the nascence of deformation where loading occurs within the build plane, with this anisotropy decreasing as deformation continued. The presence of porosity exacerbated the anisotropy within the optimised effective flow stress curves, with results suggesting increased deformation was needed before preexisting microstructural anisotropies were rendered negligible. This effect may be partially attributable to the collapse of the oriented porosity distributions known to exist in the material prior to deformation, however this has yet to be confirmed and could also be related to the competing influences of preexisting microstructural features and the generation of dislocations within the polycrystalline lattice during plasticity.

Ultimately the optimisation of the developed material model clearly demonstrated the capability to simulate as-built additively manufactured materials. The developed framework, specifically designed to minimise the barriers to effectively modelling similar additive microstructures, could be instantiated from preexisting Johnson-Cook parameter sets optimised from conventionally manufactured material responses. This equivalence reduces the need of extensive material testing when seeking to generate robust predictive capabilities supporting the incorporation of additive manufacturing techniques into engineering applications.

Concluding this thesis, it is clear that the outlook is promising for the additive manufacturing of components subjected to dynamic loading. These materials, as evidenced by the research conducted upon 316L stainless steel, offer the potential to

access a higher level of component performance once robust manufacturing routines are established. However those choosing to explore the potential benefits must remain aware of any heterogeneities within the material, whilst mild anisotropies are observed in dense additively manufactured material a far greater variance may be exhibited should porosity, potentially exhibiting spatial coherence, exist within manufactured components. Not only will porosity adversely affect the nascence and evolution of plasticity, it may also fundamentally alter the dynamic elastic transmissivity of the material, with directional scattering and attenuation of localised stress fronts found under dynamic loading generating atypical material responses. This variation in behaviour could complicate efforts to verify component performance during batch production, however it also suggests opportunities. Specifically, the potential to deliberately harness layered porosity distributions in preferentially dictating component deformation modes in attempting to preference specific failure scenarios.

Chapter 12

Future Work

In this section a series of concepts are described that mark potentially interesting extensions to the outcomes of this research. The majority of these opportunities are based around further development to the orthotropic Johnson-Cook model owing to the significant number of potentially relevant material modelling challenges this model could be applicable to.

12.1 Microscopy & EBSD

Whilst limited optical microscopy has already been undertaken on both CM and porous AM samples, microstructural characterisation is an area where research was limited due to delays in material acquisition and also in limitations with facility access during the latter stages of this research. With both porous AM and CM samples that are already prepared and as of yet unprepared dense AM samples a combination of optical and scanning electron microscopy, as well as Electron Back Scatter Diffraction (**EBSD**) would augment the existing characterisation of porosity within additive samples. Of particular benefit would be crystallographic orientation maps available from EBSD with these providing a validation of the directional microstructure that is a characteristic result of the thermospatial gradients and layer-wise epitaxial solidification intrinsic to selective laser melting. The addition of this information would serve to better contextualise the measured dynamic responses, with the aim of approaching the excellent microstructural characterisations of Wang *et al.* [86] and Zhong *et al.* [89] which provided a detailed verification of the additive microstructure, albeit paired with only quasi-static testing of material strength. The lack of both diverse and detailed microstructural characterisation simultaneously paired with precision testing is noted at the beginning of this thesis as a challenge facing the field, with this being somewhat

elusive due to the significant cost and time demands that would be placed upon multiple research stakeholders simultaneously, with each requiring access to a plethora of cutting edge scientific facilities, to produce such research.

12.2 Residual Stress

The rapid thermal cycling present within SLM are known to generate residual stress within their as-built microstructures. These are often mitigated through whole component heat treatment [128], which then limits the potential for deliberately varying microstructural characteristics throughout a component.

Techniques exist to infer these residual stress distributions through focused ion beam (**FIB**) milling techniques. These techniques, which facilitate measurement of the residual stress tensors indirectly, consider the relaxation of a small region of material following the removal of material surround it [231, 232]. The exact distortion of this relaxation, combined with the known absence of stress at free surfaces, allows the prior stress state to be inferred.

The mapping of residual stress distributions would undoubtedly prove valuable in the simulation of microplasticity. This process, not implemented in the developed model, and in other common constitutive models as well, is found in the nascent stages of yielding, and would likely be observed in locations where the orientation of loading and residual stresses align.

12.3 Computational Refinements

One of the desirable properties of a material model is the (computational) speed at which the algorithm is able to predict behaviour whilst maintaining accuracy. Whilst the eigenspace transform proposed by Versino and Bennett [158] is an improvement on previous algorithms that may be used to evaluate the evolution of plastic deformation, it is still comparatively slow when considering widely-used isotropic models that implement a classical radial return. Two key improvements to the algorithm are proposed here that seek to address this, with each requiring minor alterations to the

overall structure of the material model as currently implemented.

The first improvement suggested is the implementation of a super-cycling capability in the calculation of eigenspace transforms. As noted by Versino and Bennett in their 2018 paper, the eigenspace transform method works best when the orthotropy defined in the model remains constant regardless of the degree of plastic deformation. This idealised persistent orthotropy is not present in the model developed in this work, with the eigenspace calculated for every element undergoing plastic deformation in every given time step. By implementing a multi-scale temporal super-cycling routine the calculation of this transform could be instead retained for a finite predefined number of proceeding time steps, with the necessary assumption that changes in the degree of orthotropy remain small in comparison to the incurred increments of plastic deformation. With the transform then valid for a finite but small (< 10) number of time steps the computational cost of calculating the transforms could then be as little as the reciprocal of the number of time steps specified (5 time steps allowing a reduction to as little as $\frac{1}{5}$ of the original cost). The concept of implementing such a super-cycling method was briefly mentioned by Versino and Bennett in their paper, saying that:

> '*If the eigenvectors of the material tensors change throughout the simulation, ad hoc solutions have to be adopted: in case the change is small during each time increment, it may be sufficient to compute the eigendecomposition of the structural tensors at time* $t_{(n)}$ *and keep them unchanged for relatively small time steps.*' [158]

This would be implemented by passing the eigenvectors between time steps using history variables, simultaneously incrementing counters to ensure that no transform was retained longer than desired. Unfortunately the associated eigenvalues would still require evaluation at every time step owing to the increase in yield stress, however this would still require significantly less computational overhead than the eigendecomposition, even when leveraging the intrinsic block diagonal nature of the orthotropic material tensors to reduce the computational complexity of eigendecomposition.

A second computational improvement is potentially found in decreasing the number of radial return iterations required to evaluate a suitable increment of effective

plastic strain within the material eigenspace. Currently, a traditional Newton Raphson method is employed to converge upon a suitable plastic multiplier, however due to subtle instabilities intrinsic to the rate dependency of the Johnson-Cook model [233–235] a damping factor is applied to each iterative step in the Newton Raphson algorithm to improve the robustness of the convergence. It is suggested that employing a convergence algorithm with an awareness to the preceding states of the convergence may allow a reduction to the damping applied, in turn improving the speed of convergence. Due to the significant usage of this algorithm (every element undergoing any deformation in each time step), any slight improvements to this algorithm could lead to significant improvements when applied to large scale simulations.

12.4 Thermal Sensitivity

Currently omitted from the presented material is the validation and optimisation of temperature sensitivity within the Johnson-Cook model. Whilst there is already an implemented framework for this sensitivity the extra validation simulations and increased complexity of optimisation resulted in this specific sensitivity being left at a nominal literature value in the presented work given time constraints. A logical next step would therefore be the validation of temperature sensitivity and the corresponding optimisation that would then involve observed behaviour from Taylor impact experiments already conducted at elevated temperatures. The validation and optimisation of these sensitivities is expected to be straightforward, with the required frameworks to represent the sensitivity and validate via batch simulation already in place. The optimisation using digital twins would require a small additional task of introducing elevated temperature to the sample in the digital twin, however this is a standard procedure within LS-Dyna and is well documented within the packages literature.

12.5 Stochastic Parametrisation

Within the field of numerical material modelling there is a growing interest in recreating not only the average response of materials, but also the intrinsic variability

stemming from microstructural texture and defects introduced either unintentionally or by design. Towards this, a stochastic framework already exists within LS-DYNA [224] with a potential avenue of research involving the investigation of this framework and effective integration into the preexisting deterministic algorithm. Taking this further, the opportunity to robustly interface the developed material model with microstructurally representative polycrystalline finite element meshes would then facilitate new methods of linking high-resolution metallography with observed dynamic response. Furthermore, improvements to experimental diagnostics and analyses that facilitate the measurement of statistical distributions of material response present an opportunity to create deterministic statistically variable models that may be directly compared to populations of material data. The accurate representation of material heterogeneity will itself lead to improvements in the modelling of processes where the extremities of material population response are dominant, such as both micro-plasticity and defect driven failure.

12.6 Non-Associative Flow

One of the benefits of the developed model as implemented is the potential independence of the plastic potential from the yield criterion. Whilst the implementation in this work uses the same underlying potential to define both its yield criterion and the resulting plastic potential, such a choice is not required, allowing the use of non-associative plastic potentials to quantify the magnitude of incurred effective plastic strain. The trial of not only a variety of associative models (such as the Zerilli-Armstrong [236, 237] and Steinberg-Guinan [238] constitutive models.) under similar orthotropic projections, but also the added option to vary the plastic potential as well could open up new applications to such a directional framework.

12.7 Full Anisotropy

A potential development to the underlying theory of the developed material model would be to extend the orthotropic transform to a fully anisotropic transform, allow-

ing it to be used in the modelling of non-isotropic materials that do not follow an orthotropic response, an example of which would be the bulk response of Hexagonal Close-Packed (**HCP**) structured alloys of titanium, magnesium, and zirconium [239, 240]. Whilst this would take a significant amount of consideration, especially with regards to the conservation of the effective stress and the principle of equivalence of work during a fully anisotropic transform, the potential benefits to modelling materials without a cubic crystalline structure would be significant owing to the improvements to both accuracy and computational efficiency offered by the eigenspace transform technique. Should it be possible, leveraging such a technique could provide a link between the microstructure sensitive predictions of crystal plasticity models and the efficient continuum models by allowing continuum models to incorporate directionally dependent behaviours driven by a wider range of microstructures.

12.8 Mapping the Manufacturing Domain

Beyond immediate avenues of research, a challenge exists promising a step change within material performance in engineering, on which this thesis is concluded. Given recent computational advances, the prediction of material performance for alloys with spatially heterogeneous distributions of alloy composition and manufacturing parameters is now theoretically feasible. To achieve this, significant research remains to probe a multidimensional non-linear parameter space, linking inputs to both microstructural characteristics and material performance across a hierarchical ensemble of stochastic material models capable of predicting thermomechanical processes at the lattice level up to the component scale. This will require collaboration on a large scale, with the amalgamation of diverse high fidelity datasets linking additive powder compositions, manufacturing parameters, microstructural characteristics, and material responses across a range of scales and conditions. Such a dataset could then be used to train physics-informed neural networks, with successive iterations of computationally guided testing serving to efficiently map a wide manufacturing domain. The research detailed in this thesis, whilst limited due

to material availability issues, aims to demonstrate the overall feasibility of this concept, and lay a part of the groundwork required for its realisation.

References

[32] H. Nahme, E. Lach, and R. Rohr. "Dynamic materials behavior of a porous pressureless sintered steel and a HIPped steel". In: *J. Phys. IV* 134 (Aug. 2006), pp. 1047–1051. ISSN: 1155-4339. DOI: 10.1051/jp4:2006134160.

[86] Y. Morris Wang et al. "Additively manufactured hierarchical stainless steels with high strength and ductility". In: *Nat. Mater.* 17.1 (Jan. 2018), pp. 63–71. ISSN: 1476-1122. DOI: 10.1038/nmat5021.

[89] Yuan Zhong et al. "Intragranular cellular segregation network structure strengthening 316L stainless steel prepared by selective laser melting". In: *J. Nucl. Mater.* 470 (Mar. 2016), pp. 170–178. ISSN: 00223115. DOI: 10.1016/j.jnucmat.2015.12.034.

[128] F. Brenne, T. Niendorf, and H.J. Maier. "Additively manufactured cellular structures: Impact of microstructure and local strains on the monotonic and cyclic behavior under uniaxial and bending load". In: *J. Mater. Process. Technol.* 213.9 (Sept. 2013), pp. 1558–1564. ISSN: 09240136. DOI: 10.1016/j.jmatprotec.2013.03.013.

[158] Daniele Versino and Kane C. Bennett. "Generalized radial-return mapping algorithm for anisotropic von Mises plasticity framed in material eigenspace". In: *Int. J. Numer. Methods Eng.* 116.3 (2018), pp. 202–222. ISSN: 10970207. DOI: 10.1002/nme.5921.

[199] I. Rohr, H. Nahme, and K. Thoma. "A modified TAYLOR-test in combination with numerical simulations - a new approach for the determination of model parameters under dynamic loads". In: *J. Phys. IV* 110 (Sept. 2003), pp. 513–518. ISSN: 1155-4339. DOI: 10.1051/jp4:20020745.

[224] Livermore Software Technology Corporation (LSTC). *LS-DYNA Keyword User's Manual*. R12 Vol. 1. Livermore Software Technology Corporation, 2020. URL: https://www.lstc.com/download/manuals.

[231] Alexander M. Korsunsky, Marco Sebastiani, and Edoardo Bemporad. "Focused ion beam ring drilling for residual stress evaluation". In: *Mater. Lett.* 63.22 (Sept. 2009), pp. 1961–1963. ISSN: 0167577X. DOI: 10.1016/j.matlet.2009.06.020.

[232] Alexander M. Korsunsky, Marco Sebastiani, and Edoardo Bemporad. "Residual stress evaluation at the micrometer scale: Analysis of thin coatings by FIB milling and digital image correlation". In: *Surf. Coatings Technol.* 205.7 (Dec. 2010), pp. 2393–2403. ISSN: 02578972. DOI: 10.1016/j.surfcoat.2010.09.033.

[233] Lars Westerling. *An implicit method for a strain rate dependent constitutive model implemented in AUTODYN as a user subroutine.* Tech. rep. Tumba: FOI – Swedish Defence Research Agency Weapons and Protection, 2002. URL: https://www.foi.se/rest-api/report/FOI-R--0310--SE.

[234] S.A. Silling. "Stability and Accuracy of Differencing Methods for Viscoplastic Models in Wavecodes". In: *J. Comput. Phys.* 104.1 (Jan. 1993), pp. 30–40. ISSN: 00219991. DOI: 10.1006/jcph.1993.1004.

[235] Lars Westerling. *Test of the new implementation of the johnson-cook model in autodyn*. Tech. rep. June. 2004, FOI–R—-1280—SE. URL: https://www.foi.se/rest-api/report/FOI-R--1280--SE.

[236] Frank J. Zerilli and Ronald W. Armstrong. "Dislocation-mechanics-based constitutive relations for material dynamics calculations". In: *J. Appl. Phys.* 61.5 (Mar. 1987), pp. 1816–1825. ISSN: 0021-8979. DOI: 10.1063/1.338024.

[237] Frank J. Zerilli and Ronald W. Armstrong. "The effect of dislocation drag on the stress-strain behavior of F.C.C. metals". In: *Acta Metall. Mater.* 40.8 (Aug. 1992), pp. 1803–1808. ISSN: 09567151. DOI: 10.1016/0956-7151(92)90166-C.

[238] D. J. Steinberg, S. G. Cochran, and Michael W. Guinan. "A constitutive model for metals applicable at high-strain rate". In: *J. Appl. Phys.* 51.3 (Mar. 1980), pp. 1498–1504. ISSN: 0021-8979. DOI: 10.1063/1.327799.

[239] A.L. Oppedal et al. "Anisotropy in hexagonal close-packed structures: improvements to crystal plasticity approaches applied to magnesium alloy". In: *Philos. Mag.* 93.35 (Dec. 2013), pp. 4311–4330. ISSN: 1478-6435. DOI: 10.1080/14786435.2013.827802.

[240] Kartik Kapoor et al. "Modeling Ti–6Al–4V using crystal plasticity, calibrated with multi-scale experiments, to understand the effect of the orientation and morphology of the α and β phases on time dependent cyclic loading". In: *J. Mech. Phys. Solids* 146.April 2020 (2021), p. 104192. ISSN: 00225096. DOI: 10.1016/j.jmps.2020.104192.

Bibliography

[1] Y Koren. *Computer Control of Manufacturing Systems*. Mechanical engineering series. McGraw-Hill, 1983. ISBN: 9780070353411.

[2] Jean-Pierre Kruth. "Material Incress Manufacturing by Rapid Prototyping Techniques". In: *CIRP Ann.* 40.2 (1991), pp. 603–614. ISSN: 00078506. DOI: 10.1016/S0007-8506(07)61136-6.

[3] B. Badrinarayan and Joel W Barlow. "Metal parts from selective laser sintering of metal-polymer powders". In: *Int. Solid Free. Fabr. Symp.* 1. University of Texas at Austin, 1992, pp. 141–146. DOI: 10.15781/T2988346K.

[4] Terry Wohlers. "Future potential of rapid prototyping and manufacturing around the world". English. In: *Rapid Prototyp. J.* 1.1 (Mar. 1995), pp. 4–10. ISSN: 1355-2546. DOI: 10.1108/13552549510146630.

[5] Charles Hull et al. "Rapid prototyping: current technology and future potential". English. In: *Rapid Prototyp. J.* 1.1 (Mar. 1995), pp. 11–19. ISSN: 1355-2546. DOI: 10.1108/13552549510732026.

[6] Kaufui V. Wong and Aldo Hernandez. "A Review of Additive Manufacturing". In: *ISRN Mech. Eng.* 2012 (Aug. 2012), pp. 1–10. ISSN: 2090-5130. DOI: 10.5402/2012/208760.

[7] John O. Milewski. *Additive Manufacturing of Metals*. Vol. 258. Springer Series in Materials Science. Cham: Springer International Publishing, 2017, pp. 75–84. ISBN: 978-3-319-58204-7. DOI: 10.1007/978-3-319-58205-4.

[8] Mukesh Agarwala et al. "Direct selective laser sintering of metals". English. In: *Rapid Prototyp. J.* 1.1 (1995), pp. 26–36. ISSN: 13552546. DOI: https://doi.org/10.1108/13552549510078113.

[9] J G Conley and H L Marcus. "Rapid Prototyping and Solid Free Form Fabrication". In: *J. Manuf. Sci. Eng.* 119.4B (Nov. 1997), pp. 811–816. ISSN: 1087-1357. DOI: 10.1115/1.2836828.

[10] William E. Frazier. "Metal Additive Manufacturing: A Review". In: *J. Mater. Eng. Perform.* 23.6 (June 2014), pp. 1917–1928. ISSN: 1059-9495. DOI: 10.1007/s11665-014-0958-z.

[11] Amanda S. Wu et al. "An Experimental Investigation into Additive Manufacturing-Induced Residual Stresses in 316L Stainless Steel". In: *Metall. Mater. Trans. A* 45.13 (Dec. 2014), pp. 6260–6270. ISSN: 1073-5623. DOI: 10.1007/s11661-014-2549-x.

[12] F. Abe et al. "The manufacturing of hard tools from metallic powders by selective laser melting". In: *J. Mater. Process. Technol.* 111.1-3 (Apr. 2001), pp. 210–213. ISSN: 09240136. DOI: 10.1016/S0924-0136(01)00522-2.

[13] Hadley Brooks and Kevin Brigden. "Design of conformal cooling layers with self-supporting lattices for additively manufactured tooling". In: *Addit. Manuf.* 11 (July 2016), pp. 16–22. ISSN: 22148604. DOI: 10.1016/j.addma.2016.03.004.

[14] Adriaan B. Spierings, Thomas L. Starr, and Konrad Wegener. "Fatigue performance of additive manufactured metallic parts". In: *Rapid Prototyp. J.* 19.2 (2013), pp. 88–94. ISSN: 13552546. DOI: 10.1108/13552541311302932.

[15] Gururaja Udupa, S. Shrikantha Rao, and K.V. Gangadharan. "Functionally Graded Composite Materials: An Overview". In: *Procedia Mater. Sci.* 5 (2014), pp. 1291–1299. ISSN: 22118128. DOI: 10.1016/j.mspro.2014.07.442.

[16] Chao Wei et al. "Additive Manufacturing of Horizontal and 3D Functionally Graded 316L/Cu10Sn Components via Multiple Material Selective Laser Melting". In: *J. Manuf. Sci. Eng.* 141.8 (Aug. 2019), pp. 1–8. ISSN: 1087-1357. DOI: 10.1115/1.4043983.

[17] H.L. Wei, J. Mazumder, and T. DebRoy. "Evolution of solidification texture during additive manufacturing". In: *Sci. Rep.* 5.1 (Dec. 2015), p. 16446. ISSN: 2045-2322. DOI: 10.1038/srep16446.

[18] Zhuqing Wang, Todd A. Palmer, and Allison M. Beese. "Effect of processing parameters on microstructure and tensile properties of austenitic stainless steel 304L made by directed energy deposition additive manufacturing". In: *Acta Mater.* 110 (May 2016), pp. 226–235. ISSN: 13596454. DOI: 10.1016/j.actamat.2016.03.019.

[19] T. Mukherjee et al. "Printability of alloys for additive manufacturing". In: *Sci. Rep.* 6.1 (Apr. 2016), p. 19717. ISSN: 2045-2322. DOI: 10.1038/srep19717.

[20] T. Mukherjee et al. "Dimensionless numbers in additive manufacturing". In: *J. Appl. Phys.* 121.6 (Feb. 2017), p. 064904. ISSN: 0021-8979. DOI: 10.1063/1.4976006.

[21] Adriaan B. Spierings and G. Levy. "Comparison of density of stainless steel 316L parts produced with selective laser melting using different powder grades". In: *2009 Int. Solid Free. Fabr. Symp.* University of Texas at Austin, 2009, pp. 342–353. DOI: 10.26153/tsw/15113.

[22] Mohsen Badrossamay et al. "Improving Productivity Rate in SLM of Commercial Steel Powders". In: *Tech. Pap. - Soc. Manuf. Eng.* TP09PUB17 (2009), pp. 1–13.

[23] Adriaan B. Spierings, N. Herres, and G. Levy. "Influence of the particle size distribution on surface quality and mechanical properties in AM steel parts". In: *Rapid Prototyp. J.* 17.3 (Apr. 2011). Ed. by Dave Bourell, pp. 195–202. ISSN: 1355-2546. DOI: 10.1108/13552541111124770.

[24] A.A. Antonysamy, J. Meyer, and P.B. Prangnell. "Effect of build geometry on the β-grain structure and texture in additive manufacture of Ti6Al4V by selective electron beam melting". In: *Mater. Charact.* 84 (Oct. 2013), pp. 153–168. ISSN: 10445803. DOI: 10.1016/j.matchar.2013.07.012.

[25] B. Song et al. "Compressive and Tensile Stress–Strain Responses of Additively Manufactured (AM) 304L Stainless Steel at High Strain Rates". In: *J. Dyn. Behav. Mater.* 3.3 (Sept. 2017), pp. 412–425. ISSN: 2199-7446. DOI: 10.1007/s40870-017-0122-6.

[26] J. A. Cherry et al. "Investigation into the effect of process parameters on microstructural and physical properties of 316L stainless steel parts by selective laser melting". In: *Int. J. Adv. Manuf. Technol.* 76.5-8 (Feb. 2015), pp. 869–879. ISSN: 0268-3768. DOI: 10.1007/s00170-014-6297-2.

[27] K.G. Prashanth and J. Eckert. "Formation of metastable cellular microstructures in selective laser melted alloys". In: *J. Alloys Compd.* 707.October (June 2017), pp. 27–34. ISSN: 09258388. DOI: 10.1016/j.jallcom.2016.12.209.

[28] Pierre Muller, Pascal Mognol, and Jean-Yves Hascoet. "Modeling and control of a direct laser powder deposition process for Functionally Graded Materials (FGM) parts manufacturing". In: *J. Mater. Process. Technol.* 213.5 (May 2013), pp. 685–692. ISSN: 09240136. DOI: 10.1016/j.jmatprotec.2012.11.020.

[29] Qiang Wang et al. "Microstructure evolution and EBSD analysis of a graded steel fabricated by laser additive manufacturing". In: *Vacuum* 141 (July 2017), pp. 68–81. ISSN: 0042207X. DOI: 10.1016/j.vacuum.2017.03.021.

[30] E. Berry et al. "Preliminary experience with medical applications of rapid prototyping by selective laser sintering". In: *Med. Eng. Phys.* 19.1 (Jan. 1997), pp. 90–96. ISSN: 13504533. DOI: 10.1016/S1350-4533(96)00039-2.

[31] Junchao Li, Yanyan Zang, and Wei Wang. "Elastic modulus and stress analysis of porous titanium parts fabricated by selective laser melting". In: *J. Harbin Inst. Technol.* 23.2 (Apr. 2016), pp. 46–50. DOI: 10.11916/j.issn.1005-9113.2016.02.007.

[32] H. Nahme, E. Lach, and R. Rohr. "Dynamic materials behavior of a porous pressureless sintered steel and a HIPped steel". In: *J. Phys. IV* 134 (Aug. 2006), pp. 1047–1051. ISSN: 1155-4339. DOI: 10.1051/jp4:2006134160.

[33] Dongdong Gu et al. "Material-structure-performance integrated laser-metal additive manufacturing". In: *Science (80-.).* 372.6545 (2021). ISSN: 10959203. DOI: 10.1126/science.abg1487.

[34] Sean H Haight. "An anisotropic and asymmetric material model for simulation of metals under dynamic loading". PhD thesis. George Mason University, 2016.

[35] J Asay et al. *High-Pressure Shock Compression of Solids II: Dynamic Fracture and Fragmentation*. Ed. by Lee Davison, Dennis E. Grady, and Mohsen Shahinpoor. New York, NY: Springer New York, 1996. ISBN: 978-1-4612-7501-5. DOI: 10.1007/978-1-4612-2320-7.

[36] ASM Handbook Committee. *Mechanical Testing and Evaluation*. English. Vol. 8. 1. [Metals Park, Ohio]: ASM International, 2000. ISBN: 978-0-87170-389-7. URL: https://www.asminternational.org.

[37] Sean H Haight et al. *Development of a titanium alloy Ti-6Al-4V material model used in LS-DYNA*. Tech. rep. May. U.S. Department of Transportation, 2016, p. 353. URL: https://www.tc.faa.gov/its/worldpac/techrpt/tc15-23.pdf.

[38] Jürgen Mayer, Khaled Khairy, and Jonathon Howard. "Drawing an elephant with four complex parameters". In: *Am. J. Phys.* 78.6 (June 2010), pp. 648–649. ISSN: 0002-9505. DOI: 10.1119/1.3254017.

[39] Wayne E. King et al. "Observation of keyhole-mode laser melting in laser powder-bed fusion additive manufacturing". In: *J. Mater. Process. Technol.* 214.12 (Dec. 2014), pp. 2915–2925. ISSN: 09240136. DOI: 10.1016/j.jmatprotec.2014.06.005.

[40] Yihang Cui et al. "Effect of Porosity on Dynamic Response of Additive Manufacturing Ti-6Al-4V Alloys". In: *Micromachines* 13.3 (Mar. 2022), p. 408. ISSN: 2072-666X. DOI: 10.3390/mi13030408.

[41] Tarabay Antoun et al. *Spall Fracture*. Shock Wave and High Pressure Phenomena. New York: Springer-Verlag, 2003. ISBN: 0-387-95500-3. DOI: 10.1007/b97226.

[42] Cyril L. Williams. *Structure-Property Relationships under Extreme Dynamic Environments*. Ed. by SEM Kristin Zimmerman. Vol. 2. Synthesis / SEM Lectures on Experimental Mechanics 1. Cham: Springer International Publishing, Jan. 2019, pp. 1–155. ISBN: 978-3-031-79724-5. DOI: 10.1007/978-3-031-79725-5.

[43] V D Gluzman and G. I. Kanel. "Measurement of the tensile stresses behind a spalling plane". In: *J. Appl. Mech. Tech. Phys.* 24.4 (1984), pp. 582–585. ISSN: 0021-8944. DOI: 10.1007/BF00907912.

[44] G. I. Kanel. "Distortion of the Wave Profiles in an Elastoplastic Body upon Spalling". In: *J. Appl. Mech. Tech. Phys.* 42.2 (2001), pp. 358–362. ISSN: 1573-8620. DOI: 10.1023/A:1018804709273.

[45] T. DebRoy et al. "Additive manufacturing of metallic components – Process, structure and properties". In: *Prog. Mater. Sci.* 92 (Mar. 2018), pp. 112–224. ISSN: 00796425. DOI: 10.1016/j.pmatsci.2017.10.001.

[46] H H Zhu, J Y H Fuh, and L Lu. "Formation of Fe—Cu metal parts using direct laser sintering". In: *Proc. Inst. Mech. Eng. Part C J. Mech. Eng. Sci.* 217.1 (Jan. 2003), pp. 139–147. ISSN: 0954-4062. DOI: 10.1243/095440603762554686.

[47] T H C Childs, C Hauser, and Mohsen Badrossamay. "Selective laser sintering (melting) of stainless and tool steel powders: Experiments and modelling". In: *Proc. Inst. Mech. Eng. Part B J. Eng. Manuf.* 219.4 (Apr. 2005), pp. 339–357. ISSN: 0954-4054. DOI: 10.1243/095440505X8109.

[48] Kozo Osakada and Masanori Shiomi. "Flexible manufacturing of metallic products by selective laser melting of powder". In: *Int. J. Mach. Tools Manuf.* 46.11 (Sept. 2006), pp. 1188–1193. ISSN: 08906955. DOI: 10.1016/j.ijmachtools.2006.01.024.

[49] Mohsen Badrossamay and T.H.C. Childs. "Layer Formation Studies in Selective Laser Melting of Steel Powders". In: *Int. Solid Free. Fabr. Symp.* 2006, pp. 13–15. DOI: http://dx.doi.org/10.26153/tsw/7136.

[50] Mohsen Badrossamay and T.H.C. Childs. "Further studies in selective laser melting of stainless and tool steel powders". In: *Int. J. Mach. Tools Manuf.* 47.5 (Apr. 2007), pp. 779–784. ISSN: 08906955. DOI: 10.1016/j.ijmachtools.2006.09.013.

[51] Kamran Aamir Mumtaz, Poonjolai Erasenthiran, and Neil Hopkinson. "High density selective laser melting of Waspaloy®". In: *J. Mater. Process. Technol.* 195.1-3 (Jan. 2008), pp. 77–87. ISSN: 09240136. DOI: 10.1016/j.jmatprotec.2007.04.117.

[52] Petri Laakso et al. "Optimization and Simulation of SLM Process for High Density H13 Tool Steel Parts". In: *Phys. Procedia* 83 (2016), pp. 26–35. ISSN: 18753892. DOI: 10.1016/j.phpro.2016.08.004.

[53] John E. Smugeresky, David D. Gill, and Clinton J. Atwood. *New low cost material development technique for advancing rapid prototyping manufacturing technology*. Tech. rep. Albuquerque, NM, and Livermore, CA (United States): Sandia National Laboratories (SNL), Nov. 2007. DOI: 10.2172/926378.

[54] V. Manvatkar, A. De, and T. DebRoy. "Spatial variation of melt pool geometry, peak temperature and solidification parameters during laser assisted additive manufacturing process". In: *Mater. Sci. Technol.* 31.8 (June 2015), pp. 924–930. ISSN: 0267-0836. DOI: 10.1179/1743284714Y.0000000701.

[55] Yali Li and Dongdong Gu. "Parametric analysis of thermal behavior during selective laser melting additive manufacturing of aluminum alloy powder". In: *Mater. Des.* 63 (Nov. 2014), pp. 856–867. ISSN: 02613069. DOI: 10.1016/j.matdes.2014.07.006.

[56] C. H. Fu and Y.B. Guo. "Three-Dimensional Temperature Gradient Mechanism in Selective Laser Melting of Ti-6Al-4V". In: *J. Manuf. Sci. Eng.* 136.6 (Dec. 2014), pp. 1–7. ISSN: 1087-1357. DOI: 10.1115/1.4028539.

[57] Moataz M. Attallah et al. "Additive manufacturing of Ni-based superalloys: The outstanding issues". In: *MRS Bull.* 41.10 (Oct. 2016), pp. 758–764. ISSN: 0883-7694. DOI: 10.1557/mrs.2016.211.

[58] Xiaoyu Xie et al. "Mechanistic data-driven prediction of as-built mechanical properties in metal additive manufacturing". In: *npj Comput. Mater.* 7.1 (Dec. 2021), p. 86. ISSN: 2057-3960. DOI: 10.1038/s41524-021-00555-z.

[59] Dongju Chen et al. "Process optimization of selective laser melting 316L stainless steel by a data-driven nonlinear system". In: *Weld. World* 66.3 (Mar. 2022), pp. 409–422. ISSN: 0043-2288. DOI: 10.1007/s40194-021-01205-0.

[60] M. Averyanova, Ph Bertrand, and B. Verquin. "Studying the influence of initial powder characteristics on the properties of final parts manufactured by the selective laser melting technology". In: *Virtual Phys. Prototyp.* 6.4 (Dec. 2011), pp. 215–223. ISSN: 1745-2759. DOI: 10.1080/17452759.2011.594645.

[61] B. Verlee, T. Dormal, and J. Lecomte-Beckers. "Density and porosity control of sintered 316L stainless steel parts produced by additive manufacturing". In: *Powder Metall.* 55.4 (Sept. 2012), pp. 260–267. ISSN: 0032-5899. DOI: 10.1179/0032589912Z.00000000082.

[62] Benjamin M. Morrow et al. "Impact of Defects in Powder Feedstock Materials on Microstructure of 304L and 316L Stainless Steel Produced by Additive Manufacturing". In: *Metall. Mater. Trans. A* 49.8 (Aug. 2018), pp. 3637–3650. ISSN: 1073-5623. DOI: 10.1007/s11661-018-4661-9.

[63] F. Abe et al. "Influence of forming conditions on the titanium model in rapid prototyping with the selective laser melting process". In: *Proc. Inst. Mech. Eng. Part C J. Mech. Eng. Sci.* 217.1 (Jan. 2003), pp. 119–126. ISSN: 0954-4062. DOI: 10.1243/095440603762554668.

[64] Lore Thijs et al. "A study of the microstructural evolution during selective laser melting of Ti-6Al-4V". In: *Acta Mater.* 58.9 (2010), pp. 3303–3312. ISSN: 13596454. DOI: 10.1016/j.actamat.2010.02.004.

[65] G. Casalino et al. "Experimental investigation and statistical optimisation of the selective laser melting process of a maraging steel". In: *Opt. Laser Technol.* 65 (Jan. 2015), pp. 151–158. ISSN: 00303992. DOI: 10.1016/j.optlastec.2014.07.021.

[66] Lore Thijs et al. "Fine-structured aluminium products with controllable texture by selective laser melting of pre-alloyed AlSi10Mg powder". In: *Acta Mater.* 61.5 (Mar. 2013), pp. 1809–1819. ISSN: 13596454. DOI: 10.1016/j.actamat.2012.11.052.

[67] Xihe Liu et al. "Microstructure of selective laser melted AlSi10Mg alloy". In: *Mater. Des.* 168 (Apr. 2019), p. 107677. ISSN: 02641275. DOI: 10.1016/j.matdes.2019.107677.

[68] Kamran Mumtaz and Neil Hopkinson. "Top surface and side roughness of Inconel 625 parts processed using selective laser melting". In: *Rapid Prototyp.*

J. 15.2 (Mar. 2009), pp. 96–103. ISSN: 1355-2546. DOI: 10.1108/13552540910943397.

[69] Michael Cloots, Peter J. Uggowitzer, and Konrad Wegener. "Investigations on the microstructure and crack formation of IN738LC samples processed by selective laser melting using Gaussian and doughnut profiles". In: *Mater. Des.* 89 (Jan. 2016), pp. 770–784. ISSN: 02641275. DOI: 10.1016/j.matdes.2015.10.027.

[70] Alexander Leicht, Uta Klement, and Eduard Hryha. "Effect of build geometry on the microstructural development of 316L parts produced by additive manufacturing". In: *Mater. Charact.* 143.January (Sept. 2018), pp. 137–143. ISSN: 10445803. DOI: 10.1016/j.matchar.2018.04.040.

[71] Dan Stoia, Emanoil Linul, and Liviu Marsavina. "Influence of Manufacturing Parameters on Mechanical Properties of Porous Materials by Selective Laser Sintering". In: *Materials (Basel).* 12.6 (Mar. 2019), p. 871. ISSN: 1996-1944. DOI: 10.3390/ma12060871.

[72] Evren Yasa and Jean-Pierre Kruth. "Microstructural investigation of Selective Laser Melting 316L stainless steel parts exposed to laser re-melting". In: *Procedia Eng.* 19 (2011), pp. 389–395. ISSN: 18777058. DOI: 10.1016/j.proeng.2011.11.130.

[73] Chu Lun Alex Leung et al. "In situ X-ray imaging of defect and molten pool dynamics in laser additive manufacturing". In: *Nat. Commun.* 9.1 (Dec. 2018), p. 1355. ISSN: 2041-1723. DOI: 10.1038/s41467-018-03734-7.

[74] Sonny Ly et al. "Metal vapor micro-jet controls material redistribution in laser powder bed fusion additive manufacturing". In: *Sci. Rep.* 7.1 (Dec. 2017), p. 4085. ISSN: 2045-2322. DOI: 10.1038/s41598-017-04237-z.

[75] Cang Zhao et al. "Real-time monitoring of laser powder bed fusion process using high-speed X-ray imaging and diffraction". In: *Sci. Rep.* 7.1 (Dec. 2017), p. 3602. ISSN: 2045-2322. DOI: 10.1038/s41598-017-03761-2.

[76] H. Meier and Ch Haberland. "Experimental studies on selective laser melting of metallic parts". In: *Materwiss. Werksttech.* 39.9 (Sept. 2008), pp. 665–670. ISSN: 09335137. DOI: 10.1002/mawe.200800327.

[77] Jean-Pierre Kruth et al. "Part and material properties in selective laser melting of metals". In: *16th Int. Symp. Electromachining, ISEM 2010*. 2010, pp. 3–14. URL: https://lirias.kuleuven.be/retrieve/106724.

[78] Di Wang et al. "Fiber laser selective melting of 316L stainless steel powder". In: *High Power Laser Part. Beams* 22.8 (2010), pp. 1881–1886. ISSN: 1001-4322. DOI: 10.3788/HPLPB20102208.1881.

[79] Itziar Tolosa et al. "Study of mechanical properties of AISI 316 stainless steel processed by "selective laser melting", following different manufacturing strategies". In: *Int. J. Adv. Manuf. Technol.* 51.5-8 (Nov. 2010), pp. 639–647. ISSN: 0268-3768. DOI: 10.1007/s00170-010-2631-5.

[80] Baicheng Zhang, Lucas Dembinski, and Christian Coddet. "The study of the laser parameters and environment variables effect on mechanical properties of high compact parts elaborated by selective laser melting 316L powder". In: *Mater. Sci. Eng. A* 584 (Nov. 2013), pp. 21–31. ISSN: 09215093. DOI: 10.1016/j.msea.2013.06.055.

[81] Chandrika Kamath et al. "Density of additively-manufactured, 316L SS parts using laser powder-bed fusion at powers up to 400 W". In: *Int. J. Adv. Manuf.*

Technol. 74.1-4 (Sept. 2014), pp. 65–78. ISSN: 0268-3768. DOI: 10.1007/s00170-014-5954-9.

[82] K. Saeidi et al. "Hardened austenite steel with columnar sub-grain structure formed by laser melting". In: *Mater. Sci. Eng. A* 625 (Feb. 2015), pp. 221–229. ISSN: 09215093. DOI: 10.1016/j.msea.2014.12.018.

[83] Zhongji Sun et al. "Selective laser melting of stainless steel 316L with low porosity and high build rates". In: *Mater. Des.* 104 (Aug. 2016), pp. 197–204. ISSN: 02641275. DOI: 10.1016/j.matdes.2016.05.035.

[84] Arne Röttger et al. "Comparison of microstructure and mechanical properties of 316 L austenitic steel processed by selective laser melting with hot-isostatic pressed and cast material". In: *Mater. Sci. Eng. A* 678.October (Dec. 2016), pp. 365–376. ISSN: 09215093. DOI: 10.1016/j.msea.2016.10.012.

[85] Jason R. Trelewicz et al. "Microstructure and Corrosion Resistance of Laser Additively Manufactured 316L Stainless Steel". In: *JOM* 68.3 (Mar. 2016), pp. 850–859. ISSN: 1047-4838. DOI: 10.1007/s11837-016-1822-4.

[86] Y. Morris Wang et al. "Additively manufactured hierarchical stainless steels with high strength and ductility". In: *Nat. Mater.* 17.1 (Jan. 2018), pp. 63–71. ISSN: 1476-1122. DOI: 10.1038/nmat5021.

[87] Kai Zhang et al. "Characterization of stainless steel parts by Laser Metal Deposition Shaping". In: *Mater. Des.* 55 (Mar. 2014), pp. 104–119. ISSN: 02613069. DOI: 10.1016/j.matdes.2013.09.006.

[88] Chengcheng Wang et al. "Process parameter optimization and mechanical properties for additively manufactured stainless steel 316L parts by selective electron beam melting". In: *Mater. Des.* 147 (June 2018), pp. 157–166. ISSN: 02641275. DOI: 10.1016/j.matdes.2018.03.035.

[89] Yuan Zhong et al. "Intragranular cellular segregation network structure strengthening 316L stainless steel prepared by selective laser melting". In: *J. Nucl. Mater.* 470 (Mar. 2016), pp. 170–178. ISSN: 00223115. DOI: 10.1016/j.jnucmat.2015.12.034.

[90] Haniyeh Fayazfar et al. "A critical review of powder-based additive manufacturing of ferrous alloys: Process parameters, microstructure and mechanical properties". In: *Mater. Des.* 144 (Apr. 2018), pp. 98–128. ISSN: 02641275. DOI: 10.1016/j.matdes.2018.02.018.

[91] Elton N. Kaufmann. *Characterization of Materials: Volume 1*. Ed. by Elton N. Kaufmann. Hoboken, NJ, USA: John Wiley & Sons, Inc., Oct. 2003. ISBN: 0471266965. DOI: 10.1002/0471266965.

[92] William D. Callister and David G. Rethwisch. *Materials science and engineering : an introduction*. English. Ed. by Joseph P. Hayton and Kenneth Santor. 7th ed. New York: John Wiley & Sons, 2007. ISBN: 978-0-471-73696-7. URL: https://www.wiley.com/en-us/etextbooks-and-courseware/engineering/materials-science.

[93] Jean-Pierre Kruth et al. "Selective laser melting of iron-based powder". In: *J. Mater. Process. Technol.* 149.1-3 (June 2004), pp. 616–622. ISSN: 09240136. DOI: 10.1016/j.jmatprotec.2003.11.051.

[94] H. Khalid Rafi, Thomas L. Starr, and Brent E. Stucker. "A comparison of the tensile, fatigue, and fracture behavior of Ti–6Al–4V and 15-5 PH stainless steel parts made by selective laser melting". In: *Int. J. Adv. Manuf. Technol.*

69.5-8 (Nov. 2013), pp. 1299–1309. ISSN: 0268-3768. DOI: 10.1007/s00170-013-5106-7.

[95] Jingjing Yang et al. "Effect of crystallographic orientation on mechanical anisotropy of selective laser melted Ti-6Al-4V alloy". In: *Mater. Charact.* 127 (2017), pp. 137–145. ISSN: 10445803. DOI: 10.1016/j.matchar.2017.01.014.

[96] Hanchen Yu et al. "Comparison on mechanical anisotropies of selective laser melted Ti-6Al-4V alloy and 304 stainless steel". In: *Mater. Sci. Eng. A* 695.April (2017), pp. 92–100. ISSN: 09215093. DOI: 10.1016/j.msea.2017.04.031.

[97] Erhard Brandl et al. "Additive manufactured AlSi10Mg samples using Selective Laser Melting (SLM): Microstructure, high cycle fatigue, and fracture behavior". In: *Mater. Des.* 34 (Feb. 2012), pp. 159–169. ISSN: 02613069. DOI: 10.1016/j.matdes.2011.07.067.

[98] U. Tradowsky et al. "Selective laser melting of AlSi10Mg: Influence of post-processing on the microstructural and tensile properties development". In: *Mater. Des.* 105 (Sept. 2016), pp. 212–222. ISSN: 02641275. DOI: 10.1016/j.matdes.2016.05.066.

[99] Karolien Kempen et al. "Microstructure and mechanical properties of Selective Laser Melted 18Ni-300 steel". In: *Phys. Procedia* 12.PART 1 (2011), pp. 255–263. ISSN: 18753892. DOI: 10.1016/j.phpro.2011.03.033.

[100] Adriaan B. Spierings, Konrad Wegener, and G. Levy. "Designing material properties locally with additive manufacturing technology SLM". In: *23rd Annu. Int. Solid Free. Fabr. Symp. - An Addit. Manuf. Conf. SFF 2012*. Jan. 2012, pp. 447–455. DOI: 10.26153/tsw/15364.

[101] K.N. Amato et al. "Microstructures and mechanical behavior of Inconel 718 fabricated by selective laser melting". In: *Acta Mater.* 60.5 (Mar. 2012), pp. 2229–2239. ISSN: 13596454. DOI: 10.1016/j.actamat.2011.12.032.

[102] Ofer Tevet et al. "Measurement of the Anisotropic Dynamic Elastic Constants of Additive Manufactured and Wrought Ti6Al4V Alloys". In: *Materials (Basel).* 15.2 (Jan. 2022), p. 638. ISSN: 1996-1944. DOI: 10.3390/ma15020638.

[103] Lore Thijs et al. "Strong morphological and crystallographic texture and resulting yield strength anisotropy in selective laser melted tantalum". In: *Acta Mater.* 61.12 (July 2013), pp. 4657–4668. ISSN: 13596454. DOI: 10.1016/j.actamat.2013.04.036.

[104] Behzad Bahrami Babamiri et al. "Quantification of porosity and microstructure and their effect on quasi-static and dynamic behavior of additively manufactured Inconel 718". In: *Addit. Manuf.* 34.February (2020). ISSN: 22148604. DOI: 10.1016/j.addma.2020.101380.

[105] A. D. Brown et al. "Dynamic mechanical response of additive manufactured Ti-6Al-4V". In: *AIP Conf. Proc.* Vol. 1979. July. 2018, p. 070008. ISBN: 9780735416932. DOI: 10.1063/1.5044817.

[106] P. Ponnusamy et al. "High strain rate behaviour at high temperature of AlSi12 parts produced by selective laser melting". In: *IOP Conf. Ser. Mater. Sci. Eng.* 377.1 (June 2018), p. 012167. ISSN: 1757-8981. DOI: 10.1088/1757-899X/377/1/012167.

[107] O. L. Rodriguez et al. "Dynamic tensile behavior of electron beam additive manufactured Ti6Al4V". In: *Mater. Sci. Eng. A* 641 (2015), pp. 323–327. ISSN: 09215093. DOI: 10.1016/j.msea.2015.06.069.

[108] Refael Fadida, Amnon Shirizly, and Daniel Rittel. "Dynamic Tensile Response of Additively Manufactured Ti6Al4V With Embedded Spherical Pores". In: *J. Appl. Mech.* 85.4 (Apr. 2018), pp. 1–10. ISSN: 0021-8936. DOI: 10.1115/1.4039048.

[109] Bar Nurel et al. "Study on the dynamic properties of AM-SLM AlSi10Mg alloy using the Split Hopkinson Pressure Bar (SHPB) technique". In: *EPJ Web Conf.* Ed. by E. Buzaud et al. Vol. 183. EDP Sciences, Sept. 2018, p. 04005. ISBN: 9782759890538. DOI: 10.1051/epjconf/201818304005.

[110] D. R. Jones et al. "Spall fracture in additive manufactured Ti-6Al-4V". In: *J. Appl. Phys.* 120.13 (Oct. 2016), p. 135902. ISSN: 0021-8979. DOI: 10.1063/1.4963279.

[111] E. Zaretsky, A. Stern, and Nahum Frage. "Dynamic response of AlSi10Mg alloy fabricated by selective laser melting". In: *Mater. Sci. Eng. A* 688.February (Mar. 2017), pp. 364–370. ISSN: 09215093. DOI: 10.1016/j.msea.2017.02.004.

[112] D. R. Jones et al. "Spall fracture in additive manufactured tantalum". In: *J. Appl. Phys.* 124.22 (Dec. 2018), p. 225902. ISSN: 0021-8979. DOI: 10.1063/1.5063930.

[113] M. Laurençon et al. "Effects of additive manufacturing on the dynamic response of AlSi10Mg to laser shock loading". In: *Mater. Sci. Eng. A* 748.December 2018 (Mar. 2019), pp. 407–417. ISSN: 09215093. DOI: 10.1016/j.msea.2019.02.001.

[114] A. Charmi et al. "Mechanical anisotropy of additively manufactured stainless steel 316L: An experimental and numerical study". In: *Mater. Sci. Eng. A* 799.June 2020 (Jan. 2021), p. 140154. ISSN: 09215093. DOI: 10.1016/j.msea.2020.140154.

[115] Michał Zietala et al. "The microstructure, mechanical properties and corrosion resistance of 316L stainless steel fabricated using laser engineered net shaping". In: *Mater. Sci. Eng. A* 677 (Nov. 2016), pp. 1–10. ISSN: 09215093. DOI: 10.1016/j.msea.2016.09.028.

[116] Minh-Son Pham, Bogdan Dovgyy, and P.A. Hooper. "Twinning induced plasticity in austenitic stainless steel 316L made by additive manufacturing". In: *Mater. Sci. Eng. A* 704.July (Sept. 2017), pp. 102–111. ISSN: 09215093. DOI: 10.1016/j.msea.2017.07.082.

[117] Chola Elangeswaran et al. "Effect of post-treatments on the fatigue behaviour of 316L stainless steel manufactured by laser powder bed fusion". In: *Int. J. Fatigue* 123.February (June 2019), pp. 31–39. ISSN: 01421123. DOI: 10.1016/j.ijfatigue.2019.01.013.

[118] Holly D. Carlton et al. "Damage evolution and failure mechanisms in additively manufactured stainless steel". In: *Mater. Sci. Eng. A* 651 (Jan. 2016), pp. 406–414. ISSN: 09215093. DOI: 10.1016/j.msea.2015.10.073.

[119] Anne Mertens et al. "Microstructures and Mechanical Properties of Stainless Steel AISI 316L Processed by Selective Laser Melting". In: *Mater. Sci. Forum* 783-786.3 (May 2014), pp. 898–903. ISSN: 1662-9752. DOI: 10.4028/www.scientific.net/MSF.783-786.898.

[120] T. Niendorf et al. "Highly Anisotropic Steel Processed by Selective Laser Melting". In: *Metall. Mater. Trans. B* 44.4 (Aug. 2013), pp. 794–796. ISSN: 1073-5615. DOI: 10.1007/s11663-013-9875-z.

[121] Tomasz Kurzynowski et al. "Correlation between process parameters, microstructure and properties of 316 L stainless steel processed by selective laser melting". In: *Mater. Sci. Eng. A* 718.January (Mar. 2018), pp. 64–73. ISSN: 09215093. DOI: 10.1016/j.msea.2018.01.103.

[122] M. A. Bevan et al. "Mechanical Properties and Behavior of Additive Manufactured Stainless Steel 316L". In: *Miner. Met. Mater. Ser.* Vol. Part F7. February. 2017, pp. 577–583. ISBN: 9783319513812. DOI: 10.1007/978-3-319-51382-9_63.

[123] Patrick R. Carlson et al. "Mechanical behaviour and high strain rate deformation of stainless steel 316L processed by selective laser melting". In: *Int. J. Rapid Manuf.* 9.1 (2020), p. 84. ISSN: 1757-8817. DOI: 10.1504/IJRAPIDM.2020.10026158.

[124] Jie Chen et al. "Dynamic mechanical properties of 316L stainless steel fabricated by an additive manufacturing process". In: *J. Mater. Res. Technol.* 11 (2021), pp. 170–179. ISSN: 22387854. DOI: 10.1016/j.jmrt.2020.12.097.

[125] G.T. Gray III et al. "Structure/property (constitutive and dynamic strength/damage) characterization of additively manufactured 316L SS". In: *EPJ Web Conf.* 94 (Sept. 2015). Ed. by E. Cadoni, p. 02006. ISSN: 2100-014X. DOI: 10.1051/epjconf/20159402006.

[126] S. Tsopanos et al. "The Influence of Processing Parameters on the Mechanical Properties of Selectively Laser Melted Stainless Steel Microlattice Structures". In: *J. Manuf. Sci. Eng.* 132.4 (Aug. 2010), pp. 0410111–04101112. ISSN: 1087-1357. DOI: 10.1115/1.4001743.

[127] B. Gorny et al. "In situ characterization of the deformation and failure behavior of non-stochastic porous structures processed by selective laser melting". In: *Mater. Sci. Eng. A* 528.27 (Oct. 2011), pp. 7962–7967. ISSN: 09215093. DOI: 10.1016/j.msea.2011.07.026.

[128] F. Brenne, T. Niendorf, and H.J. Maier. "Additively manufactured cellular structures: Impact of microstructure and local strains on the monotonic and cyclic behavior under uniaxial and bending load". In: *J. Mater. Process. Technol.* 213.9 (Sept. 2013), pp. 1558–1564. ISSN: 09240136. DOI: 10.1016/j.jmatprotec.2013.03.013.

[129] Martin Jäcklein et al. "Dynamic compression of 3D printed metallic mesostructures with in-situ X-ray imaging". In: *Proc. ISIE 2019 10th Int. Symp. Impact Eng.* Gmunden: Trauner Verlag, 2019.

[130] Jean-Pierre Kruth et al. "Consolidation phenomena in laser and powder-bed based layered manufacturing". In: *CIRP Ann.* 56.2 (2007), pp. 730–759. ISSN: 00078506. DOI: 10.1016/j.cirp.2007.10.004.

[131] Dirk Herzog et al. "Additive manufacturing of metals". In: *Acta Mater.* 117 (Sept. 2016), pp. 371–392. ISSN: 13596454. DOI: 10.1016/j.actamat.2016.07.019.

[132] Todd M. Mower and Michael J. Long. "Mechanical behavior of additive manufactured, powder-bed laser-fused materials". In: *Mater. Sci. Eng. A* 651 (Jan. 2016), pp. 198–213. ISSN: 09215093. DOI: 10.1016/j.msea.2015.10.068.

[133] J.P. Oliveira, A.D. LaLonde, and J. Ma. "Processing parameters in laser powder bed fusion metal additive manufacturing". In: *Mater. Des.* 193 (Aug. 2020), p. 108762. ISSN: 02641275. DOI: 10.1016/j.matdes.2020.108762.

[134] G. Asala, J. Andersson, and O. A. Ojo. "Improved dynamic impact behaviour of wire-arc additive manufactured ATI 718Plus®". In: *Mater. Sci. Eng. A* 738.May (Dec. 2018), pp. 111–124. ISSN: 09215093. DOI: 10.1016/j.msea.2018.09.079.

[135] G. Asala, J. Andersson, and O. A. Ojo. "Analysis and constitutive modelling of high strain rate deformation behaviour of wire–arc additive-manufactured ATI 718Plus superalloy". In: *Int. J. Adv. Manuf. Technol.* 103.1-4 (July 2019), pp. 1419–1431. ISSN: 0268-3768. DOI: 10.1007/s00170-019-03616-2.

[136] C.M Sellars and W.J. McTegart. "On the mechanism of hot deformation". In: *Acta Metall.* 14.9 (Sept. 1966), pp. 1136–1138. ISSN: 00016160. DOI: 10.1016/0001-6160(66)90207-0.

[137] Y.C. Lin, Xiao-Min Chen, and Ge Liu. "A modified Johnson–Cook model for tensile behaviors of typical high-strength alloy steel". In: *Mater. Sci. Eng. A* 527.26 (Oct. 2010), pp. 6980–6986. ISSN: 09215093. DOI: 10.1016/j.msea.2010.07.061.

[138] Yanhua Zhao et al. "A comparative study on Johnson-Cook and modified Johnson-Cook constitutive material model to predict the dynamic behavior laser additive manufacturing FeCr alloy". In: *J. Alloys Compd.* 723 (Nov. 2017), pp. 179–187. ISSN: 09258388. DOI: 10.1016/j.jallcom.2017.06.251.

[139] Arman Ahmadi et al. "Finite Element Modeling of Selective Laser Melting 316L Stainless Steel Parts for Evaluating the Mechanical Properties". In: *Vol. 2 Mater. Biomanufacturing; Prop. Appl. Syst. Sustain. Manuf.* American Society of Mechanical Engineers, June 2016, pp. 1–5. ISBN: 978-0-7918-4990-3. DOI: 10.1115/MSEC2016-8594.

[140] T. Wang et al. "Grain morphology evolution behavior of titanium alloy components during laser melting deposition additive manufacturing". In: *J. Alloys Compd.* 632 (May 2015), pp. 505–513. ISSN: 09258388. DOI: 10.1016/j.jallcom.2015.01.256.

[141] Benjamin Thomas Spencer Cousins. "Development of Improved Numerical Techniques for High Strain Rate Deformation Behaviour of Titanium Alloys". PhD thesis. 2016.

[142] Oana Cazacu and Frédéric Barlat. "A criterion for description of anisotropy and yield differential effects in pressure-insensitive metals". In: *Int. J. Plast.* 20.11 (Nov. 2004), pp. 2027–2045. ISSN: 07496419. DOI: 10.1016/j.ijplas.2003.11.021.

[143] Douglas J. Bammann et al. *On the formulation, parameter identification and numerical integration of the EMMI model :plasticity and isotropic damage.* Tech. rep. Report No. SAND2006-0200. Albuquerque, NM, and Livermore, CA (United States): Sandia National Laboratories (SNL), Jan. 2006. DOI: 10.2172/883488.

[144] Douglas J. Bammann. "An internal variable model of viscoplasticity". In: *Int. J. Eng. Sci.* 22.8-10 (1984), pp. 1041–1053. ISSN: 00207225. DOI: 10.1016/0020-7225(84)90105-8.

[145] Livermore Software Technology Corporation (LSTC). *LS-DYNA Keyword User's Manual*. R12 Vol. 2. Livermore Software Technology Corporation, 2020. URL: https://www.lstc.com/download/manuals.

[146] R. Hill. "A theory of the yielding and plastic flow of anisotropic metals". In: *Proc. R. Soc. London. Ser. A. Math. Phys. Sci.* 193.1033 (May 1948), pp. 281–297. ISSN: 0080-4630. DOI: 10.1098/rspa.1948.0045.

[147] Michael A. Slawinski. *Waves and Rays in Elastic Continua*. WORLD SCIENTIFIC, Sept. 2010, pp. 1–583. ISBN: 978-981-4289-00-9. DOI: 10.1142/7486.

[148] John Frederick Nye. *Physical properties of crystals: their representation by tensors and matrices*. Oxford university press, 1985. ISBN: 9780198511656. URL: https://global.oup.com/academic/product/physical-properties-of-crystals-9780198511656?cc=gb%7B%5C&%7Dlang=en%7B%5C&%7D.

[149] R v. Mises. "Mechanik der festen Körper im plastisch- deformablen Zustand." In: *Nachrichten von der K. Gesellschaft der Wissenschaften.* 1 (1913), pp. 582–592. URL: http://gdz.sub.uni-goettingen.de/dms/resolveppn/?PPN=GDZPPN002503697.

[150] Heinrich Hencky. "Zur Theorie plastischer Deformationen und der hierdurch im Material hervorgerufenen Nachspannungen". In: *ZAMM - Zeitschrift für Angew. Math. und Mech.* 4.4 (Jan. 1924), pp. 323–334. ISSN: 00442267. DOI: 10.1002/zamm.19240040405.

[151] R. Hill. "Theoretical plasticity of textured aggregates". In: *Math. Proc. Cambridge Philos. Soc.* 85.1 (Jan. 1979), pp. 179–191. ISSN: 0305-0041. DOI: 10.1017/S0305004100055596.

[152] R. Hill. *The Mathematical theory of plasticity*. 11th ed. Oxford: Oxford University Press, 1998. ISBN: 9780198503675. URL: https://global.oup.com/academic/product/the-mathematical-theory-of-plasticity-9780198503675.

[153] Prasad Dasappa, Kaan Inal, and Raja Mishra. "The effects of anisotropic yield functions and their material parameters on prediction of forming limit diagrams". In: *Int. J. Solids Struct.* 49.25 (2012), pp. 3528–3550. ISSN: 00207683. DOI: 10.1016/j.ijsolstr.2012.04.021.

[154] G.R. Johnson and W.H. Cook. "A constitutive model and data for metals subjected to large strains, high strain rates and high temperatures." In: *Proc. 7th Int. Symp. Ballist.* The Hague The Netherlands, 1983, pp. 541–547.

[155] G.R. Johnson and W.H. Cook. "Fracture characteristics of three metals subjected to various strains, strain rates, temperatures and pressures". In: *Eng. Fract. Mech.* 21.1 (Jan. 1985), pp. 31–48. ISSN: 00137944. DOI: 10.1016/0013-7944(85)90052-9.

[156] E Orowan. "Problems of plastic gliding". In: *Proc. Phys. Soc.* 52.1 (Jan. 1940), pp. 8–22. ISSN: 0959-5309. DOI: 10.1088/0959-5309/52/1/303.

[157] Jean-Paul Poirier. *Creep of Crystals*. Cambridge University Press, Feb. 1985. ISBN: 9780521261777. DOI: 10.1017/CBO9780511564451.

[158] Daniele Versino and Kane C. Bennett. "Generalized radial-return mapping algorithm for anisotropic von Mises plasticity framed in material eigenspace". In: *Int. J. Numer. Methods Eng.* 116.3 (2018), pp. 202–222. ISSN: 10970207. DOI: 10.1002/nme.5921.

[159] J.C. Simo and R. L. Taylor. "A return mapping algorithm for plane stress elastoplasticity". In: *Int. J. Numer. Methods Eng.* 22.3 (1986), pp. 649–670. ISSN: 10970207. DOI: 10.1002/nme.1620220310.

[160] J.C. Simo. "A framework for finite strain elastoplasticity based on maximum plastic dissipation and the multiplicative decomposition. Part II: Computational aspects". In: *Comput. Methods Appl. Mech. Eng.* 68.1 (May 1988), pp. 1–31. ISSN: 00457825. DOI: 10.1016/0045-7825(88)90104-1.

[161] V.A. Lubarda. "Mechanics of Materials: Plasticity". In: *Ref. Modul. Mater. Sci. Mater. Eng.* March 2015. Elsevier, 2016. ISBN: 9780128035818. DOI: 10.1016/B978-0-12-803581-8.02841-1.

[162] William John Macquorn Rankine. "XV. On the thermodynamic theory of waves of finite longitudinal disturbance". In: *Philos. Trans. R. Soc. London* 160 (Jan. 1870), pp. 277–288. ISSN: 0261-0523. DOI: 10.1098/rstl.1870.0015.

[163] H Hugoniot. "Mémoire sur la propagation du mouvement dans un fluide indéfini (seconde Partie)". In: *J. Math. Pures Appl.* 4 (1888), pp. 153–168. URL: https://eudml.org/doc/233955.

[164] Jerry W Forbes. *Shock Wave Compression of Condensed Matter*. Berlin, Heidelberg: Springer Berlin Heidelberg, 2012. ISBN: 978-3-642-32534-2. DOI: 10.1007/978-3-642-32535-9.

[165] S A Novikov and A G Ivanov. "Failure of steel, aluminium and copper under explosive shock loading". In: *Fiz. Met. i Metalloved.* 21.4 (1966), pp. 608–615.

[166] G. V. Stepanov. "Spalling produced by elastoplastic waves in metals". In: *Strength Mater.* 8.8 (Aug. 1976), pp. 942–947. ISSN: 0039-2316. DOI: 10.1007/BF01529805.

[167] Richard J. Williams et al. "In situ thermography for laser powder bed fusion: Effects of layer temperature on porosity, microstructure and mechanical properties". In: *Addit. Manuf.* 30.March (Dec. 2019), p. 100880. ISSN: 22148604. DOI: 10.1016/j.addma.2019.100880.

[168] M. Naveed Ahsan, Robert Bradley, and Andrew J. Pinkerton. "Microcomputed tomography analysis of intralayer porosity generation in laser direct metal deposition and its causes". In: *J. Laser Appl.* 23.2 (May 2011), p. 022009. ISSN: 1042-346X. DOI: 10.2351/1.3582311.

[169] Fiorello Losano et al. "Computed tomography in the automotive field. Development of a new engine head case study". In: *Comput. Tomogr. Ind. Appl. Image Process. Radiol.* 1999, pp. 65–73. URL: https://www.dgzfp.de/Portals/24/PDFs/BBonline/bb%7B%5C_%7D67-CD/bb67%7B%5C_%7Dv10.pdf.

[170] A. Thompson, I. Maskery, and R. K. Leach. "X-ray computed tomography for additive manufacturing: a review". In: *Meas. Sci. Technol.* 27.7 (July 2016), p. 072001. ISSN: 0957-0233. DOI: 10.1088/0957-0233/27/7/072001.

[171] Nobuyuki Otsu. "A Threshold Selection Method from Gray-Level Histograms". In: *IEEE Trans. Syst. Man. Cybern.* 9.1 (Jan. 1979), pp. 62–66. ISSN: 0018-9472. DOI: 10.1109/TSMC.1979.4310076.

[172] Oliver T. Strand et al. "Velocimetry using heterodyne techniques". In: *26th Int. Congr. High-Speed Photogr. Photonics*. Ed. by Dennis L. Paisley et al. Vol. 5580. Mar. 2005, p. 593. DOI: 10.1117/12.567579.

[173] Oliver T. Strand et al. "Compact system for high-speed velocimetry using heterodyne techniques". In: *Rev. Sci. Instrum.* 77.8 (Aug. 2006), p. 083108. ISSN: 0034-6748. DOI: 10.1063/1.2336749.

[174] E. A. Moro. "New developments in photon Doppler velocimetry". In: *J. Phys. Conf. Ser.* 500.14 (May 2014), p. 142023. ISSN: 1742-6596. DOI: 10.1088/1742-6596/500/14/142023.

[175] D. H. Dolan. "Extreme measurements with Photonic Doppler Velocimetry (PDV)". In: *Rev. Sci. Instrum.* 91.5 (2020). ISSN: 10897623. DOI: 10.1063/5.0004363.

[176] L. M. Barker and R. E. Hollenbach. "Interferometer Technique for Measuring the Dynamic Mechanical Properties of Materials". In: *Rev. Sci. Instrum.* 36.11 (Nov. 1965), pp. 1617–1620. ISSN: 0034-6748. DOI: 10.1063/1.1719405.

[177] Max Born et al. *Principles of Optics: Electromagnetic Theory of Propagation, Interference and Diffraction of Light*. 7th ed. Cambridge University Press, Oct. 1999. ISBN: 9780521642224. DOI: 10.1017/CBO9781139644181.

[178] Tommy Ao and Daniel H Dolan. *SIRHEN : a data reduction program for photonic Doppler velocimetry measurements.* Tech. rep. June. Albuquerque, NM, and Livermore, CA (United States): Sandia National Laboratories (SNL), June 2010, pp. 1–66. DOI: 10.2172/989357.

[179] Daniel H Dolan. *Velocimetry signal synthesis with fringen.* Tech. rep. February. Albuquerque, NM, and Livermore, CA (United States): Sandia National Laboratories (SNL), Feb. 2011. DOI: 10.2172/1008143.

[180] D. H. Dolan, T. Ao, and O. Hernandez. "Note: Frequency-conversion photonic Doppler velocimetry with an inverted circulator". In: *Rev. Sci. Instrum.* 83.2 (Feb. 2012), p. 026109. ISSN: 0034-6748. DOI: 10.1063/1.3688851.

[181] R W Hamming. *Digital Filters (3rd Ed.)* Dover Publications, 1989. ISBN: 9780486650883. URL: https://store.doverpublications.com/048665088x.html.

[182] D. H. Dolan. "Accuracy and precision in photonic Doppler velocimetry". In: *Rev. Sci. Instrum.* 81.5 (May 2010), p. 053905. ISSN: 0034-6748. DOI: 10.1063/1.3429257.

[183] Harry J R Dutton. *Understanding Optical Communications*. Tech. rep. IBM Corporation, 1998.

[184] NKT Photonics GmbH. *Koheras AdjustiK E15 Datasheet*. 2022. URL: https://www.photonicsolutions.co.uk/upfiles/AdjustiK-E15.pdf (visited on 11/24/2022).

[185] Teledyne Lecroy. *WaveMaster 8 Zi-B Oscilloscopes*. 2022. URL: https://teledynelecroy.com/oscilloscope/wavemaster-sda-dda-8-zi-b-oscilloscopes/wavemaster-808zi-b (visited on 11/24/2022).

[186] Liam C. Smith. *PDVTool*. 2022. URL: https://github.com/liamcsmith/PDVTool.

[187] D. B. Holtkamp. "Survey of Optical Velocimetry Experiments - Applications of PDV, A Heterodyne Velocimeter". In: *2006 IEEE Int. Conf. Magagauss Magn. F. Gener. Relat. Top.* IEEE, Nov. 2006, pp. 119–128. ISBN: 978-1-4244-2061-2. DOI: 10.1109/MEGAGUSS.2006.4530668.

[188] Geoffrey Taylor. "The use of flat-ended projectiles for determining dynamic yield stress I. Theoretical considerations". In: *Proc. R. Soc. London. Ser. A. Math. Phys. Sci.* 194.1038 (Sept. 1948), pp. 289–299. ISSN: 0080-4630. DOI: 10.1098/rspa.1948.0081.

[189] D. J. Allen, W. K. Rule, and S.E. Jones. "Optimizing material strength constants numerically extracted from taylor impact data". In: *Exp. Mech.* 37.3 (Sept. 1997), pp. 333–338. ISSN: 0014-4851. DOI: 10.1007/BF02317427.

[190] Paul J. Maudlin et al. "On the modeling of the Taylor cylinder impact test for orthotropic textured materials: experiments and simulations". In: *Int. J. Plast.* 15.2 (Mar. 1999), pp. 139–166. ISSN: 07496419. DOI: 10.1016/S0749-6419(98)00058-8.

[191] J.W. House et al. "Film data reduction from Taylor impact tests". In: *J. Strain Anal. Eng. Des.* 34.5 (July 1999), pp. 337–345. ISSN: 0309-3247. DOI: 10.1243/0309324991513678.

[192] A. Mishra. "Reverse Taylor Tests on Ultrafine Grained Copper". In: *AIP Conf. Proc.* Vol. 845. 2006. AIP, 2006, pp. 757–760. ISBN: 0735403414. DOI: 10.1063/1.2263433.

[193] J.B. Hawkyard. "A theory for the mushrooming of flat-ended projectiles impinging on a flat rigid anvil, using energy considerations". In: *Int. J. Mech. Sci.* 11.3 (Mar. 1969), pp. 313–333. ISSN: 00207403. DOI: 10.1016/0020-7403(69)90049-6.

[194] S.E. Jones, Peter P. Gillis, and Joseph C. Foster. "On the equation of motion of the undeformed section of a Taylor impact specimen". In: *J. Appl. Phys.* 61.2 (1987), pp. 499–502. ISSN: 00218979. DOI: 10.1063/1.338249.

[195] S.E. Jones, Paul J. Maudlin, and Joseph C. Foster. "An engineering analysis of plastic wave propagation in the Taylor test". In: *Int. J. Impact Eng.* 19.2 (Feb. 1997), pp. 95–106. ISSN: 0734743X. DOI: 10.1016/S0734-743X(96)00020-6.

[196] D.C. Erlich and D.A. Shockey. "Dynamic flow curve of 4340 steel as determined by the symmetric rod impact test". In: *Shock Waves Condens. Matter 1983*. Elsevier, 1984, pp. 129–132. DOI: 10.1016/B978-0-444-86904-3.50030-0.

[197] Joel W. House. *Taylor Impact Testing*. Tech. rep. September. 1989, p. 120. URL: https://apps.dtic.mil/sti/pdfs/ADA215018.pdf.

[198] Donald R. Snyder, Leonard L. Wilson, and Joel W. House. "Analysis Of High Speed Framing Camera Data For The Development Of Material Models Used In Penetration Mechanics." In: *Ultrah. Speed High Speed Photogr. Photonics, Videogr. '89 Seventh a Ser.* 1155.January 1990 (1990), p. 34. ISSN: 1996756X. DOI: 10.1117/12.962401.

[199] I. Rohr, H. Nahme, and K. Thoma. "A modified TAYLOR-test in combination with numerical simulations - a new approach for the determination of model parameters under dynamic loads". In: *J. Phys. IV* 110 (Sept. 2003), pp. 513–518. ISSN: 1155-4339. DOI: 10.1051/jp4:20020745.

[200] L. M. Barker and R. E. Hollenbach. "Laser interferometer for measuring high velocities of any reflecting surface". In: *J. Appl. Phys.* 43.11 (Nov. 1972), pp. 4669–4675. ISSN: 0021-8979. DOI: 10.1063/1.1660986.

[201] David J. Chapman et al. "Shock induced void nucleation during Taylor impact". In: *Int. J. Fract.* 134.1 (July 2005), pp. 41–57. ISSN: 0376-9429. DOI: 10.1007/s10704-005-7151-1.

[202] S.M. Walley et al. "A novel technique for performing symmetric Taylor impact". In: *EPJ Web Conf.* 94 (Sept. 2015). Ed. by E. Cadoni, p. 01029. ISSN: 2100-014X. DOI: 10.1051/epjconf/20159401029.

[203] Cavitar Ltd. *Cavitar Products*. 2022. URL: https://www.cavitar.com/products.

[204] Joel W. House, Leonard L. Wilson, and Michael E. Nixon. "High Strain-Rate Material Behavior Using Taylor Anvil Experiments". In: *Mech. Behav. Mater. VI, Proc. Sixth Int. Conf. Kyoto, Japan, 29 July - 2 August 1991*. Ed. by Masahiro Jono and Tatsuo Inoue. Kyoto: Elsevier, 1992, pp. 343–349. DOI: 10.1016/B978-0-08-037890-9.50061-2.

[205] E. Wielewski et al. "A method for the in situ measurement of evolving elliptical cross-sections in initially cylindrical Taylor impact specimens". In: *J. Strain Anal. Eng. Des.* 45.6 (Aug. 2010), pp. 429–437. ISSN: 0309-3247. DOI: 10.1243/03093247JSA639.

[206] Daniel E. Eakins and N.N. Thadhani. "Analysis of dynamic mechanical behavior in reverse Taylor anvil-on-rod impact tests". In: *Int. J. Impact Eng.* 34.11 (Nov. 2007), pp. 1821–1834. ISSN: 0734743X. DOI: 10.1016/j.ijimpeng.2006.11.001.

[207] Daniel E. Eakins and N.N. Thadhani. "Instrumented Taylor anvil-on-rod impact tests for validating applicability of standard strength models to transient deformation states". In: *J. Appl. Phys.* 100.7 (Oct. 2006), p. 073503. ISSN: 0021-8979. DOI: 10.1063/1.2354326.

[208] I. Rohr, H. Nahme, and K. Thoma. "Material characterization and constitutive modelling of ductile high strength steel for a wide range of strain rates". In: *Int. J. Impact Eng.* 31.4 (Apr. 2005), pp. 401–433. ISSN: 0734743X. DOI: 10.1016/j.ijimpeng.2004.02.005.

[209] I. Rohr et al. "Material characterisation and constitutive modelling of a tungsten-sintered alloy for a wide range of strain rates". In: *Int. J. Impact Eng.* 35.8 (Aug. 2008), pp. 811–819. ISSN: 0734743X. DOI: 10.1016/j.ijimpeng.2007.12.006.

[210] F. Bagusat and I. Rohr. "Modified Taylor-tests with miniaturized samples". In: *EPJ Web Conf.* 26 (Aug. 2012), p. 01007. ISSN: 2100-014X. DOI: 10.1051/epjconf/20122601007.

[211] J. C. Jonsson et al. "Effect of texture on elastic precursor decay in magnesium alloy AZ31B". In: *AIP Conf. Proc.* 2272.November (2020). ISSN: 15517616. DOI: 10.1063/12.0000818.

[212] Cyril L. Williams, K. T. Ramesh, and D. P. Dandekar. "Spall response of 1100-O aluminum". In: *J. Appl. Phys.* 111.12 (June 2012), p. 123528. ISSN: 0021-8979. DOI: 10.1063/1.4729305.

[213] Michael E. Rutherford et al. "Probing the early stages of shock-induced chondritic meteorite formation at the mesoscale". In: *Sci. Rep.* 7.1 (May 2017), p. 45206. ISSN: 2045-2322. DOI: 10.1038/srep45206.

[214] Emilio M. Escauriza et al. "Ultra-high-speed indirect x-ray imaging system with versatile spatiotemporal sampling capabilities". In: *Appl. Opt.* 57.18 (2018), p. 5004. ISSN: 1559-128X. DOI: 10.1364/ao.57.005004.

[215] Emilio M. Escauriza et al. "Ultra-high-speed X-ray imaging of shock-induced cavity collapse in a solid medium". In: *AIP Conf. Proc.* 2272.November (2020). ISSN: 15517616. DOI: 10.1063/12.0000933.

[216] Lukasz Farbaniec et al. "In-situ visualisation of dynamic fracture and fragmentation of an L-type ordinary chondrite by combined synchrotron

X-ray radiography and microtomography". In: *Icarus* 359.December 2020 (2021), p. 114346. ISSN: 10902643. DOI: 10.1016/j.icarus.2021.114346.

[217] Robert M. Malone et al. "Photonic Doppler velocimetry probe used to measure grain boundaries of dynamic shocked materials". In: *Opt. Syst. Alignment, Toler. Verif. XI*. Ed. by José Sasián and Richard N. Youngworth. Vol. 1037704. August 2017. SPIE, Aug. 2017, p. 3. ISBN: 9781510612112. DOI: 10.1117/12.2276436.

[218] G. D. Owen et al. "Spall behaviour of single crystal aluminium at three principal orientations". In: *J. Appl. Phys.* 122.15 (Oct. 2017), p. 155102. ISSN: 0021-8979. DOI: 10.1063/1.4999559.

[219] Jacek J. Skrzypek and Artur W. Ganczarski. *Mechanics of Anisotropic Materials*. Ed. by Jacek J. Skrzypek and Artur W. Ganczarski. Engineering Materials. Cham: Springer International Publishing, 2015. ISBN: 978-3-319-17159-3. DOI: 10.1007/978-3-319-17160-9.

[220] William Prager. "Recent developments in the mathematical theory of plasticity". In: *J. Appl. Phys.* 20.3 (1949), pp. 235–241. ISSN: 00218979. DOI: 10.1063/1.1698348.

[221] D. C. Drucker. "Some implications of work hardening and ideal plasticity". In: *Q. Appl. Math.* 7.4 (1950), pp. 411–418. ISSN: 0033-569X. DOI: 10.1090/qam/34210.

[222] D. C. Drucker. "A more fundamental approach to plastic stress-strain relations". In: *Proc. 1st U.S. Natl. Congr. Appl. Mech.* 1951, pp. 487–491.

[223] D. C. Drucker, W. Prager, and H. J. Greenberg. "Extended limit design theorems for continuous media". In: *Q. Appl. Math.* 9.4 (1952), pp. 381–389. ISSN: 0033-569X. DOI: 10.1090/qam/45573.

[224] Livermore Software Technology Corporation (LSTC). *LS-DYNA Keyword User's Manual*. R12 Vol. 1. Livermore Software Technology Corporation, 2020. URL: https://www.lstc.com/download/manuals.

[225] Livermore Software Technology Corporation and (LSTC). *LS-DYNA Keyword User's Manual*. R12 Vol. 3. Livermore Software Technology Corporation, 2020. URL: https://www.lstc.com/download/manuals.

[226] N. Tounsi et al. "From the basic mechanics of orthogonal metal cutting toward the identification of the constitutive equation". In: *Int. J. Mach. Tools Manuf.* 42.12 (Sept. 2002), pp. 1373–1383. ISSN: 08906955. DOI: 10.1016/S0890-6955(02)00046-9.

[227] H. Chandrasekaran, R. M'Saoubi, and H. Chazal. "Modelling of material flow stress in chip formation process from orthogonal milling and split Hopkinson tests." In: *Mach. Sci. Technol.* 9.1 (Mar. 2005), pp. 131–145. ISSN: 1091-0344. DOI: 10.1081/MST-200051380.

[228] D. Umbrello, R. M'Saoubi, and J.C. Outeiro. "The influence of Johnson–Cook material constants on finite element simulation of machining of AISI 316L steel". In: *Int. J. Mach. Tools Manuf.* 47.3-4 (Mar. 2007), pp. 462–470. ISSN: 08906955. DOI: 10.1016/j.ijmachtools.2006.06.006.

[229] Anthony Atkinson, Alexander Donev, and Randall Tobias. *Optimum Experimental Designs, With SAS*. Vol. 34. OUP Oxford, 2007. ISBN: 9780199296606. URL: https://global.oup.com/academic/product/optimum-experimental-designs-with-sas-9780199296606.

[230] Nielen Stander et al. *LS-OPT User's Manual*. 4.1. December. Livermore Software Technology Corporation, 2010. URL: https://www.lstc.com/download/manuals.

[231] Alexander M. Korsunsky, Marco Sebastiani, and Edoardo Bemporad. "Focused ion beam ring drilling for residual stress evaluation". In: *Mater. Lett.* 63.22 (Sept. 2009), pp. 1961–1963. ISSN: 0167577X. DOI: 10.1016/j.matlet.2009.06.020.

[232] Alexander M. Korsunsky, Marco Sebastiani, and Edoardo Bemporad. "Residual stress evaluation at the micrometer scale: Analysis of thin coatings by FIB milling and digital image correlation". In: *Surf. Coatings Technol.* 205.7 (Dec. 2010), pp. 2393–2403. ISSN: 02578972. DOI: 10.1016/j.surfcoat.2010.09.033.

[233] Lars Westerling. *An implicit method for a strain rate dependent constitutive model implemented in AUTODYN as a user subroutine.* Tech. rep. Tumba: FOI – Swedish Defence Research Agency Weapons and Protection, 2002. URL: https://www.foi.se/rest-api/report/FOI-R--0310--SE.

[234] S.A. Silling. "Stability and Accuracy of Differencing Methods for Viscoplastic Models in Wavecodes". In: *J. Comput. Phys.* 104.1 (Jan. 1993), pp. 30–40. ISSN: 00219991. DOI: 10.1006/jcph.1993.1004.

[235] Lars Westerling. *Test of the new implementation of the johnson-cook model in autodyn.* Tech. rep. June. 2004, FOI–R—-1280—SE. URL: https://www.foi.se/rest-api/report/FOI-R--1280--SE.

[236] Frank J. Zerilli and Ronald W. Armstrong. "Dislocation-mechanics-based constitutive relations for material dynamics calculations". In: *J. Appl. Phys.* 61.5 (Mar. 1987), pp. 1816–1825. ISSN: 0021-8979. DOI: 10.1063/1.338024.

[237] Frank J. Zerilli and Ronald W. Armstrong. "The effect of dislocation drag on the stress-strain behavior of F.C.C. metals". In: *Acta Metall. Mater.* 40.8 (Aug. 1992), pp. 1803–1808. ISSN: 09567151. DOI: 10.1016/0956-7151(92)90166-C.

[238] D. J. Steinberg, S. G. Cochran, and Michael W. Guinan. "A constitutive model for metals applicable at high-strain rate". In: *J. Appl. Phys.* 51.3 (Mar. 1980), pp. 1498–1504. ISSN: 0021-8979. DOI: 10.1063/1.327799.

[239] A.L. Oppedal et al. "Anisotropy in hexagonal close-packed structures: improvements to crystal plasticity approaches applied to magnesium alloy". In: *Philos. Mag.* 93.35 (Dec. 2013), pp. 4311–4330. ISSN: 1478-6435. DOI: 10.1080/14786435.2013.827802.

[240] Kartik Kapoor et al. "Modeling Ti–6Al–4V using crystal plasticity, calibrated with multi-scale experiments, to understand the effect of the orientation and morphology of the α and β phases on time dependent cyclic loading". In: *J. Mech. Phys. Solids* 146.April 2020 (2021), p. 104192. ISSN: 00225096. DOI: 10.1016/j.jmps.2020.104192.

Part V

Appendix

Within the following section extra data are presented that were deemed too in-depth for the main body of the work and therefore omitted. However, this data is still important to the project, so is included here for completeness.

Chapter 13

Additional Experimental Data

Within this chapter, an example is provided for light gate analysis, referenced in both Taylor and spallation sections previously. Following this the dataset from reverse Taylor surface velocimetry is given for completeness.

13.1 Light Gate Example

Within all experimental setups for both reverse Taylor or spallation testing presented in this thesis, paired laser light gates were fielded in order to provide reliable triggering and redundant impact velocity measurement. Needed for both ultra high speed imaging and laser velocimetry diagnostics that are significantly limited in measurement duration, simple edge based triggers depending upon the signal magnitude allowed reliable digitiser timings with delay pulse generators then used to account for large muzzle target standoff distances.

As seen in figure 13.1, processing of light gate waveforms for redundant velocity calculations was achieved by fitting each raw voltage signal with a complementary error function defined such that,

$$V = x_1 \operatorname{erf}\left(x_2 \left(t - x_3\right)\right) + x_4.$$

With x a 4 element set of coefficients evaluated by standard regression techniques, V the signal voltage, and t the signal time. Given suitable initial coefficient estimations, a fit as seen in figure 13.1b is achieved, with the characteristic trigger time evaluated at the 50 % point, by definition equal to the offset x_3. From here the second voltage waveform is fitted with the delay between 50 % points providing a time delay between light gates at a known spacing, with errors in the resultant velocity propagated from errors in fitting with standard procedures.

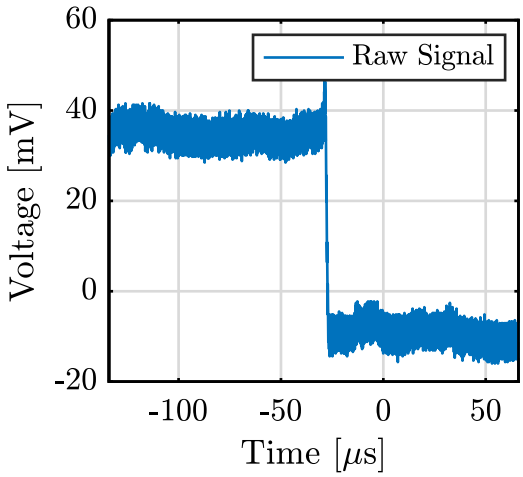

(a) Raw signal.

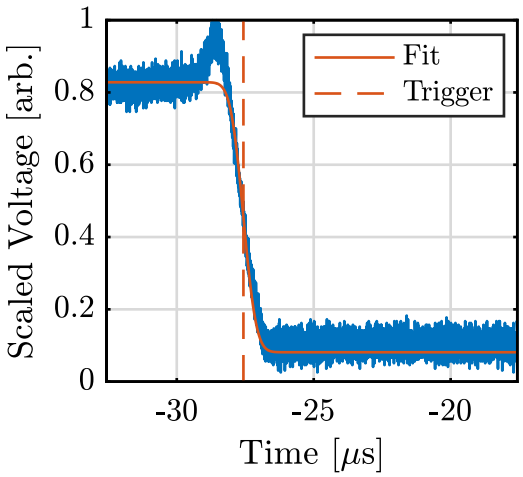

(b) Fit result.

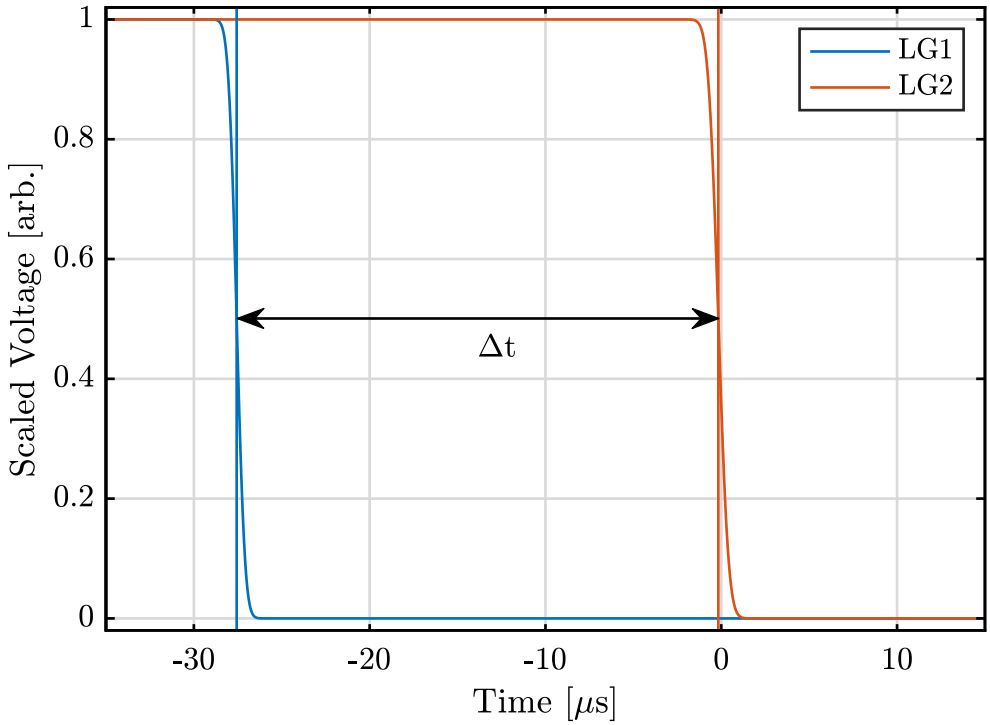

(c) Trigger delay, Δt, between fitted light gate waveforms.

Figure 13.1: Example of an impact velocity calculation using light gate signal(s) shown from raw to processed states using a complementary error function to reliably identify the 50 % signal level. It should be noted that diagnostic triggers, whilst still using the same signal, instead applied regular edge-type triggers to identify the signal falling through a preset threshold.

13.2 Reverse Taylor Impact Data

For completeness, recorded surface velocimetry traces are presented below. In each plot both flyer impact surface and target rear surface histories are given. Linking the presented data to the rest of the thesis, the unique ShotID given in the caption.

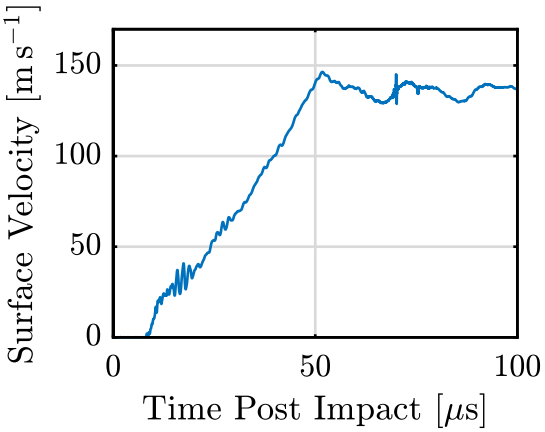

(a) Target rear surface.

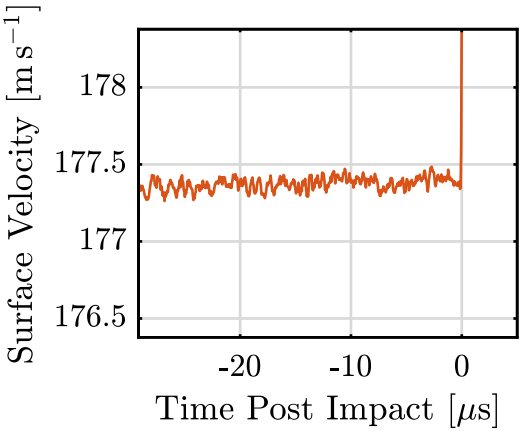

(b) Flyer impact surface.

Figure 13.2: Velocity data for experiment CM RT TT 1.

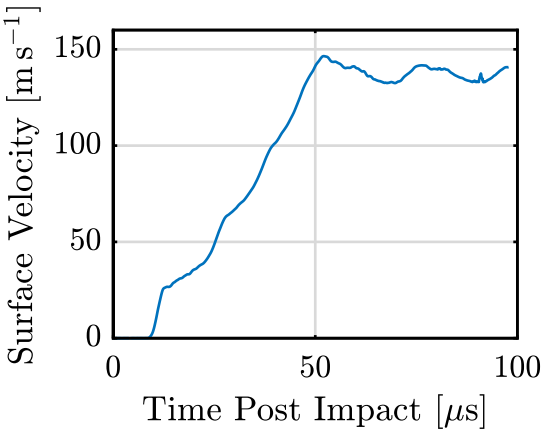

(a) Target rear surface.

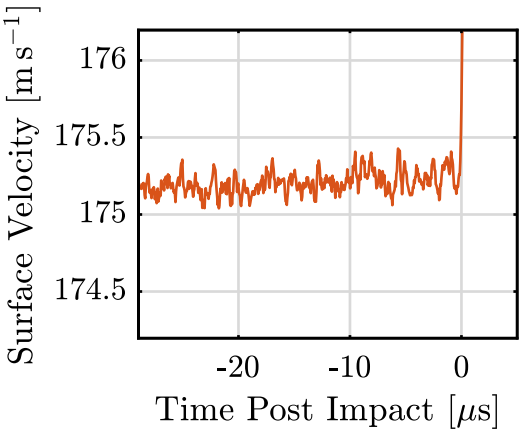

(b) Flyer impact surface.

Figure 13.3: Velocity data for experiment AM V POR RT TT 1

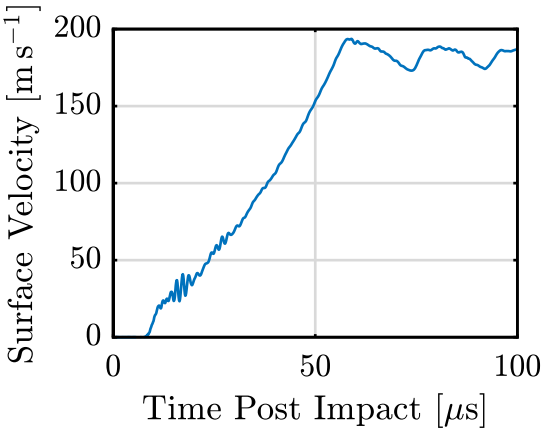

(a) Target rear surface.

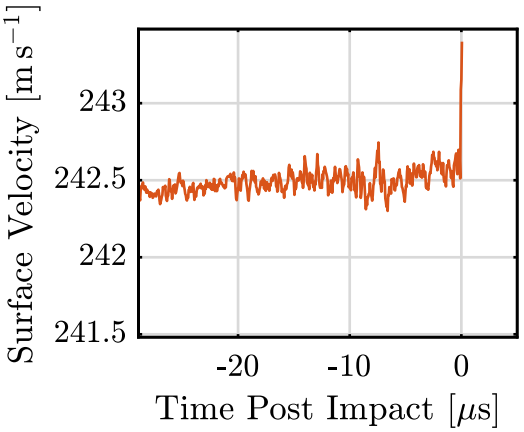

(b) Flyer impact surface.

Figure 13.4: Velocity data for experiment CM RT TT 2

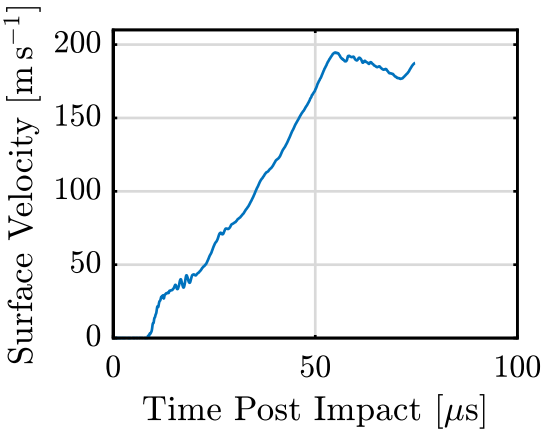

(a) Target rear surface.

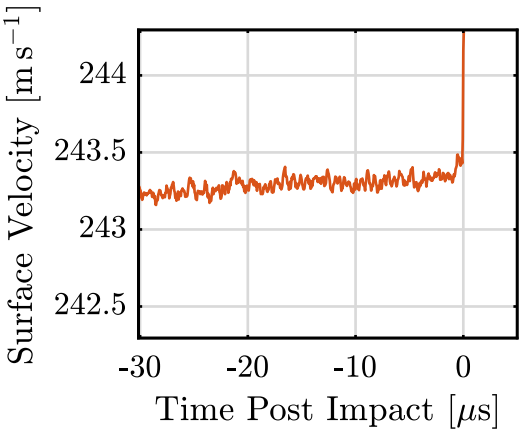

(b) Flyer impact surface.

Figure 13.5: Velocity data for experiment AM H POR RT TT 2

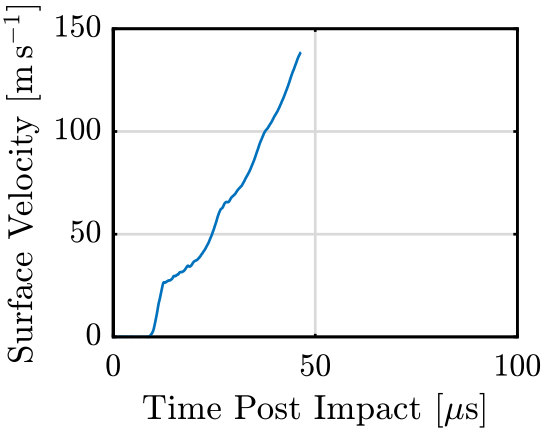

(a) Target rear surface.

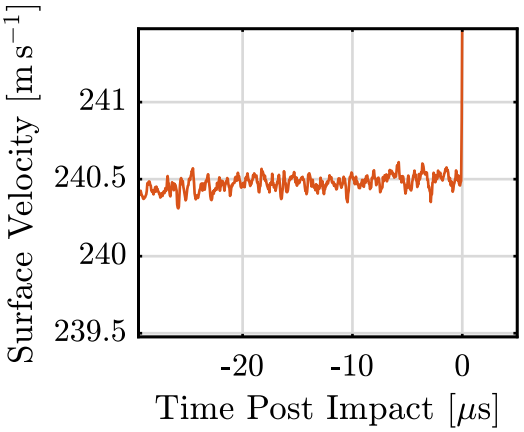

(b) Flyer impact surface.

Figure 13.6: Velocity data for experiment AM V POR RT TT 2

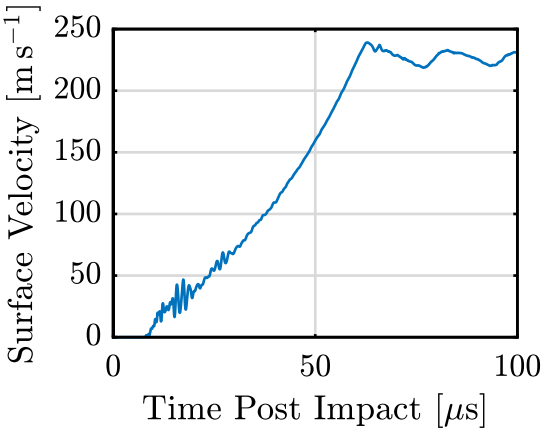

(a) Target rear surface.

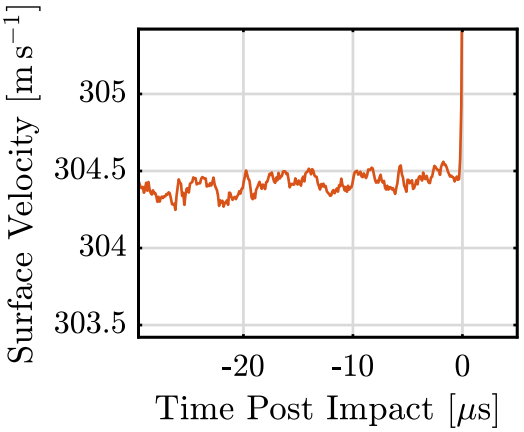

(b) Flyer impact surface.

Figure 13.7: Velocity data for experiment CM RT TT 3

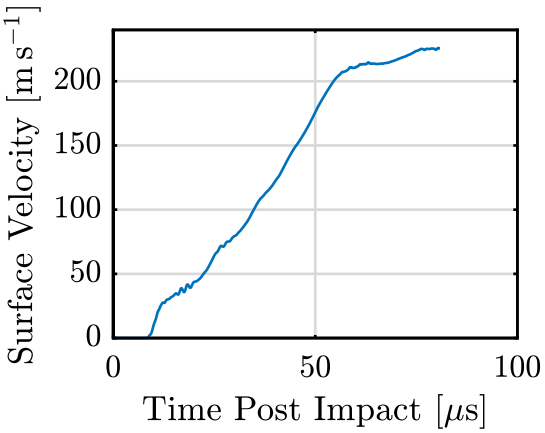

(a) Target rear surface.

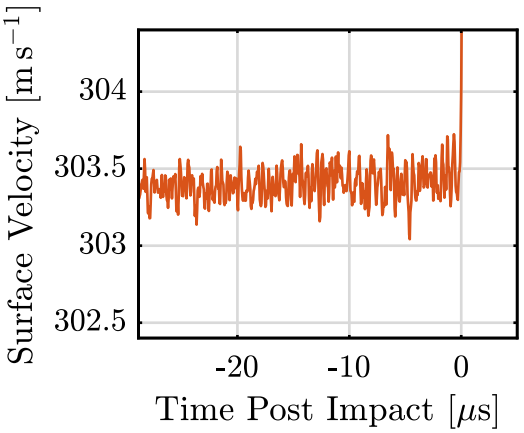

(b) Flyer impact surface.

Figure 13.8: Velocity data for experiment AM H POR RT TT 3

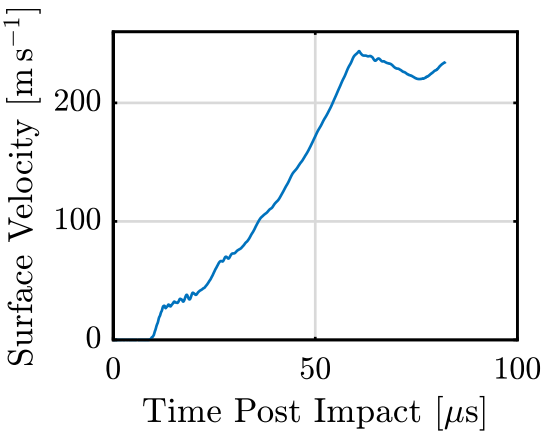

(a) Target rear surface.

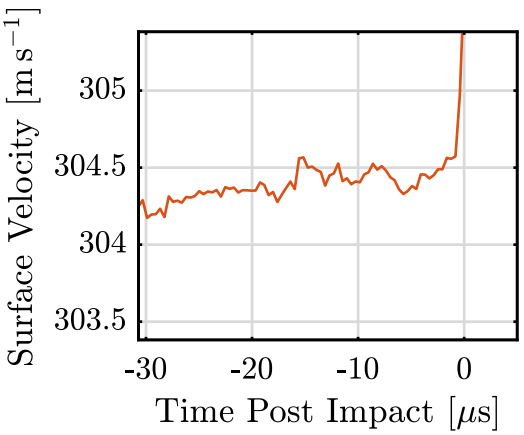

(b) Flyer impact surface.

Figure 13.9: Velocity data for experiment AM V POR RT TT 3

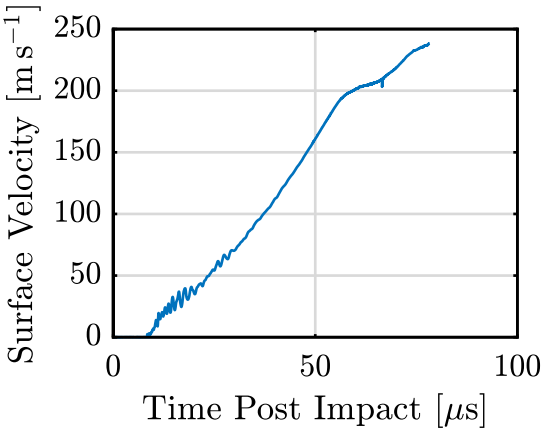

(a) Target rear surface.

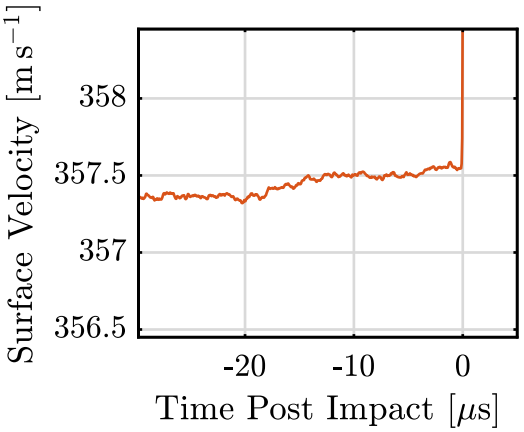

(b) Flyer impact surface.

Figure 13.10: Velocity data for experiment CM RT TT 4

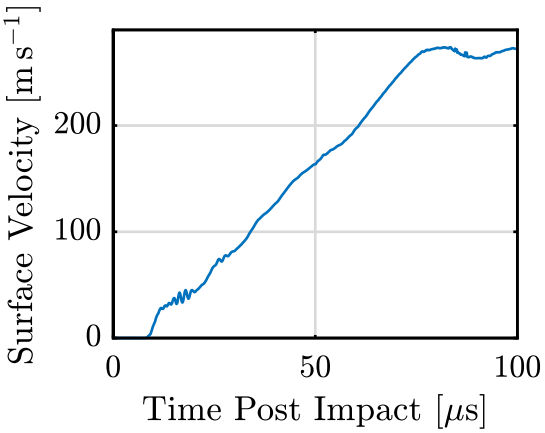

(a) Target rear surface.

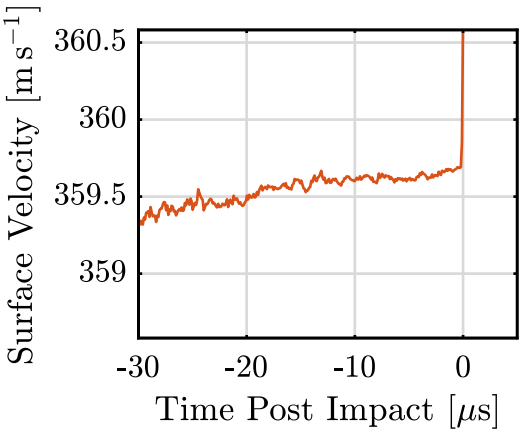

(b) Flyer impact surface.

Figure 13.11: Velocity data for experiment AM H POR RT TT 4

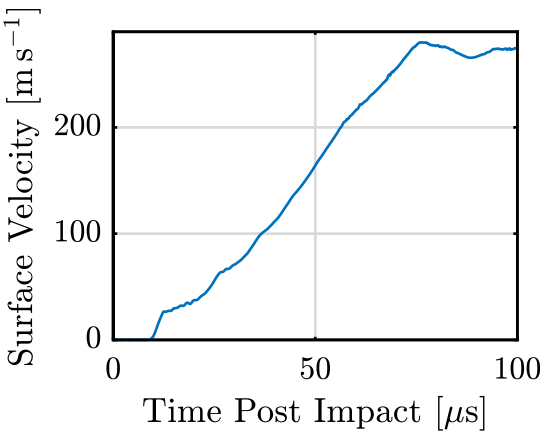

(a) Target rear surface.

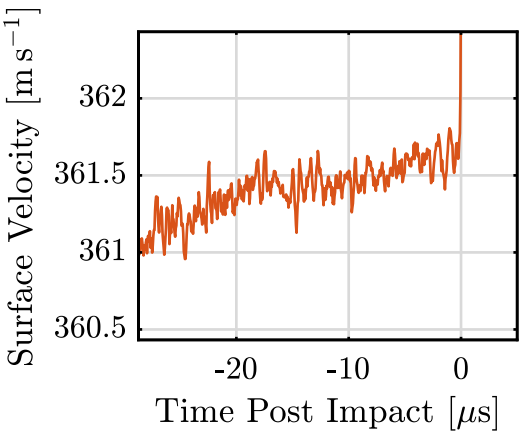

(b) Flyer impact surface.

Figure 13.12: Velocity data for experiment AM V POR RT TT 4

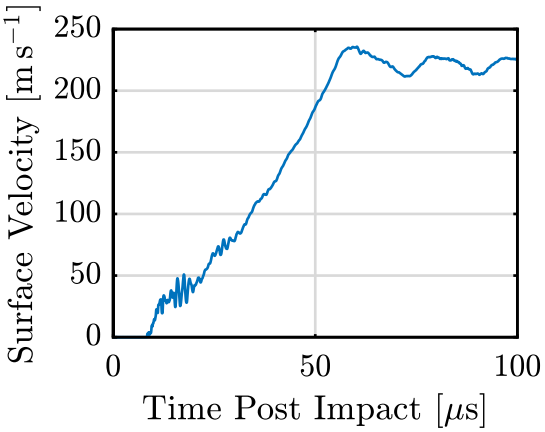

(a) Target rear surface.

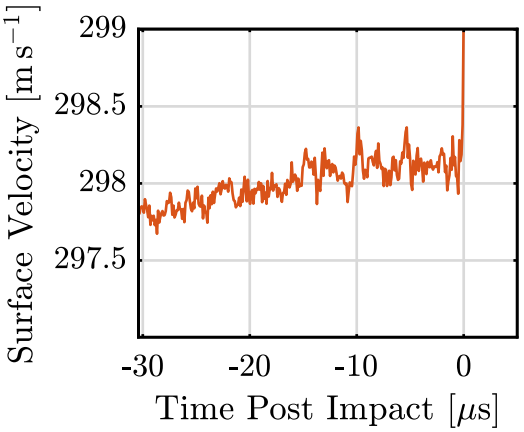

(b) Flyer impact surface.

Figure 13.13: Velocity data for experiment AM V DEN RT TT 2

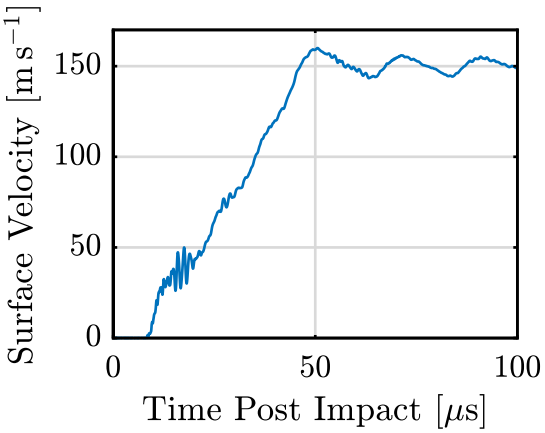

(a) Target rear surface.

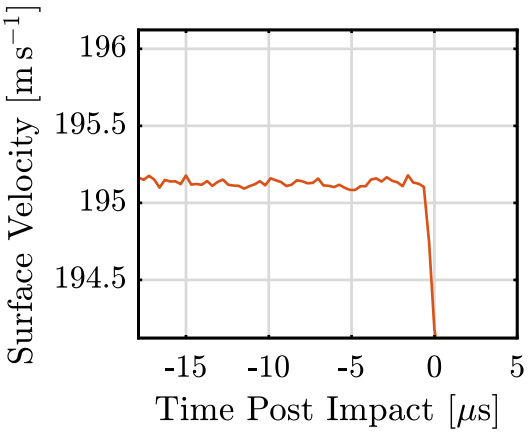

(b) Flyer impact surface.

Figure 13.14: Velocity data for experiment AM H DEN RT TT 1

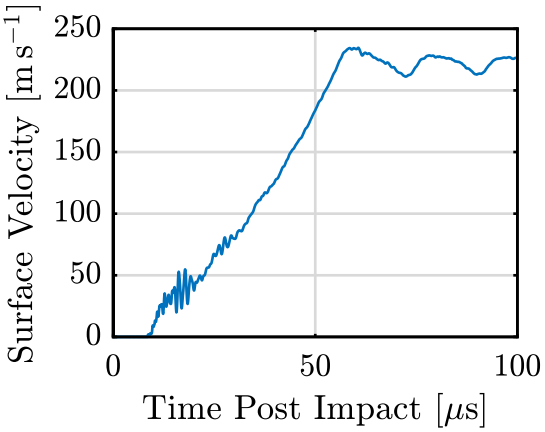

(a) Target rear surface.

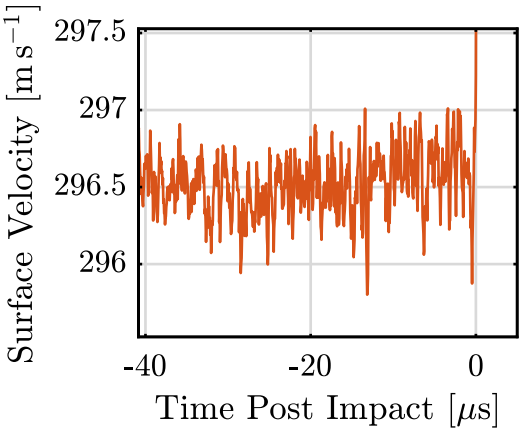

(b) Flyer impact surface.

Figure 13.15: Velocity data for experiment AM H DEN RT TT 2

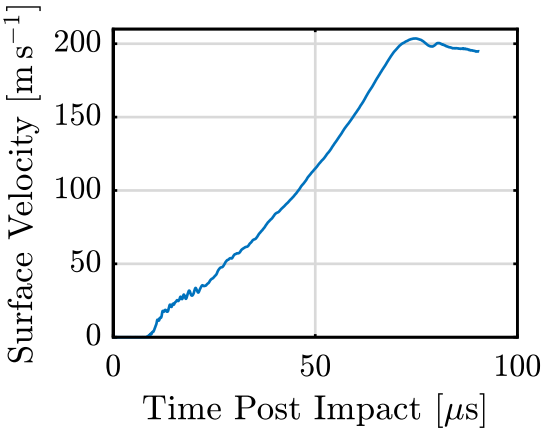

(a) Target rear surface.

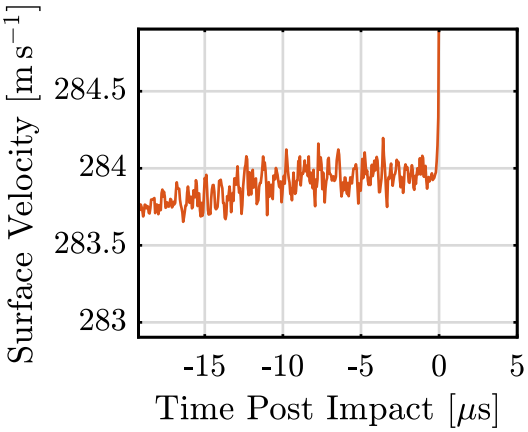

(b) Flyer impact surface.

Figure 13.16: Velocity data for experiment AM H DEN HT TT 1

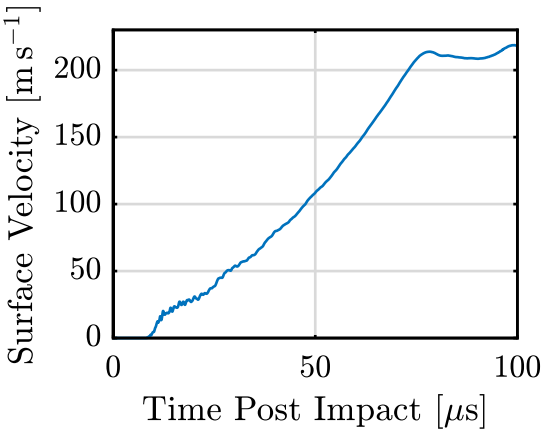

(a) Target rear surface.

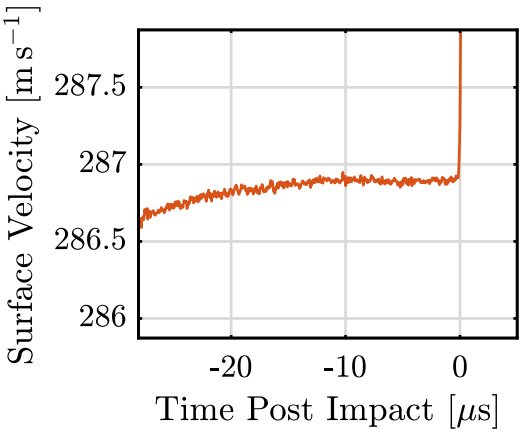

(b) Flyer impact surface.

Figure 13.17: Velocity data for experiment AM V DEN HT TT 1

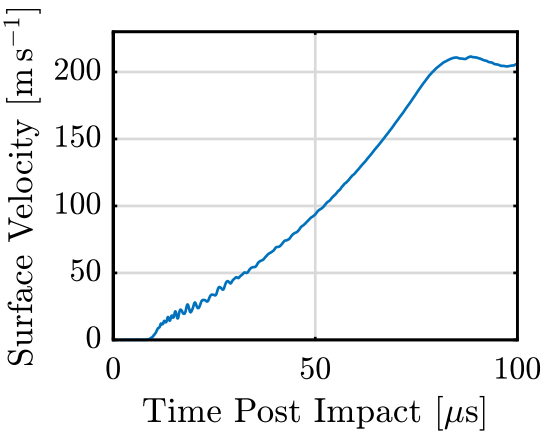

(a) Target rear surface.

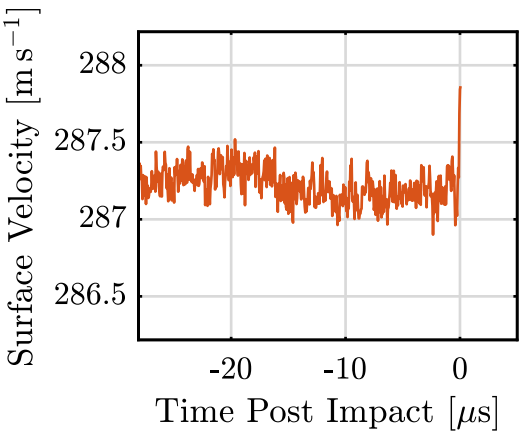

(b) Flyer impact surface.

Figure 13.18: Velocity data for experiment CM HT TT 1